

The Development of a Research Technique for Low Speed Aeroacoustics

by

Adam D. McPhee

A thesis
presented to the University of Waterloo
in fulfillment of the
thesis requirement for the degree of
Master of Applied Science
in
Mechanical Engineering

Waterloo, Ontario, Canada, 2008

© Adam D. McPhee 2008

I hereby declare that I am the sole author of this thesis. This is a true copy of the thesis, including any required final revisions, as accepted by my examiners.

I understand that my thesis may be made electronically available to the public.

Abstract

The aerodynamic sound generated by wind turbines was identified as a growing concern within the industry. Prior to performing wind turbine aeroacoustic research, however, a technique suitable for studying low speed airfoils needed to be designed, serving as the primary research objective. A review of aeroacoustic theory and literature indicated that low speed flows are best studied using experimental methods, leading to the design of a near field pressure measurement technique. To facilitate the near field pressure measurements, a custom piezoelectric sensor was developed, exhibiting a pressure and frequency range of approximately 67 to 140[dB], and 100 to 10 000[Hz], respectively. As a secondary research objective, a series of experiments were performed to validate the designed technique. The experiments were performed in a non-anechoic wind tunnel using a cylindrical test specimen. Using the near field pressure measurements, as well as a simple far field measurement, the sources of aerodynamic sound were effectively resolved. The Strouhal numbers corresponding to the contributing flow structures were generally within 1.5[%] of correlation based predictions. The near field pressures were consistently 10 to 15[dB] higher than the far field, quantifying the benefit of the near field technique. The method was also effective in detecting the decreasing coherence of the aeroacoustic sources with increasing Reynolds number. A minor deficiency was observed in which the ability to localize aeroacoustic sources was impeded, however, the cylinder experiments were particularly vulnerable to such a deficiency. Although the near field pressure measurements were shown to be effective in characterizing the aeroacoustic sources, a number of recommendations are presented to further improve the flexibility and measurement uncertainty of the experimental technique.

Acknowledgements

I would like to thank the individuals at the university who have made this research possible. To my supervisor, Dr. David Johnson, thank you for allowing me to pursue an area of research of personal interest and for supporting my development efforts. Furthermore, thank you for developing my interest in experimental methods, providing me with a wealth of experimental theory, and your continuous input into my research. To Dr. Serhiy Yarusevych, thank you for the numerous academic discussions and providing insight into my research. Finally, to Stephen Orlando, thank you for your help in manufacturing experimental setups and for performing LDV measurements to characterize the wind tunnel.

I would also like to extend a special thanks to my family. To my brother Kevin, thank you for finding the time to proof this thesis with such an attention to detail. To my brother Dwayne, thank you for your continued motivational support. Having both you and Kevin close has truly made the past few years both enjoyable and memorable. To my parents, Bill and Sharon, I cannot thank you enough for your continued motivational, emotional, and financial support in all of my endeavours. My academic abilities, attention to detail, and work ethic are truly a reflection of my strong upbringing, in which you have always emphasized the importance of education and challenged me by humorously inquiring about the remaining one percent. This thesis is as much a statement of your contributions, as it is mine, and it is with great honour that I dedicate it to you, with love.

...when you can measure what you are speaking about, and express it in numbers, you know something about it; but when you cannot measure it, when you cannot express it in numbers, your knowledge is of a meagre and unsatisfactory kind; it may be the beginning of knowledge, but you have scarcely in your thoughts advanced to the state of Science, whatever the matter may be.

- Lord Kelvin

Contents

List of Tables	xi
List of Figures	xiii
Nomenclature	xix
1 Introduction	1
1.1 Problem Statement	1
1.2 Objectives	3
1.3 Outline	3
2 Aeroacoustic Theory	5
2.1 Equations of Motion	5
2.2 Wave Equation of Classical Acoustics	6
2.3 Lighthill's Acoustic Analogy	9
2.4 Ffowcs Williams-Hawkings Equation	10
2.5 Summary	11
3 Literature Review	13
3.1 Analytical Techniques	13
3.2 Numerical Techniques	14
3.3 Experimental Techniques	17
3.3.1 Far Field Pressure Measurements	17
3.3.2 Near Field Pressure Measurements	27
3.3.3 Near Field Flow Measurements	30
3.4 Semi-Empirical Techniques	34
3.5 Summary	39

4	Evaluation of Experimental Techniques	41
5	Design of Experimental Technique	45
5.1	Near Field Pressure Measurements	46
5.1.1	Sensor Constraints	46
5.1.2	Sensor Criteria	48
5.1.3	Sensor Technology Evaluation	49
5.1.4	Sensor Design	53
5.1.5	Sensor Calibration	70
5.2	Far Field Pressure Measurements	83
5.3	Data Acquisition	83
6	Validation of Experimental Technique	87
6.1	Experimental Setup	88
6.1.1	Wind Tunnel	88
6.1.2	Test Specimen	105
6.1.3	Far Field Pressure Measurements	112
6.1.4	Data Acquisition	113
6.2	Procedure	116
6.3	Results and Analysis	118
6.3.1	Data Processing	118
6.3.2	Quantifying Aeroacoustic Sources	121
6.3.3	Locating Aeroacoustic Sources	125
6.3.4	Near Field Symmetry	128
7	Conclusions	131
8	Recommendations	135
	References	137
	Appendices	
A	Sensor Calibration: LabVIEW Software	145
B	Wind Tunnel Test Section: Manufacturing Drawings	155

C Validation Experiments: LabVIEW Software	159
D Validation Experiments: MATLAB Software	165
E Validation Experiments: Results	179

List of Tables

4.1	Evaluation of experimental techniques.	43
5.1	Evaluation of proposed sensor technologies.	52
5.2	PVDF film specifications. (<i>Data from Measurement Specialties [59].</i>)	53
5.3	Electrical conductivity (s_r) and permeability (m_r) of select materials relative to copper. (<i>Data from Paul [79].</i>)	58
5.4	Characteristics of operational amplifiers for typical operating param- eters.	59
5.5	Comparison of data acquisition systems.	84
5.6	Specifications for data acquisition boards.	84
6.1	Wind tunnel specifications.	90
6.2	Pitot-static tube pressure transducers' specifications.	97
6.3	Pitot-static tube pressure transducers' RMS noise measurements.	98
6.4	Test specimen constraints.	108
6.5	Validation experiments.	118

List of Figures

1.1	Airfoil flow mechanisms contributing to aerodynamic sound. (<i>Adapted from Brooks et al. [14].</i>)	2
1.2	Sound pressures of individual aeroacoustic sources versus mean wind speed for a full scale wind turbine. (<i>Data from Moriarty and Migliore [65].</i>)	3
2.1	Directivity of multipole acoustic sources.	8
3.1	Experimental technique: simple far field measurement.	18
3.2	Far field noise measurement for a full scale wind turbine. (<i>From Huskey et al. [41].</i>)	18
3.3	Experimental technique: acoustic mirror.	19
3.4	Experimental technique: transducer pair.	20
3.5	Cross-correlation for microphone pair in NASA airfoil self-noise study. Arrows indicate predicted values of τ . (<i>From Brooks and Marcolini [11].</i>)	21
3.6	Experimental technique: phased array.	22
3.7	Phased array sensor arrangements.	23
3.8	Phased array results for an S822 airfoil. (<i>From Migliore and Oerlemans [63].</i>)	24
3.9	Comparison of phased array (solid line) to NASA experimental results for NACA 0012 airfoil trailing edge noise. (<i>From Migliore and Oerlemans [63].</i>)	24
3.10	Phased array measurements for the swept area of a full scale wind turbine. The coordinates are shown in meters and the range of the contour scale is 12[dB]. (<i>From Oerlemans and López [75].</i>)	26
3.11	Experimental technique: near field pressure.	27
3.12	Measured (solid line) and predicted (based on near field pressure, dashed line) trailing edge noise for a NACA 0012 airfoil. (<i>From Brooks and Hodgson [9].</i>)	29

3.13	Near to far field correlation at the flap side edge for different fence configurations. (<i>From Guo et al. [25].</i>)	30
3.14	Experimental technique: near field flow.	31
3.15	Scaling of sound pressure level versus Strouhal number for NACA 0012 airfoils using measured boundary layer characteristics. (<i>From Brooks and Marcolini [11].</i>)	32
3.16	Measured and predicted boundary layer characteristics versus angle of attack for a NACA 0012 airfoil. (<i>From Brooks and Marcolini [13].</i>)	32
3.17	HWA based prediction of turbulence ingestion noise for a 4-bladed fan rotor. (<i>From Lynch et al. [55].</i>)	33
3.18	PIV vorticity measurements of flap side edge noise structures: (c) without and (1) with active flow control. (<i>From Koop et al. [46].</i>) .	34
3.19	Semi-empirical prediction of turbulence ingestion noise. (<i>From Paterson and Amiet [78].</i>)	35
3.20	Semi-empirical prediction of aeroacoustic emissions for a full scale wind turbine. (<i>From Grosveld [24].</i>)	36
3.21	Semi-empirical prediction and experiment results for a NACA 0012 airfoil self-noise at $\alpha_c=6^\circ$. (<i>From Brooks et al. [14].</i>)	37
3.22	Semi-empirical prediction of aeroacoustic emissions versus wind speed for a full scale wind turbine. (<i>From Migliore and Oerlemans [63].</i>) .	38
5.1	Normalized pressure versus frequency for the sensing line measurement of a sinusoidal source.	47
5.2	Airfoil geometry common to aeroacoustic experiments.	48
5.3	Comparison of pressure sensor technologies.	50
5.4	PVDF film samples.	54
5.5	Sensor prototype: first generation.	56
5.6	Proper grounding of electrical shielding.	58
5.7	Sensor amplification circuit.	60
5.8	Sensor prototype: second generation.	61
5.9	Sensor components.	62
5.10	Methods of fixing the diaphragm to the sensor inner.	63
5.11	Frequency response of a pressure transducer for both an ideal and an improper sensing port. (<i>From Mueller [67].</i>)	66
5.12	Frequency response of the sensing port and the resulting effect on the sensor.	67

5.13	Sensor design.	68
5.14	Sensor mounting.	69
5.15	Sensor prototype: third generation.	70
5.16	Anechoic foam design.	73
5.17	Anechoic chamber.	73
5.18	Frequency response of speakers selected for the calibration setup. (Data from B&C [8][7].)	75
5.19	Anechoic chamber with speakers installed.	75
5.20	Amplification circuit design for the anechoic chamber speakers.	76
5.21	Amplification circuit and speaker connectors.	76
5.22	Sensor calibration coupling tube.	78
5.23	Frequency response of piezoelectric prototype and reference B&K sensor.	82
5.24	Amplitude response of piezoelectric prototype sensor.	82
6.1	University of Waterloo 0.61 by 0.91[m] variable wall wind tunnel.	89
6.2	University of Waterloo 0.15 by 0.15[m] closed return wind tunnel.	89
6.3	Wind tunnel test section geometry.	90
6.4	Wind tunnel test section mounting holes.	92
6.5	Wind tunnel test section revised.	92
6.6	Wind tunnel test section mounting to the inlet contraction.	93
6.7	Intermediate section serving as the transition between the inlet con- traction and the test section.	94
6.8	Mounted Pitot-static tube with plug.	95
6.9	Velocity error versus pressure for various Pitot-static tube pressure transducer uncertainties.	96
6.10	Velocity error versus velocity for defined Pitot-static tube pressure transducers.	96
6.11	Noise induced velocity RMS versus velocity for defined Pitot-static tube pressure transducers.	99
6.12	Wind tunnel axial fan.	100
6.13	Screen installed at outlet of wind tunnel test section.	101
6.14	Wind tunnel mean velocity and temperature versus drive frequency at 100[mm] from inlet.	103

6.15	Wind tunnel RMS velocity and turbulence intensity versus centreline velocity at 100[mm] from inlet.	103
6.16	Wind tunnel static pressure versus centreline velocity at 100[mm] from inlet.	104
6.17	Wind tunnel turbulence intensity and spatial uniformity versus centreline velocity at 100[mm] from inlet. (<i>Data from Orlando [77].</i>) . .	105
6.18	Unsteady flow structures for a cylinder subject to a cross-flow at $Re = 3.8 \cdot 10^4$	106
6.19	Strouhal number versus Reynolds number for a cylinder subject to a cross flow. (<i>From Fey et al. [22].</i>)	107
6.20	Test specimen specifications.	110
6.21	Test specimen showing nylon sleeve for near field pressure sensor. .	110
6.22	Test specimen completed.	111
6.23	Test specimen angular positioning disk.	112
6.24	Test specimen installed in wind tunnel.	113
6.25	Wind tunnel far field sensor mount.	114
6.26	Sensor voltages versus frequency for wind tunnel noise measurements at a velocity of 10[m s ⁻¹] and sampling rate of 192[kHz].	115
6.27	Near field pressure measurements for a nominal velocity of 15[m s ⁻¹] and cylinder angle of 135[°].	120
6.28	Far field pressure measurements for a nominal velocity of 15[m s ⁻¹] and cylinder angle of 135[°].	120
6.29	Temperature and Reynolds number versus corrected free stream velocity.	121
6.30	Near field pressure spectra for a range of corrected velocities and a cylinder angle of 135[°].	122
6.31	Far field pressure spectra for a range of corrected velocities and a cylinder angle of 135[°].	122
6.32	Measured and predicted peak Strouhal number versus Reynolds number.	124
6.33	Peak pressures and signal-to-noise ratios versus Reynolds number. .	124
6.34	Near field pressure spectra spatial plot for a nominal velocity of 5[m s ⁻¹].	126
6.35	Near field pressure spectra spatial plot for a nominal velocity of 10[m s ⁻¹].	126
6.36	Near field pressure spectra spatial plot for a nominal velocity of 20[m s ⁻¹].	126

6.37	Near field pressure spectra spatial symmetry plot for a nominal velocity of 15[m s ⁻¹].	129
E.1	Near field noise pressure spectra for a range of corrected velocities. .	180
E.2	Far field noise pressure spectra for a range of corrected velocities. .	180

Nomenclature

Roman symbols

b	Thickness [m]
c	Speed of sound [m s^{-1}]
C	Capacitance [F]
C_d	Drag coefficient
d	Diameter [m]
D	Piezoelectric strain constant [$\text{m m}^{-1} \text{Pa}^{-1}$]
E	Young's modulus [Pa]
f	Frequency [Hz]
f_n	Frequency, natural [Hz]
f_s	Frequency, sampling [Hz]
f_{sl}	Frequency, shear layer vortex shedding [Hz]
f_v	Frequency, wake region vortex shedding [Hz]
\mathbf{F}	Force vector [N]
\mathcal{F}	Generalized pressure source
G	Piezoelectric stress constant [$\text{V m}^{-1} \text{Pa}^{-1}$]
h	Height [m]
H	Heaviside function
I	Turbulence intensity
l	Length [m]
L_p	Sound pressure level [dB]
m_r	Electrical permeability, relative
M	Mach number
N	Number of samples
p	Pressure [Pa]
Q	Charge [C]
r	Radius [m]
R	Electrical resistance [Ω]
\mathcal{R}	Gas constant [$\text{J kg}^{-1} \text{K}^{-1}$]

Re	Reynolds number
s_r	Electrical conductivity, relative
S	Surface
St	Strouhal number
t	Time [s]
T	Temperature [K]
T_{ij}	Lighthill's stress tensor
u	Velocity, reference [m s^{-1}]
U	Voltage [V]
\mathbf{v}	Velocity, vector [m s^{-1}]
v	Velocity, scalar [m s^{-1}]
V_s	Volume, sensing line [m^3]
V_t	Volume, transducer [m^3]
\mathbf{x}, \mathbf{y}	Position [m]

Greek symbols

α	Angle of attack [$^\circ$]
δ	Kronecker delta
ϵ	Strain [m m^{-1}]
γ	Specific heat ratio
μ	Dynamic viscosity [$\text{kg m}^{-1} \text{s}^{-1}$]
ρ	Density [kg m^{-3}]
σ	Stress [Pa]
τ	Time delay [s]
θ	Angle [$^\circ$]
ζ	Damping ratio

Subscripts

c	Corrected
i, j, k	Vector and tensor indices
o	Mean
ref	Reference
rms	Root mean square

Superscripts

$'$	Fluctuating
-----	-------------

Chapter 1

Introduction

The need to investigate the aerodynamic sound generated by wind turbines required the development of a suitable research technique. This research falls under the field of aeroacoustics, which more generally encompasses the study of sound generated by fluid-borne structures and aerodynamic surfaces. The unsteady nature of aeroacoustics presents an inherently challenging area of fluid mechanics research, placing significant demands on analytical, numerical, and experimental techniques. As such, careful consideration of theory and literature was required to establish the most effective approach.

1.1 Problem Statement

The aerodynamic sound generated by wind turbines has become a significant concern within the industry. Attempts to lower energy production costs have significantly increased the size and power output of individual turbines, resulting in a corresponding increase in sound emissions [53]. Although aerodynamic sound has negligible effect on turbine efficiency, it is a very relevant issue because of the human perception of the sound being “subjectively annoying” [53]. Concerns have also been raised regarding the potential ecological impact of sound emissions, however, much of this research is still in its infancy. With the increasing prevalence of wind turbines, there has been a corresponding increase in public awareness, forcing governments to impose stringent noise regulations. Satisfying these regulations has often forced manufacturers to limit the tip speed of the device, which for smaller turbines, can lead to a substantial decrease in efficiency [63]. Developers have also been forced to limit the number of turbines in installations, decreasing the profitability of projects. Thus, aerodynamic sound can indirectly have substantial effects on energy production costs.

Attempts to mitigate aerodynamic sound are complicated by the numerous contributing flow mechanisms. For a typical airfoil, six distinct aeroacoustic sources may exist, as illustrated in Figure 1.1 which is based on a diagram by Brooks et

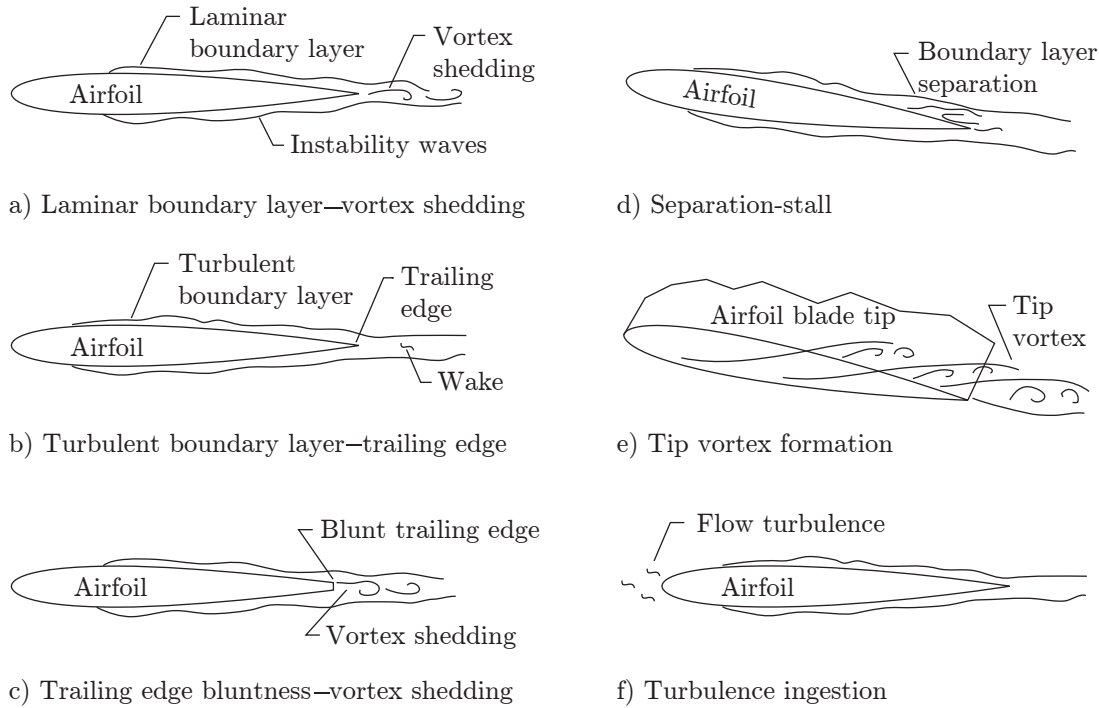


Figure 1.1: Airfoil flow mechanisms contributing to aerodynamic sound. (Adapted from Brooks *et al.* [14].)

al. [14]. Five of these sources are classed as self-noise, as they result from airfoil flow instabilities. These self-noise sources include laminar boundary layer vortex shedding (LBL-VS), turbulent boundary layer trailing edge (TBL-TE) interaction, trailing edge bluntness vortex shedding, separation-stall, and tip vortex formation. The sixth aeroacoustic source, which is not attributed to an airfoil flow instability, is referred to as turbulence ingestion noise. It is the summation of these individual sources which determines the overall aeroacoustic emissions.

Analysis of the contributing flow structures is further complicated by the numerous dependencies, such as wind velocity, airfoil angle of attack, inflow turbulence, airfoil geometry, and surface roughness, to name a few. Each of the flow structures exhibit a unique response to these parameters, thus, the dominant aeroacoustic source may vary depending on the conditions. The results from a prediction model by Moriarty and Migliore [65], shown in Figure 1.2, clearly illustrate the wind velocity dependency of the aeroacoustic sources for a full scale wind turbine.

While the flow structures contributing to airfoil noise are well established, a majority of this research has resulted from the aviation industry, where sound emissions have long been a concern. While this research has proven useful in understanding and predicting aeroacoustic emissions, the applicability to modern wind turbines is restricted, in part due to the low speed and unique geometry of wind turbine airfoils. Thus, to establish more accurate predictive models or to effectively attenuate aeroacoustic sources, it is necessary to expand upon the existing body of research.

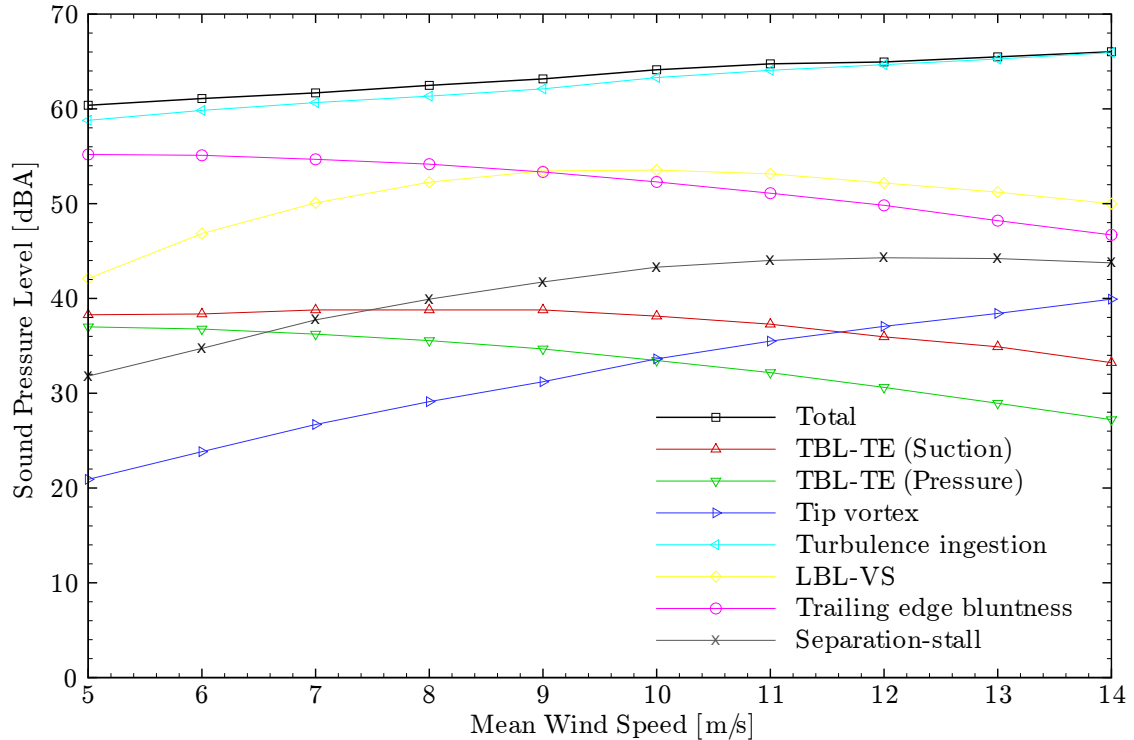


Figure 1.2: Sound pressures of individual aeroacoustic sources versus mean wind speed for a full scale wind turbine. (*Data from Moriarty and Migliore [65].*)

1.2 Objectives

Prior to performing research on wind turbine specific airfoils, the inherent complexities of aeroacoustics required the development of a suitable approach. Thus, the primary objective of this research was to design a technique specifically for studying the aerodynamic sound generated by low speed airfoils. With the basic flow structures already well established in research, the technique would serve to quantify the aeroacoustic sources and provide greater detail regarding the origins of the contributing structures. Ideally, the technique would be applicable to both 2D and 3D models, with potential applications to rotating airfoils. As a secondary objective, it was desired to evaluate the proposed technique using a simple geometry, permitting a comparison of the results to existing literature. By performing the development and validation of the technique, the necessary foundations would be in place to facilitate future aeroacoustics research.

1.3 Outline

To provide the necessary background for the development of a suitable research technique, Chapter 2 provides a review of aeroacoustic theory. In addition to establishing common expressions and terminology, a number of important analytical

acoustic relations are presented. These relations are used to define the sources of aerodynamic sound, providing a better understanding of the contributing physical mechanisms. The theoretical relations are also used to discern fundamental differences between research techniques.

With the theory established, Chapter 3 provides a detailed review of relevant aeroacoustic research. The literature is grouped by analytical, numerical, experimental, and semi-empirical methods. In addition to providing details of the various approaches, the benefits and deficiencies of each are discussed throughout. Using past research and aeroacoustic theory, justification is provided for pursuing an experimental technique.

A more structured evaluation of the experimental techniques is presented in Chapter 4. The techniques are far and near field pressure, as well as near field flow measurements. Criteria are established to facilitate the evaluation, with justification provided for pursuing the near field pressure measurement technique.

The development of the selected experimental technique, the primary objective of the research, is detailed in Chapter 5. For the near field pressure measurements, an evaluation of sensor technology is presented and justification is provided for designing and fabricating a custom piezoelectric sensor. The sensor design is discussed in detail, covering material, electrical, and mechanical considerations. The development and fabrication of prototype sensors is discussed throughout the design process. The necessary sensor calibration setup is also discussed, outlining the calibration method, anechoic chamber development, procedure, and software. The resulting sensor calibration and performance characteristics are presented. Aside from the near field pressure measurements, selection of a far field reference sensor is discussed. Lastly, a data acquisition system is specified which serves to facilitate the experimental technique.

The validation of the proposed experimental technique, the secondary research objective, is covered in Chapter 6. Details regarding the selection of the wind tunnel facility is provided, as well as a discussion pertaining to the resolution of tunnel deficiencies. Justification is provided for the use of a cylindrical geometry, as opposed to an airfoil, presenting the necessary aeroacoustic theory. Details regarding the specimen design and manufacturing are also provided. Accommodation of the far field measurements is discussed and data acquisition considerations presented. The experimental procedure is justified and summarized in the form of a test matrix. Following a discussion regarding the processing of the data, the experimental results are presented and compared to existing literature. The results are also used to evaluate the efficacy of the technique compared to others presented in literature.

Conclusions regarding the development and evaluation of the proposed research technique are presented in Chapter 7. Recommendations for improving the technique are discussed in Chapter 8, as well as a proposed methodology for effectively applying the technique to wind turbine aeroacoustics.

Chapter 2

Aeroacoustic Theory

To establish sufficient background knowledge for the study of aeroacoustics, a review of pertinent terms and expressions is provided. The development of theoretical relations provides a foundation for analytical and numerical models, while a more detailed analysis illustrates the inherent challenges associated with low speed flows. The theoretical relations are also used to establish the physical mechanisms responsible for the production of aerodynamic sound, enabling distinct acoustic source types to be characterized. Further analysis of the aeroacoustic relations permits a preliminary evaluation of the numerous research techniques.

2.1 Equations of Motion

Fluid motion can be generally defined by conservation of mass and momentum; differential expressions derived from consideration of an infinitesimally small fluid element. The conservation of mass is defined by Equation 2.1. For a Newtonian fluid, conservation of momentum reduces to the Navier-Stokes relation, defined by Equation 2.2. For inviscid flows, a further simplification to the momentum relation yields Euler's equation. Both conservation of mass and momentum can be further simplified by assuming that the flow is incompressible.

$$\frac{1}{\rho} \frac{D\rho}{Dt} + \nabla \cdot \mathbf{v} = 0 \quad (2.1)$$

$$\rho \frac{D\mathbf{v}}{Dt} = -\nabla p + \nabla \cdot \boldsymbol{\sigma}_{ij} + \mathbf{F} \quad (2.2)$$

In fluid mechanics research, dimensionless variables are often used to characterize a flow field, independent of specific length or time scales. One of the most prevalent terms is the Reynolds number, defined for a reference length l and velocity u by Equation 2.3. This dimensionless term is essentially the ratio of inertial

to viscous forces. High Reynolds number flows are inherently unsteady and are the primary focus of aeroacoustics.

$$Re = \frac{\rho ul}{\mu} \quad (2.3)$$

Another dimensionless term, Strouhal number, is commonly used with unsteady flows to characterize periodic structures. This term, defined by Equation 2.4, enables the frequencies of a periodic event to be effectively scaled using a reference length and velocity.

$$St = \frac{fl}{u} \quad (2.4)$$

When considering compressible flows, the dimensionless Mach number is often utilized. The Mach number, defined by Equation 2.5, requires the evaluation of the speed of sound, which may be approximated using Equation 2.6. The low speed airfoils of interest are characterized as having a $M < 0.3$.

$$M = \frac{u}{c_o} \quad (2.5)$$

$$c_o \approx \sqrt{\gamma \mathcal{R}T} \quad (2.6)$$

To describe an unsteady flow field, the instantaneous properties may be considered in two parts, comprised of a mean (ρ_o, v_o, p_o) and fluctuating (ρ', v', p') component. For aeroacoustics, the fluctuating pressure is often the only component of interest, with the prime notation being dropped for simplicity. For sound, which is defined as a fluctuating pressure, the sound pressure level (SPL) is commonly expressed in decibels. The relationship between the SI unit of pascals and decibels is presented in Equation 2.7, where the reference pressure in air is taken to be the threshold of human hearing of $20[\mu\text{Pa}]$. In situations involving relatively small fluctuating pressures, a dynamic pressure sensor is often utilized to eliminate the mean component and improve the dynamic range of the measurements.

$$L_p = 20 \log_{10} \left(\frac{p_{rms}}{p_{ref}} \right) \quad (2.7)$$

2.2 Wave Equation of Classical Acoustics

The generation and propagation of sound is governed by the differential equations of motion, the same equations which govern the motion of a fluid. For the flow field, it is often desired to assume incompressible flow, to enable a solution to be readily obtained. Such an assumption, however, would prevent the sound waves

from being resolved, since the sound manifests as density fluctuations. To address this deficiency, the common approach has been to obtain the flow field, or hydrodynamic solution, independent of the acoustic field. The ability to consider the relations independently is a result of the acoustic field having negligible effect on the hydrodynamic solution [37]. Evaluation of the hydrodynamic solution is not limited to an exact analytical solution and may also be obtained by numerical or experimental methods. The aeroacoustic theory presented herein pertains to the evaluation of the acoustic field given knowledge of the hydrodynamic solution. Although the theory is common to many aeroacoustic texts, the following is largely based on the works of Howe [37].

For the acoustic field, a simple solution may be obtained by considering conservation of mass and momentum for an inviscid, stationary, and homentropic fluid. The conservation relations yield the wave equation of classical acoustics, defined by Equation 2.8 [37]. By evaluating the expression for p , which defines the acoustic or fluctuating pressure, the entire acoustic field can be evaluated.

$$\left(\frac{\partial^2}{c_o^2 \partial t^2} - \nabla^2 \right) p = \mathcal{F}(\mathbf{x}, t) \quad (2.8)$$

The generalized pressure source $\mathcal{F}(\mathbf{x}, t)$ encompasses the terms which are introduced into the conservation equations to represent acoustic sources. Terms such as volume sources, body forces, and Reynolds stresses can contribute to the production of sound. These sources may be generally expressed by Equation 2.9 [37], defining a multipole of order 2^n .

$$\mathcal{F}(\mathbf{x}, t) = \frac{\partial^n F_{ijk\dots}}{\partial x_i \partial x_j \partial x_k \dots} \quad (2.9)$$

The primary source types are defined as multipoles of order one, two, and four, being referred to as monopoles, dipoles, and quadrupoles, respectively. A monopole represents a volume source, an example of which would be the open end of a pipe organ. A dipole is associated with a body force, such as the force exerted on a fluid due to the variation in airfoil lift. A quadrupole is used to represent fluid stresses, a consequence of turbulence within the fluid. Whereas monopole and dipole sources are a result of surface interactions, quadrupole sources are limited to flow structures originating within the fluid [37].

A generic solution may be obtained for the generalized pressure source using Green's function [37]. An important factor in the solution is the observer's location. The acoustic near field defines a region within a wavelength of the source origin, whereas the far field is only defined many wavelengths from the source [37]. For a point \mathbf{x} in the acoustic far field, the general solution to the wave equation may be expressed by Equation 2.10 [37].

$$p(\mathbf{x}, t) \approx \frac{(-1)^n x_i x_j x_k \dots}{4\pi c_o^n |\mathbf{x}|^{n+1}} \frac{\partial^n}{\partial t^n} \int_{-\infty}^{\infty} F_{ijk\dots}(\mathbf{y}, t - |\mathbf{x} - \mathbf{y}|/c_o) d^3\mathbf{y} \quad (2.10)$$

The solution to the wave equation is referred to as the retarded potential, representing the pressure at a point \mathbf{x} and time t as the superposition of a volume of point sources located at positions \mathbf{y} about the origin. The individual point sources are evaluated at a time $t - |\mathbf{x} - \mathbf{y}|/c_o$, accounting for the time required for the source to reach the point \mathbf{x} . Observing the solution in the frequency domain, it is noted that the frequency of the resulting acoustic pressure is coincident with the source.

A number of observations can be made based on the wave equation solutions for the distinct source types. First, the intensity of the far field pressure decreases with \mathbf{x} , independent of the source type [37]. The same cannot be said about the directivity of the sources, which exhibit unique intensity fields, as shown in Figure 2.1. This directivity presents a challenge in performing experimental measurements. For far field measurements, without sufficient spatial resolution, the true intensity of the source may not be resolved. Furthermore, the use of far field measurements to locate acoustic sources assumes a monopole type distribution, which can result in appreciable error. Alternatively, if the near field were measured directly, the pressures would be non-directional and the source would be accurately captured.

Performing a scale analysis on the wave equation solutions, it is possible to compare the efficiencies of the numerous sources. In the far field, the radiation efficiency decreases with increasing number of poles, with the relative efficiencies of a monopole, dipole, and quadrupole expressed as the ratio of $1 : M^2 : M^4$, respectively [37]. This emphasizes the importance of fluid-structure interactions,

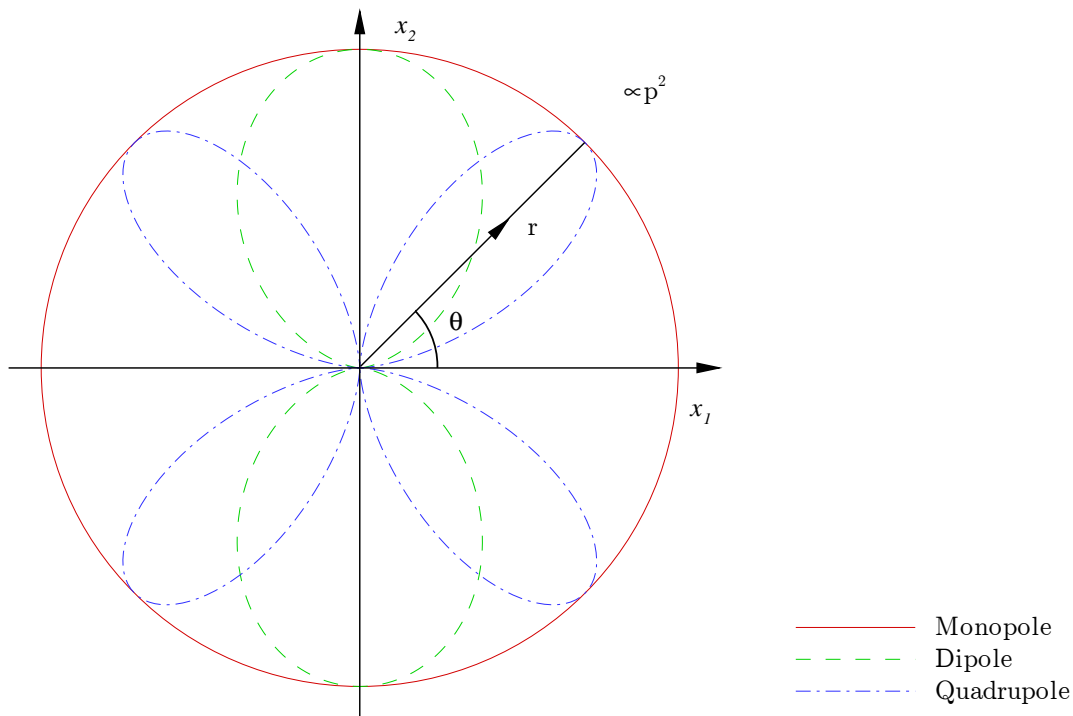


Figure 2.1: Directivity of multipole acoustic sources.

as at low Mach numbers, the efficiencies of monopole and dipole sources are much greater than quadrupole sources. Thus, the sound generated by structures generally dominates the far field emissions. Although structures may radiate directly, say by exerting a force on the fluid, it is possible for the kinetic energy added to the fluid to be convected downstream and generate sound at a later time. An example is shed vorticity, in which sound may be produced far downstream of where the vorticity was generated. Using far field measurements to locate such sources would provide little insight as to the origin of the structures. Therefore, performing near field measurements would provide a better picture of the root cause of the aeroacoustic emissions.

2.3 Lighthill's Acoustic Analogy

The wave equation of classical acoustics provides excellent insight. The solution, however, omits the effects of viscosity and requires knowledge of the pressure source. Lighthill's acoustic analogy, defined by Equations 2.11 and 2.12 [37], is less restrictive. Using conservation of mass and momentum, the omitted terms of the Navier-Stokes relation are included, with the exception of body forces. As such, the Lighthill relation is only suitable for turbulent regions. The term T_{ij} represents the Lighthill stress tensor, a forcing function, and accounts for the additional terms which appear in the Navier-Stokes relation. The Lighthill stress tensor is defined by the solution to the flow field, thus, the stress tensor governs both the production of sound and the flow phenomena.

$$\left(\frac{\partial^2}{c_o^2 \partial t^2} - \nabla^2 \right) [c_o^2(\rho - \rho_o)] = \frac{\partial^2 T_{ij}}{\partial x_i \partial x_j} \quad (2.11)$$

$$T_{ij} = \rho v_i v_j + ((p - p_o) - c_o^2(\rho - \rho_o))\delta_{ij} - \sigma_{ij} \quad (2.12)$$

The solution to Lighthill's equation is analogous to that of a quadrupole source. Assuming $M^2 \ll 1$, the Lighthill stress tensor may be approximated as $T_{ij} \approx \rho_o v_i v_j$, and the solution expressed by Equation 2.13 [37]. Alternatively, Lighthill's equation may be transformed to express the resulting sound pressure in terms of vorticity. Such a formulation would be useful to relate experimental vorticity measurements to far field emissions.

$$p(\mathbf{x}, t) \approx \frac{x_i x_j}{4\pi c_o^2 |\mathbf{x}|^3} \frac{\partial^2}{\partial t^2} \int \rho_o v_i v_j(\mathbf{y}, t - |\mathbf{x} - \mathbf{y}|/c_o) d^3 \mathbf{y} \quad (2.13)$$

Performing a scale analysis on the solution to Lighthill's analogy, it can be shown that the acoustic power generated by an eddy is $\approx l^2 \rho_o v^3 M^5$ [37]. This is known as Lighthill's "eighth power" law due to the eighth power dependency on velocity. Comparing this result to the rate at which power must be supplied to the

flow, it can be shown that the efficiency at which the kinetic energy of the flow is converted to acoustic energy is proportional to M^5 [37]. Thus, for low Mach number flows, the energy dissipated by sound is considered infinitesimal. Given the low efficiency, attempts to predict the aerodynamic sound using knowledge of Lighthill's stress tensor are often accompanied by significant error. This is simply because it is difficult to discern small variations in the stress tensor when compared to the large variations associated with the flow structures [37]. Such predictive methods are often implemented in computational fluid dynamics (CFD) solutions with varying success, often limited to higher Mach number flows where efficiencies are closer to unity. A low efficiency also implies that near field pressures would be much larger in magnitude than far field pressures, indicating that measurements in the near field would provide a much greater signal-to-noise ratio.

2.4 Ffowcs Williams-Hawkings Equation

While Lighthill's equation provides insight into the production of aerodynamic sound, it is limited to turbulence or vorticity generated sound and is unable to account for the interaction with solid bodies. Given that monopole and dipole sources dominate far field emissions in the presence of a structure, their consideration becomes important. To account for these dominant sources, the Ffowcs Williams-Hawkings (FW-H) equation introduces surfaces which may be thought of as a distribution of monopole and dipole sources. The solution of the FW-H equation may then be expressed by Equations 2.14 and 2.15 [37].

$$\begin{aligned}
 Hc_o^2(\rho - \rho_o) &= \frac{\partial^2}{\partial x_i \partial x_j} \int_{V(\tau)} [T_{ij}] \frac{d^3 \mathbf{y}}{4\pi |\mathbf{x} - \mathbf{y}|} & (2.14) \\
 &- \frac{\partial}{\partial x_i} \oint_{S(\tau)} [\rho v_i (v_j - \bar{v}_j) + p'_{ij}] \frac{dS_j(\mathbf{y})}{4\pi |\mathbf{x} - \mathbf{y}|} \\
 &+ \frac{\partial}{\partial t} \oint_{S(\tau)} [\rho (v_j - \bar{v}_j) + \rho_o \bar{v}_j] \frac{dS_j(\mathbf{y})}{4\pi |\mathbf{x} - \mathbf{y}|}
 \end{aligned}$$

$$p'_{ij} = (p - p_o)\delta_{ij} - \sigma_{ij} \quad (2.15)$$

The value \bar{v} represents the velocity of the surface S and the quantities in square brackets are evaluated at $\tau = t - |\mathbf{x} - \mathbf{y}|/c_o$. The FW-H equation is useful in predicting the sound emissions resulting from a distribution of monopole and dipole sources. However, given the low efficiency at low Mach numbers, small errors in prescribing monopole and dipole sources can amount to significant errors in the predicted aerodynamic sound [37].

While the FW-H relation serves as an effective means for evaluating far field emissions, like Lighthill's acoustic analogy, the sound is assumed to be producing

into a quiescent medium. As a result, features of the flow field can have a significant effect on the predicted emissions. This has led to the development of numerous source specific analogies, providing a more representative prediction of far field emissions. One such formulation is for trailing edge noise, which accounts for the scattering of sound caused by the near field surface. These source specific analogies have facilitated the development of more accurate prediction models.

2.5 Summary

Evaluation of aeroacoustic theory has shown that the radiation efficiency of aeroacoustic sources is very low for the Mach numbers common to low speed airfoils. As a result, the numerical evaluation of the acoustic and flow field relations can amount to significant errors, suggesting a benefit of experimental methods. The low efficiency also indicates that pressure measurements in the near field would be orders of magnitude larger than the far field. The source directivity was discussed and presented as a significant source of error for far field measurements.

Chapter 3

Literature Review

The past 50 years of aeroacoustics research has seen the introduction of many new technologies, in pursuit of a better understanding of the sources of aerodynamic sound. Originally, analysis was generally limited to exact analytical solutions of simple flows. However, with advances in computing technology, the use of numerical solvers has permitted the analysis of more complex flows, providing detailed insight into contributing flow mechanisms. While experimental techniques have always played a critical role in aeroacoustics, the tools have evolved to become more powerful and provide greater insight, in part because of the evolution of data acquisition and processing technology. The numerous analytical and experimental efforts have also spurred the development of semi-empirical models, providing an efficient means for predicting aeroacoustic emissions.

Details of the aforementioned research techniques, along with supporting examples from recent literature, are presented in the following sections. The benefits and deficiencies of each are discussed, facilitating the evaluation of an appropriate research technique for low speed airfoils.

3.1 Analytical Techniques

The analytical expressions defining aeroacoustic emissions have often been considered in two parts, evaluating the hydrodynamic and acoustic responses independently, as discussed in Section 2.2. The hydrodynamic solution, which defines the flow field and aeroacoustic sources, may be obtained by evaluating the equations of motion. An analytical acoustic relation, such as Lighthill's acoustic analogy, may then be used to evaluate the generation and propagation of the aerodynamic sound. While the hydrodynamic and acoustic relations may be evaluated numerically and experimentally, an exact analytical solution can accurately resolve the flow and acoustic field without the introduction of numerical or measurement error. Analytical solutions, however, are not without limitations, as they are unable to account for non-ideal effects such as turbulence.

For the hydrodynamic flow field, exact analytical solutions are limited to simple flows. Hanson [26] formulated an exact solution for a propeller blade using helicoidal surface theory, enabling the prediction of far field emissions. A more flexible approach to resolving the hydrodynamic flow field involves the use of CFD, which can evaluate the basic Navier-Stokes relation for very complex flows. The deficiency with this technique, however, is that it often requires numerous assumptions and is susceptible to numerical error.

Exact analytical solutions may also be obtained for acoustic analogies, but is once again limited to simple flows for which an exact hydrodynamic solution exists. An important exact solution can be obtained for the sound generated by a counter-rotating vortex pair. This solution serves as an excellent test case for the evaluation of numerical software. It is also possible to obtain an exact solution for more complex flows, such as vortex-airfoil interaction or trailing edge noise, by making a number of simplifications [37]. More recently, the use of numerical methods to evaluate the acoustic analogies has permitted greater flexibility, enabling far field emissions to be obtained based on numerical or experimental flow field solutions.

3.2 Numerical Techniques

Advances in computing technology have enabled the numerical evaluation of both hydrodynamic and acoustic relations. Using CFD, a solution to the hydrodynamic relation, subject to a number of simplifications, may be obtained for any flow situation. The solution may then be processed using computational aeroacoustics (CAA), the acoustic counterpart to CFD, enabling the radiation and propagation of sound to be obtained. CAA implementations are not limited to simple acoustic analogies, rather, they may be considered in two distinct classifications, direct and hybrid.

The direct CAA approach involves obtaining a single solution which defines both the acoustic and flow field simultaneously, requiring the evaluation of the compressible Navier-Stokes equation. Using CFD, the equation must be evaluated using a time-resolved direct numerical simulation (DNS), an approach that presents numerous challenges. First, the vast range of both spatial and temporal scales impose significant grid size and time step constraints. Second, the necessity to resolve both the near and far field regions requires a sufficiently large domain. Given that DNS simulations can be time consuming for even a simple 2D steady-state solution, the use of DNS for aeroacoustics is currently well beyond commercial means. Even within aeroacoustics literature, the use of DNS has been limited to a select few problems [19].

The alternative to direct CAA is hybrid CAA, which has been the focus of a great deal of research during the past decade. The hybrid method involves solving the flow and acoustic field independently. As such, hybrid CAA is not limited to hydrodynamic solutions obtained using CFD and may be equally applied to

analytical or experimental results. For the CFD solution, use of the hybrid approach greatly reduces simulation demands, as only the aeroacoustic sources need to be resolved. With the dominant sources originating near surfaces, as discussed in Section 2.2, accurately resolving the contributing flow structures only requires a fine grid resolution in the surface region. Furthermore, without having to resolve the sound propagation, the spatial domain may be considerably smaller. Finally, an unsteady Reynolds-averaged Navier-Stokes (RANS) or large-eddy simulation (LES) may be used to model turbulence, as opposed to the more computationally intensive DNS method. While the hybrid approach offers significant benefits over the direct evaluation, performing an aeroacoustic CFD simulation remains computationally intensive.

To implement the hybrid approach, the acoustic response may be coupled to the flow field by a number of means. The traditional approach involves the use of an acoustic analogy, as presented in Section 2.4. For a low speed flow ($M < 0.3$), the viscous flow field may be modelled using an incompressible Navier-Stokes relation and evaluated using a suitable time-resolved CFD simulation. Using the near field solution, the FW-H relation may be used to numerically evaluate the far field emissions, integrating the pressure sources along the surface. To more readily evaluate the FW-H equation, numerous simplified relations have been derived. Farassat [21] provides a detailed summary of such linearized acoustic formulas. Many of the linearized acoustic formulas are based on the FW-H relation, relying on a variety of assumptions in an attempt to reduce processing time. Although the various acoustic formulas were historically derived out of necessity, because of limitations in processing power, the benefits are still realized in modern numerical processing.

While the acoustic analogy serves as an efficient means of evaluating far field emissions, it does possess a number of deficiencies. First, it is assumed that the acoustic sources are located on the surface, although the sources may actually exist away from the surface. This can lead to significant errors, with one particular example being trailing edge noise where reflections and scattering occurs at the airfoil surface. The acoustic analogy also requires that the sources be considered compact, which can lead to significant deviations for high speed flows. Wang [91] provides a more detailed discussion of these and other such acoustic analogy deficiencies. Although acoustic analogies are limited in their use, the method has been used extensively with good success.

To address deficiencies with the acoustic analogy, one approach is to model the flow as compressible, even for low speed flows. To obtain the acoustic field, an arbitrary control surface is defined in the flow field and evaluated using the permeable surface FW-H equation. By measuring the aeroacoustic sources away from the surface, this technique can account for sources which exist within the flow as well as the effects of scattering and reflections, addressing the primary deficiencies with the incompressible solution. The success of this approach, however, is largely dependent on the selection of an appropriate control surface. This compressible flow method was used by König et al. [45] in their investigation of aeroacoustic sources for a high lift device. König et al. [45] compared the acoustic field obtained

using just the CFD solution to the use of the hybrid method. It was shown that the CFD solution alone greatly underpredicted the far field emissions, emphasizing the importance of the hybrid solution.

An alternative hybrid approach has been suggested by Hardin and Pope [27], involving a two-step procedure suitable for the evaluation of low speed incompressible flows. The first part of the procedure involves the evaluation of the viscous hydrodynamic flow field, either through an exact analytical solution or by performing an unsteady incompressible CFD simulation. Using the resulting fluctuating pressure field, a density correction is applied to the constant density of the flow through the use of an isentropic relation. The density correction, as well as the properties of the hydrodynamic flow field, are used to numerically evaluate the linearized Euler equations which govern the compressible acoustic field. According to Ekaterinaris [19], the benefit of this method over the use of acoustic analogies is that the source strength is obtained directly from the unsteady flow field. As a result, the method more accurately predicts the radiation and scattering of sound, even in the presence of solid bodies. This method is also capable of evaluating both compact and distributed acoustic sources.

While the development of CAA methods has enabled the effective use of CFD in aeroacoustic research, Morris et al. [66] emphasize the current limitations of the technology. To evaluate a full scale wind turbine, for which the ratio of largest to smallest length scales is on the order of 10^5 , a massive number of grid points is required. Furthermore, resolving frequencies upward of 10[kHz] to good precision would require numerous time samples, substantially increasing the time required to obtain a solution. As a result, the use of CFD for aeroacoustics is often limited to smaller domains and 2D approximations. These limitations, of course, are largely dependent on the current state of processing technology.

To assess the current capabilities of CFD, consider the recent simulations performed by Lin and Loh [52]. The simulations were performed to validate the predictability of far field emissions using Boeing's unsteady CFD solver, TIDAL. The simulation results were to be validated against well known experimental results, one of which involved flow over a cylinder. For the simulation, the cylinder domain was modelled as a 2D compressible flow using a RANS based turbulence model. This basic simulation required a total CPU time of 126[hours] using a modern desktop processor. Comparing the results to experimental data, the correlation of the frequency spectra was shown to be largely grid dependent, deviating by as much as 14[%] for the coarse grid. While the fine grid correlated to within a few percent for the frequency spectra, the amplitudes deviated significantly, likely because of the lack of an appropriate acoustic analogy. The broadband acoustic spectra was also largely underpredicted, deviating by approximately 20[dB] for the fine grid simulation.

Aside from CFD considerations, the numerical solver used for CAA has also been subject to numerous developments. Ekaterinaris [19] evaluated the use of a high-order accurate, upwind-biased numerical scheme for determining the acoustic field

based on the Hardin and Pope [27] method. To evaluate the numerical solver, the acoustic relations defining a counter-rotating vortex pair were utilized. Comparing the results to the exact analytical solution, Ekaterinaris [19] provides a detailed evaluation of order-accuracy and grid spacing effects.

A similar analysis was performed by Shen and Sorensen [86], also validating a numerical solver based on the Hardin and Pope [27] method. For their validation, an incompressible CFD simulation was performed for flow over a NACA 0015 airfoil using a RANS based turbulence model. Shen and Sorensen [86] demonstrated a significant sensitivity of the results to the specified grid spacing. Furthermore, comparison of the Hardin and Pope [27] method versus the FW-H relation showed that the later approach overpredicted the aeroacoustic emissions. It was also found that the RANS based turbulence model only resolved key frequency spectra, suggesting that the use of LES or DNS would more accurately predict the broadband aeroacoustic sources, similar to the findings of Morris et al. [66].

In general, the numerical evaluation of both the CFD and CAA solutions are complicated by the small magnitude of aeroacoustic emissions, orders of magnitude smaller than the hydrodynamic pressure field. Evaluation of the high-order derivatives, which appear in the acoustic analogy, can also serve as a significant source of error. As such, determining far field emissions by computational methods are highly susceptible to numerical errors. The accuracy of the solutions, however, are largely dependent on, among other things, the numerical solver, residuals, and grid geometry. Numerical errors are less of a concern for high speed flows, where both the Mach number and aeroacoustic source efficiencies approach unity.

3.3 Experimental Techniques

3.3.1 Far Field Pressure Measurements

Performing far field measurements has always played an important role in aeroacoustics. In the most basic regard, it enables the quantification of far field acoustic emissions. In the past 40 years, however, advances in technology and data processing have enabled the measurements to not only quantify, but also locate, sources of the acoustic emissions.

Simple far field measurements can be performed using a single transducer, as shown Figure 3.1, providing significant details regarding acoustic emissions. In addition to quantifying broadband and tonal intensity, a microphone may be traversed about the acoustic field to assess source directivity. This information may then be used to infer the contributing acoustic sources.

A single far field measurement was used by Huskey et al. [41] to characterize the sound generated by a full scale wind turbine. To perform the experiment, a microphone was placed downwind of the rotor at a distance of the hub height plus one half the rotor diameter. The resulting measurements show the acoustic

spectra over a range of wind speeds, one of which is shown in Figure 3.2. This information may be used by manufacturers and developers to accurately predict the emissions that will reach surrounding residents. The peaks in frequency spectra, shown in Figure 3.2, are attributed to distinct tonal sources and are of particular interest when considering human interactions. Similar experiments were performed by Migliore et al. [62] to quantify the acoustic spectra associated with eight different wind turbines.

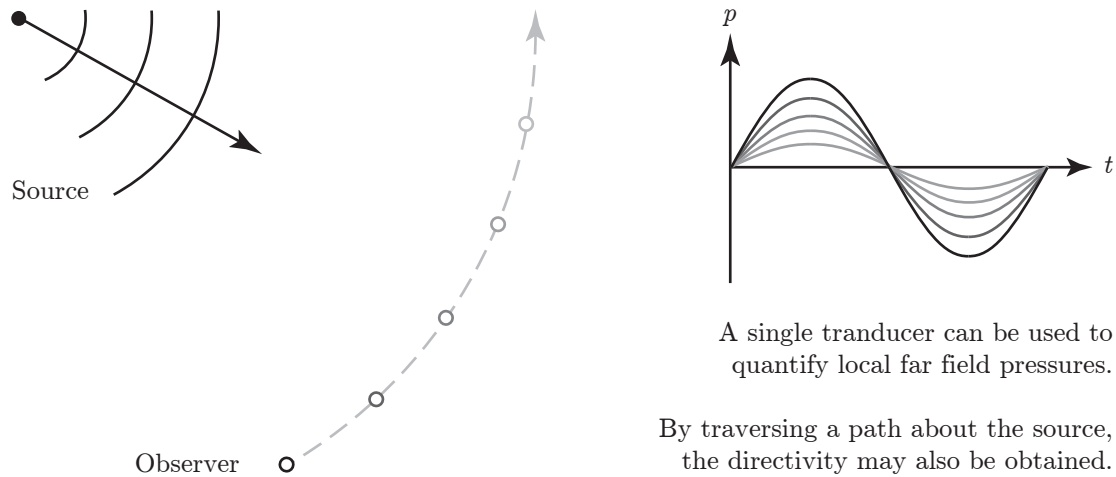


Figure 3.1: Experimental technique: simple far field measurement.

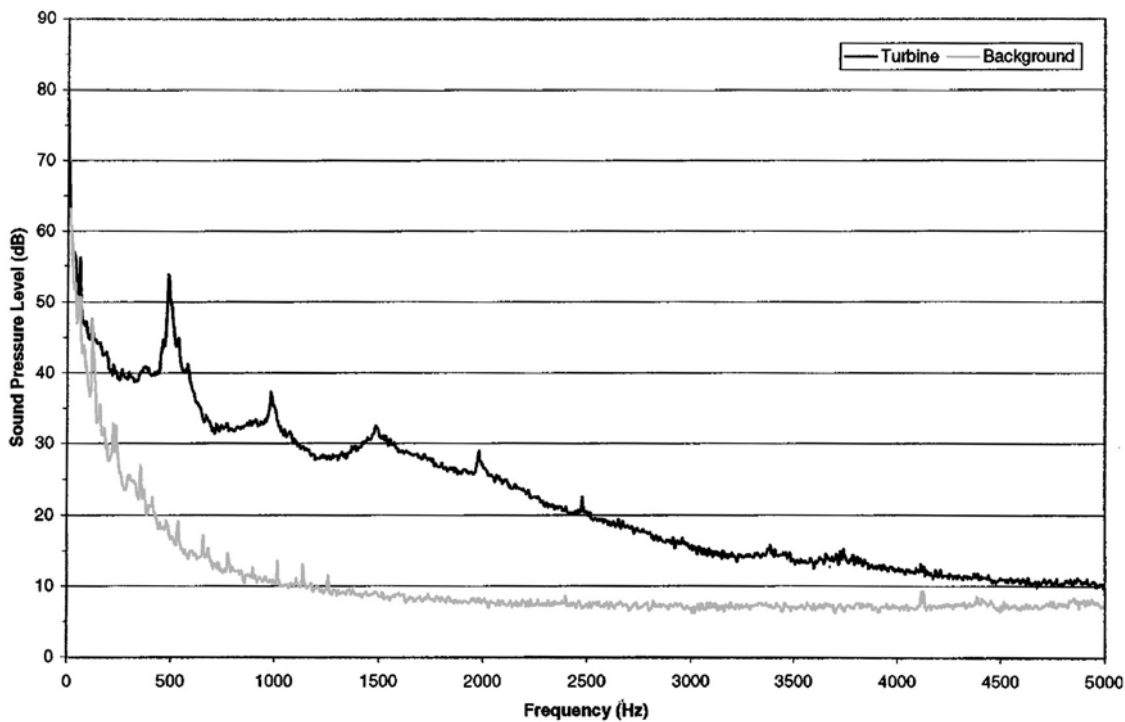


Figure 3.2: Far field noise measurement for a full scale wind turbine. (From Huskey et al. [41].)

Paterson and Amiet [78] used six independent far field pressure measurements in the study of inflow turbulence. The intent of capturing the far field pressures was to assess the predictability of a theoretical formulation based on near field measurements. Grosveld [24] also performed a single far field measurement to validate the prediction of a semi-empirical aeroacoustic model.

Although a single transducer can provide some insight into the contributing acoustic sources, it is difficult to make any conclusive statements based on a single measurement alone. To gain additional insight into the contributing flow mechanisms, the transducer must be coupled with an independent measurement of the near field. Another deficiency with the single point measurement is that the resulting signal is susceptible to noise, although this can usually be compensated for by performing a noise measurement and subtracting it from the results.

To address the deficiencies associated with using a single transducer, past researchers have elected to use an acoustic mirror. This device is essentially a concave surface which turns a transducer into a directional device with a defined focal point, as illustrated in Figure 3.3. By focusing the mirror at a specified region, only the sound radiating from that location will be resolved, minimizing the sources of external noise. Using the acoustic mirror, it is also possible to locate acoustic sources. This is accomplished by moving the focal point and attempting to maximize the signal strength. Thus, the acoustic mirror not only reduces the noise of a single transducer measurement but also enables acoustic sources to be effectively located.

While the use of an acoustic mirror is a relatively antiquated technique, it is still used in modern research to a limited extent. Recently, Herr and Dobrzynski [30] used an acoustic mirror to evaluate the trailing edge noise of an airfoil for a proposed low noise design. The use of the acoustic mirror in this situation was well justified, as the acoustic sources' locations were known and the mirror effectively eliminated irrelevant noise sources from the results.

There are a number of reasons why the acoustic mirror is rarely used in modern

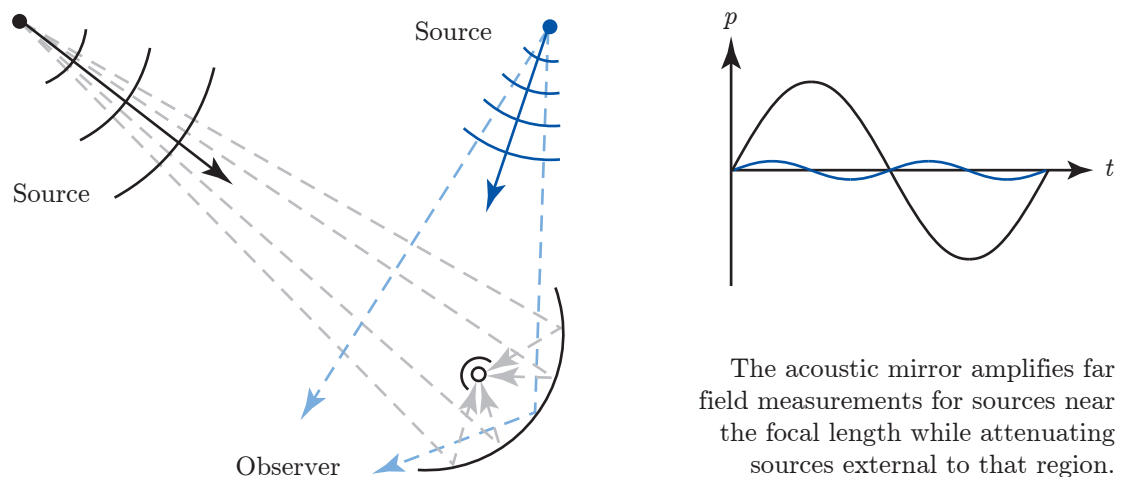


Figure 3.3: Experimental technique: acoustic mirror.

research. First, to resolve the spatial acoustic field, the mirror must be physically moved. In addition to preventing operation in a closed wind tunnel, the positioning of the mirror can serve as a significant source of error in locating the acoustic sources. Furthermore, locating individual sources can be time consuming. Another deficiency is the large size of acoustic mirrors required for the sufficient resolution of low frequency sources. For Herr and Dobrzynski [30], the approximately 1[m] diameter elliptical mirror limited the lowest measurable frequency to 630[Hz]. Thus, the use of an acoustic mirror is best suited for studying known regions where the frequencies of interest are high.

An alternative approach to the acoustic mirror, which offers many of the same advantages, involves a pair of transducers separated by a finite distance. To illustrate this technique, consider the two sensor arrangement presented in Figure 3.4. When sound is radiated from a source, the sound waves propagate at the speed of sound. Due to the varying distance between the source and individual sensors, the signal is received by one sensor prior to the other. By sampling the signals simultaneously, a cross-correlation may be performed on the time-resolved signals, enabling the phase or time variance to be resolved and source location to be approximated. Performing a cross-correlation has the additional advantage of eliminating non-coherent transducer noise from the results. This technique has been used extensively in research, in part because of the ability to both quantify and locate individual acoustic sources with the use of just two transducers.

The two sensor approach was used extensively by the National Aeronautics and Space Administration (NASA) during the 1980s for a series of airfoil self-noise studies. The intent of performing these experiments was to establish a database for which aeroacoustic predictions could be both developed and evaluated. Initially, experiments were performed by Brooks and Hodgson [9], performing a thorough investigation of the TBL-TE and trailing edge bluntness noise using a series of 2D NACA 0012 airfoils. Brooks and Marcolini [11] performed a range of experiments to characterize LBL-VS and TBL-TE noise sources using both flat plates and 2D

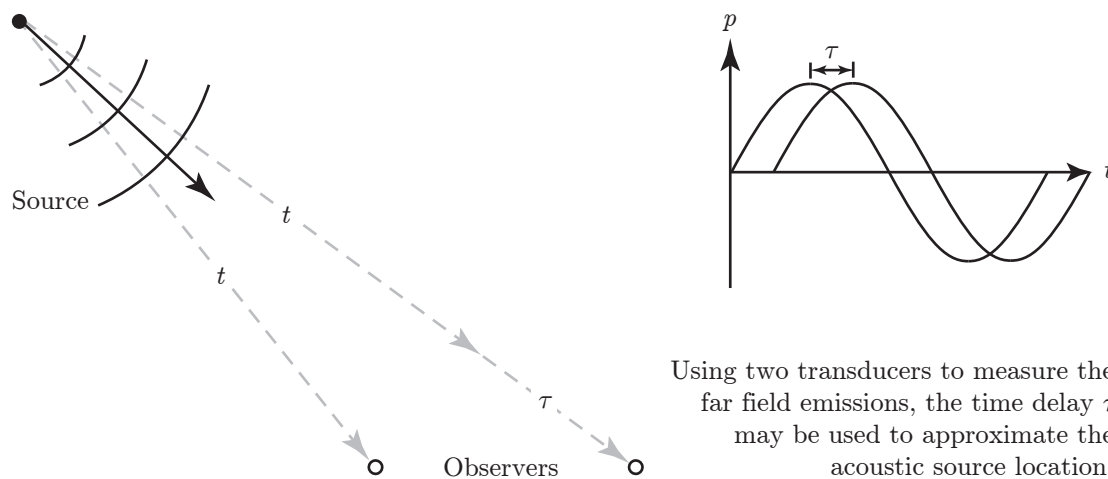


Figure 3.4: Experimental technique: transducer pair.

NACA 0012 airfoils. A series of experiments were also performed by Brooks and Marcolini [12] using 3D NACA 0012 airfoils to quantify the tip vortex formation noise. The test setup for the preceding NASA experiments were similar, using an open jet anechoic wind tunnel and a total of eight microphones to resolve the aeroacoustic emissions. The microphones were analyzed in pairs by performing a cross-correlation, with sample results presented in Figure 3.5. Flow measurements were also performed to enable the acoustic measurements to be normalized. The experiments performed by NASA would establish one of the most detailed aeroacoustics databases in existence, and with the work of Pope [14], would form the groundwork for the development of modern predictive methods, details of which are presented in Section 3.4.

Similar acoustic experiments have been performed by Gershfeld et al. [23], who investigated trailing edge noise for two different airfoil geometries. For their experiments, an open jet anechoic tunnel and a single pair of microphones were utilized.

Although the use of two transducers permits identification and quantification of acoustic sources, the technique alone cannot precisely locate acoustic sources. This can be addressed by increasing the number of transducers further, leading to the development of the modern phased (directional) microphone array.

According to Humphreys et al. [39], the origins of the phased microphone array are attributed to early radio and radar antennas. Applications to acoustics date

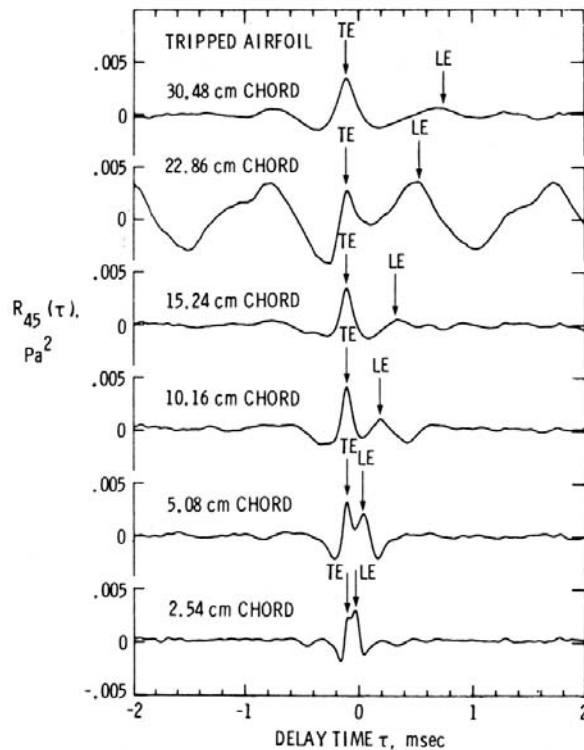


Figure 3.5: Cross-correlation for microphone pair in NASA airfoil self-noise study. Arrows indicate predicted values of τ . (From Brooks and Marcolini [11].)

back to World War II, when the US Navy experimented with hydrophone arrays for the detection of submarines. Soderman and Noble [87] were amongst the first to apply the technology to aeroacoustics in 1974, developing a four sensor 1D microphone array for the purpose of studying jet noise [39]. Since that point in time, extensive research has gone into the development of the technology, leading to more elaborate and effective 2D microphone arrays.

The principles of a phased microphone array are similar to the two sensor arrangement, relying on the phase difference between three or more spatially distributed transducers to locate a common source. As with the two sensor arrangement, the signals must be acquired simultaneously. While the theory remains the same, processing the phased array data using a common delay-and-sum technique is more analogous to the acoustic mirror. For a specified point in space, the distance to the individual transducers is used to determine the time or phase variation, as shown in Figure 3.6. The individual transducer signals are then delayed or offset by the determined amounts, essentially focusing the array at the specified point. The values are then summed over numerous transducers to determine the acoustic intensity. Unlike the acoustic mirror, the array does not need to be repositioned to evaluate the acoustic field. Rather, the analysis software simply iterates the delay-and-sum technique for the entire flow field, enabling the spatial acoustic field to be precisely determined.

The phased array technique addresses many of the deficiencies associated with the other far field techniques. Compared to the single and paired transducer approach, the phased array offers the benefit of quantifying the entire spatial acoustic field. While the acoustic mirror offers similar benefits, the acoustic array provides the same information at a fraction of the effort. Furthermore, the 2D nature of the acoustic array enables effective operation in both open and closed wind tunnels. For these reasons, the phased microphone array has become commonplace in modern aeroacoustic research.

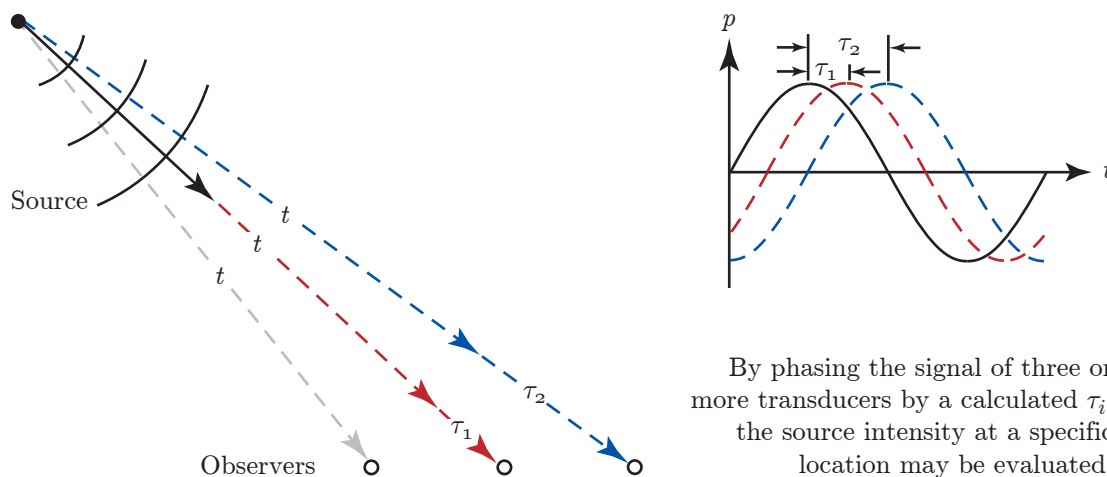


Figure 3.6: Experimental technique: phased array.

In the past three decades, a great deal of research has focused on the physical layout of phased microphone arrays. Similar to the acoustic mirror, the spatial resolution at low frequencies is limited by the outer dimensions of the 2D array, defined as the array's aperture. For high frequencies, however, it is desirable to minimize the inter-sensor spacing to avoid spatial aliasing. While the high frequency characteristics could be obtained by reducing the aperture size, the only way to satisfy both the low and high frequency response is through the use of a large aperture array with a high sensor count. Increasing the aperture size, however, is not without deficiencies, as spatial variations due to source directivity are increased and can lead to significant sources of error [39]. With modern arrays containing upward of 200 individual sensors, implementation of the device can quickly become cost prohibitive. This has led to the development of more efficient sensor arrangements. While initial arrays were based on a square lattice, most modern arrays are based on a logarithmic spiral design, as shown in Figure 3.7, providing a greater frequency response for the same number of sensors [67].

Migliore and Oerlemans [63] used a 48-microphone array, with a usable frequency range of 1 to 20[kHz], to assess the aerodynamic sound generated by six airfoils common to small wind turbines. Using a semi-anechoic wind tunnel, they were effectively able to characterize dominant trailing edge and leading edge aeroacoustic sources, as shown in Figure 3.8. The results were shown to be in good agreement with the experiments performed by Brooks et al. [14], as presented in Figure 3.9. The experiments also illustrated a deficiency with the technique, as extraneous noise sources, shown in Figure 3.8, were observed at the corners of airfoils for a number of low magnitude trailing edge measurements.

Koop and Ehrenfried [46] used a 128-microphone array in the investigation of flap side edge noise. Unlike the commonly used spiral array design, the authors used a random placement approach, providing good side-lobe suppression over a broad frequency range [46]. Experiments were performed using a 3D airfoil model, in which the use of flap side edge modifications were investigated. The authors

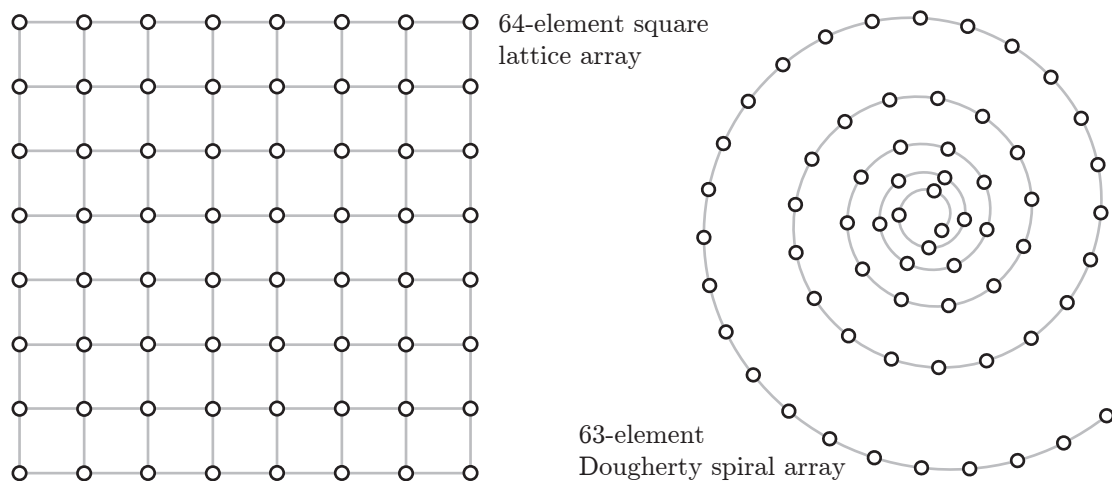


Figure 3.7: Phased array sensor arrangements.

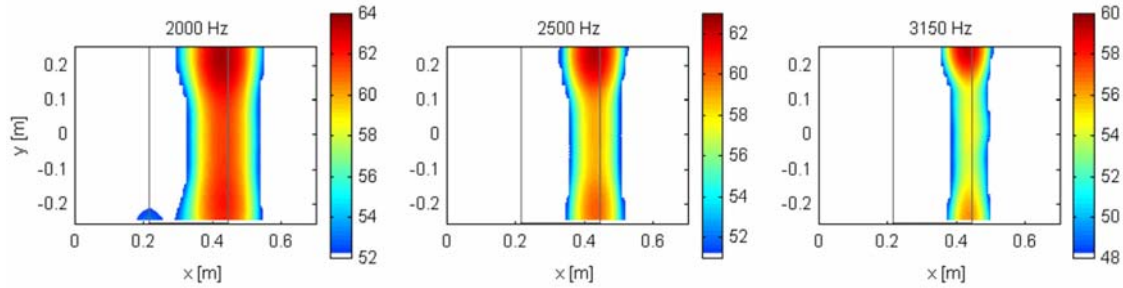


Figure 3.8: Phased array results for an S822 airfoil. (From Migliore and Oerlemans [63].)

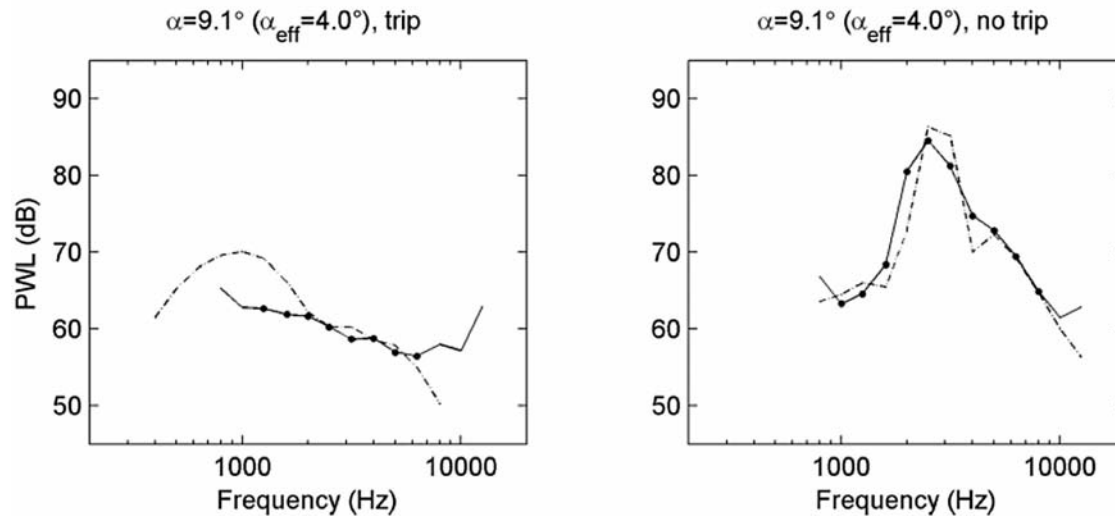


Figure 3.9: Comparison of phased array (solid line) to NASA experimental results for NACA 0012 airfoil trailing edge noise. (From Migliore and Oerlemans [63].)

also investigated blowing at the surface as an active control approach to mitigating aeroacoustic sources. The use of the microphone array was effective in both locating and quantifying the sources thus determining the efficacy of each of the proposed control devices.

While it is desirable to use a single array for a range of experiments, other researchers have satisfied experimental constraints by using a pair of arrays. A large aperture directional array (LADA) is often used to resolve a large acoustic field over a broad range of frequencies. A small aperture directional array (SADA) exhibits a higher frequency response, increased mobility, and less spatially induced errors, at the sacrifice of low frequency resolution. The use of multiple arrays also permits a cross-spectrum (CSM) analysis to be performed, enabling source locations to be more accurately determined over the traditional summation method [96].

Humphreys et al. [39] developed two such arrays for use in an open jet anechoic wind tunnel to investigate sound generated by high lift configurations. The LADA measured 864[mm] diagonally, contained 35 microphones, and exhibited a usable

frequency range of 2-30[kHz]. The SADA measured 197[mm] diagonally, contained 33 microphones, with a frequency range of 5-60[kHz]. Both were based on the logarithmic spiral configuration. The SADA array was designed to be movable about the test specimen, enabling directivity information to be ascertained for the measured sources. Using this experimental setup, a series of experiments were performed by Meadows et al. [57] in the investigation of wing-flap noise sources. The LADA array was used to localize acoustic sources, while the SADA array was used to quantify the acoustic spectra. The SADA was also used to measure the directivity of the observed acoustic sources, exhibiting classic dipole radiation. During the experiments, erroneous acoustic sources were observed at the edges of the model, which the authors attributed to side plate reflection cancellation and reinforcement. This was observed only at low frequencies due to the limited aperture of the phased array. This experimental setup was also used by Mendoza et al. [61] in the investigation of wing-slat noise sources.

Andreou et al. [6] also investigated the sound generated by high lift devices, using two differently sized phased arrays each containing 48 microphones. For this study, the effect of leading edge slat surface treatments was investigated as a means of reducing trailing edge noise.

Horne et al. [34] used a pair of much larger phased microphone arrays, with apertures of 1[m] and 2.43[m], in the investigation of airframe noise. With experiments being performed using a large scale model in the NASA Ames 40- by 80-Foot Wind Tunnel, the size of the arrays was required to satisfy both resolution and low frequency constraints.

A majority of phased microphone array testing has been conducted in open jet anechoic wind tunnels. In addition to exhibiting very low background noise, an open jet wind tunnel enables the microphone arrays to be placed external to the flow field, avoiding turbulence induced noise. The presence of a jet shear layer, however, alters the direction of the sound waves and must be properly compensated for when processing the results. Phased microphone arrays have also been used successfully in closed wind tunnels, however, the presence of solid walls increases background noise and creates the potential for acoustic reflections. With the array being mounted flush with the tunnel wall, the measurements are also susceptible to boundary layer noise, however, it can be minimized by design.

Phased microphone arrays have also been used successfully in less controlled settings, because of the ability to attenuate external noise sources. Oerlemans and López [75] used a 152-microphone array to investigate the acoustic sources for an installed 58[m] wind turbine. Based on the results, they were able to conclude that the aerodynamic sound was the dominant source of the wind turbine noise. Furthermore, a blade which was intentionally tripped was found to produce greater aeroacoustic emissions. The aerodynamic sound was also found to be predominately generated near the tip and during the downward motion of the blade, as shown in Figure 3.10. These results emphasize the potential of the phased array even when subject to less than ideal conditions.

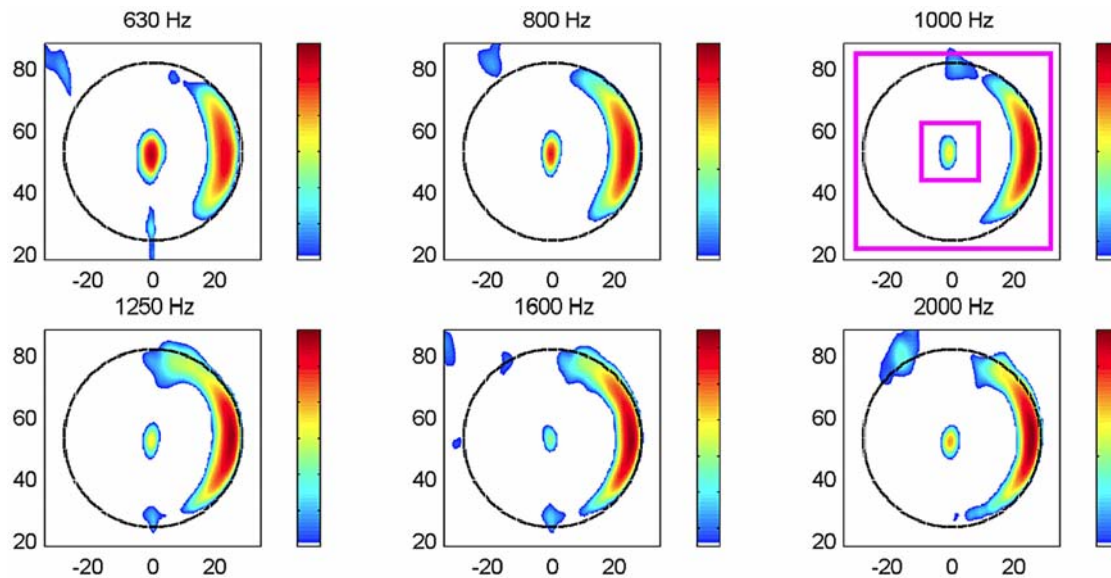


Figure 3.10: Phased array measurements for the swept area of a full scale wind turbine. The coordinates are shown in meters and the range of the contour scale is 12[dB]. (From Oerlemans and López [75].)

The desire to improve phased array results has led to a substantial increase in array size and sensor count, generating both extensive costs and manufacturing complexities. To address these concerns, Humphreys et al. [40] investigated the use of low cost micro-electro-mechanical system (MEMS) microphones to determine whether these devices could be effectively used in a phased array. Compared to the traditional high quality condenser microphones, these MEMS devices come at one-thousandth the cost and offer benefits in terms of mounting. To perform the investigation, an array was fabricated using 128 of the MEMS sensors. Using a closed wind tunnel, a series of measurements were performed for a landing gear assembly. The acoustic sources were effectively captured by the array, with the low cost MEMS sensors exhibiting significant potential.

As opposed to increasing the number of sensor elements to improve quality, recent efforts have focused on the processing of the data. Brooks and Humphreys [10] present an alternative to the traditional delay-and-sum approach, referred to as a deconvolution approach for the mapping of acoustic sources (DAMAS). The benefits of this processing technique are numerous, with results from identical data exhibiting less spatial and amplitude uncertainty. The DAMAS method has also been shown to be less computationally intensive than the delay-and-sum approach. Finally, presentation of DAMAS results are said to be more explicit and without the complexity of beam forming characteristics.

The use of far field measurements certainly provides an efficient means for locating and characterizing sources of aeroacoustic emissions. This technique, however, does not provide much insight into the contributing flow structures. To illustrate this deficiency, consider the phased array experiments performed by Andreou et

al. [6] in the investigation of leading edge slat treatments. The unsteady structures generated by leading edge slats only produce sound upon passing over the trailing edge. Without prior knowledge of the contributing structures, use of the phased array technique alone would have led the researchers to investigate the trailing edge geometry. Thus, if the intent of the aeroacoustic research is to effectively attenuate sound emissions, rather than simply quantifying the acoustic field, it is necessary to study the flow structures responsible for the production of sound.

3.3.2 Near Field Pressure Measurements

To quantify the flow structures contributing to aeroacoustic emissions, past researchers have elected to perform surface pressure measurements, as shown in Figure 3.11. By performing measurements at the surface, the dominant aeroacoustic sources can be effectively resolved, providing an indirect measurement of the sources' strength. The observed pressures may then be used in a similar manner to numerical solutions, using an appropriate acoustic analogy to predict the far field emissions.

Paterson and Amiet [78] used surface pressure measurements in a series of experiments investigating turbulence ingestion noise. The experiments were performed in an open jet anechoic wind tunnel using a NACA 0012 airfoil. To resolve the surface pressures, five transducers were flush mounted in a chordwise arrangement along the suction side of the airfoil. Far field measurements were also performed using six independent microphones. Performing a cross-correlation between the near and far field measurements, the presence of coherent sources was validated. The chordwise distribution of the surface pressures was used to confirm that the dominant aeroacoustic source was located at the leading edge. To validate the predictive capabilities of the surface pressures, the results were indirectly compared to the far field emissions by means of the turbulent flow characteristics, exhibiting

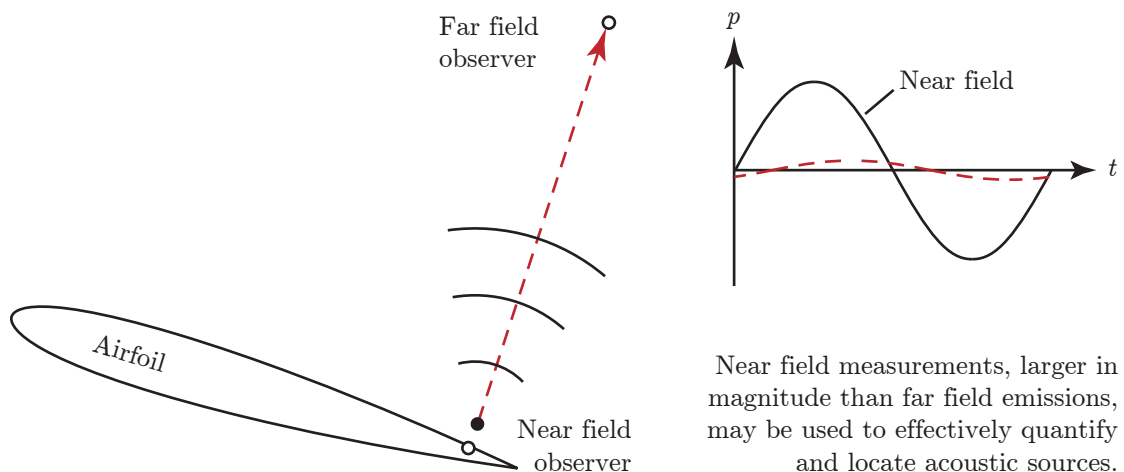


Figure 3.11: Experimental technique: near field pressure.

good agreement. The deviation between the measured and predicted pressures was largely attributed to deficiencies in the analytical prediction model.

The NASA self-noise studies, discussed in Section 3.3.1, also incorporated the use of surface pressure measurements for select experiments. In the investigation of trailing edge noise sources, Brooks and Hodgson [9] assessed the use of surface pressure measurements for the prediction of aerodynamic sound. The motivation to perform surface pressure measurements was due to the small magnitude of the trailing edge noise sources. The use of far field measurements was considered insufficient due to the extraneous noise sources present in open jet wind tunnels. Furthermore, Brooks and Hodgson [9] intended to use the measurements to further develop the theory of the aeroacoustic sources.

The Brooks and Hodgson [9] experiments were performed in an open jet anechoic wind tunnel for both blunt and sharp trailing edge NACA 0012 airfoils. Piezoresistive transducers were flush mounted on both the suction and pressure sides of airfoils in a chordwise and spanwise arrangement. A total of eight far field microphones were used to quantify the aeroacoustic emissions. The surface pressure measurements were processed using a cross-spectra technique, enabling the resolution of coherent pressure sources and the characterization of flow structures. For the TBL-TE noise source, the periodic structures were resolved well upstream of the trailing edge, confirming the upstream origin of the contributing flow structures. The trailing edge bluntness noise source was also effectively resolved, leading to a number of conclusions regarding incident and scattered pressure fields of the aeroacoustic sources. Using Howe's analytical expression [9], the near field measurements were used to predict the far field emissions, exhibiting good agreement as shown in Figure 3.12. Compared to an alternative prediction method based on turbulence measurements, it was found that surface pressure measurements were more readily obtainable. The predictive capabilities of the two techniques were considered equal, as surface pressures are a direct consequence of turbulence. Based on the agreement of the results, it was concluded that surface pressure based analytical relations serve as a viable method in predicting aeroacoustic emissions.

Gershfeld et al. [23] also investigated trailing edge noise using surface pressure measurements. Using a blunt and sharp trailing edge airfoil, a number of piezoresistive transducers were mounted flush to the airfoils' surface. The sensors were placed on both the suction and pressure side of the airfoils in a chordwise and spanwise arrangement. An open anechoic wind tunnel was used for the experiments and far field measurements were acquired using a pair of microphones. The resulting surface pressures accurately captured the unsteady structures, with the blunt trailing edge airfoil generating a nearly tonal signal. In addition to using the surface pressures to obtain the unsteady flow spectra, a cross-spectra analysis was performed to ascertain the length scales of flow structures. Using an analytical relation, the near field pressures were used to predict the far field emissions. The predictions were in good agreement with the measured far field values, being within 2[db] for the sensor nearest to the trailing edge.

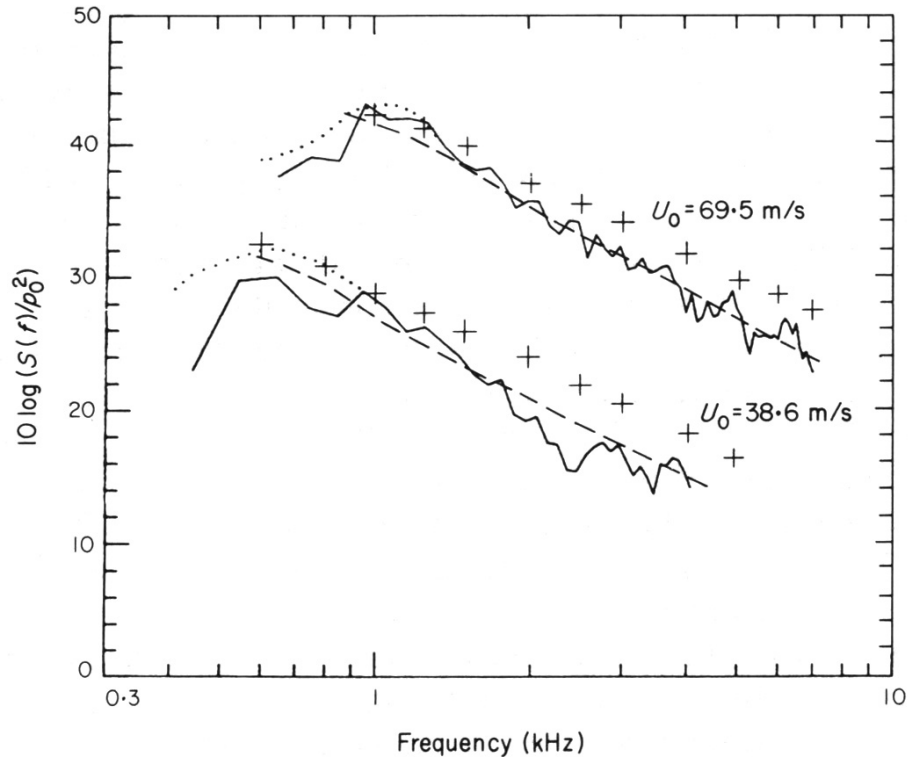


Figure 3.12: Measured (solid line) and predicted (based on near field pressure, dashed line) trailing edge noise for a NACA 0012 airfoil. (From Brooks and Hodgson [9].)

To investigate wing-flap noise sources, Meadows et al. [57] also used surface pressure measurements. The experiments were performed in an open jet anechoic wind tunnel with a pair of phased arrays used to resolve the far field emissions, as discussed in Section 3.3.1. A scaled airfoil and flap were instrumented with a total of 212 static and dynamic pressure sensors. The dynamic pressure sensors, comprised of a variety of piezoresistive transducers, were flush mounted to the surface. The surface pressures were analyzed in pairs to resolve only the coherent sources. Comparing the surface pressure measurements to the phased array, the dominant far field frequencies were observed in the near field pressures at both the flap side edge and the flap edge upper surface. Based on these results, it was concluded that the source of dominant aeroacoustic emissions was related to the development of a vortex structure at the flap side edge.

Guo et al. [25] also used surface pressure measurements in the investigation of flap side edge noise, assessing the efficacy of fences in attenuating aeroacoustic sources. The experiments were performed using a scaled DC-10 model in the NASA Ames 40- by 80-Foot Wind Tunnel. For the near field pressures, a variety of piezoresistive transducers were flush mounted to the surface, being primarily situated in the flap region. A total of four independent microphones were used to measure the far field emissions. Performing a cross-correlation between the near and far field measurements, the coherent sources were able to be localized and the

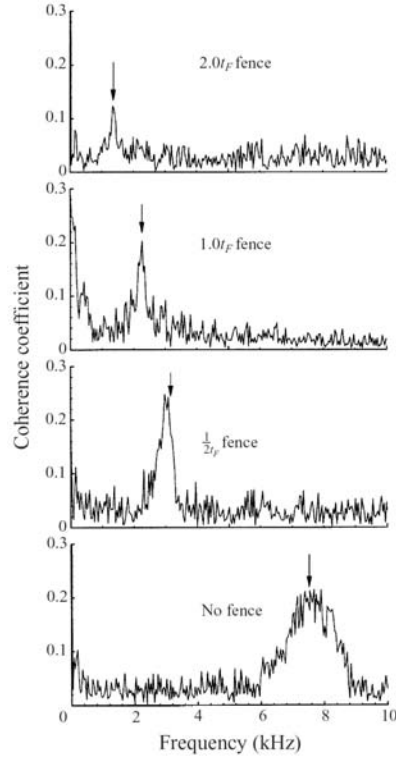


Figure 3.13: Near to far field correlation at the flap side edge for different fence configurations. (From Guo et al. [25].)

effects of the fences quantified, as shown in Figure 3.13. These results show that the fences effectively shift the energy of the flow structures to a lower frequency. The use of the surface pressures in their research also enabled the emissions to be effectively attributed to the flow separation occurring at the flap side edge.

The use of surface pressure measurements has been shown to be an effective means of characterizing the flow structures responsible for the production of aerodynamic sound. Compared to the far field techniques, this approach enables the origins of the aeroacoustic sources to be obtained and provides a greater understanding of the effects of aerodynamic geometry on the contributing flow structures.

3.3.3 Near Field Flow Measurements

An alternative approach to resolving the flow structures is by quantifying the flow field, as shown in Figure 3.14. The benefits of this approach are similar to numerical simulations, providing detailed insight into the contributing flow structures and, using an appropriate acoustic analogy, the ability to predict far field emissions. Compared to numerical results, however, this approach exhibits less uncertainty. Although numerous flow measurement techniques have been used in aeroacoustics, hot-wire anemometry (HWA) remains the most common, as the technology is well suited for high frequency measurements.

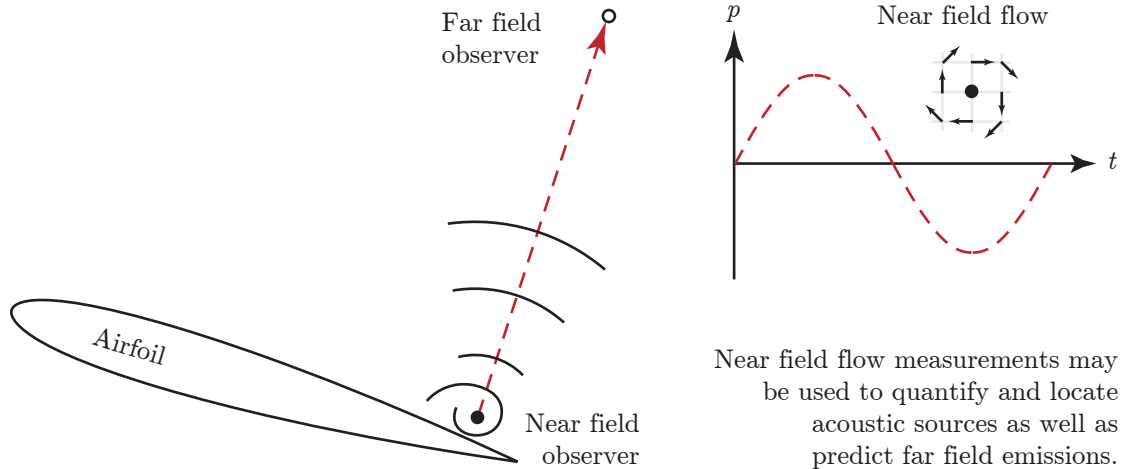


Figure 3.14: Experimental technique: near field flow.

For the NASA self-noise experiments, the use of surface pressure measurements was succeeded by flow measurements. Brooks and Marcolini [11] investigated the scaling of airfoil self-noise using measured flow parameters and analytical expressions. The experiments performed focused on the prediction of the LBL-VS and TBL-TE noise sources. As presented in Section 3.3.1, these experiments were performed for a series of flat plate and 2D NACA 0012 airfoils using an open jet anechoic wind tunnel, with far field measurements being performed using eight independent microphones. The boundary layer was characterized using a 0.5[mm] cross-wire probe, traversing the flow at the trailing edge of the airfoil. These measurements were used to ascertain the boundary layer thickness and integral properties over an extensive range of velocities and angles of attack. Based on proposed scaling laws, the measured boundary layer properties were used to normalize the measured far field emissions, in which the results coalesced to within 7[db], as shown in Figure 3.15. The results effectively showed that the boundary layer thickness, when combined with an appropriate analytical expression, can serve as an excellent predictor of the resulting far field emissions. Brooks and Marcolini [13] performed additional boundary layer characterizations and compared the results with those obtained using boundary layer prediction software, as shown in Figure 3.16. Similar experiments were performed by Brooks and Marcolini [11] in the investigation of tip vortex noise. For these experiments, HWA was used to characterize the vortex structures, serving as an effective means of scaling the far field emissions. The results of the numerous NASA self-noise experiments are summarized by Brooks et al. [14].

Numerous researchers have used HWA in the investigation of trailing edge flows. To evaluate low noise trailing edge designs, Herr and Dobrzynski [30] used HWA in addition to far field measurements. The measured boundary layer properties provided an alternative approach to assess the efficacy of the noise reduction techniques. The HWA measurements clearly resolved the periodic flow structures and, using an acoustic analogy, were found to be in good agreement with far field emis-

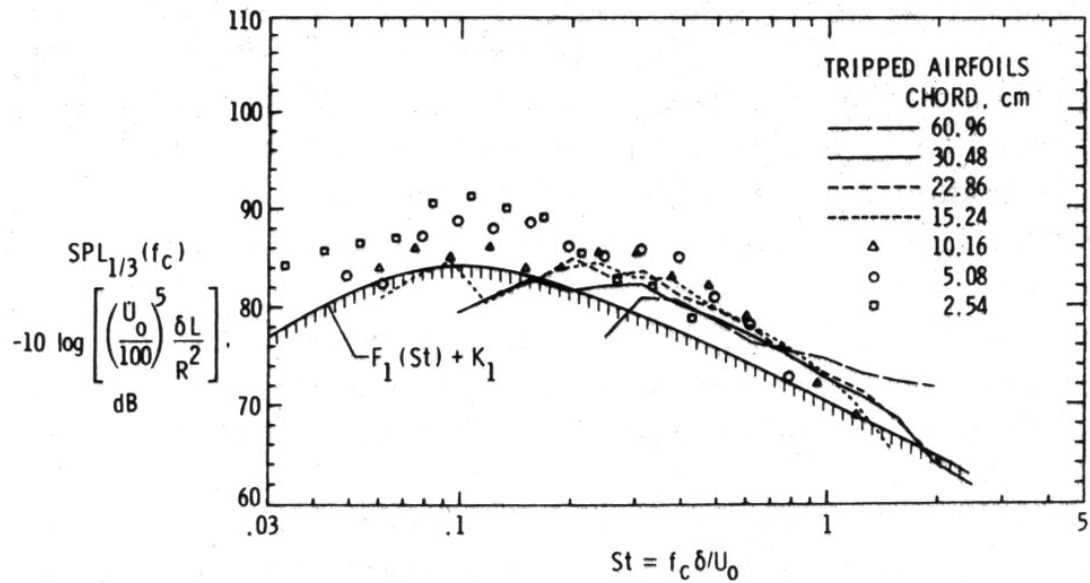


Figure 3.15: Scaling of sound pressure level versus Strouhal number for NACA 0012 airfoils using measured boundary layer characteristics. (From Brooks and Marcolini [11].)

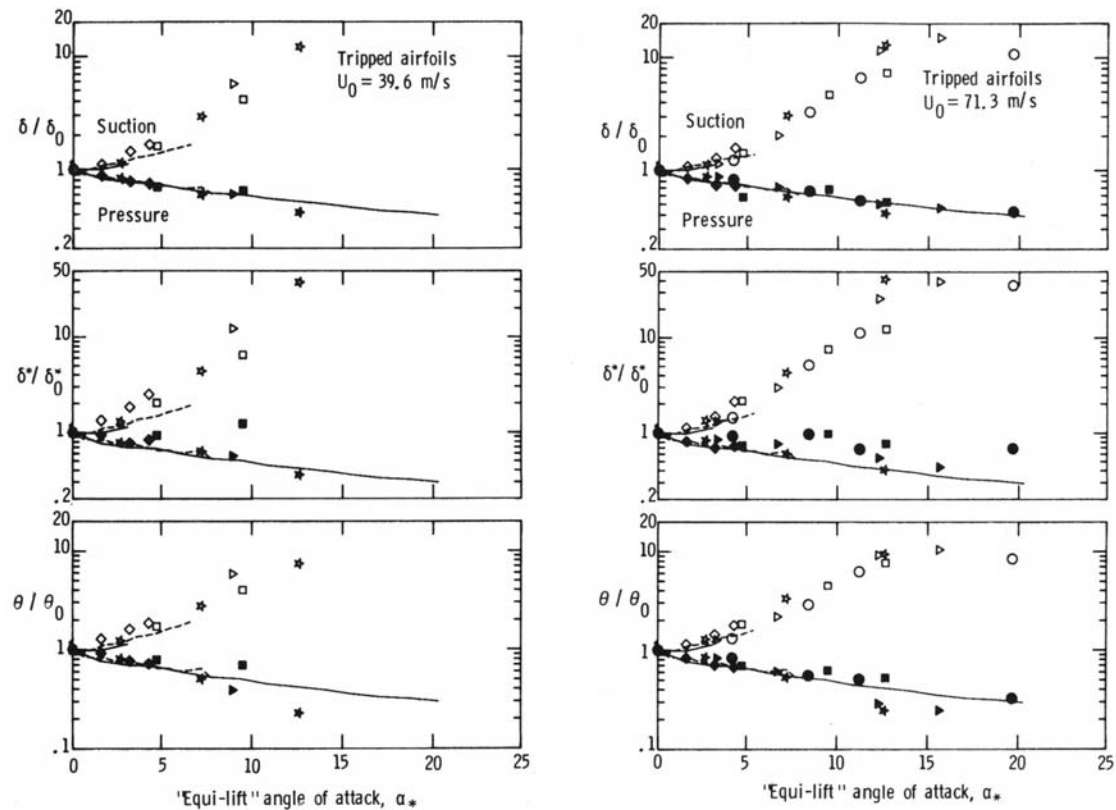


Figure 3.16: Measured and predicted boundary layer characteristics versus angle of attack for a NACA 0012 airfoil. (From Brooks and Marcolini [13].)

sions. The benefits of trailing edge modifications were demonstrated, as both the HWA and far field measurements effectively resolved the attenuation of the periodic structures. Herrig et al. [31] also performed an investigation into trailing edge noise for a NACA 0012 airfoil, opting to use a pair of HWA probes to resolve only the coherent sources. Using the measured flow parameters and an acoustic analogy, the predicted and measured far field emissions exhibited excellent agreement, with the overall sound pressure deviating by less than 2[dB].

HWA has also been used extensively in the investigation of turbulence ingestion noise. To investigate this noise mechanism, Lynch et al. [55] performed a series of experiments using a 4-bladed fan rotor in an open jet anechoic wind tunnel. An analytical model was used to predict the far field emissions based on the classic integral length scale measurements, exhibiting excellent agreement with the far field measurements, as shown in Figure 3.17. Wojno et al. [94][95] also used HWA to investigate turbulence ingestion noise for both a 10- and 4-bladed fan rotor.

Although aeroacoustics research has primarily relied on HWA to quantify a flow field, recent advances in technology have enabled particle image velocimetry (PIV) to serve as a viable alternative. Koop et al. [46] used PIV in addition to far field measurements during the investigation of flap side edge noise and the use of passive

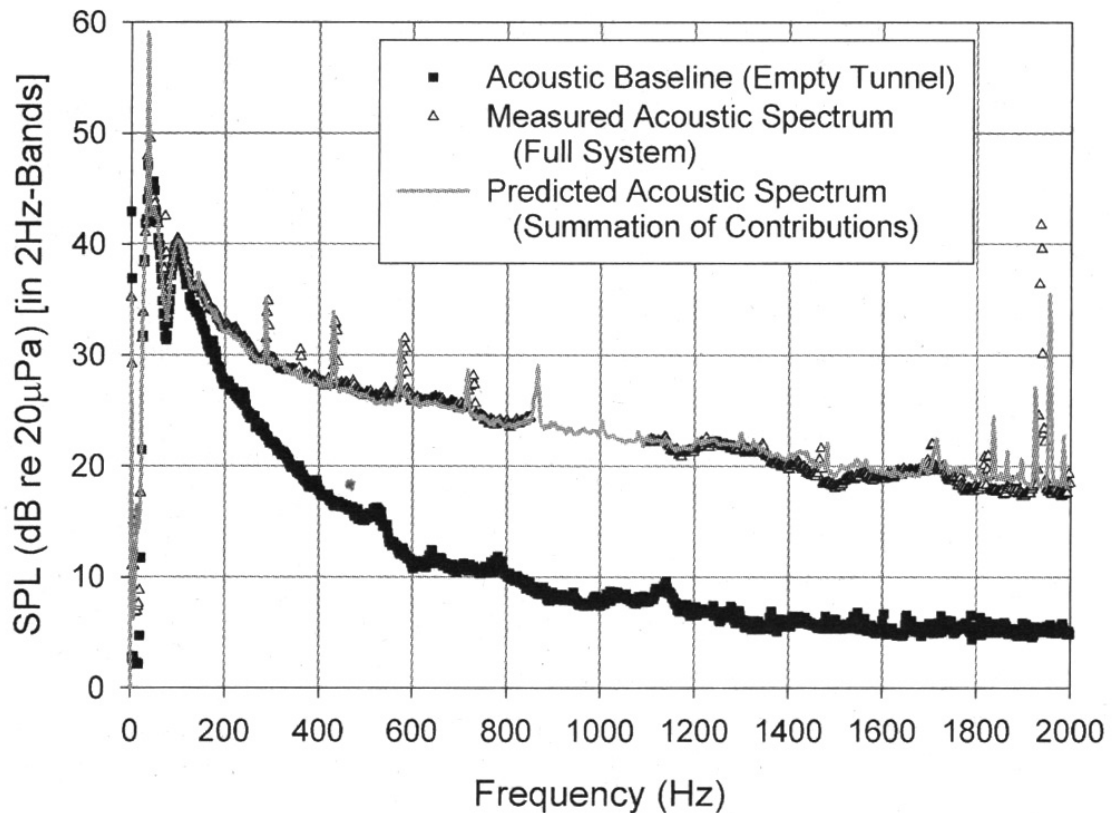


Figure 3.17: HWA based prediction of turbulence ingestion noise for a 4-bladed fan rotor. (From Lynch et al. [55].)

and active flow controls. The PIV setup consisted of two Nd-YAG-II lasers and a CCD camera, enabling the 2D flow field to be quantified at various chord locations. Time-averaged vorticity plots were generated based on the PIV results, providing detailed insight into the flow mechanisms contributing to the flap side edge noise. The results clearly demonstrate that the effective nature of the active flow control is a consequence of the vortex structure being broken into smaller structures and displaced from the surface, as shown in Figure 3.18. No direct comparison was made between the PIV and far field measurements, having been limited by the sampling rate of the PIV setup.

Schröder et al. [84] used PIV to investigate trailing edge noise sources. A series of experiments were performed using a flat plate in an open jet anechoic wind tunnel. PIV measurements were facilitated using a dual cavity Nd-YLF laser and a high speed camera capable of a full frame sampling rate of 2[kHz]. Using the PIV results, the upstream flow mechanisms contributing to sound production were able to be resolved. Furthermore, an acoustic analogy was utilized in the prediction of the far field emissions based on the PIV results. It was concluded that the use of optical based measurements serve as an effective means of detecting aeroacoustic sources, without the necessity of an anechoic facility.

Similar to the near field pressure measurements, the use of flow measurements has been shown to be an effective means of both quantifying contributing flow structures and predicting far field aeroacoustic emissions.

3.4 Semi-Empirical Techniques

Extensive experimental and analytical aeroacoustics research has facilitated the development of numerous semi-empirical models for the prediction of aerodynamic

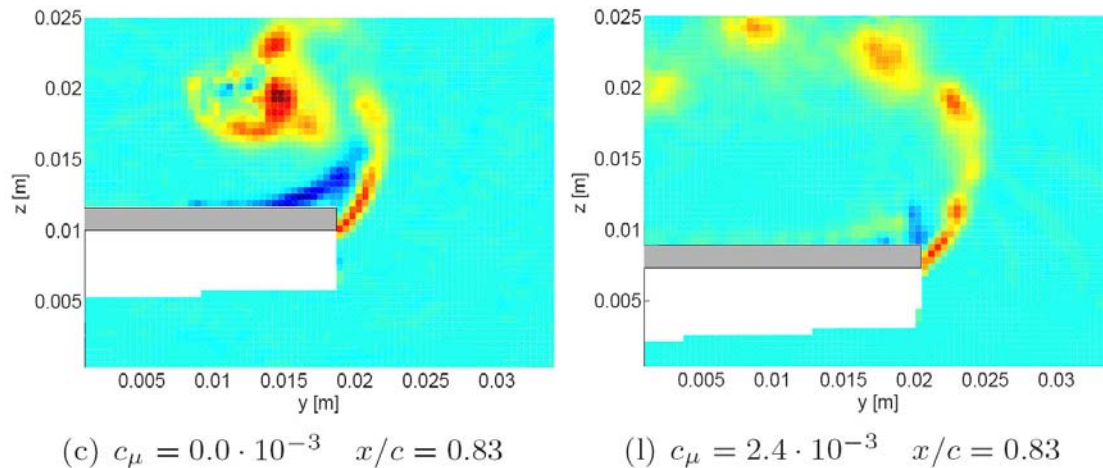


Figure 3.18: PIV vorticity measurements of flap side edge noise structures: (c) without and (l) with active flow control. (From Koop et al. [46].)

sound. These models serve as effective tools for industry, enabling aerodynamic designers to approximate aeroacoustic emissions without the necessity of performing physical measurements.

Early prediction efforts for airfoils focused on turbulence ingestion noise, relevant to the research of high speed propellers at the time. Paterson and Amiet [78] performed a series of ingestion noise experiments for a NACA 0012 airfoil, quantifying the inflow turbulence as well as near and far field pressures. A theoretical relation was derived to predict the far field emissions based on the turbulence measurements. Given that the predictive method was based on theory alone, without the use of empirical constants, the agreement between the predicted and measured far field pressures was considered excellent, as shown in Figure 3.19.

Theoretical relations were similarly derived for sources of airfoil self-noise. In an attempt to predict the aerodynamic sound generated by a horizontal axis wind turbine, Grosveld [24] presents a method based on three semi-empirical models, resolving TBL-TE, trailing edge bluntness, and turbulence ingestion noise sources. The models were used to predict the far field emissions for a number of full scale wind turbines. The predictions were found to be in good agreement with simple far field measurements, as shown in Figure 3.20, deviating by 4[dB] at most. While the method yielded good predictions, only two of the five self-noise sources were resolved, limiting the applicability of the model. Furthermore, the boundary layer

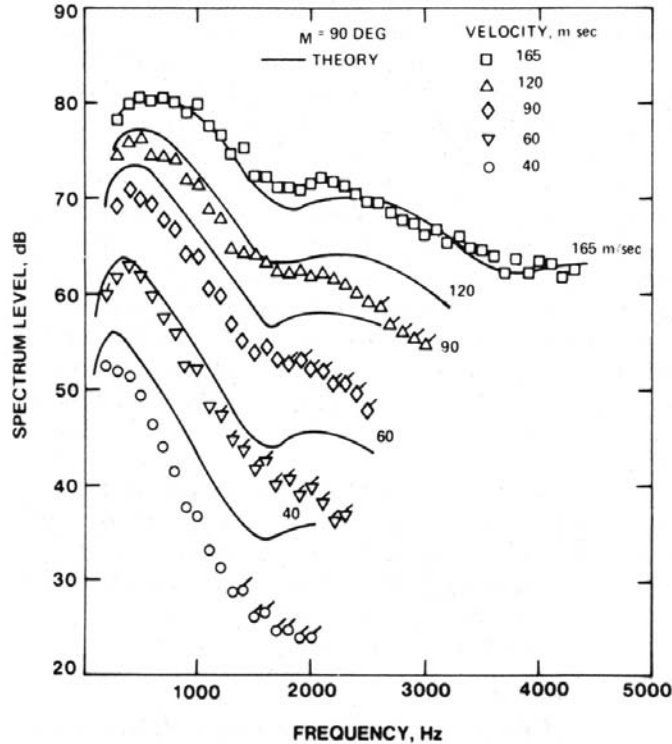


Figure 3.19: Semi-empirical prediction of turbulence ingestion noise. (From Paterson and Amiet [78].)

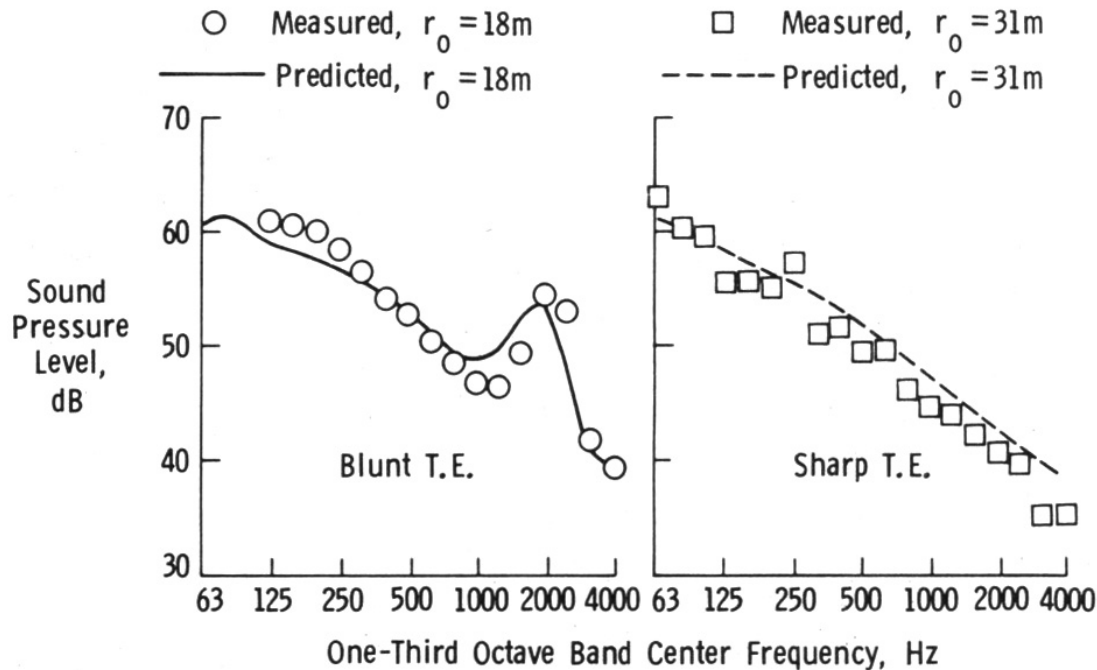


Figure 3.20: Semi-empirical prediction of aeroacoustic emissions for a full scale wind turbine. (From Grosveld [24].)

properties used in the evaluation of the semi-empirical models were derived from flat-plate theory. This method, as proposed by Grosveld [24], has been used by other researchers with good success. Lowson [54] used a similar model to predict far field emissions from several full scale turbines, exhibiting a combined accuracy of 1.6[dBA] when compared to experimental measurements.

To develop a more complete and precise prediction of airfoil self-noise, Brooks and Marcolini [11][12][13] performed a series of experiments, as previously discussed. The results of the experiments were summarized by Brooks et al. [14]. The authors outline the theoretical development of semi-empirical scaling laws for each of the five self-noise sources. The resulting scaling laws enable the prediction of far field emissions based on geometry and flow field quantities alone. The total acoustic spectra may then be determined by the superposition of the individual sources. The intent behind experiments performed by Brooks and Marcolini was to ascertain the actual flow field properties, as opposed to relying on flat-plate theory as employed by Grosveld [24]. The experiments were limited to a NACA 0012 airfoil, but were conducted over a vast range of angles of attack, velocities, and chord lengths. Comparing the predicted and measured far field emissions, the degree of correlation was considered good, with select results shown in Figure 3.21. The scaling laws were deemed suitable for the prediction of aerodynamic sound for low to moderate speed flows such as helicopter rotors, wind turbines, or airframes. Brooks et al. [14] also developed a program called PREDICT to facilitate self-noise calculations.

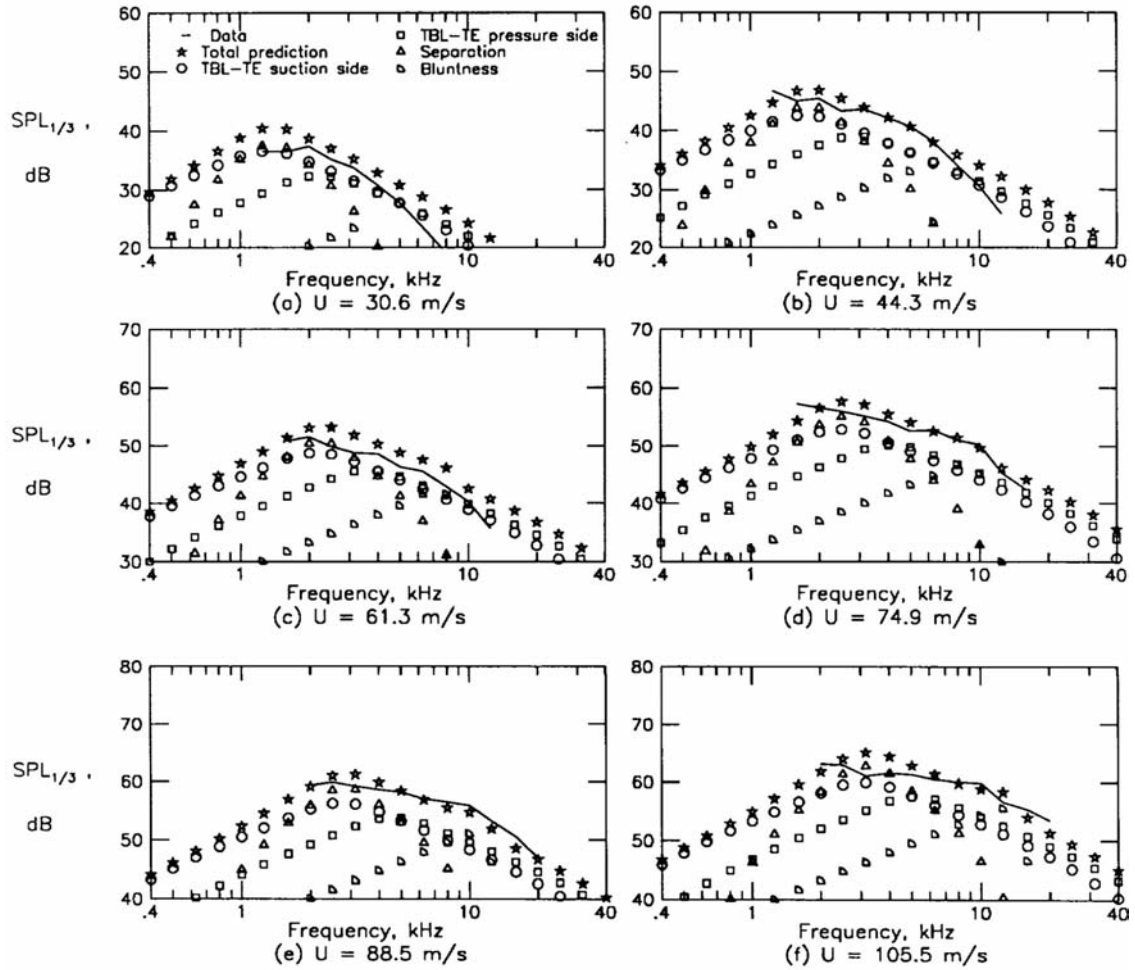


Figure 3.21: Semi-empirical prediction and experiment results for a NACA 0012 airfoil self-noise at $\alpha_c=6^\circ$. (From Brooks et al. [14].)

The method outlined by Brooks et al. [14] has been used successfully in the prediction of wind turbine noise. One such example is the semi-empirical wind turbine aeroacoustics software developed by NREL, as presented by Moriarty and Migliore [65]. In addition to the five self-noise sources, the turbulence ingestion noise was modelled based on the works of Lawson [54] and Amiet [78]. To provide the flow field and geometry necessary for the prediction, the models were integrated into the NREL aeroelastic simulation software FAST. Given that the semi-empirical models are based on 2D airfoil data, it was necessary to discretize the 3D blade geometry into many 2D segments. With a majority of the sound being produced at the outer part of the blade, the assumption of 2D flow was considered valid. The local velocity and angle of attack were used to evaluate the individual aeroacoustic emissions, summing the individual segments to obtain the total acoustic spectra.

To validate the capabilities of the NREL prediction software, a simple 2D NACA 0012 and S822 airfoil were assessed, for which far field acoustic data were

previously obtained by Migliore and Oerlemans [63]. The predictions for the NACA 0012 airfoil were within 2-6[dB], not surprising given that the NACA 0012 airfoil was used in the development of the semi-empirical model. The results for the S822 airfoil were less promising, exhibiting significant deviations at higher frequencies. It was suggested that a more accurate evaluation of the boundary layer thickness, one which accounts for the variation in geometry, would yield an improved prediction. In addition to the 2D airfoils, the prediction software was applied to a full scale turbine that was used in previous experiments performed by Migliore et al. [62]. The resulting far field predictions were in good agreement with the measurements, as shown in Figure 3.22, with the overall sound pressure deviating by a maximum 2-3[dB]. It was noted that the predictions were highly sensitive to the specified inflow turbulence, with no turbulence model underpredicting far field emissions by 10-20[dB]. Given that the prediction model is based on the evaluation of the individual aeroacoustic sources, the dominant and periodic sources can be readily resolved, as previously presented in Figure 1.2. This information can prove incredibly useful for both designers and developers in evaluating potential human impacts. The prediction software also enabled parametric studies to be readily performed, assessing the effects of turbulence, pitch angles, boundary layer tripping, and trailing edge bluntness on the resulting aeroacoustic emissions. Moriarty et al. [64] discuss a number of improvements made to the original software, addressing the sensitivity to inflow turbulence as well as the boundary layer characterization.

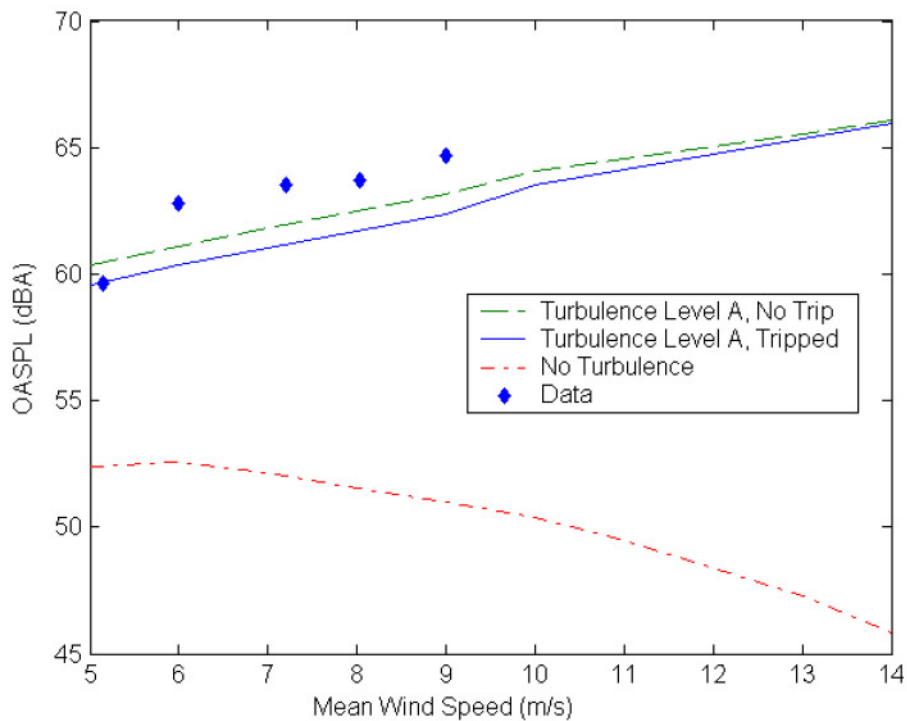


Figure 3.22: Semi-empirical prediction of aeroacoustic emissions versus wind speed for a full scale wind turbine. (From Migliore and Oerlemans [63].)

The use of semi-empirical models serves as an effective means of predicting far field emissions for low speed airfoils. While this approach is useful for manufacturers and developers, it does not provide any insight into the origins of contributing flow structures.

3.5 Summary

A thorough evaluation of past aeroacoustic research techniques has been presented to establish a suitable technique for studying low speed airfoils and the flow mechanisms responsible for the production of aerodynamic sound. While analytical techniques have been shown to be effective in aeroacoustics, the complexity of airfoil flows do not lend themselves to exact analytical solutions. Numerical methods have largely addressed the limitations of analytical techniques, serving as an effective means of understanding the aeroacoustic sources and predicting the radiated sound. However, given the low radiation efficiency of the sound generation mechanisms at low Mach numbers, numerical methods are often subject to significant error. Thus, the only definitive way to resolve sources of aerodynamic sound is through the use of experimental methods. With numerous experimental techniques presented in literature, a more structured evaluation was required to determine the best approach.

Chapter 4

Evaluation of Experimental Techniques

A review of aeroacoustic theory and literature has demonstrated the advantages of experimental techniques for investigating low speed airfoil flow structures contributing to aerodynamic sound. The experimental techniques presented in literature may be considered in three main groups, being primarily based on far field pressure, near field pressure, or near field flow measurements. To evaluate the most appropriate technique for the desired experiments, four important criteria were established: initial costs, continuous costs, flexibility, and measurement uncertainty.

For far field pressure measurements, the only technique considered adequate for providing the necessary detail is the phased microphone array. While phased microphone arrays have proven effective in research, the technology requires extensive initial costs. These costs are largely attributed to the extensive number of calibrated microphones as well as the corresponding demands on data acquisition equipment. Attempts to minimize costs by limiting the number of sensors has the undesirable consequence of increasing measurement uncertainty and limiting frequency response. Low cost arrays have been developed using more cost efficient sensors [40], however, the data acquisition costs remain prohibitively high. Furthermore, resolving low magnitude far field emissions often demands the use of an anechoic wind tunnel, adding to the already extensive initial costs.

While the initial costs of a phased array are high, the technique exhibits excellent flexibility and low operating costs. Once a phased array is installed, any number of test specimens can be mounted in the tunnel section and results readily obtained. With such flexibility, it is clear why such an experimental setup is commonplace, especially in a design-iteration environment. This flexibility, however, is not without compromise. Although the microphone arrangement and anechoic tunnel effectively reduce background noise, the fact remains that the phased array technique relies on low magnitude far field measurements. This deficiency was evident in experiments performed by Migliore and Oerlemans [63], in which the low magnitude trailing edge noise sources were obstructed by extraneous noise. Given

the limited accuracy of even the best microphones, a significant amount of uncertainty remains in accurately locating acoustic sources. Another deficiency with the phased array technique is the inability to provide definitive evidence as to the origin of the aerodynamic sound, as discussed in Section 3.3.1. Thus, if the intent is to study the flow structures contributing to aerodynamic sound, the phased array technique may not provide sufficient detail.

The use of near field pressure measurements addresses some of the deficiencies of the phased array technique. As previously stated, structures serve as the dominant source of aerodynamic sound for low Mach number flows. By measuring the surface pressure, in combination with a simple far field measurement, the sources of aerodynamic sound may be indirectly quantified. With near field pressures orders of magnitude larger than the far field, an anechoic wind tunnel is not required, significantly decreasing initial costs. Furthermore, the sensors do not require the precision imposed by the phased array technique, decreasing sensor costs. Thus, initial costs are limited to the number of sensors required to provide sufficient spatial resolution. Unlike the phased array technique, however, a reduction in sensors does not reduce the accuracy or frequency response of the measurements. Furthermore, it is not required to sample the sensors simultaneously. These reduced data acquisition requirements result in a significant reduction in initial costs.

Although the initial costs of surface pressure measurements are low, the continuous costs can be high. While pressure sensors may be reused, each test specimen must be manufactured to accommodate the sensors, presenting limitations in terms of flexibility. This is likely the reason why the phased array technique has superseded the use of surface pressure measurements. Limitations also exist in terms of spatial resolution, as it is largely governed by sensor geometry and must be determined prior to specimen manufacturing. Although continuous costs are higher and flexibility is limited, surface pressure measurements offer the benefit of reduced error, due to the higher intensity of near field pressures. Measuring the near field pressures also enables accurate determination of the aeroacoustic sources' origin, addressing the primary deficiency of the phased array technique.

For near field flow measurements, the use of PIV was considered over traditional hot-wire measurements. PIV enables the efficient quantification of flow field vorticity, which when combined with a simple far field measurement, enables the determination of flow structures responsible for aeroacoustic emissions. While promising, the initial costs of the technology can be substantial, due to the requirement of a high speed camera and laser. Compared to the other techniques, however, the use of flow field measurements avoids the requirement of an anechoic tunnel. Furthermore, data acquisition requirements are greatly simplified. Thus, the initial costs are limited to the required camera and laser equipment.

Although PIV exhibits high initial costs, the repeatable costs are minimal and flexibility is equivalent to that of the phased array technique. The PIV technique, however, is not without error. The required seeding particles can serve as a significant source of error for unsteady flows [56], the primary focus of aeroacoustics

research. Seeding particles can also present challenges in the measurement of vorticity. While measurement error is an issue with PIV, the results would still provide detailed insight into the origins of contributing flow structures.

A summary of the criteria for each of the proposed experimental techniques is presented in Table 4.1. Based on these results, it was elected to pursue the use of surface pressure measurements. It was decided that measurement uncertainty was more important than flexibility for the desired experiments. Furthermore, the phased array and PIV techniques were considered cost prohibitive. While the PIV technique was not selected, the technology possesses great promise and the feasibility will be re-evaluated in future research.

Technique	Criteria			
	Initial cost	Continuous cost	Flexibility	Uncertainty
Far field pressure	–	+	+	–
Near field pressure	+	–	–	+
Near field flow	–	+	+	–

Table 4.1: Evaluation of experimental techniques.

Chapter 5

Design of Experimental Technique

Based on the evaluation of past research techniques, it was elected to design an experimental technique based primarily on surface pressure measurements. This technique would satisfy the primary research objective, enabling the evaluation of both 2D and 3D airfoils.

For the surface pressure measurements, selection of an appropriate sensor was complicated by numerous experimental constraints. A detailed criterion-based evaluation of sensor technologies is presented and used to justify the development of a custom piezoelectric sensor. The development of the sensor is presented in detail, including material, electrical, and mechanical considerations. The design, manufacturing, and testing of three sensor prototypes is also discussed. Evaluation of the sensor prototypes required the development of a custom calibration facility. The design and manufacturing of an anechoic chamber, acoustic source, sensor setup, and calibration software is outlined. Using the calibration setup, the performance of the final sensor was quantified, the results of which are presented and analyzed.

Although the technique is primarily based on surface pressure measurements, the desire to correlate the results to the acoustic far field required the evaluation of an appropriate far field sensor. Due to the limited constraints, a brief discussion is presented on the selection of an appropriate sensor.

The final consideration for the design of the experimental technique pertained to the selection of suitable data acquisition hardware. A detailed evaluation is provided and specifications are presented for a setup which satisfies the experimental constraints.

5.1 Near Field Pressure Measurements

5.1.1 Sensor Constraints

A critical component of the experimental design involved the selection of a sensor for performing the surface pressure measurements. Low speed airfoil aeroacoustics places numerous constraints on the sensor selection, including the amplitude and frequency of observed pressures, as well as sensor geometry.

For the amplitude of pressure measurements, it was previously established that the fluctuating pressure was the only component required for aeroacoustics research. With the fluctuating component being orders of magnitude lower than the static pressure, attempts to resolve both components using a single sensor would result in significant error, a result of sensor noise and uncertainty. By using a dynamic pressure sensor, which effectively attenuates the static component, the relatively small fluctuating component can be accurately resolved. Sensing technology, whether dynamic or not, can be modified to perform dynamic pressure measurements. To establish the required pressure range, results from prior low speed airfoil experiments were referenced. For the turbulence ingestion noise experiments performed by Paterson and Amiet [78], the root-mean-square (RMS) surface pressures were upward of 10[Pa]. In the trailing edge noise experiments performed by Brooks and Hodgson [9], the surface pressures were significantly lower, with RMS values limited to approximately 0.7[Pa]. With these experiments representing the dominant aeroacoustic sources, a constraint was imposed on the sensor range of ± 20 [Pa], providing a sufficiently large range for anticipated pressure measurements.

For the frequency response, previous experimental results were once again referenced. Based on the self-noise experiments performed by Brooks et al. [14], as well as Migliore and Oerlemans [63], the frequency range was constrained to a minimum of 100 to 10 000[Hz]. In addition to this frequency range encompassing the tonal sources, this range also corresponds to the portion of the audible spectrum most sensitive to humans [83].

The frequency constraint had a significant influence on the selection of a sensor. Typically, surface pressure measurements are performed by drilling a small hole in the surface and connecting it to the sensor using a sensing line. This implementation works efficiently when dealing with low frequency or mean pressures. However, with frequencies upward of 10 000[Hz], sensing line lengths can serve as a significant source of error. These errors are attributed to both sensing line resonance and damping. To determine the response of a sensing line, the contained volume of air may be modelled as a second-order system subject to a sinusoidal input. The solution, defined by Equation 5.1 [67], may be used to quantify amplitude errors for a given natural frequency f_n and damping ratio ζ , as illustrated in Figure 5.1. For values increasing toward the natural frequency, the measured amplitudes are substantially increased due to resonance. Beyond the natural frequency, the damping of the sensing line effectively attenuates the high frequency measurements.

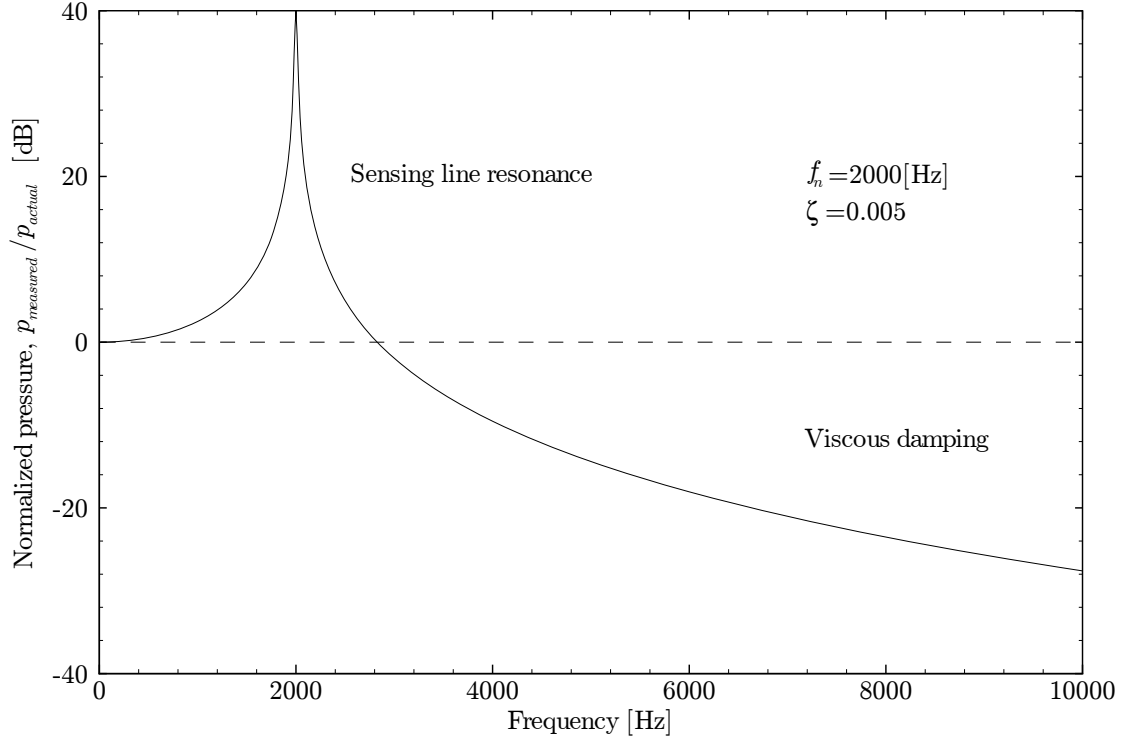


Figure 5.1: Normalized pressure versus frequency for the sensing line measurement of a sinusoidal source.

$$\frac{p_{measured}}{p_{actual}} = \left[\left(1 - \frac{f^2}{f_n^2} \right)^2 + \left(\frac{2\zeta f}{f_n} \right)^2 \right]^{-1/2} \quad (5.1)$$

The primary method of controlling sensing line errors is to establish a natural frequency greater than the highest anticipated frequencies. For a given sensing line geometry, this frequency may be estimated using Equations 5.2 and 5.3, as provided by Hougen et al. [36]. Based on these relations, it is clear that the natural frequency can be increased most effectively by decreasing the length of the sensing line. With the effects of line resonance extending well beyond the defined natural frequency, as shown in Figure 5.1, it is not sufficient to evaluate the required sensing line length based on a natural frequency equal to the highest anticipated frequency. In fact, selecting a natural frequency an order of magnitude higher than the maximum anticipated frequency, the observed amplitude would still be inflated by approximately 1% [92]. Assuming 1% error is acceptable at 10 000[Hz], the corresponding line length based on Equation 5.2 would be approximately 0.8[mm]. A line length longer than this value would potentially obscure measurements. Based on this result, a constraint was imposed that the pressure sensors be mounted flush to the surface, obtaining a zero line length and minimizing sensing line errors.

$$f_n = \frac{c_o}{2\pi l \sqrt{0.5 + V_t/V_s}} \quad (5.2)$$

$$\zeta = \frac{16\mu l}{\rho c_o d^2} \sqrt{0.5 + \frac{V_t}{V_s}} \quad (5.3)$$

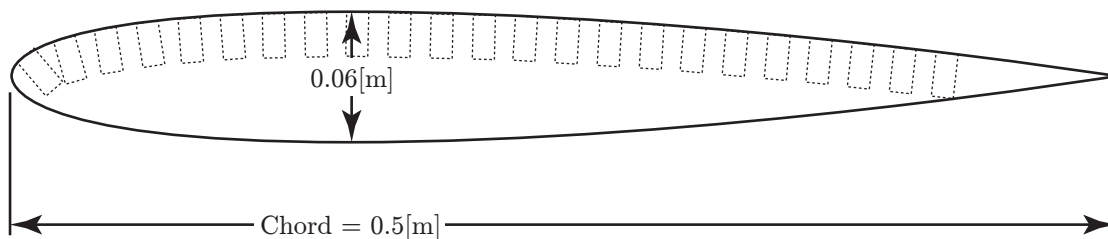
Aside from pressure measurement constraints, the slenderness of the anticipated test specimens imposed geometric constraints on the sensor selection. Figure 5.2 illustrates the scale of a typical 0.5[m] chord airfoil to be evaluated using this experimental technique. With a maximum thickness of 0.06[m], significant constraints are placed on the sensor geometry, particularly at the leading and trailing edge portions of the airfoil. Other researchers, such as Brooks and Hodgson [9], and Gershfeld et al. [23], have addressed these constraints by using miniaturized piezoresistive transducers. However, with the sensors exhibiting a pressure range of $\pm 34\,500$ [Pa], the ability to resolve low intensity pressures was significantly compromised.


5.1.2 Sensor Criteria

The low magnitude and large frequency range of aeroacoustic measurements places significant demands on the selection of an appropriate sensor. To evaluate the applicability of different sensors, several criteria were selected, including frequency response, sensitivity, noise, accuracy, dynamic range, geometry, cost, and reliability.

For the frequency response, the primary objective was to satisfy the imposed range constraints. Beyond the constraints, however, the frequency range serves as an important criterion in selection of a sensor. A larger frequency range provides greater flexibility in the selection of test specimens and enables the experimental setup to be used in the evaluation of geometries other than airfoils.

While the maximum anticipated pressure serves as an important constraint, a more important consideration is the ability to resolve the low magnitude pressures. With anticipated pressures on the order of 1[Pa], both sensitivity and sensor



 Sample sensor geometry, $d = 0.01$ [m], $l = 0.02$ [m]

NACA 0012 airfoil

Figure 5.2: Airfoil geometry common to aeroacoustic experiments.

noise are important considerations, establishing the lowest measurable pressure. The greater the sensitivity, the larger the resulting signal, thus reducing the relative intensity of the noise. While the sensitivity of a sensor is a readily available specification, information regarding sensor noise is often convoluted within sensor accuracy. While sensor noise cannot be extracted from this parameter, sensor accuracy itself serves as a significant criterion. With a desire to compare spatial variations in the pressure field, small sensor-to-sensor variations can significantly impact efforts to locate sources. This is especially true given the small magnitude of the anticipated pressures.

While sensor noise serves as an important criterion in evaluating the lowest measurable pressure, the dynamic range establishes the highest possible pressure. Operating beyond this upper limit can result in undesirable distortion or saturation. Although the anticipated pressure at one frequency may be well within this upper limit, the experimental results will undoubtedly be comprised of many high intensity pressure fluctuations. Thus, the dynamic range serves as an important sensor characteristic, as the low intensity pressures contributing to the far field emissions may otherwise be lost. A high dynamic range also provides greater flexibility in measurable pressures, as the same sensor can be used to resolve both low and high pressures.

For the geometry considerations, the imposed experimental constraints are fairly generous, simply requiring the sensor to fit within the envelope of a 0.5[m] chord NACA 0012 airfoil. To obtain meaningful results, however, the spatial resolution within the leading and trailing edge portions of the airfoil are critical. Thus, the geometry criterion for the sensor selection was to minimize the sensor dimensions so to maximize the spatial resolution. Minimizing the sensor geometry would also permit greater applicability to smaller aerodynamic surfaces.

A significant reason for pursuing the use of surface pressure measurements was to minimize cost. Given the high number of sensors required to provide sufficient spatial resolution, selection of a cost effective sensor would serve to minimize experimental costs.

The final criterion to be considered was reliability, as it pertains to environmental conditions. With a desire to perform PIV measurements simultaneously with near field pressures, the sensors would need to be impervious to the moisture of the required seeding particles.

5.1.3 Sensor Technology Evaluation

Given the large number of sensor criteria, it was initially elected to evaluate distinct technologies rather than specific sensors. It is the underlying sensor technology that establishes a majority of the sensor specifications and provides a more fundamental means of comparison. In evaluating pressure sensors, three technologies were considered potentially viable, including piezoresistive, condenser, and piezoelectric,

as outlined in Figure 5.3. Each of these technologies are strain-based devices and present unique characteristics.

Probably the most prevalent technology for performing pressure measurements is the piezoresistive type. The term piezoresistive means that the material undergoes a change in resistance when strained. Silicon is most often used as the sensing material, due its low cost and ease of manufacture. As with most sensor technologies, a diaphragm configuration is used to increase the amount of strain, thus increasing the signal intensity. The piezoresistive material is applied to a base diaphragm in a strain bridge configuration, enabling the change in resistivity to be measured as a voltage.

The prevalence of piezoresistive sensors would suggest that they have desirable characteristics, which is certainly the case for low frequency and high intensity measurements. For mean pressure measurements, piezoresistive sensors are commonly available in ranges varying from 1000 to 300 000[Pa]. The deficiencies arise when considering the technology for high frequency and low magnitude measurements, as piezoresistive material exhibits relatively low sensitivity. To enhance the output of the sensor, the diaphragm would need to be increased in diameter or decreased in thickness. These changes subsequently lower the natural frequency of the sensor and have a dramatic effect on the frequency response. Most commercially available piezoresistive sensors exhibit a natural frequency well below 10[kHz]. While maintaining a small sensor diameter can address both frequency response and geometry criterion, it is at the compromise of an already diminished sensitivity. Thus,

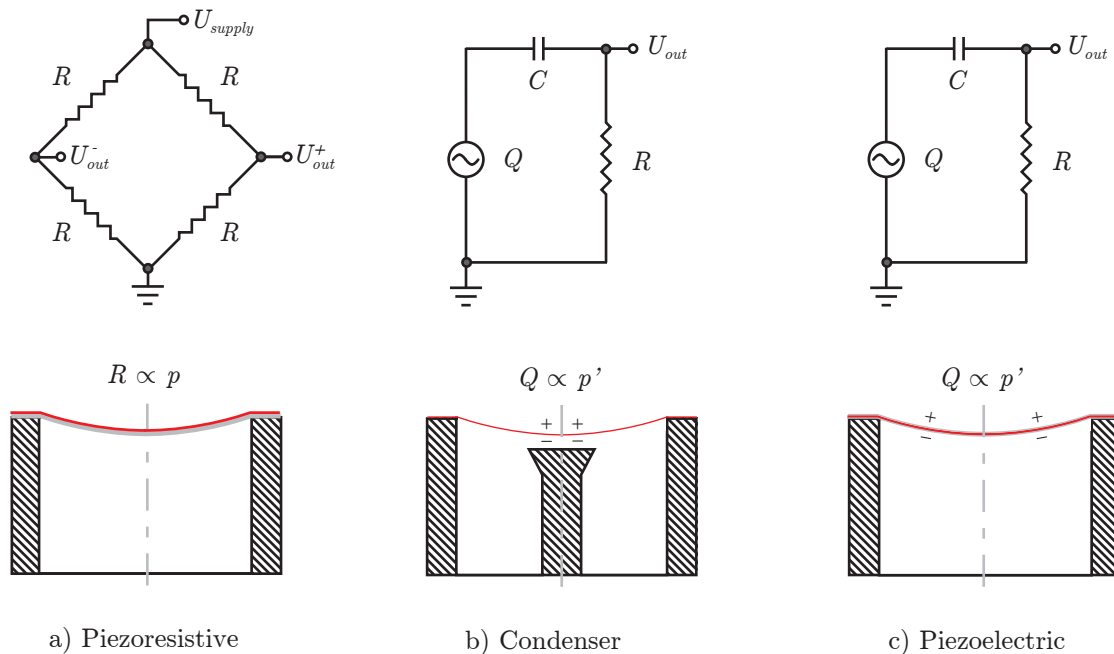


Figure 5.3: Comparison of pressure sensor technologies.

piezoresistive sensors are poorly suited for high frequency and low magnitude measurements.

Although piezoresistive material exhibits low sensitivity, it benefits from minimal electrical noise, due to the low impedance of the circuit. As such, amplification circuitry is often not required. To further manage noise and permit low pressure measurements, more expensive piezoresistive sensors tend to use amplification circuitry. This has the benefit of increasing the dynamic range, which otherwise is quite limited due to the low sensitivity. While piezoresistive sensors tend to be low cost and reliable, those without amplification circuitry particularly exemplify these characteristics. Piezoresistive sensors also exhibit good accuracy, due to the precision of silicon manufacturing.

Condenser type sensors are just as prevalent as the piezoresistive type, only they are intended for a different application. These sensors are most commonly referred to as condenser microphones, as they are typically used to measure sound. The sensors consist of thin metal film stretched tightly over an orifice, to which an electric potential is applied. A post on the underside is separated from the film by a small distance. Small displacements of the film due to an applied pressure causes a charge to transfer between the post and the metal film, generating a change in voltage potential.

The characteristics of condenser microphones are very different from the piezoresistive type. These sensors exhibit excellent sensitivity and are capable of measuring from 0.00001 to 10 000[Pa]. Unlike piezoresistive sensors, however, this technology cannot be used to measure a mean pressure, which is not a concern for the desired experiments. The frequency response of condenser microphones is extensive, with ranges covering from 1 to 100 000[Hz]. In terms of electrical noise, the high impedance formed between the film and post make the signal particularly vulnerable, necessitating a preamplifier circuit. The high sensitivity of the device, when combined with an appropriate amplifier, provides an exceptional dynamic range. These sensors also exhibit excellent accuracy, limited by the precision and calibration of the device and serving as the primary factor in determining cost. Given that the technology is well established, manufactured in large quantities, and common to many consumer electronics, lower quality condenser microphones can be purchased at a minimal cost. The higher sensitivities also permit the technology to be packaged more compactly while maintaining a sufficient sensitivity. One of the primary deficiencies with the technology pertains to reliability, as the less than 1[μm] thick metal diaphragm is highly susceptible to physical and moisture damage.

The final technology to be considered was the piezoelectric type, the least common of the three. The term piezoelectric simply defines a material which generates a charge when strained. In terms of sensing technologies, these materials manifest in two forms. The first, a ceramic, is well established for use at high pressures and temperatures, due to the material's moderate sensitivity and temperature stability. The second, which is of particular interest, is a piezoelectric polymeric film. Similar to the other technologies, the film is most effective in a diaphragm arrangement,

generating an electrical charge subject to an applied pressure. The resulting pressure measurement may be obtained by measuring the voltage potential across the thickness of the film.

The characteristics of piezoelectric film lie somewhere between the condenser microphone and piezoresistive technology. The high sensitivity and extensive dynamic range of piezoelectric film permits the use of a smaller sensor diaphragm, subsequently providing a higher frequency response. Similar to the condenser type, piezoelectric materials cannot be used to obtain a mean pressure measurement. Furthermore, the high impedance of the piezoresistive material requires a preamplifier to reduce noise susceptibility. The accuracy of the piezoresistive material is limited to the design and manufacturing, but is benefited by the simplicity of the technology. This simplicity also means that the technology is relatively low cost. Furthermore, the polymer film is very robust in terms of reliability and would be well suited for non-ideal environmental conditions.

Although piezoelectric films exhibit favourable characteristics, there are few commercial products which utilize the technology, the exception being hydrophones [59]. Piezoelectric sensors have been used occasionally in aeroacoustics research, as performed by Horowitz et al. [35], Lee and Sung [50], and Huang et al. [38]. For each of the experiments, however, the researchers were forced to develop their own piezoelectric sensors. This lack of commercial viability could be for a number of reasons. First, the sensitivity of piezoelectric materials lies somewhere between the two other technologies. Compared to condenser microphones, which are intended for audio applications, piezoelectric types serve as a poor alternative. Similarly, for applications where piezoresistive sensors would be utilized, the improved sensitivity is either not required or resolution of the mean pressure is the primary focus. Thus, the measurement of moderate intensity fluctuating pressures is likely limited to research or, as previously stated, commercial hydrophones.

A summary of the criteria for each of the technologies is presented in Table 5.1. For piezoresistive sensors, costly MEMS based devices are able to meet the experimental constraints, such as Kulite models CCQ-062 [48], MIC-062 [47], or LQ-062 [49], or Endevco model 8507C [20]. However, with a minimum pressure range of approximately 7000[Pa], the limited dynamic range would inhibit the ability to resolve low pressure fluctuations. Thus, with the desired experiments focusing on high frequency and low amplitude measurements, piezoresistive devices are not a viable option. For condenser microphones, a number of cost effective devices are

Technology	Criteria							
	Frequency	Sensitivity	Noise	Accuracy	Dynamic range	Geometry	Cost	Reliability
Piezoresistive	-	-	+	+	-	-	+	+
Condenser	+	+	-	+	+	+	-	-
Piezoelectric	+	+	-	+	+	+	+	+

Table 5.1: Evaluation of proposed sensor technologies.

available which exhibit a sufficiently small geometry, such as Knowles Acoustics model MB3015ASC-2H [44]. The problem with these sensors, however, is that they are prepolarized and exhibit a poor dynamic range. As a result, the anticipated pressures would exceed the allowable distortion limit. Without a commercially viable option, it was elected to pursue the development of a piezoelectric sensor, similar to the path taken by previous researchers.

5.1.4 Sensor Design

Piezoelectric Considerations

The first stage of the sensor development was to obtain piezoelectric film for testing. While a number of manufacturers exist, Measurement Specialties [58] offers a number of piezoelectric films intended primarily for measurement purposes. More specifically, the films are of good dimensional accuracy with a metallization applied to either side of the film. This metallization is required for performing measurements, as it is used to collect the charge when the material is strained. The Measurement Specialties films are manufactured exclusively from polyvinylidene fluoride (PVDF); a polymer which exhibits excellent piezoelectric properties, as outlined in Table 5.2 [59]. The first and second numerical subscripts on the parameters represents the electrical and mechanical indexes, respectively. The values of 1, 2, and 3 represent the directions along the film length, width, and thickness, respectively. For example, G_{31} defines the electrical charge generated across the thickness of the film subject to a stress applied in the length direction. Using these properties, along with Equation 5.4 [59], the resulting open circuit voltage may be evaluated for a defined material stress. It should be noted that the inability of piezoelectric material to resolve mean pressures is due to charge leakage, as the concept of an open circuit is merely an idealization. The piezoelectric films are available in large sheets with a film thickness of 28, 52, or 110[μm]. Two metallization options are available, including silver ink and sputtered copper-nickel.

Symbol	Parameter	Value	Units
b	Thickness	28, 52, 110	[μm]
D_{31}	Piezo strain constant	$23 \cdot 10^{-12}$	[$\text{m m}^{-1} \text{Pa}^{-1}$]
D_{33}	Piezo strain constant	$-33 \cdot 10^{-12}$	[$\text{m m}^{-1} \text{Pa}^{-1}$]
G_{31}	Piezo stress constant	$213 \cdot 10^{-3}$	[$\text{V m}^{-1} \text{Pa}^{-1}$]
G_{33}	Piezo stress constant	$-330 \cdot 10^{-3}$	[$\text{V m}^{-1} \text{Pa}^{-1}$]
C	Capacitance, 28[μm], 1[kHz]	$3.80 \cdot 10^{-6}$	[F m^{-2}]
E	Young's modulus	$2 - 4 \cdot 10^9$	[Pa]
σ	Yield strength	$45 - 50 \cdot 10^6$	[Pa]
T	Temperature range	-40 to 80	[$^{\circ}\text{C}$]

Table 5.2: PVDF film specifications. (*Data from Measurement Specialties [59].*)

$$U = G_{3i}\sigma_i b \quad (5.4)$$

An undesirable characteristic of PVDF film is a sensitivity to variations in temperature, known as a pyroelectric effect [59]. The resulting voltage, however, is dependent on the rate of change of the temperature, the frequency of which would be much lower than the anticipated pressures. Therefore, the pyroelectric effect for the desired experiments was considered negligible.

For the initial evaluation of the piezoelectric film, it was simply desired to establish important mechanical and electrical considerations. As opposed to purchasing large quantities of various piezoelectric films, it was elected to obtain samples fabricated specifically for end use, as shown in Figure 5.4. These pieces were provided by Measurement Specialties, free of cost, in both 28 and 52[μm] thicknesses. Some of the samples were provided with electrical leads already attached, further aiding in the evaluation process. While only silver ink films were provided, the metallization has little bearing on the sensitivity of the film and was left to future consideration.

Using the piezoelectric samples, it was desired to develop a rudimentary prototype sensor. Prior to fabricating the sensor, however, a number of general considerations were required. Initial calculations were also required to establish approximate geometric parameters.

The first consideration in the sensor design was the manner in which the material is strained subject to an applied pressure. The simplest solution would be to bond

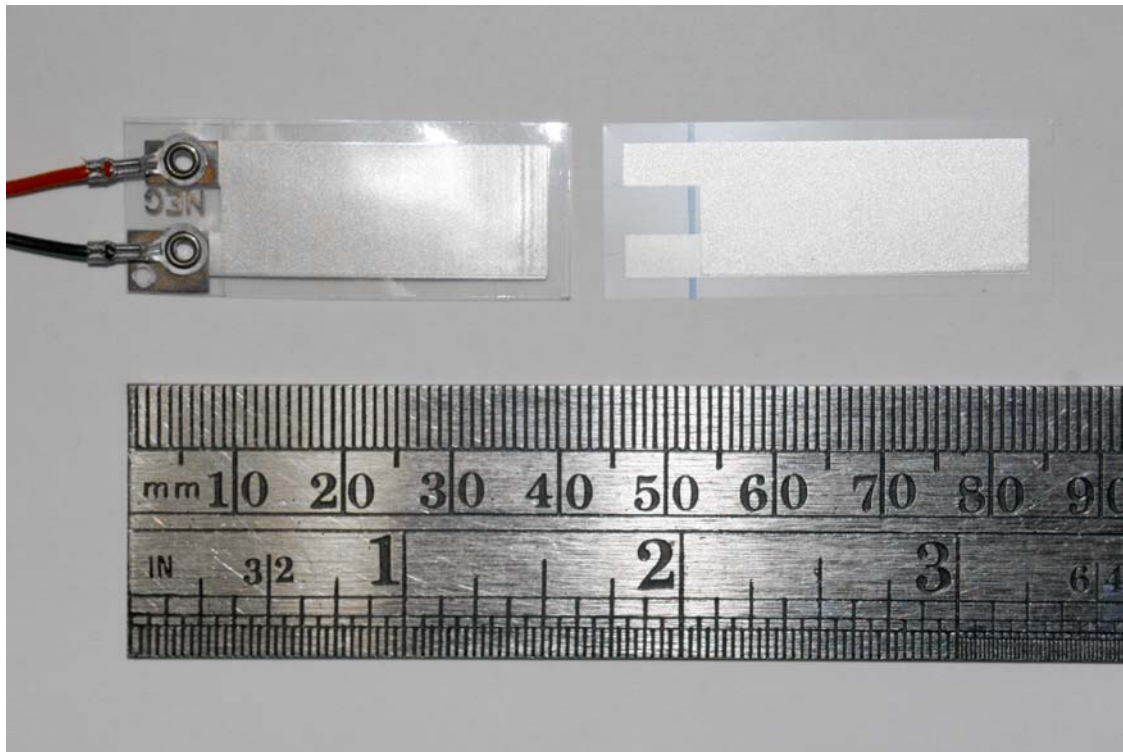


Figure 5.4: PVDF film samples.

the material directly to a planar surface, with the pressure straining the material in the thickness direction. The deficiency with this method, however, is that the resulting material stress is simply equal to the low magnitude pressure, as defined by Equation 5.5 [32]. A preferred method of implementation, particularly when dealing with low pressure measurements, is to place the material over a circular orifice. This diaphragm configuration effectively increases the magnitude of the resulting material stress. To approximate the resulting stress due to an applied pressure, the diaphragm may be considered as a thin walled spherical shell, as defined by Equation 5.6 [32]. An additional deformation relation was derived, defined by Equation 5.7, to provide an implicit solution for the unknown radius appearing in Equation 5.6.

$$\sigma_3 = p_3 \quad (5.5)$$

$$\sigma_1 = \frac{p_3 r}{2b} \quad (5.6)$$

$$\sigma_1 = E \left(\frac{2r \sin^{-1}(d/2r)}{d} - 1 \right) \quad (5.7)$$

Proceeding with the diaphragm configuration, Equations 5.4, 5.6, and 5.7 were used to approximate the voltage corresponding to a particular diaphragm and applied pressure. With the intention of using amplification circuitry, it was not required for the resulting voltage to be high. Rather, the calculations were used as a first approximation to ensure that a measurable voltage would result from a reasonably sized orifice. In other words, the diaphragm size was driven primarily by the geometric constraints. For the material thickness, the thinnest of the piezoelectric materials was selected, providing greater sensitivity as indicated by Equation 5.6. Selecting a diaphragm size of 0.003[m], it was determined that for a pressure of 1[Pa] and thickness of 28[μm], a voltage of 0.043[V] would result. With a resulting stress of 7140[Pa], four orders of magnitude larger than the applied normal stress, this configuration is clearly more effective than the alternative.

Another important consideration was the housing used to retain the diaphragm. The easiest method would be to bond the film directly to the surface of the test specimen. While simple, bonding the material to the surface would result in the undesirable effect of measuring specimen strain which, for the strain common to large scale airfoils, would interfere with pressure measurements. Bonding to the surface would also prevent the sensors from being reused, presenting challenges in terms of calibration, and would inevitably interfere with the flow. These deficiencies can be addressed by placing the diaphragm in a separate housing, at a small cost of complexity. However, doing so has the additional benefit of controlling electrical noise, as will be discussed further below.

Sensor Prototype: First Generation

With the basics of the sensor design established, a prototype was fabricated as shown in Figure 5.5. The prototype consists of two copper washers which firmly clamp the piezoelectric film, with an electrical lead connecting to each. The inner diameter of the washers determines the active diameter of the diaphragm. The nylon housing provides electrical isolation while retaining the washers. Removable fasteners enable the copper washers to be interchanged, permitting the evaluation of numerous diaphragm sizes and material thicknesses.

To evaluate the prototype, a 50.8[mm] speaker was driven by a frequency generator. A pure tone of 1000[Hz] was generated at an arbitrary magnitude. Without a calibrated reference, initial tests were simply used to assess the ability of piezoelectric material to detect an acoustic source at relatively low pressures. A hardware spectrum analyzer was utilized to process the signal, providing immediate feedback regarding the sensors ability to detect the tone amongst background noise.

During the evaluation of the prototype, the pure tone was easily resolved, as anticipated. The resulting pressure spectrum, however, was dominated by additional tones which were attributed to electrical noise. Although care was taken to shield the electrical leads, the lack of an amplification circuit during this first revision made the sensor particularly vulnerable. This was not unexpected, as the importance of an amplification circuit due to the high impedance of the piezoelectric film was previously established. Thus, although the sensitivity of the sensor

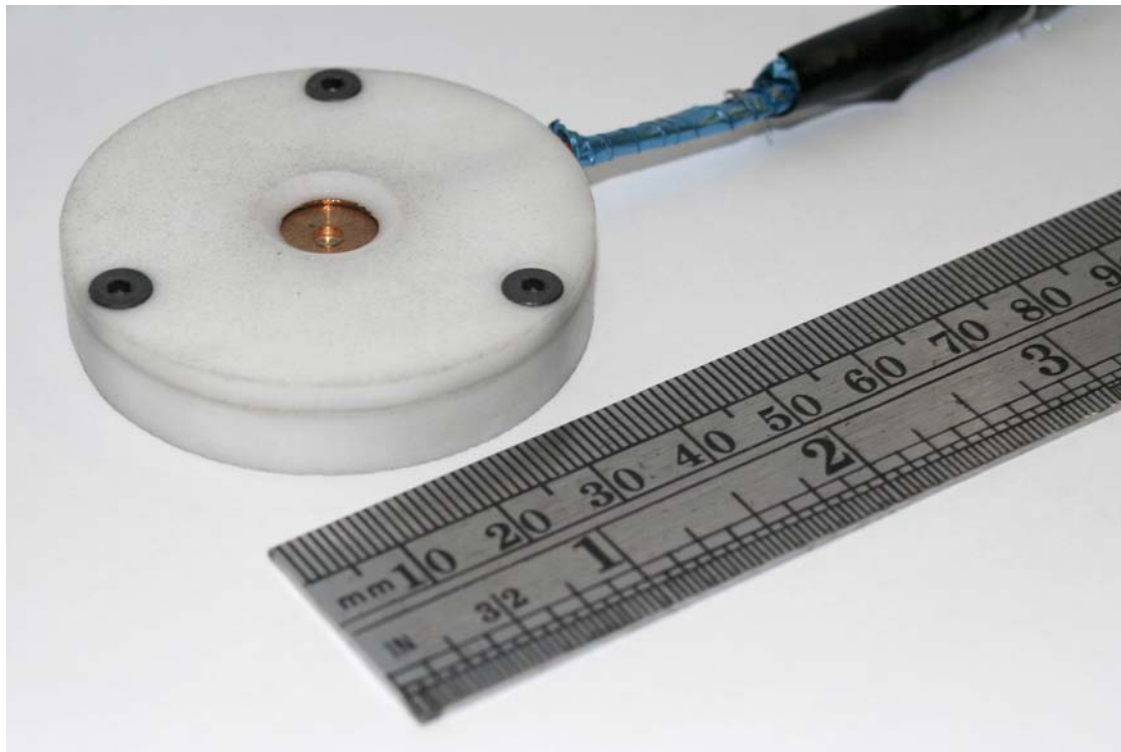


Figure 5.5: Sensor prototype: first generation.

was sufficient, it quickly became apparent that the success of future designs would be largely dependent on the management of electrical noise.

Electrical Considerations

The issue of electrical noise is not limited to sensors. Rather, it plays a significant role in the design of almost any electric device. While numerous sources of electrical noise exist, electro-magnetic interference (EMI) is the most commonly observed noise in measurement systems. EMI occurs any time an alternating current flows through a wire, generating a corresponding magnetic field which radiates outward. When this magnetic field intersects another wire, an undesirable voltage or current is induced, which is perceived as EMI. The effects of this interference can be substantial, as was the case with the initial prototype. Another common form of electrical noise is radio frequency interference (RFI), which is identical in nature to EMI but occurs at frequencies well above those of interest. EMI is a significant concern not only when performing dynamic measurements, but also when performing static measurements. Without sufficient measures to control EMI, the resulting noise can lead to the generation of a DC bias, significantly affecting the resulting measurements. Controlling electrical noise is an important consideration for any measurement system, including power supplies and wiring, and not limited to the specifics of a sensor design.

Eliminating or reducing EMI can be accomplished in a number of ways, both actively and passively. In terms of active methods of control, an effective means is to consider the sources of EMI. In a lab environment, EMI primarily results from the power cables which supply equipment. These high amperage power cables generate strong EMI which exhibits a distinct 60[Hz] frequency. It was this source which dominated the sensor signal during the initial stages of testing. To manage these EMI sources, the equipment should be placed far away from the measurement area to reduce the intensity of the magnetic field. While these measures are the most proactive, they can also be difficult to accommodate. For example, data acquisition equipment and power supplies will undoubtedly need to be placed near the test section. Also, while power cables serve as the primary source of EMI, other uncontrollable sources will inevitably exist. As such, other measures of reducing EMI, other than reducing the source intensity, needed to be considered.

A more common approach to actively reducing EMI is through the use of electrical shielding, effectively blocking the magnetic field. This can be accomplished by shielding the sensor leads, circuit, and housing with any number of materials. A summary of commonly used materials and their shielding characteristics is presented in Table 5.3 [79]. Favourable materials exhibit a high magnetic reflectivity ($s_r m_r^{-1}$) or absorptivity ($s_r m_r$). Simply surrounding the sensor with a material does not make for an efficient shield. Rather, the material must be able to reject the absorbed magnetic field to a sink, often using the ground of an electrical circuit. It is important when shielding not to form ground loops, as illustrated in Figure 5.6,

Material	s_r	m_r	$s_r m_r$	$s_r m_r^{-1}$
Silver	1.05	1.0	1.05	1.05
Copper	1.0	1.0	1.0	1.0
Aluminum	0.61	1.0	0.61	0.61
Brass	0.26	1.0	0.26	0.26
Nickel	0.2	100	20.0	$2.0 \cdot 10^{-3}$
Stainless steel (430)	0.02	500	10.0	$4.0 \cdot 10^{-5}$
Mumetal at 1[kHz]	0.03	$2.0 \cdot 10^4$	600	$1.5 \cdot 10^{-6}$
Superpermalloy at 1[kHz]	0.03	$1.0 \cdot 10^5$	$3.0 \cdot 10^3$	$3.0 \cdot 10^{-7}$

Table 5.3: Electrical conductivity (s_r) and permeability (m_r) of select materials relative to copper. (Data from Paul [79].)

as the EMI can be intensified as a result. Shielding serves as an effective means of attenuating EMI, while permitting operation in electrically noisy environments.

Aside from active methods of EMI control, simple passive techniques can sometimes be applied with good success. During data acquisition, a filter may be applied to the data to remove undesirable frequencies. Such a process, however, does not have the ability to discern noise from the actual signal. For the desired experiment, removing the 60[Hz] component could eliminate an important signal. As such, passive measures will only be pursued upon exhausting active alternatives.

Although EMI can be reduced, shielding can only provide finite protection. Shielding was used for the first generation prototype, and yet, electrical noise remained a significant problem. Some of the noise was in part due to the housing not being adequately shielded, however, a majority of the noise was attributed to the high impedance of the piezoelectric film. The reason that these high impedance circuits are particularly vulnerable to noise is due to correspondingly low current. As a result, the insignificant EMI induced currents of low impedance circuits can represent non-negligible contributions at high impedance. Therefore, in dealing

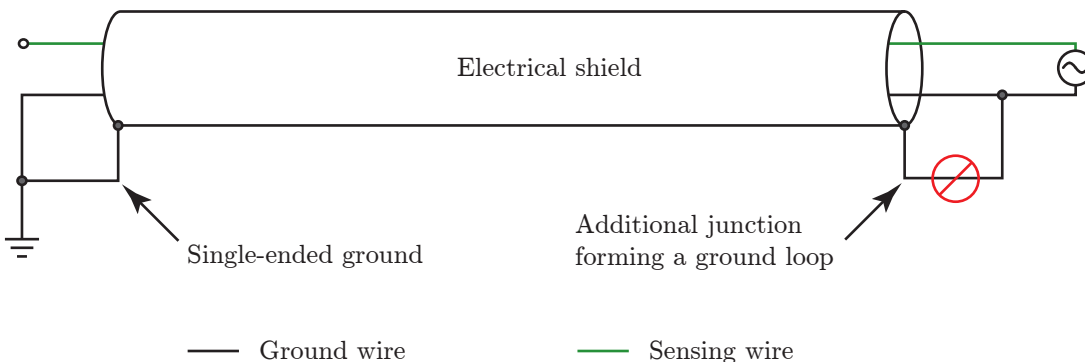


Figure 5.6: Proper grounding of electrical shielding.

with high impedance circuits, even the slightest break in shielding can result in the generation of a significant amount of noise.

To address the sensor’s vulnerability to noise, it was decided to use an operational amplifier (op-amp). While this device is traditionally used to apply a gain to a signal, its greater purpose in this design is to transform the circuit from a high to low impedance. As a result, the low impedance conductors can extend great lengths with minimal susceptibility to EMI. To further reduce the potential for EMI, it was decided to place the amplifier nearest to the sensor element, as to reduce the length of the high impedance conductors. Ideally, the amplification circuit would be placed within the sensor housing, serving as an effective EMI shield.

The selection of an appropriate op-amp was based on a number of criteria. First, a sufficiently high input impedance was required, as this parameter determines the lowest measurable frequency of the piezoelectric circuit, as defined by Equation 5.8 [59]. It was also desired to minimize the input leakage current, which serves as a potential source of error due to the high impedance of the piezoelectric film. Given the low magnitude of the input signal and the anticipation of high gains, it was desired to minimize the total harmonic distortion (THD) and maximize the common mode rejection ratio (CMRR) of the op-amp. A high CMRR ensures that the dynamic range of the input signal is retained, enabling small voltages to be perceived amongst large amplitude measurements. Another consideration involved matching the operating voltage of the op-amp to the data acquisition input range, as to minimize sources of measurement error. Finally, the geometry of the op-amp was an important criterion, as it was desired to place the circuit within the sensor housing. The op-amp operating frequency was given little consideration as it is typically orders of magnitude greater than the anticipated frequencies. Subject to the numerous criteria, a number of op-amps were selected from National Semiconductor, specifications of which are listed in Table 5.4 [72][73][74]. A primary distinction between the op-amps is the packaging, selecting the larger DIP pin format for the purpose of prototyping.

$$f_c = \frac{1}{2\pi RC} \quad (5.8)$$

For the selected op-amps, the sensor amplification circuit is presented in Figure 5.7. This circuit relies on the use of a dual polarity supply, with capacitors acting to decouple the supply and preventing noise from entering the circuit. The two resistors, R_1 and R_2 , are used to determine the gain of the amplifier, as de-

Model	Impedance [Ω]	Leakage [A]	Supply ΔU [V]	CMRR [dB]	THD [%]	Package
LMC6001AIN [72]	$> 10^{12}$	$0.025 \cdot 10^{-12}$	-0.3 to +16.0	72	0.01	8-pin DIP
LMP7701MF [73]	$> 10^{12}$	$0.2 \cdot 10^{-12}$	+2.7 to +12.0	138	0.02	5-Pin SOT23
LMP7715MF [74]	$> 10^{12}$	$0.1 \cdot 10^{-12}$	+0.6 to +6.0	100	0.001	5-Pin SOT23

Table 5.4: Characteristics of operational amplifiers for typical operating parameters.

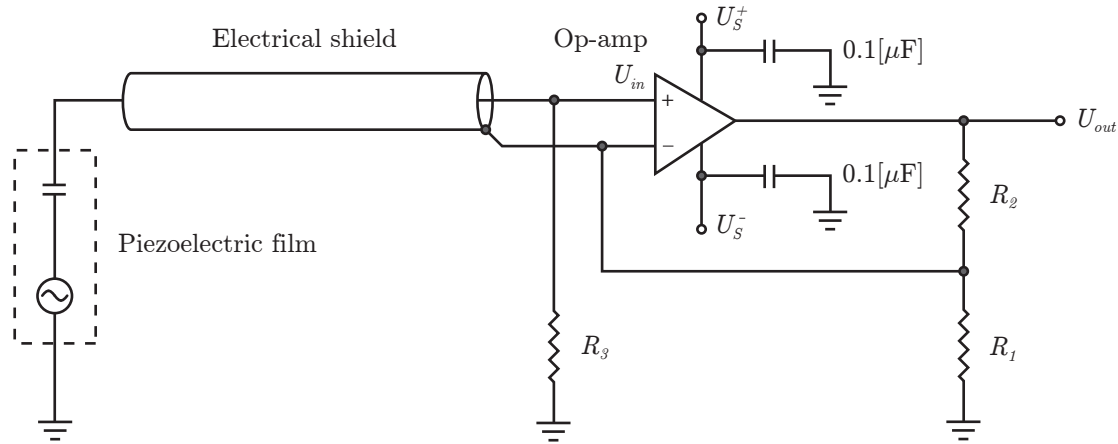


Figure 5.7: Sensor amplification circuit.

finned by Equation 5.9. While it was desired to obtain a sufficiently high input impedance, the resulting op-amp was considered too high, as the resulting low frequency response would make the measurements susceptible to pyroelectric effects. To increase the low frequency cutoff, a third resistor R_3 was placed across the input. To evaluate the low frequency cutoff using Equation 5.8, the resistance may be approximated by R_3 . Finally, while the electrical shielding is traditionally connected to ground, it has been alternatively connected to the negative input of the op-amp, as recommended by Rich [82] for high impedance circuits.

$$\frac{U_{out}}{U_{in}} = 1 + \frac{R_2}{R_1} \quad (5.9)$$

Sensor Prototype: Second Generation

Using the knowledge acquired from the initial prototype, a second generation sensor was designed and manufactured, as shown in Figure 5.8. For this generation, an amplification circuit was fabricated based on the schematic presented in Figure 5.7. For this particular circuit, the LMC6001AIN op-amp [72] was utilized, due to its favourable DIP pin form factor. An amplifier gain of 100 was selected based on the results from the initial prototype. The 3.0[mm] sensor diaphragm was placed directly on the amplifier circuit board, to minimize the resulting EMI, and was fabricated from 28[μm] film. An aluminum housing was used to both retain the diaphragm and shield the amplification circuit.

Evaluation of the second generation prototype was performed in a similar manner to the first, using a small speaker and frequency generator to produce a pure tone of 1000[Hz]. With the focus of this prototype design being the management of electrical noise, this simple experimental setup was considered sufficient, as it was not required to ascertain an exact sensitivity. Performing a series of tests with the sensor, it was found that the background noise of the second prototype was greatly

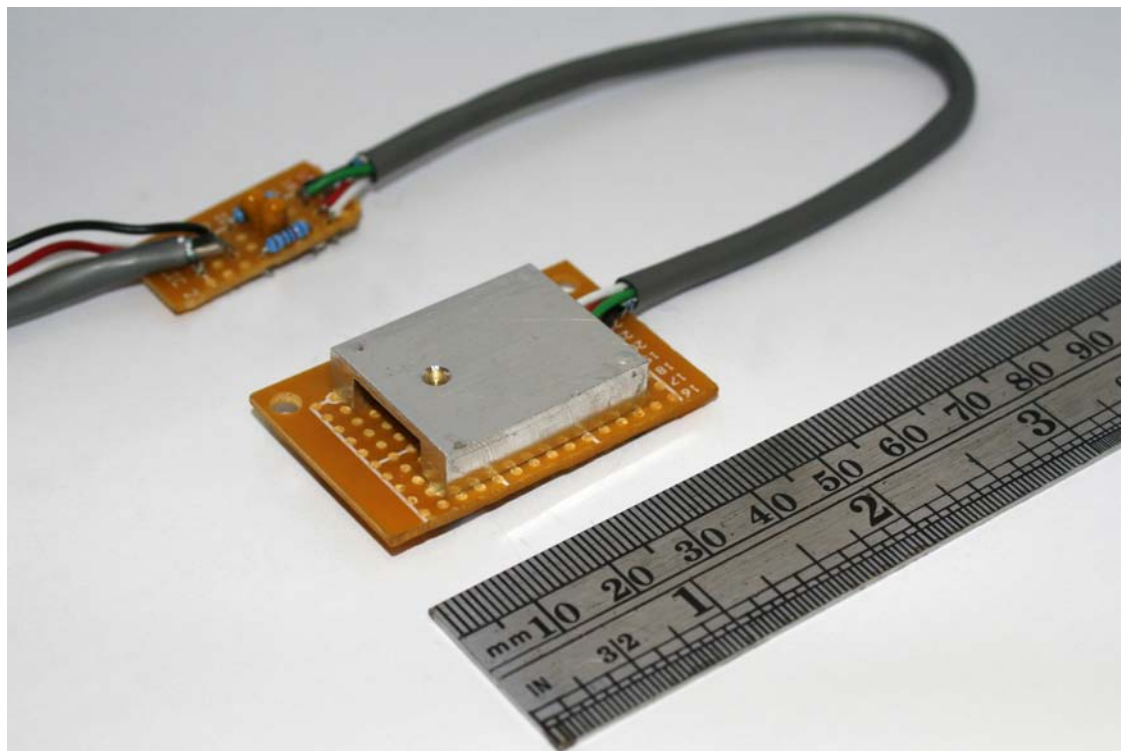


Figure 5.8: Sensor prototype: second generation.

improved from the first, with the broadband noise decreasing from approximately 10 to 2[mV]. This decrease in noise was considered significant, as the noise was measured after the 100 times amplifier gain. As a result, the signal-to-noise ratio (SNR) was improved by approximately 54[dB], likely a consequence of reducing the lengths of the high impedance conductors. Although the experimental setup could not quantify the sensitivity of the prototype, it was possible to resolve the pure tones from low intensity whistling. Based on these results, it was concluded that the 3.0[mm] diameter diaphragm with thickness of 28[μm] would provide sufficient sensitivity.

One deficiency that arose during testing was a remaining susceptibility to EMI. Placing the sensor near high amperage power cables would cause the signal to be dominated by 60[Hz] noise. Careful inspection of the design revealed a number of shielding deficiencies. First, the housing used to shield the electrical components was fabricated from aluminum, a relatively weak shielding material. Furthermore, the housing only covered the top portion of the circuit, leaving the underside entirely exposed. Another deficiency with the shield is that it formed part of the sensor ground, as opposed to being connected to the negative input of the amplifier. This method was initially considered adequate, as it has been used extensively by sensor manufacturers such as Brüel & Kjær (B&K) [17]. However, the evaluation of both B&K microphones and the prototype have revealed the reduced efficacy of the shield as a result. To address these deficiencies, the housing would need to encompass the entire circuit, only be connected to the circuit via the negative am-

plifier input, and be fabricated from a more effective shielding material, such as steel. These numerous deficiencies further emphasize the importance of shielding when measuring a high impedance signal.

Mechanical Considerations

With the electrical considerations completed, the numerous mechanical considerations required to facilitate the physical pressure measurement needed to be addressed. As previously stated, the piezoelectric sensor was to be self contained and not bonded to the specimen surface. With a criterion to minimize the size of the sensor, the outer diameter was initially specified at 5.0[mm]. This was considered the minimum size which could be readily manufactured using available mill and lathe equipment. Furthermore, a 5.0[mm] housing diameter easily accommodates the desired 3.0[mm] diaphragm. Upon making further refinements to the design, and obtaining a better measure of the sensor's performance, more expensive manufacturing options may be evaluated to further reduce the dimensions of the sensor. Working within the design constraints, the sensor design was broken into four components: the sensor outer, insulator, inner, and circuit, as presented in Figure 5.9.

For the sensor outer, stainless steel was selected as the material, providing both electrical shielding and resilience to environmental conditions. With the 4xx series of stainless steels being the only series to exhibit magnetism, it is the only series which exhibits strong shielding characteristics. As a result, 416 stainless steel was selected, offering a good balance of shielding and machining characteristics. For the outer to serve as an effective EMI shield, it needed to be connected to the circuit only via the negative amplifier input, as previously discussed.

The purpose of the insulator portion of the sensor was to provide the necessary electrical isolation between the inner and outer components. To provide this isolation, while not dramatically reducing the inner diameter of the sensor, the use

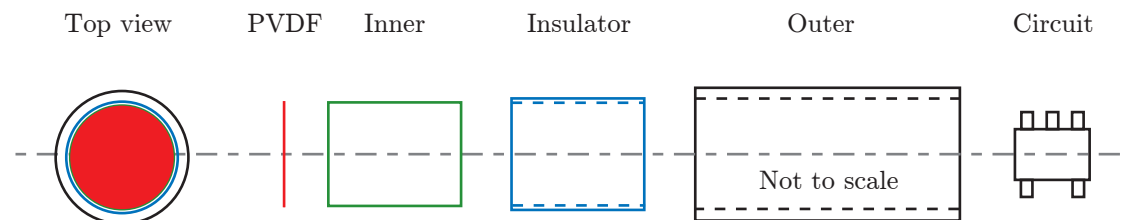


Figure 5.9: Sensor components.

of polytetrafluoroethylene (PTFE) light weight wall tubing was investigated. This tubing provides excellent electrical insulation and, for a tube with an inner diameter of 3.76[mm], has a diminutive wall thickness of 0.20[mm]. Samples of PTFE light weight wall tubing were provided by Zeus Inc. [97] for the purpose of prototyping. Using this light weight wall tubing, the inner portion of the sensor was able to be maximized to a diameter of 4.0[mm].

A significant portion of the sensor design focused on the development of the sensor inner, as this component serves a number of purposes. The primary purpose of the sensor inner is to provide an orifice to accommodate the movement of the diaphragm. An important consideration involved the manner in which the piezoelectric material was fixed to the sensor inner, for which three methods were investigated, as presented in Figure 5.10. The first method utilized compression, sealing the diaphragm by applying pressure between the inner and outer components. This technique exhibits a number of deficiencies. First, the quality of the seal is largely dependent on an applied pressure which would be difficult to manufacture consistently. As a result, too little pressure would yield a poor seal while too high a pressure could damage the diaphragm. Another limitation of this technique is that the diaphragm would need to be recessed within the sensor outer, preventing a flush mount configuration. The second method investigated also involved compression, relying on a press fit of the diaphragm between the sensor inner and outer. While this would enable the diaphragm to be flush with surface, the quality of the seal would be highly dependent on the manufacturing process, for the required tolerances would be difficult to obtain. Greater potential would also exist of deforming the piezoelectric material during the assembly process. The third method of fixing the diaphragm involved bonding the material to the sensor inner. This technique addresses the reliability concerns associated with the compression techniques, providing an excellent seal while enabling the film to be flush with the top of the sensor. While bonding was selected for the final design, numerous challenges remained in terms of manufacturing.

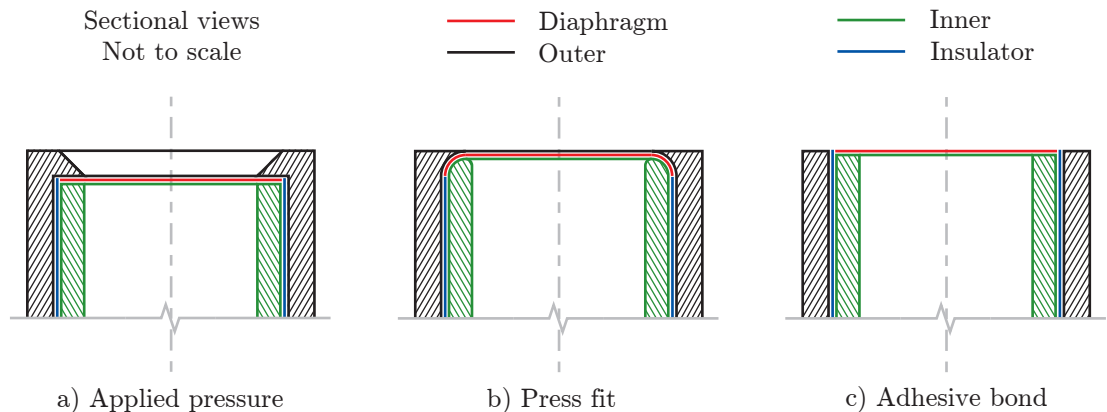


Figure 5.10: Methods of fixing the diaphragm to the sensor inner.

To establish the numerous manufacturing considerations for the bonding process, a series of experiments were performed. For the sensor inner, cylindrical pieces of both brass and aluminum were fabricated, having an inner and outer diameter of 3 and 4[mm], respectively. The selection of materials was primarily for electrical considerations. Piezoelectric elements were fabricated from the 28[μm] film, using a custom 4[mm] punch.

The first series of bond tests were to evaluate the effect of surface roughness of the sensor inner on the resulting bond strength. The surfaces of both the aluminum and brass samples were roughened using 80, 120, 180, 240, and 300 grit emery paper. For the initial bond tests, Loctite E-120HP [29] high strength epoxy was utilized. Prior to application of the adhesive, the surface of the cylinders were cleaned using acetone. The epoxy was then spread thinly over a flat plate and the sensor inners were placed firmly in the layer of epoxy. This approach was used to control the application of the epoxy, as excess adhesive might act to reduce the active area of the diaphragm and subsequently decrease the sensitivity of the sensor. With the epoxy applied to the sensor inners, the piezoelectric elements were carefully put in place. During the curing process, slight pressure was applied to the samples using a flat plate. Following a 24-hour curing period, a qualitative assessment of the bond strength was performed. One bonding deficiency became immediately obvious, as the simple act of handling the samples led to numerous failures. These failures were occurring at an unexpected location, between the silver ink metallization and the PVDF, attributed to a low peel strength. In hindsight, this finding was not particularly surprising, as polymer bonds are typically very weak. With no failures occurring in the epoxy layer or at the surface of the sensor inner, the effects of surface roughness in this situation were considered negligible.

The deficiency with the bond strength for silver ink metallization is that it is applied to a relatively smooth film surface. The alternative metallization, which uses copper-nickel, is applied using sputtered metal deposition. This process essentially pits the surface of the film, replacing the material with the copper-nickel alloy. With the sputter metallization process only occurring within a very thin layer of the surface, the resulting metallization thickness measures approximately 50 to 100[nm], compared to the 5 to 10[μm] of the silver paint. While this reduction in metallization thickness provides a marginal increase in sensitivity, it was anticipated that the sputtered metallization technique would provide a greater peel strength. To evaluate potential improvements in bond strength, the copper-nickel metallized film was acquired from Measurement Specialties. A qualitative peel test was performed by bonding a 4[mm] strip of both the sputtered metallization and silver painted film to a flat plate. Although both samples still failed between the metallization and the polymer, the sputtered metallization exhibited a significant improvement in peel strength.

For the copper-nickel film, bond tests were once again performed using the aluminum and brass sensor inners, with the intent of quantifying the bond strength. For these tests, the surfaces were prepared exclusively using 240 grit emery paper. Handling of the samples after the 24 hour cure period did not result in any

premature failures, an indication of the significantly improved peel strength. To quantify the bond strength, a static pressure of 100[kPa] was applied to the bottom of the sensor inner using a regulated pressure source, greatly exceeding the required specification of 20[Pa]. The pressure was applied for a period of 1[hr] during which the samples were submerged in water to easily identify failures. The three samples tested all passed successfully. Although this test did not evaluate fatigue of the bond subject to a dynamic pressure, the ability to withstand such a large static pressure provided confidence in the strength of the bond.

In addition to the sensor inner serving as an orifice for the diaphragm, the cavity behind the diaphragm forms what is known as the sensor volume. This volume serves as an important consideration in the presence of mean pressures, as it is only desired to resolve the fluctuating component for aeroacoustics. With the mean pressure potentially orders of magnitude larger than the fluctuating component, a sensitive piezoresistive sensor can easily become saturated. While the nature of the piezoelectric circuit effectively attenuates these low frequency pressures, the mean pressure still acts on the diaphragm and serves to reduce the sensitivity of the sensor. Thus, the intent of the sensor volume is to establish a pressure equal to mean pressure of the flow. With the mean pressures equal on either side of the diaphragm, subject to a fluctuating pressure, the vertical displacement of the diaphragm will be equidistant from the nominal position. As a result, the sensitivity of the sensor will remain constant, independent of the mean pressure.

To equalize the pressure of the sensor volume to the mean pressure of the flow, numerous design challenges were presented, largely in terms of manufacturing. It was necessary to connect the sensor volume to the top of the sensor using a restrictive passage, herein referred to as the sensing port. The idea is that the passage will be sufficiently restrictive to only respond to slow changes in surface pressures, say at a maximum rate of 20[Hz]. Any pressure fluctuations faster than this frequency will be damped by the restriction, with the sensor volume pressure remaining approximately constant. Alternatively, pressure fluctuations below the specified frequency will enable the sensor volume to adjust to the variation in pressure, effectively attenuating the low frequency measurement. Great care must be taken in the design of the sensing port, as an insufficiently restrictive port would act to reduce the low frequency response of the sensor, as illustrated in Figure 5.11.

Designing an effective sensing port is a relatively simple fluid mechanics problem. In fact, the same equations which were used in Section 5.1.1 to evaluate the sensing line resonance and viscous damping may be applied to the sensing port design. Unlike the sensing line problem, however, it was desired to maximize the damping ratio of the sensing port to improve the attenuation at high frequencies. With the reduction in sensitivity of the sensor being equal to the response of the sensing port, a high pass frequency was defined as the value corresponding to a 3[dB] reduction in sensitivity. Based on Equations 5.1, 5.2 and 5.3, a long, small diameter sensing port was required. Evaluating the expressions for a high pass frequency of 20[Hz], using a arbitrary length of 5[mm], it was determined that a port diameter of 1.4[μm] was required. While this diameter may be obtainable

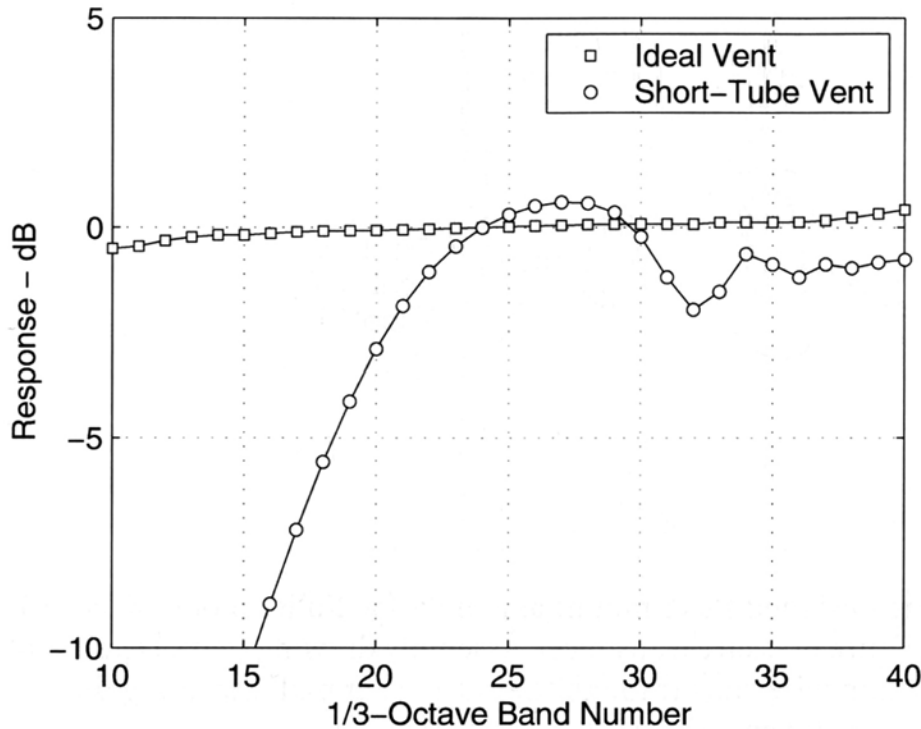


Figure 5.11: Frequency response of a pressure transducer for both an ideal and an improper sensing port. (From Mueller [67].)

using laser drilling techniques, the required depth would certainly be unobtainable. Even if it were possible, the use of laser drilling would be cost prohibitive for such a low volume production. Evaluating the expression for a diameter of 0.5[mm], obtainable using traditional drilling techniques, the required length would need to be 8.0[m], greatly exceeding the geometric constraints of the sensor. To address these manufacturing constraints, an innovative sensor port design was created. With a high pass frequency of 16.4[Hz], the resulting design satisfied both frequency response and geometric constraints. The frequency response of the sensing port and the effect on the overall sensor response are shown in Figure 5.12.

The final consideration for the sensor volume pertained to the size of the volume itself, as controlled by the depth. The requirement of a finite sensor volume is due to the movement of the diaphragm, which causes the compression and expansion of the fluid volume. The resulting change in pressure within the volume acts against the diaphragm movement, diminishing the sensitivity. Ideally, the volume would be infinitely large, such that the relative change in volume would have negligible effect on the resulting pressure. Evaluating the diaphragm deflection for a diameter of 3.0[mm] and maximum pressure of 20[Pa], based on Equations 5.6 and 5.7, the resulting change in volume was determined to be approximately 0.027[mm³]. Selecting a sensor volume depth of 5[mm], with a corresponding volume of 35.3[mm³], the resulting change in pressure within the volume would be approximately 77.5[Pa].

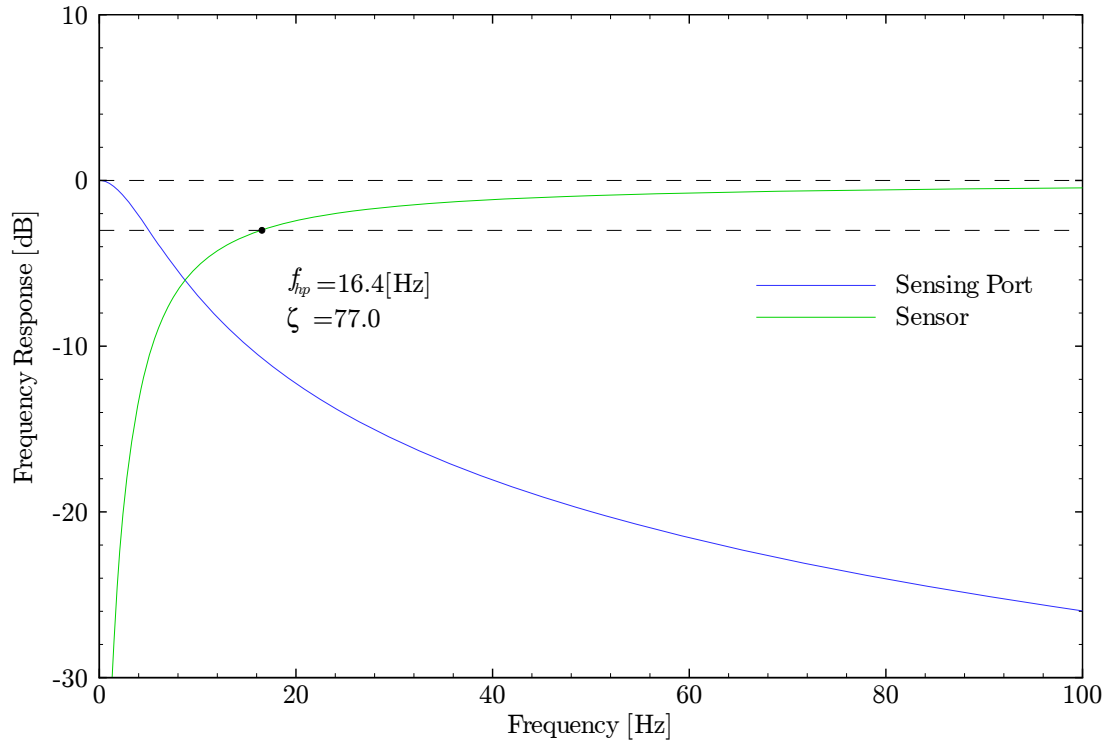


Figure 5.12: Frequency response of the sensing port and the resulting effect on the sensor.

To address this significant source of error, the diaphragm would need to be reduced in diameter or increased in thickness, as the depth cannot be increased appreciably. However, prior to making any changes, the sensor needed to be evaluated experimentally to determine whether this represents an appreciable source of error, as the deflection calculations are highly idealized. This evaluation was left to future consideration.

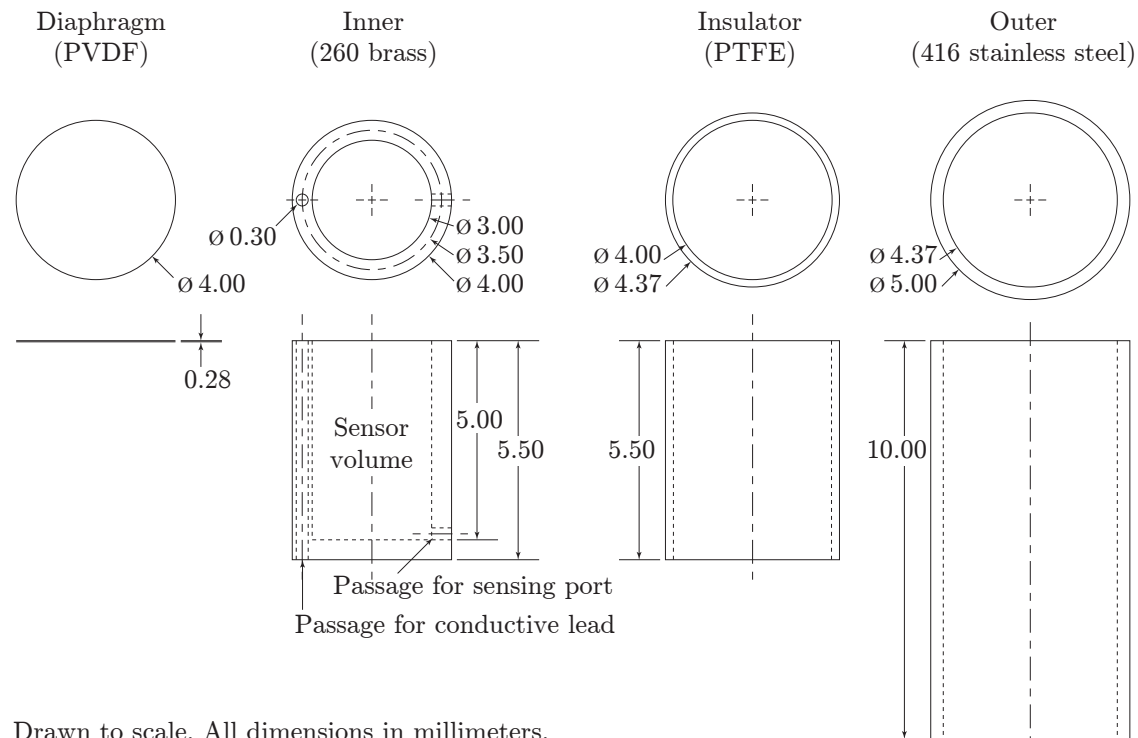
Another important consideration for the sensor inner design pertained to the electrical connectivity of the diaphragm. With the sensor outer serving purely as an EMI shield, the two conductive leads connecting to the piezoelectric film needed to be accommodated by the sensor inner. It was elected to use the sensor inner itself as one of the conductors. To provide continuity between the bottom of the piezoelectric film and the sensor inner, a silver impregnated electrically conductive epoxy was selected, using Loctite 3888 [28]. Bond tests were not performed for the conductive epoxy, as the slight reduction in peel strength was not considered significant. With the sensor inner acting as a conductor, brass was select as the material due to its favourable electrical conductivity and corrosion resistance. The second conductor, which needed to connect to the top of the piezoelectric film, was accommodated by drilling a 0.3[mm] hole lengthwise through the sensor inner. An epoxy coated wire, common to motor windings, was used as the second conductor as it possesses a minimal amount of electrical insulation. Upon bonding the wire in the 0.3[mm] passage, connectivity with the top of the piezoelectric film is accomplished

by using the electrically conductive epoxy.

The fourth and final component of the sensor design involved accommodation of the circuit within the sensor housing. To minimize the dimensions of the circuit, the LMP7701MF op-amp [74] was selected, measuring 2.9x2.8x1.0[mm]. The circuit also required two capacitors and resistors, selecting surface mount types with each measuring 1.6x0.8x0.5[mm]. The manufacturing of the final circuit design presented numerous challenges, details of which were left to future consideration. However, using the dimensions of the individual components, the overall sensor length was fixed at 10[mm].

To provide connectivity between the circuit and the data acquisition system, a four conductor cable was required. The cable was to be fixed to the housing permanently, as accommodation of a connector would significantly increase the dimensions of the sensor. With the additional requirement that the cable be shielded, difficulties were encountered in finding a suitable product. The Pro Power 7-1-4C cable [80] met these stringent requirements, containing four 0.055[mm²] conductors, braided steel shielding, with an outer diameter of just 3.3[mm]. A compatible four conductor LEMO connector [51], inline type 00, was selected to provide a robust connection and for ease of removal.

The final sensor design is presented in Figure 5.13. Although extensive efforts went into the manufacturing of the numerous sensor components, many of the details have been omitted for brevity.



Drawn to scale. All dimensions in millimeters.

Figure 5.13: Sensor design.

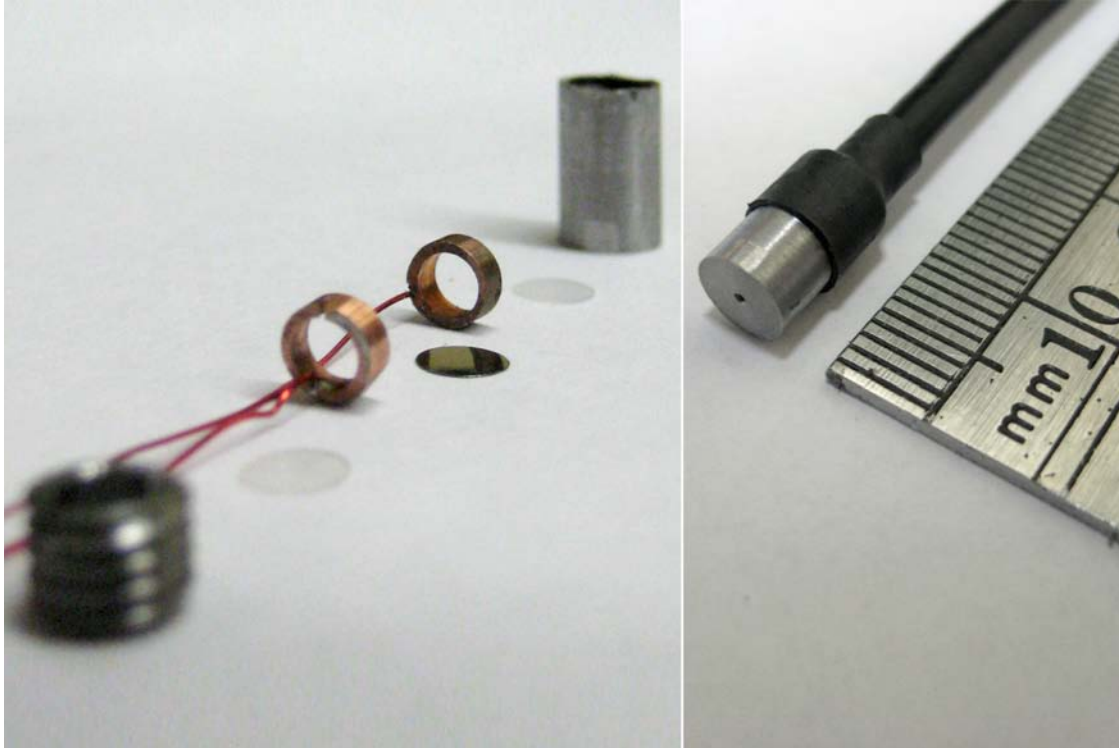


Figure 5.15: Sensor prototype: third generation.

using metal foil and to ensure the shield did not form a ground loop. While the compromises in design may appear numerous, the greater focus of the research was to quantify the performance of the sensor and to validate its use in performing near field aeroacoustic measurements. Thus, these compromises did not detract from the intended goals.

During a qualitative assessment of the sensor's performance, a small deficiency was noticed in the circuit design. When handling the sensor during operation, the sensor's output would occasionally saturate. This behaviour was attributed to the pyroelectric effect, as the $10[\text{M}\Omega]$ resistor across the input caused low frequency temperature variations to be resolved. Decreasing the resistor value to $1[\text{M}\Omega]$ effectively eliminated the pyroelectric effects at a slight compromise to low frequency response. During the initial assessment, it was also observed that the sensor noise was diminished significantly and the presence of EMI sources had little effect on the resulting signal, a vast improvement from the first prototypes. To provide a quantitative assessment of the sensor's performance, a calibration setup was required.

5.1.5 Sensor Calibration

Overview

To facilitate the calibration of the piezoelectric sensor, a comparison method was selected. This technique involves the generation of a known acoustic pressure source,

as quantified by a calibrated reference sensor. By performing a simultaneous measurement for the uncalibrated sensor, the sensitivity of the device can be determined for a given frequency and amplitude. The development of a suitable calibration setup involved numerous considerations, including environment, source, reference sensor, procedure, and software. While the setup was developed specifically for the piezoelectric sensor, the facility could be used to evaluate any number of pressure sensors.

Environmental Considerations

The environment in which a calibration is performed can have a significant impact on the accuracy of the results. One source of error is attributed to the radiation characteristics of the acoustic source, with the pressure waves emanating in directions other than toward the sensors. These radiated pressure waves can reflect off nearby surfaces and act to interfere with the calibration, often in an unpredictable manner. As a result, potential reflections within the environment should be minimized. Another source of error with the environment can result from EMI radiation. While efforts were made during the design process to control the EMI susceptibility, any remaining interference can be eliminated by shielding the environment.

To address the potential sources of error, an anechoic chamber was developed. An anechoic chamber may be thought of as a “noise free” environment, both in terms of acoustics and electro-magnetics. Internally, the surfaces of the chamber act to attenuate reflected sound and electro-magnetic waves. Furthermore, the chamber walls effectively block external acoustic and EMI sources from entering the chamber. Thus, the use of an anechoic chamber would effectively reduce the sources of error experienced during the calibration process. An additional benefit of the anechoic chamber is that it effectively contains the high intensity acoustic source, enabling calibration to be performed in a populated lab.

The design of the anechoic chamber was largely governed by the chamber volume. It is well established that the chamber absorption efficiency increases with chamber volume, simply because the sound must travel a greater distance and can be absorbed by a much larger area. Ideally, an anechoic chamber would be infinitely large, eliminating potential reflections all together. This relationship explains why anechoic chambers are traditionally the size of a room and orders of magnitude larger than the desired test specimen. While a large scale anechoic chamber would be efficient, it was considered cost prohibitive. Instead, the chamber size was selected to be easily placed on a bench. As such, the internal dimensions of the chamber were defined by a cubic volume with an edge length of 305[mm]. While such a small chamber would inevitably exhibit a diminished absorption efficiency, it would still serve as an efficient EMI shield and prevent excessive sound from exiting the chamber.

Another important aspect of the chamber design involved the material used to line the inner walls, as it is this material which serves to attenuate the acoustic

reflections. The selection of an appropriate material involved two considerations. The first consideration was the geometry, which often assumes the characteristic shape of a wedge. The wedge geometry serves as an efficient absorber, as the incident sound waves are internally reflected. Additional considerations for the wedge geometry include spacing, height, and angle, each of which have a substantial effect on the resulting absorption efficiency. It should be noted that the resulting absorption efficiency is a frequency dependent phenomenon, with lower frequencies exhibiting much lower efficiencies. The second design consideration pertained to the composition of the material. It is desirable to select a material which exhibits good absorption properties, often found in porous media. Commonly used materials include fibreglass and polyurethane foams. More exotic materials, such as carbon impregnated foams, provide the additional attenuation of electro-magnetic reflections.

Given the relatively small anechoic chamber geometry, the effective placement of the anechoic material necessitated the development of a custom anechoic wedge. Rather than performing an exhaustive design process for the wedge, it was decided to base the design on a suitable commercial product. Selecting the Acoustical Solutions Alphamax anechoic wedge foam [2], a one-third scale design was created to accommodate the internal geometry of the chamber. Scaling of the anechoic foam was at the compromise of low frequency absorption. Due to the custom dimensions, the wedges were manufactured in-house using $22.0[\text{kg m}^{-3}]$ polyurethane foam, as shown in Figure 5.16. The foam pieces were then adhered to the inner surface of the chamber using a permanent spray adhesive.

The final design consideration for the anechoic chamber pertained to the material used for the walls. For the walls to serve as both a rigid structure and an effective EMI shield, they were fabricated from $3.18[\text{mm}]$ mild sheet steel. Rather than permanently welding the structure, the walls were fastened together using countersunk fasteners, enabling future alterations to the chamber. A hinge was used on the front of the chamber to permit quick access to the test section. The anechoic chamber was entirely manufactured using available resources, with the final assembly shown in Figure 5.17.

Acoustic Source

The acoustic source required for the calibration process was subject to numerous constraints. To properly evaluate the frequency response of the sensor, the source would need to produce a range of 100 to 10 000[Hz]. Furthermore, to evaluate the amplitude response of the sensor, a range of 1 to 100[Pa], or 94 to 134[dB], was required. While obtaining the desired frequency range was considered a relatively simple task, producing 134[dB] presented numerous design challenges.

The acoustic pressure source was to be generated using a speaker, the selection of which was largely based on sensitivity. This frequency dependent parameter serves as a measure of the device's efficiency, defining the sound pressure level generated

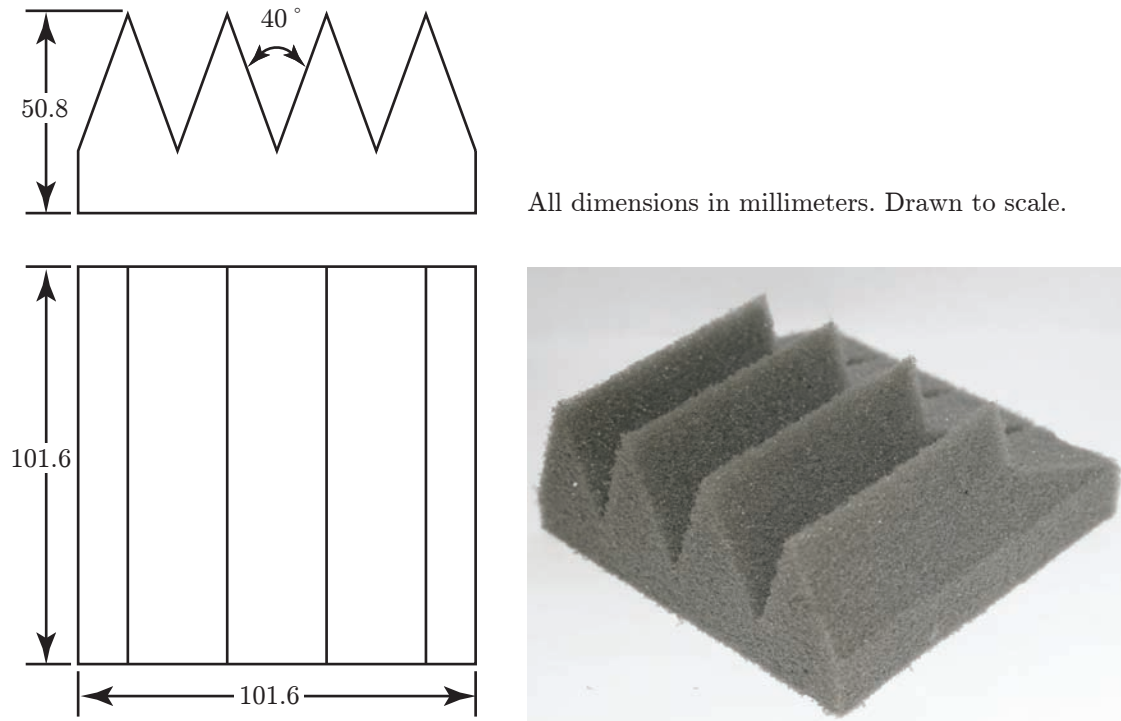


Figure 5.16: Anechoic foam design.



Figure 5.17: Anechoic chamber.

by 1[W] of power at a distance of 1[m]. To minimize the amplifier requirements, the sensitivity of the speakers needed to be maximized. Although numerous design parameters establish the overall sensitivity, quality serves as an important factor.

The frequency response of the calibration setup also played an important role in the speaker selection. Small speakers are inherently efficient at higher frequencies, exhibiting poor sensitivity at lower frequencies. The opposite is true for larger speakers, which are best suited for lower frequencies. While a full range speaker could be obtained which covers the entire frequency range, it does so at the compromise of sensitivity. Thus, to maximize the sensitivity over the range of frequencies, two differently sized speakers were to be utilized. The sensitivity of the selected speakers was also desired to be relatively constant, as the maximum power output is also constant over the range of frequencies.

The final considerations for the speaker selection were geometric. To avoid the speakers from pressurizing the anechoic chamber, the speakers needed to be mounted internally. To minimize the resulting volume reduction, the depths of the selected speakers needed to be minimized. Furthermore, based on the internal geometry of the chamber, the maximum speaker diameter was not to exceed 180[mm].

Subject to the numerous constraints, a 25[mm] speaker (B&C DE10) [8] and a 170[mm] speaker (B&C 6MDN44) [7] were acquired, each exhibiting a maximum depth of 73[mm]. The combined sensitivities of the two speakers yielded a favourable response, as shown in Figure 5.18 [8][7]. Over the range of frequencies of 100 to 10 000[Hz], the minimum sensitivity is 83.5[dB m W⁻¹]. Given the high sensitivity of the speakers, the maximum power ratings easily satisfied the output requirements.

To mount the speakers within the anechoic chamber, the speakers were fastened to an 3.18[mm] aluminum sheet. The rigidity of the sheet was increased by bonding it to a medium-density fibreboard (MDF). This approach was used to minimize the depth of the assembly. To prevent acoustic reflections within the chamber, foam wedges were adhered to the surfaces of the assembly. The entire assembly was rigidly mounted to the top wall of the anechoic chamber using aluminum stand offs and threaded fasteners, as shown in Figure 5.19, enabling the assembly to be removed if necessary. Two electrical connectors were mounted on the top wall of the chamber, enabling external power to be supplied to the installed speakers.

To power the speakers, an amplifier circuit was manufactured based on a National Semiconductor design, as shown in Figure 5.20. To provide the maximum required sound pressure level of 134[dB], at a specified distance of 0.10[m], it was determined that a 31.6[W] amplifier was required, based the minimum speaker sensitivity. To satisfy these power requirements, the National Semiconductor LM1875 op-amp [71] was selected, due to its low noise and high power output. To dissipate heat generated by the op-amp during operation, a heat sink was attached to the device, as shown in Figure 5.21. With only one circuit fabricated, the amplifier needed to be shared between the two speakers. To enable the output to be easily

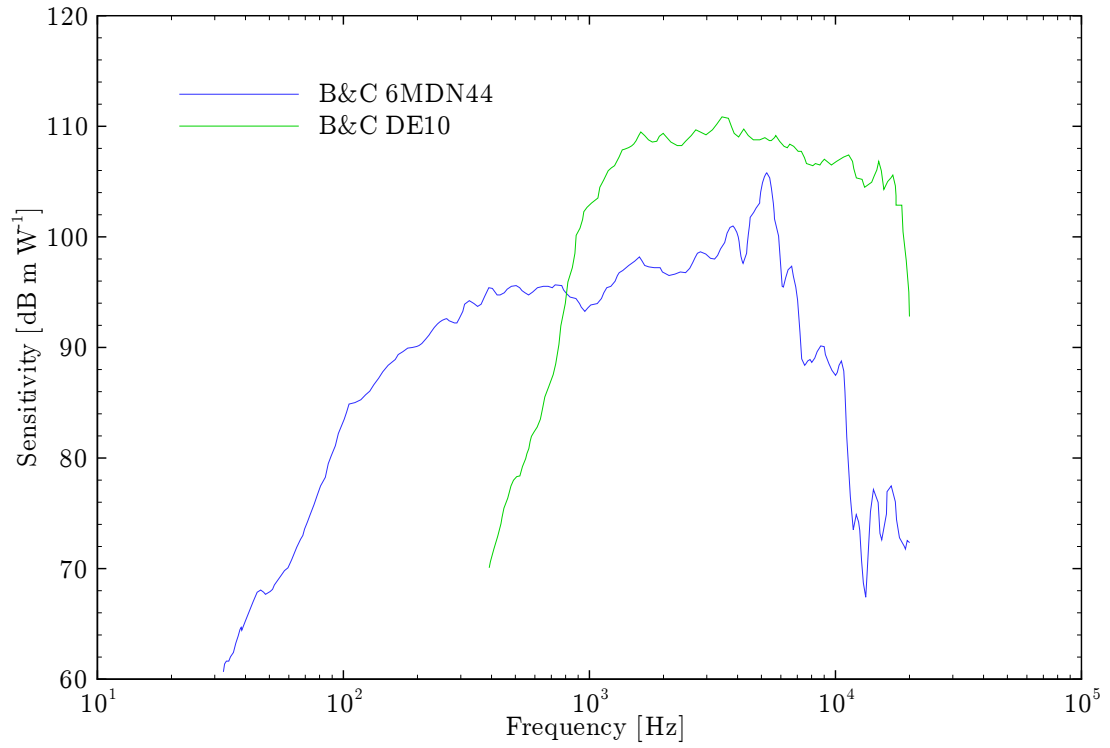


Figure 5.18: Frequency response of speakers selected for the calibration setup. (Data from B&C [8][7].)

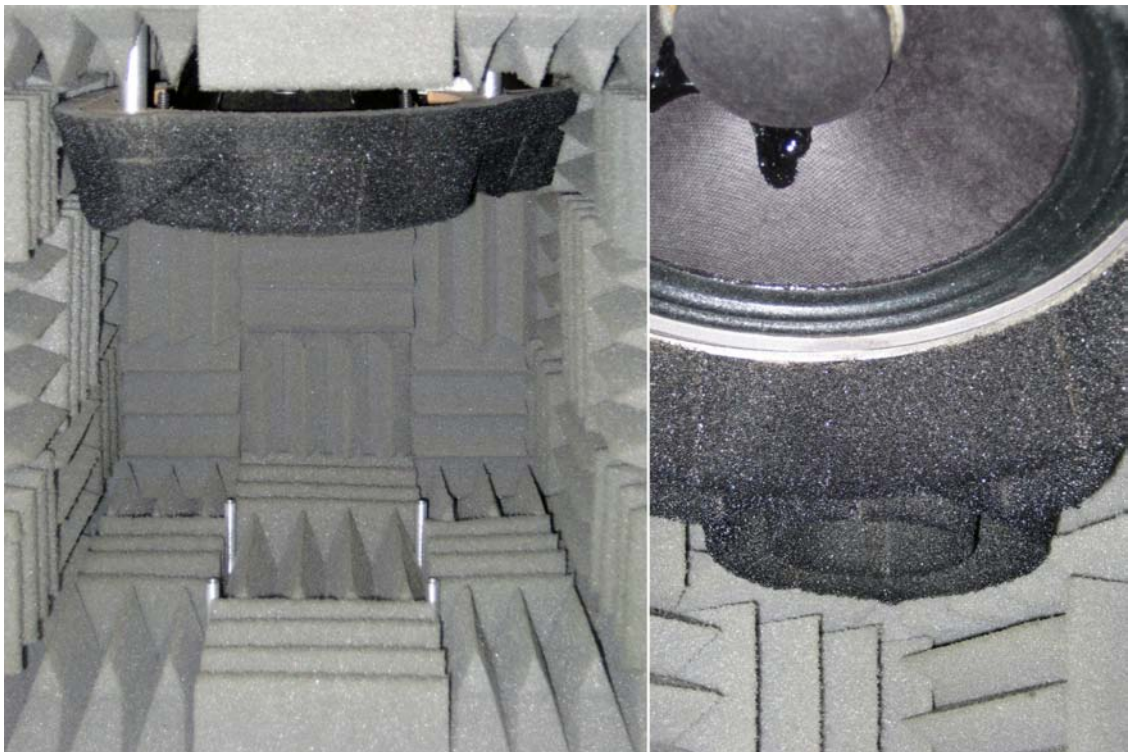


Figure 5.19: Anechoic chamber with speakers installed.

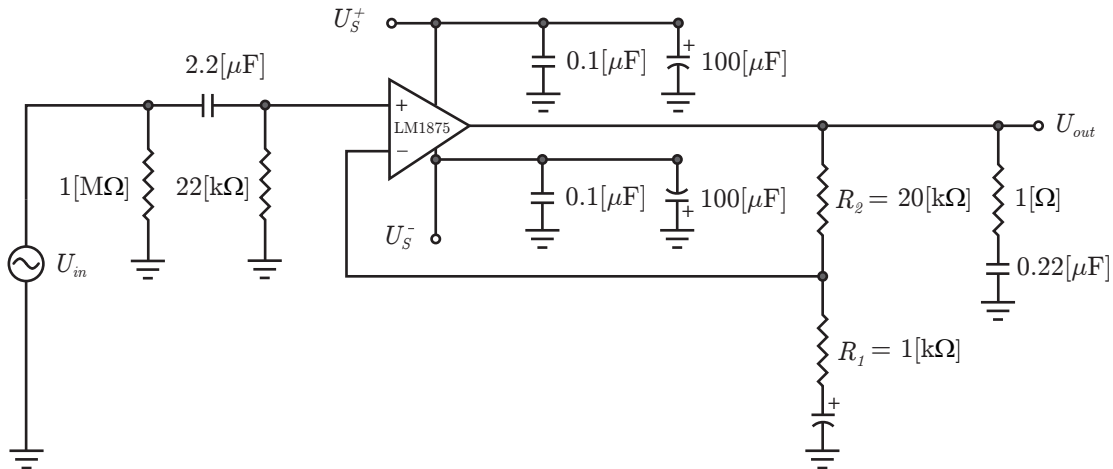


Figure 5.20: Amplification circuit design for the anechoic chamber speakers.

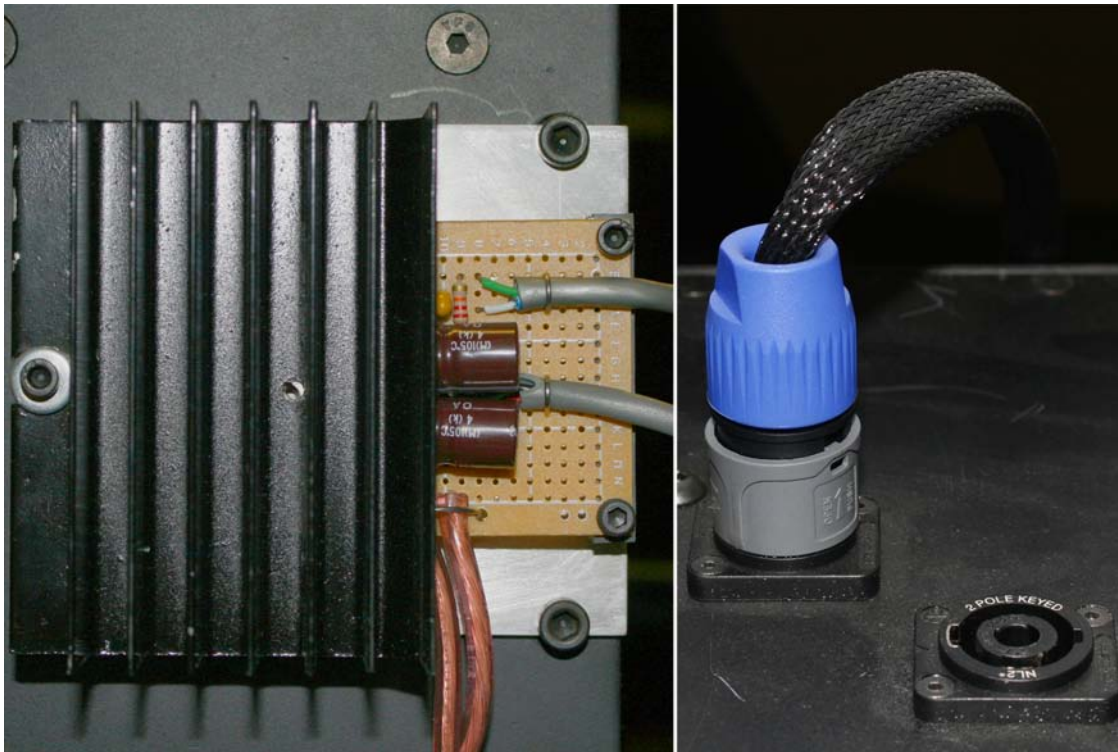


Figure 5.21: Amplification circuit and speaker connectors.

switched, quick connectors were used at the wall of the chamber, as shown in Figure 5.21. The input of the amplifier could be driven by a number of sources, while power to the amplifier was supplied by a dual polarity Agilent (E3631A) power supply [3].

Reference Sensor

Determining the sensitivity of the uncalibrated sensor requires knowledge of the source intensity, necessitating the use of a calibrated reference sensor. The constraints for the reference sensor were identical to the source requirements, requiring a frequency response of 100 to 10 000[Hz] and a pressure range of 1 to 100[Pa]. While the upper limit of 100[Pa] was retained as the maximum value, it was desired to minimize the lowest measurable pressure to provide greater flexibility in the calibration of future devices.

With fairly conservative constraints, a B&K 4192 microphone [18] was selected as the reference sensor for a number of reasons. First, the microphone exhibits an excellent dynamic range of 19 to 162[dB] with a frequency response of 3.15 to 20 000[Hz]. The high sensitivity of the sensor is partially attributed to the large 12.7[mm] diameter, a geometry which can be easily accommodated. A B&K preamplifier (2669-C) [15] and a single channel conditioning amplifier (2690-A-0S1) [16] were also acquired to provide the necessary microphone amplification. The justification for a high quality microphone was in part due to the provided calibration, with a 0.1[dB] uncertainty.

Sensor Setup

The setup of both the reference and uncalibrated sensor within the anechoic chamber was largely dependent on whether the pressure field or free field response of the uncalibrated sensor was required. The distinguishing factor between the two responses is that the free field response accounts for the effects of the sensor being physically immersed in the pressure field. The resulting interaction of the sound waves with the sensor housing can significantly alter the perceived pressure. Thus, the pressure field and free field responses must be considered independently. Given that the piezoelectric sensors will be placed internal to the test specimen, used to measure near field pressures as opposed to the impinging pressure waves, only the pressure field response was required. If the sensors were used to resolve impinging pressure waves, the free field response would need to be evaluated in-situ.

To perform the pressure field calibration, a coupling tube was used, as shown in Figure 5.22. The volume of air within the 25.4[mm] tube essentially couples the speaker output to both the reference and uncalibrated sensor. Using this approach, the 25[mm] speaker serves as a piston, providing a plane pressure wave within the tube and removing the free field response. An additional benefit of the coupling tube is that the output is constrained to a relatively small volume, enabling the speaker to obtain a much higher sensitivity. This enabled the single 25[mm] speaker to be used to calibrate the entire frequency spectrum at pressure levels upward of 140[dB], thus satisfying the constraints of the calibration setup. A potential deficiency with the coupling tube was that the sensors were subject to a finite vibration due to the rigid connection that was formed between the speaker and the sensors. While the

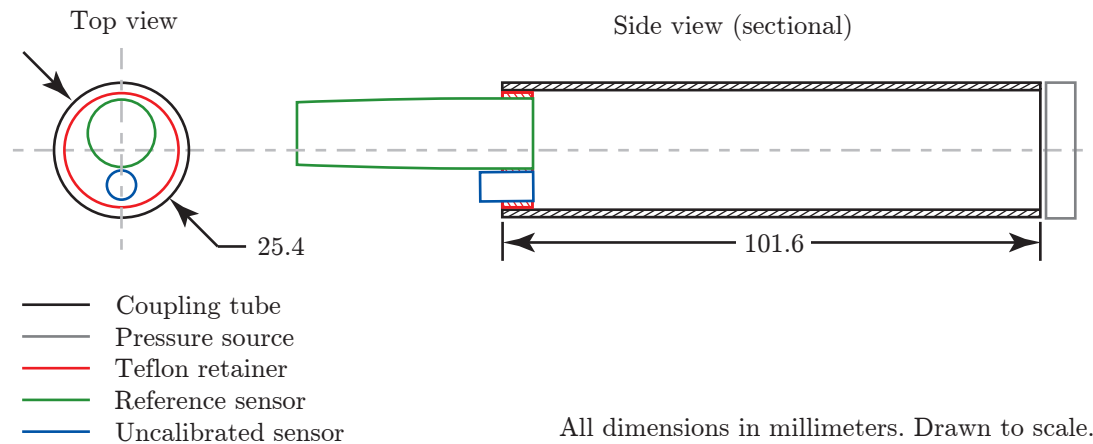


Figure 5.22: Sensor calibration coupling tube.

effects of this vibration on the resulting calibration were not quantified, it was not considered a significant source of error.

If a free field calibration was required, both the reference and uncalibrated sensor would need to be mounted in front of the acoustic sources. The sensors must be placed symmetrically about the axis of either speaker, due to the directionality of the intensity fields. Placing the sensors at a distance of 0.1[m], a maximum sound pressure level of 134[dB] would be obtainable over the range of frequencies. Using the calibrated response of the reference B&K microphone, the free field response of the uncalibrated sensor could then be determined. To facilitate future free field calibrations, removable aluminum standoffs were fabricated for the bottom of the chamber.

Procedure

To characterize the piezoelectric sensor, it was necessary to quantify the device's sensitivity, or response, over a range of frequencies and amplitudes. Performing this calibration enables the sensor measurements to be corrected for the variation in sensitivity. The amplitude and frequency response also provide detailed insight into the sensor's design. To perform the calibration, the frequency and amplitude response were considered independently.

To evaluate the frequency response, one approach involves the generation of white noise, a source which contains equal power across the entire frequency spectrum. This method was used by Lee and Sung [50] in calibration of a PVDF array. While this approach enables the frequency response to be obtained quickly, this technique exhibits a number of deficiencies. First, it is difficult to achieve a speaker output which identically represents white noise, causing the output amplitude to vary across the frequency spectrum. As a result, any variation in amplitude sensitivity would be improperly attributed to the frequency response. Second, the

power requirements of the speaker and amplifier would be greater, as the maximum intensity generated by a distributed white noise would be significantly lower than for a single frequency. To address these deficiencies, it was elected to perform the calibration using a single frequency, also referred to as a pure tone. To perform the calibration, the source amplitude was held constant at 10[Pa], or 114[dB]. The frequency was then varied incrementally from 100 to 10 000[Hz], in 1/12-th octave increments, as recommended by the ISO 266:1997 acoustic measurement standard [42]. Another common calibration amplitude is 1[Pa], or 94[dB], however, the higher of the two was selected to minimize the relative intensity of the background noise.

To evaluate the amplitude response, the frequency was held constant at 1000[Hz]. The amplitude was then varied from 1 to 100[Pa], or 94 to 134[dB]. Other common frequencies are 250 and 251.2[Hz], however, 1000[Hz] was selected due to the higher sensitivity of the speaker.

In addition to measuring the frequency and amplitude response, the lowest measurable pressure was to be determined by quantifying the sensor noise. Furthermore, the upper limit of the sensor's operation was to be evaluated by measuring the distortion, thus establishing the sensor's dynamic range.

FFT Analysis

The fast Fourier transform (FFT) serves as an efficient means of transforming data from a time to frequency domain, enabling the frequency spectrum to be obtained for a time resolved data set. The quality of the resulting FFT is affected by a number of parameters, all of which needed to be considered prior to collecting data.

The primary consideration in performing an FFT analysis is the required sampling rate. The sampling rate should be twice the highest observed frequency, commonly referred to as the Nyquist criterion. With the resulting frequency spectrum ranging from zero to one-half the sampling frequency, sampling below the Nyquist criterion will cause high frequency measurements to be misrepresented at lower frequencies, an error known as aliasing. Given that the aliased result cannot be discerned from the true frequency spectrum, aliasing can serve as a significant source of error. Increasing the sampling rate beyond the Nyquist criterion does not provide any additional benefits, rather, it simply places greater demands on the data acquisition equipment. Determining the required sampling rate can be challenging, as it requires prior knowledge of the maximum frequency.

Another important FFT consideration pertains to the desired frequency resolution. The resolution is governed by the sampling rate and number of samples, but may be expressed simply in terms of sampling duration, as defined by Equation 5.10.

$$\Delta f = \frac{1}{t} = \frac{N}{f_s} \quad (5.10)$$

The finite frequency resolution of an FFT can result in a phenomenon known as spectral leakage. This leakage occurs when the energy from one frequency is misrepresented by a neighbouring value, a consequence of a discretely sampled waveform. The effect of spectral leakage can be mitigated by windowing the data; a technique which involves applying a function to discretely sampled data such that it more closely represents a continuous waveform. Although a number of windows exist, the Hamming window is often used in acoustics. As such, it was used exclusively in the processing of FFT results.

A final consideration of the FFT pertains to averaging. Similar to time resolved data, averaging can be used to reduce the effects of spurious samples and to decrease the uncertainty of the results. To perform FFT averaging, the FFT analysis must be applied to a number of independent data sets. The average frequency spectrum may then be obtained by averaging the discrete frequencies across the data sets. Thus, compared to time resolved data, a large number of samples is required to obtain an equivalent convergence.

Software

During the design process, the sensor's performance was quantified using a simple frequency generator and hardware spectrum analyzer. However, due to the complexities of the calibration procedure, as well as to reduce potential sources of error, a more robust solution needed to be developed. To address these deficiencies, an application was created using National Instruments LabVIEW [70], facilitating the entire calibration process.

The first component of the LabVIEW program involved the generation of a source signal for the amplifier. Using a National Instruments PCI-6251 data acquisition board [69], a 16-bit digital-to-analog converter (DAC) was used to output a sinusoidal waveform at a rate of 2.5[MHz]. Given that the output was discretely sampled, the data rate was maximized in an attempt to best represent a continuous waveform. The voltage output of the signal was also maximized to avoid discretization of the signal waveform. To obtain a specified calibration amplitude, the output of the source was regulated using the reference sensor measurements in a closed-loop control logic.

The second aspect of the LabVIEW program involved the acquisition of voltages for both the reference and uncalibrated sensors. To facilitate the measurements, a National Instruments PCI-6143 data acquisition board [68] was utilized. This board enables simultaneous sampling using dedicated 16-bit analog-to-digital converters (ADC) at a rate of 250[kHz], permitting measurements to be performed concurrently with the source output. To resolve frequencies upward of 20[kHz], the inputs were sampled at a rate of 40[kHz], as per the Nyquist criterion. After

applying an FFT, a peak detection was used to extract the voltages for the defined frequency. Using the measured voltage and sensitivity for the reference sensor, the sound pressure level was determined. With knowledge of the sound pressure level, the voltage of the uncalibrated sensor was used to evaluate the unknown sensitivity.

The LabVIEW program was implemented with three distinct operating modes. The first mode provided manual operation, holding the source fixed at a specified frequency and amplitude. The second and third modes executed the frequency and amplitude sweep, respectively, as per the procedural outline. For a given frequency and amplitude, sensitivity measurements were not performed until the source was within 0.1[%] of the nominal values. Upon obtaining the defined source, the sensitivity of the sensor was evaluated at a rate of 1[Hz] until the mean sensitivity covered to within 1[%] and a minimum of 10 samples were obtained. The strict convergence requirements ensured that the calibration process was repeatable. Upon obtaining convergence, the mean sensitivity and corresponding convergence parameters were written to a data file. The source was continuously monitored during the calibration process, and if amplitude or frequency deviated beyond the specified limits, the sampling process for the given frequency and amplitude would be reset and restarted upon obtaining a constant source. Additional details of the LabVIEW application are presented in Appendix A.

Results and Analysis

Using the calibration setup, the third generation prototype sensor was evaluated, exhibiting a sensitivity of $0.0039[\text{V Pa}^{-1}]$ at $1000[\text{Hz}]$. Details of the frequency and amplitude response are presented in Figure 5.23 and 5.24, respectively.

Observing the frequency response, the sensor exhibits a smooth and continuous curve, suggesting the calibration was performed successfully. Comparing the response to the reference B&K microphone, it is apparent that the design could be improved significantly to obtain a flatter frequency response. While a constant sensitivity is desirable, the frequency dependency can be readily compensated for during the analysis process. In terms of the low frequency response, the diminished sensitivity is likely due to a poor seal formed by the compression of the piezoelectric diaphragm. It also possible that the response is attributed to the cutoff frequency of the circuit design. Observing the high frequency response, an increase in sensitivity is apparent, characteristic of sensor resonance. This resonance could be a result of the finite sensing port required for the compression technique. Alternatively, the resonance could be a consequence of insufficient compression, as the reduced rigidity of the diaphragm would act to decrease the natural frequency. These deficiencies could be partially addressed by bonding the diaphragm, as per the intended design.

For the amplitude response, a relatively constant sensitivity was observed, as anticipated. Given the constant sensitivity, the use of white noise to evaluate the frequency response would have served as a valid technique. A slight deviation in

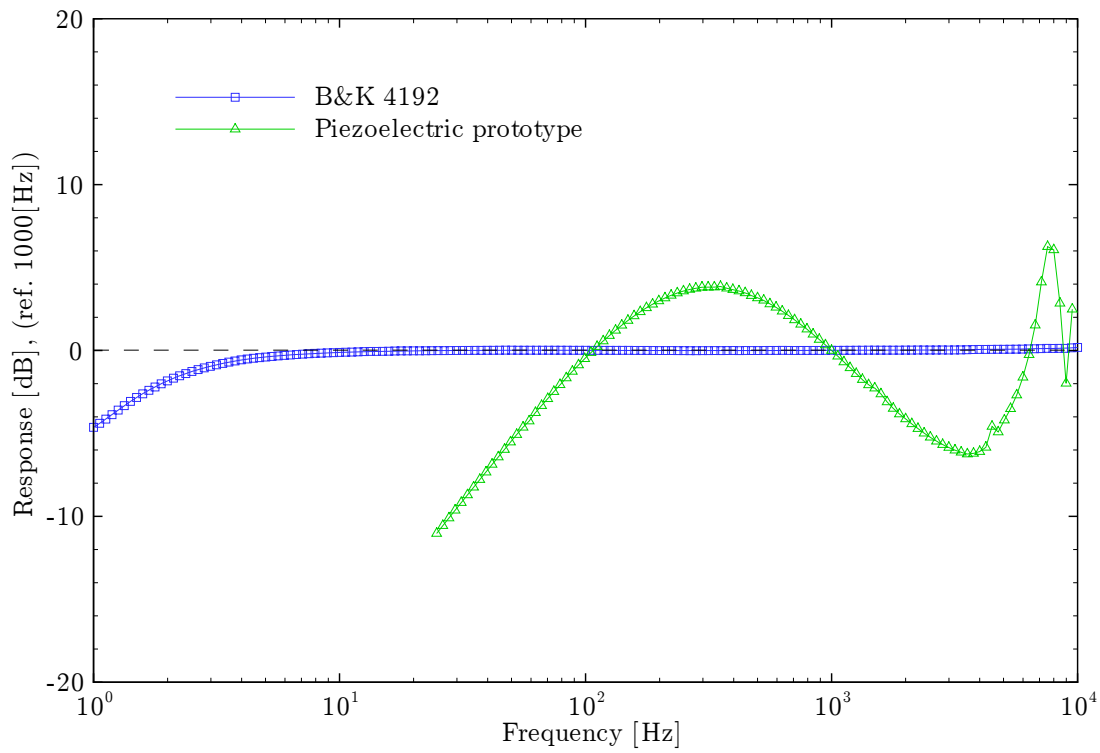


Figure 5.23: Frequency response of piezoelectric prototype and reference B&K sensor.

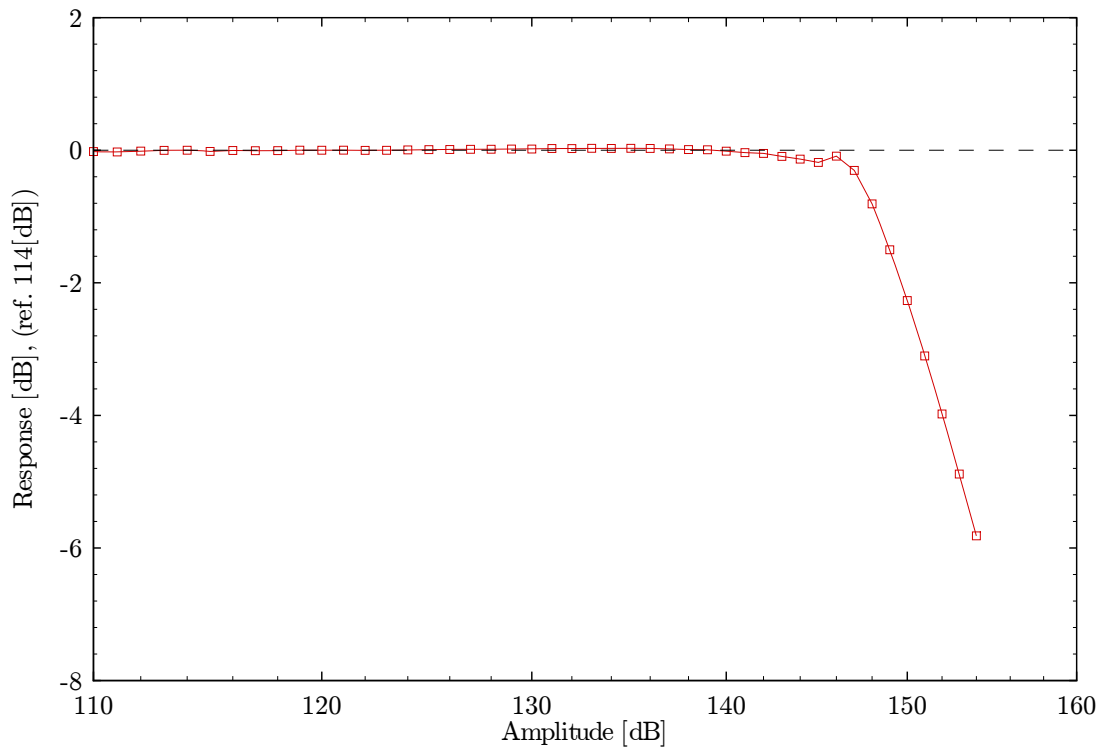


Figure 5.24: Amplitude response of piezoelectric prototype sensor.

sensitivity was observed at the higher amplitude, an indication that the distortion limit has been reached. As such, the maximum measurable amplitude of the sensor was specified as 200[Pa], or 140[dB]. The lowest measurable amplitude was unable to be quantified, as the calibration could only be performed down to approximately 1[Pa], or 94[dB]. The inability to calibrate lower values was partially attributed to amplifier noise, as the low amplitude source waveform was susceptible to discretization. If lower intensity measurements were required, the noise could be effectively reduced by decreasing the gain of the amplifier and increasing the amplitude of the generated waveform.

In addition to resolving the frequency and amplitude responses, a number of additional experiments were performed to further characterize the sensor. Disconnecting the source from the anechoic chamber, the sensor noise was determined to be 0.04[Pa], or 67[dB], providing an indication of the lowest measurable pressure. The ambient noise, which was quantified using the reference microphone, exhibited a peak amplitude of 39[dB] and remained below 19[dB] above 250[Hz]. To quantify the sensor distortion at higher amplitudes, the total harmonic distortion (THD) was evaluated. The THD is defined as the ratio of the power contained in the harmonics to the power of fundamental frequency. For a frequency of 1000[Hz] and 114[dB], the sensor exhibited a THD of 2.7[%]. By comparison, the reference B&K microphone subject to the same acoustic source exhibited a THD of 0.6[%]. The distortion test was performed using a hardware frequency generator as to eliminate the software as a potential source of noise.

5.2 Far Field Pressure Measurements

To relate the surface pressure measurements to the resulting aerodynamic sound, a single far field measurement needed to be performed. The constraints for the far field sensor were substantially less restrictive than for the near field, only requiring a specific amplitude and frequency response. Based on the experiments performed by Migliore and Oerlemans [63], it was anticipated that the far field emissions for airfoils of interest would be in the range of 50 to 70[dB] with frequencies of 100 to 10 000[Hz]. With fairly conservative constraints, it was elected to use the same B&K 4192 microphone used for calibration purposes.

5.3 Data Acquisition

To facilitate the near and far field pressure measurements, a suitable data acquisition system was required. A primary constraint for the system pertained to the required number of analog voltage input channels, as it was anticipated that upward of 30 channels were necessary to provide sufficient spatial resolution for the near field measurements. With anticipated frequencies upward of 10[kHz], a minimum per channel sampling rate of 20[kHz] was imposed. In addition to cost, the input

resolution also served as an important criterion, as it effectively limits the dynamic range and accuracy of the resulting measurements.

Data acquisition systems may be generally grouped into two distinct categories, hardware based, which operate independently, and software based, which require a computer to function. To evaluate the best solution for the desired experiments, the two groups were generally compared, as outlined in Table 5.5. Based on the channel and sampling rate constraints, it was concluded that the software based products are better suited and provide a more cost effective solution.

Pursuing the use of software based devices, two different National Instruments data acquisition boards were selected, details of which are summarized in Table 5.6 [69][68]. The PCI-6251 device was selected due to its high channel count and sampling rate, as well as its variable voltage range for analog inputs. The variable voltage range enables the measured voltages to utilize the entire range, compensating for the limited 16-bit resolution of ADC. One deficiency with the PCI-6251 is that the high channel count is obtained by multiplexing the input channels across a single ADC, presenting a number of limitations. Most notably, the sampling rate of the individual measurements decreases with increasing number of channels. This does not present a problem for the desired experiments, as the per channel sampling is still in excess of 50[kHz]. An additional consequence of multiplexing is that the channels are measured sequentially, as opposed to simultaneously, inhibiting the ability to perform a temporal analysis. To satisfy the necessary channel count, and to provide additional channels for anticipated thermocouple and mean pressure measurements, two PCI-6251 cards were acquired.

To provide greater flexibility in the experimental setup, a PCI-6143 data acquisition board was acquired. With eight dedicated ADCs, the individual channels may be simultaneously sampled at a rate of 250[kHz]. One deficiency with this board, however, is that the input range is fixed and the resolution is limited to 16-bits. While the board is limited to eight channels, if it is used for near field

Device type	Criteria						
	Sampling rate	Resolution	Filtering	Noise	Voltage extremes	Cost	Durability
Hardware	-	+	+	+	+	-	+
Software	+	+	-	-	-	+	-

Table 5.5: Comparison of data acquisition systems.

Device	Specifications				
	Sampling rate [kHz]	Simultaneous	Analog inputs	Resolution	Voltage ranges
NI PCI-6251 [69]	1000, combined	No	16	16-bit	7
NI PCI-6143 [68]	250, per channel	Yes	8	16-bit	1

Table 5.6: Specifications for data acquisition boards.

measurements, it may not be necessary to sample all 30 sensors simultaneously.

A number of other features were evaluated in the selection of the data acquisition system. The limitation of input resolution could be addressed by obtaining a 24-bit data acquisition board. However, in addition to exhibiting a significant reduction in channel count, these devices are limited in sampling rate and come at a significant cost. Given the variable voltage range of the PCI-6251, the increased resolution was considered infeasible. Hardware filters, which enable electrical noise to be effectively removed from the measurements, were also evaluated. However, this feature exhibits similar deficiencies to the higher resolution cards, with the primary deficiency being cost. Rather than implementing hardware filters, the sources of noise were to be controlled through the use of shielding.

Chapter 6

Validation of Experimental Technique

With the design of the experimental technique completed, a series of validation experiments were required to assess the efficacy of the technique in characterizing sources of aeroacoustic emissions. To evaluate the applicability of the technique to noisy environments, the experiments were to be performed in a non-anechoic wind tunnel. The objective of the experiments was to validate the technique and not to expand upon the fundamental theory of aeroacoustics. As such, the validation was to be performed using a simple, well known geometry, permitting a more direct comparison to past research.

To establish an experimental setup for the validation experiments, available wind tunnel facilities needed to be evaluated. The selection of an appropriate wind tunnel is discussed in detail, along with the measures necessary to address deficiencies with the wind tunnel. Calibration of the tunnel facility is provided, along with detailed measurements of spatial uniformity and turbulence intensity. The design of an appropriate test specimen, based on a number of constraints, is also presented. Integration of the near field pressure sensor into the test specimen is discussed, as well as mounting considerations for the far field pressure sensor. To facilitate experimental measurements, an evaluation of data acquisition systems is provided along with specifications for the selected equipment.

With the experimental setup completed, an outline is provided for the experimental procedure. Processing of the experimental data is discussed and results are presented. An analysis of the results is provided and relied upon to draw conclusions pertaining to the use and limitations of the experimental technique.

6.1 Experimental Setup

6.1.1 Wind Tunnel

The selection of an appropriate wind tunnel was primarily based on turbulence intensity; a measure of the velocity fluctuations within the flow. These fluctuations can have a significant impact on the resulting unsteady flow structures that contribute to aeroacoustic emissions. To prevent the turbulence from affecting the results, and to enable comparison to existing research, it was desired to minimize the turbulence intensity of the selected tunnel. The turbulence intensity is governed by the conditioning performed at the wind tunnel inlet and, as a consequence, is inherent to the tunnel design.

Another important consideration in the selection of the wind tunnel related to blockage, which, for 2D objects, is defined as the ratio of the specimen's frontal area to the area of the test section. This reduction in cross-sectional area generates an increase in local velocity, which can affect the unsteady flow structures even for low blockages. Thus, the area of the test section needed to be maximized in order to minimize the resulting blockage effects.

A minor consideration for the selection of the wind tunnel was the available free stream velocities, contributing to the range of Reynold's numbers over which the intended specimen could be evaluated. Based on preliminary research, however, the unsteady flow structures of interest occur over a vast range of Reynold's numbers, thus negating strict requirements for the velocities.

Two wind tunnels, pictured in Figures 6.1 and 6.2, were considered for the experiments. The specifications of each tunnel are presented in Table 6.1 [43][88]. Both tunnels were considered adequate in terms of free stream velocities and turbulence intensity. In terms of blockage, the variable wall tunnel exhibited favourable characteristics, with a test section height six times greater than the alternative tunnel. The resulting increase in area could be used to reduce the blockage of the test section or accommodate a larger test specimen, enabling the near field sensor to be more easily integrated into the specimen's surface. The variable wall feature of this tunnel also serves to reduce blockage effects, however, this functionality was not in place at the time of testing. Unfortunately, the variable wall geometry of this tunnel presents numerous challenges in mounting the test specimen and the far field sensor. Furthermore, intending to repeat the experiments using PIV in the future, the smaller closed-loop tunnel was favoured, due to particle seeding considerations. For these reasons, the smaller tunnel was selected to perform the validation experiments. In making this decision, it was determined that the test specimen could be appropriately sized to accommodate the near field sensor while maintaining a sufficiently low blockage.

With the tunnel selected, prior to performing any experiments, a number of obvious deficiencies needed to be resolved. The tunnel was originally fabricated with a removable test section, defined as the portion between the inlet contraction



Figure 6.1: University of Waterloo 0.61 by 0.91[m] variable wall wind tunnel.

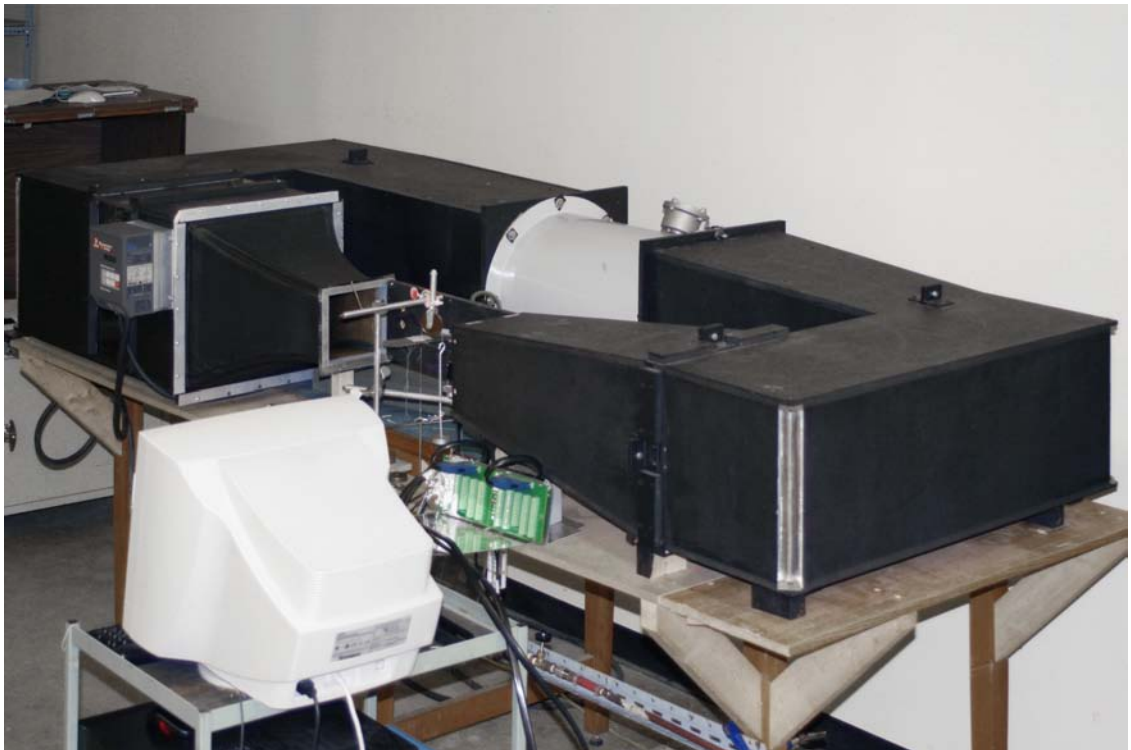


Figure 6.2: University of Waterloo 0.15 by 0.15[m] closed return wind tunnel.

Wind Tunnel	Specifications			
	Max. velocity [m s^{-1}]	Streamwise turbulence [%]	Test section [m]	Closed return
Variable wall [43]	80	0.25	0.61 by 0.91 (var.)	No
Closed return [88]	40	1.80	0.15 by 0.15	Yes

Table 6.1: Wind tunnel specifications.

and outlet expansion, as shown in Figure 6.3. This test section is comprised of four walls which are fastened together. The resulting serviceability serves as one of the tunnel's greatest strengths, enabling easy modification of the tunnel walls to permit mounting of the test specimen. However, this serviceability also means that the walls are subject to greater alterations, rendering the test section unusable after a number of setups. A number of the walls that were in poor condition needed to be replaced, a task complicated by the fact that the existing walls were not manufactured to a standard specification. In fact, over the period of a few years, the dimensions of the test section deviated significantly from the original specifications presented in Figure 6.3. To provide the best quality test section, restore the original dimensions, and to establish a standard for which the walls could be accurately reproduced in the future, the test section needed to be completely redesigned and manufactured.

Originally, the test section was manufactured from 12.7[mm] acrylic plate. Acrylic was used to permit optical access for laser illumination and imaging, enabling PIV experiments to be performed. To retain this ability, two of the test section walls were manufactured from polycarbonate. The 12.7[mm] thickness was retained to prevent flexion of the tunnel walls. To prevent the obstruction of optical access, mounting of the test specimen and the far field sensor was confined to the remaining two walls, for which optical access was not required. For these walls, the primary concern was the accurate placement and rigidity of the mounted components. This

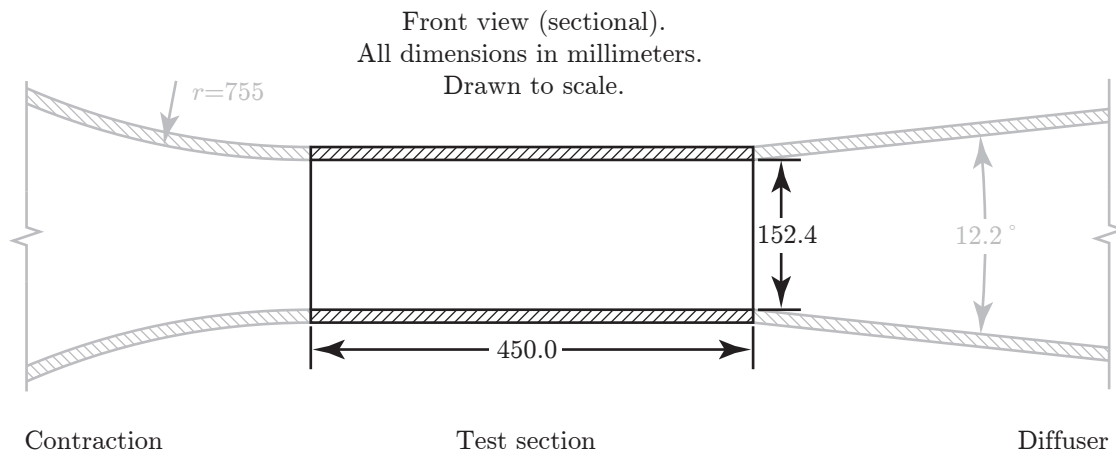


Figure 6.3: Wind tunnel test section geometry.

is particularly true for the test specimen, as a decrease in rigidity can cause the specimen to resonate, causing an unpredictable intensification of the unsteady flow structures. Furthermore, using a dimensionally accurate material would permit the manufacture of exact test section dimensions. Based on these requirements, the remaining two walls were fabricated from 12.7[mm] aluminum plate. Although the material thickness was more than sufficient to provide the necessary rigidity, the thickness was chosen in part due to mounting and fastener considerations.

To manufacture the polycarbonate and aluminum walls, 12.7[mm] plate was milled to the specified dimensions. Holes were machined and tapped to accommodate the 20 fasteners used to complete the structure. A total of 8 dowel holes were machined into the four walls to ensure that the dimensions of the completed assembly were within the desired tolerances. This served as one of the primary deficiencies with the previous design, as the fasteners alone were used to establish the dimensions of the test section.

In terms of mounting, the test section was attached to the tunnel using four fasteners at each end. To facilitate mounting of components within the tunnel, such as the test specimen and the far field sensor, a hole was fabricated in each of the aluminum walls. The holes were located along the centreline of the test section at a distance of 150.00[mm], one-third of the total test section length, from the inlet. This lengthwise position was selected to permit the study of the test specimen wake region, a common area of interest. The mounting holes, measuring 12.700[mm] and 19.050[mm], were sized differently to accommodate numerous components. The holes were manufactured to within $+13[\mu\text{m}]$ to prevent excess movement and to ensure accurate placement of the mounted components. Mounting of the components within the two holes differed based on the intended purpose. The smaller hole, intended for the test specimen, relies on the use of a shouldered specimen and a retaining fastener. The larger hole, which was intended to serve a more general purpose, needed to be flush with the inside of the tunnel wall. As such, two threaded holes were manufactured into the tunnel wall to retain the mounted component. Details of the mounting techniques are presented in Figure 6.4.

To facilitate future PIV measurements, the inner surface of the aluminum walls were painted matte black. The completed test section, with overall dimensions within $50[\mu\text{m}]$ of nominal, is shown in Figure 6.5. Detailed manufacturing drawings of the numerous test section components are presented in Appendix B.

Additional tunnel deficiencies became apparent during the installation of the completed test section. In the previous design, metal brackets were attached to both the test section and inlet contraction and subsequently fastened together, as shown in Figure 6.6. This clamping method made it difficult to maintain proper alignment of the two sections. Furthermore, the exacting dimensions of the new test section emphasized irregularities in the contraction, with a step upward of 1[mm] occurring at the transition. This step can have a significant impact on the quality of the flow, as it serves to generate turbulence. Thus, to improve the quality of the flow, the deviation between the two sections needed to be reduced. A deviation was

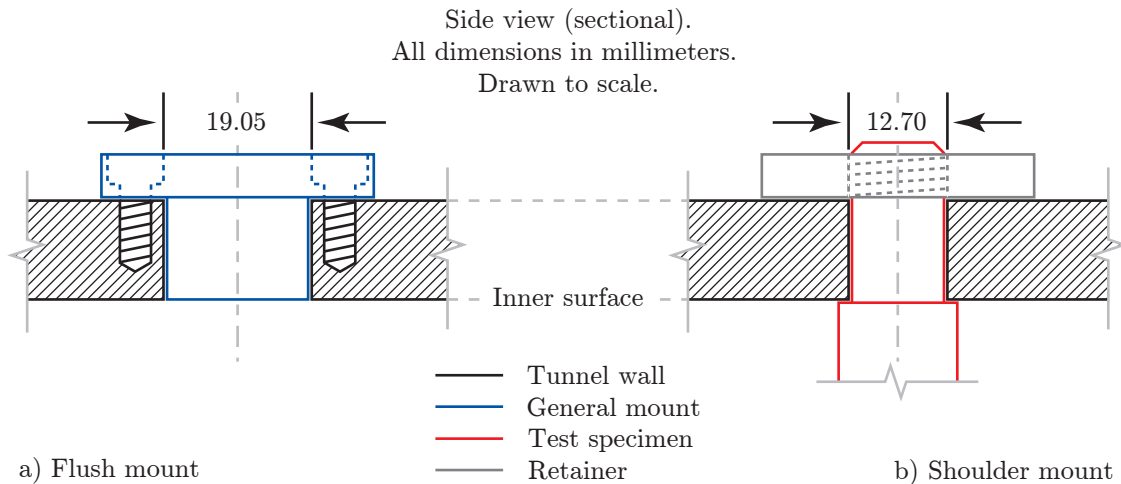


Figure 6.4: Wind tunnel test section mounting holes.



Figure 6.5: Wind tunnel test section revised.

also observed at the outlet, however, the resulting effect on upstream measurements was considered negligible.

To address the deficiencies at the transition, both in terms of alignment and geometric irregularities, an intermediate section was fabricated. Using a single piece of aluminum, the opening of the intermediate section was manufactured to the exact dimensions of the test section. Flanges were made integral to the intermediate section to positively locate two of the test section surfaces relative to the opening, with four holes used to simply retain the test section. The intermediate

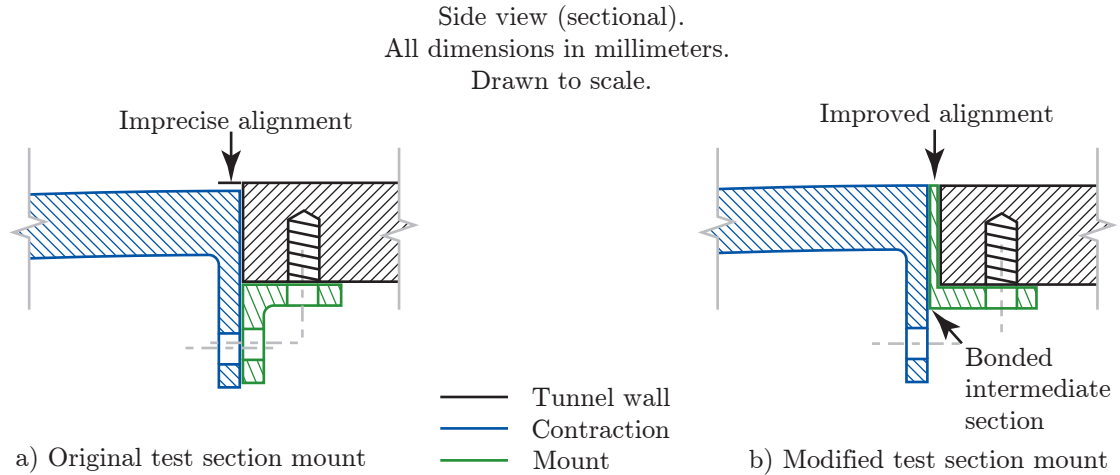


Figure 6.6: Wind tunnel test section mounting to the inlet contraction.

section was aligned and permanently bonded to the inlet contraction using a high strength epoxy. After a 24 hour curing period, a filler material was used to fair the contraction to the intermediate section. With the intermediate section manufactured to precise dimensions, and with the use of a sandable filler material, it was a relatively straight forward task to obtain a smooth and exact transition. Given the filler material's susceptibility to moisture absorption, a primer was applied to the transition to ensure longevity, as shown in Figure 6.7. Upon installing the test section the maximum observed deviation between the two surfaces was effectively reduced to 0.2[mm], the effect of which was considered negligible. In addition to reducing the deviation, the intermediate section enables the test section to be more easily removed.

With the test section in place, attention was turned to the control of the tunnel velocity. The tunnel uses a variable frequency drive (VFD) to control the speed of the axial fan which provides the air flow. The setting of the VFD drive is continuously variable from 0 to 60[Hz], representing the minimum and maximum velocities, respectively. A prior calibration was performed by Sperandei [88] to establish the relationship between the drive frequency and the corresponding velocity. Preliminary experiments, however, suggested a measurable deviation from the provided calibration. Given that the last calibration was performed over 6 years ago, the observed deviation is likely a result of the diminished drive and motor efficiencies. Given the long period since the last calibration, a simple calibration of the tunnel was required to evaluate if the relationship had in fact changed.

To perform the tunnel calibration, only a centreline velocity measurement was required, for which a United Sensor PCC-8-KL Pitot-static tube [90] was selected. The Pitot-static tube essentially converts the velocity to a differential pressure measurement, which may be used with Equation 6.1 to obtain the velocity. The Pitot-static tube serves as an excellent means of performing simple velocity measurements. Furthermore, for low to moderate Mach numbers, Pitot-static tubes themselves exhibit negligible error [90].

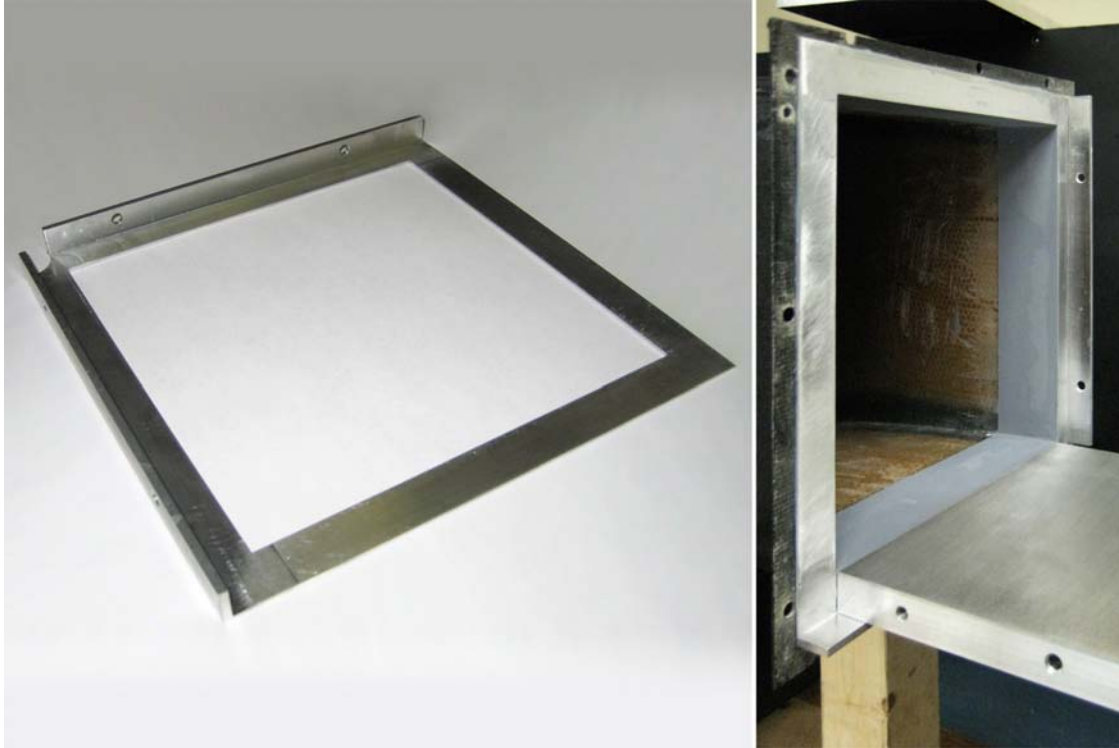


Figure 6.7: Intermediate section serving as the transition between the inlet contraction and the test section.

$$v = \sqrt{\frac{2\Delta p}{\rho}} \quad (6.1)$$

To retain the Pitot-static tube in the tunnel, an adapter was fabricated for the 19.05[mm] mounting hole, as shown in Figure 6.8. For the calibration, the tunnel was to be operated without the test specimen in place, as it would inevitably result in a non-uniform velocity field for which a single centreline measurement would not suffice. Performing the calibration without the specimen was assumed to be just as precise, as the low blockage of the test specimen would not appreciably change the average tunnel velocity. To fill the 12.70[mm] hole normally occupied by the test specimen, a flush nylon plug was fabricated. Upon locating and aligning the Pitot-static tube along the centreline, the position was fixed by tightening a set screw on the tunnel mount.

To determine the velocity using the Pitot-static tube, the differential pressure needed to be measured. With the anticipation of low pressures, only two devices were considered, the inclined manometer and the pressure transducer. The pressure transducer was selected to perform the experiments for a number of reasons. First, the pressure transducer provides the required sensitivity to perform the low pressure measurements. Second, the accuracy of a pressure transducer is specified, whereas the accuracy of an inclined manometer is a function of numerous param-



Figure 6.8: Mounted Pitot-static tube with plug.

ters. Finally, it was desired to acquire the pressure measurements to obtain a time average velocity, whereas manometer measurements must be performed manually.

While the Pitot-static tube itself contributes negligible error, the error introduced by a pressure measurement device can be substantial. The accuracy of a pressure transducer is often specified as a percentage of full scale, or maximum measurable pressure. Based on this specification, measurements performed at relatively low pressures are subject to a greater percentage error, as illustrated in Figure 6.9. Thus, when considering pressure transducers for performing velocity measurements, the required uncertainty plays an important role in the selection of an appropriate pressure transducer.

For the calibration experiment, the velocities of interest ranged from approximately 5 to 30 $[\text{m s}^{-1}]$. Assuming an ambient temperature and pressure of 20 $[\text{°C}]$ and 101.325 $[\text{kPa}]$, respectively, the corresponding pressure range extended from 15 to 542 $[\text{Pa}]$. The maximum uncertainty for the velocity measurements was specified at 2 $[\%]$, which was considered sufficient given the large range of velocities being calibrated. To facilitate the measurements within the specified uncertainty, three different pressure transducers were required, each exhibiting a different pressure range. The specifications of the pressure transducers are presented in Table 6.2 [85][4][33]. Based on the specified transducer accuracy, the corresponding measurement uncertainty for the range of velocities is presented in Figure 6.10.

To prevent having to switch the transducers over the defined pressure ranges, the sensors needed to be operated simultaneously. This was accommodated by

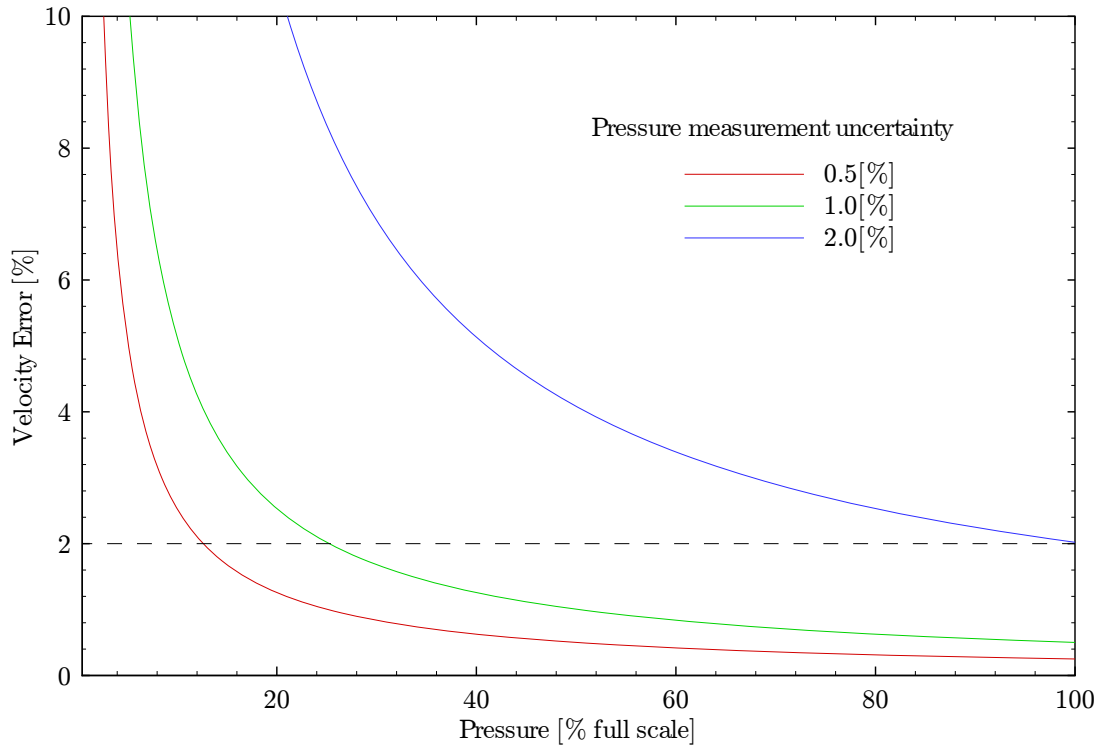


Figure 6.9: Velocity error versus pressure for various Pitot-static tube pressure transducer uncertainties.

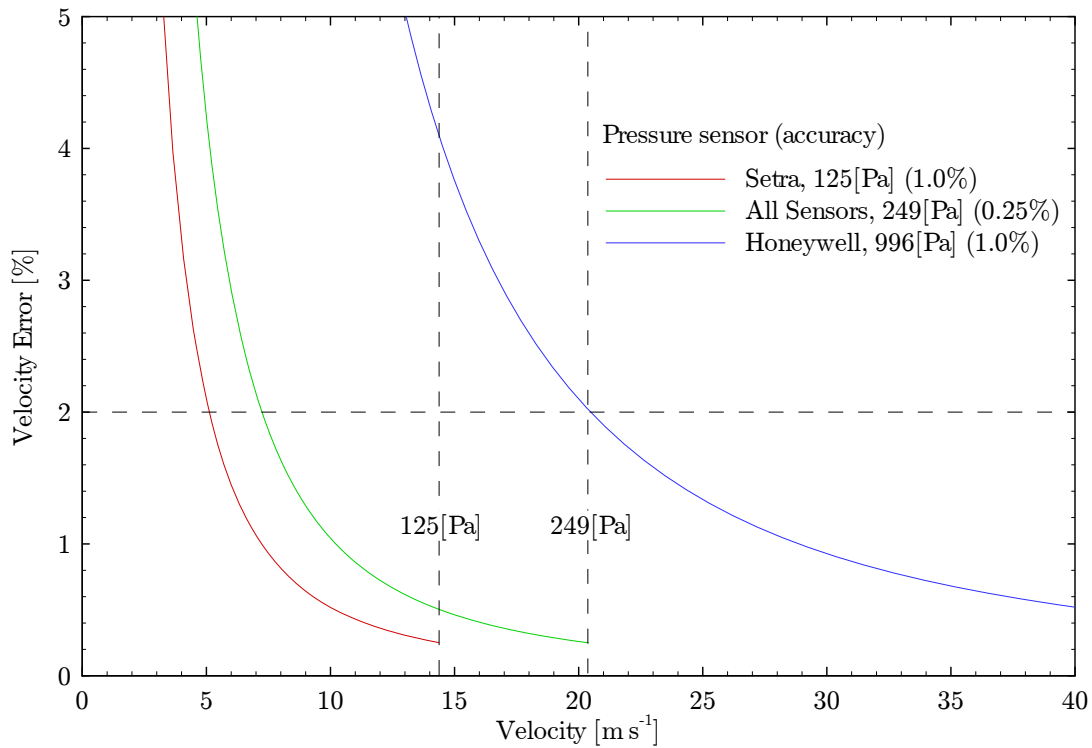


Figure 6.10: Velocity error versus velocity for defined Pitot-static tube pressure transducers.

Pressure transducer	Specifications			
	Type	Range [Pa]	Accuracy [% FS]	Amplified
Setra, 26710R5WB2EG1CN [85]	Differential	± 124.5	± 1.0	Yes
All Sensors, 1 INCH-Dx-4V-MINI [4]	Differential	± 249.1	± 0.25	Yes
Honeywell, XPCL04DTC [33]	Differential	± 996.4	± 1.0	No

Table 6.2: Pitot-static tube pressure transducers' specifications.

connecting the transducers to common manifolds, which were attached to the two pressure taps of the Pitot-static tube. Overpressure of the transducers was not a concern, as the pressures were well within the specified limits of the sensors.

Power to the transducers was provided by an Agilent triple-output DC power supply, with the resulting supply voltages within 1[mV] of nominal. The precision of the power supply was desirable, as the voltage output for two of the transducers was proportional to the supplied voltage. To facilitate the measurements, the three transducers were connected to a National Instruments PCI-6251 data acquisition card. Care was taken to use shielded cabling and to ensure that the grounds were properly connected.

In addition to the pressure transducers, a K-type thermocouple [76] was installed at the outlet of the test section to determine the temperature of flow. Monitoring of the tunnel temperature was a necessity, as the recirculated air is subject to continuous heating from the axial fan. Based on previous experiments, the tunnel temperature increases with velocity, reaching upward of 15[°C] above ambient [56]. In addition to using the tunnel temperature to accurately determine the fluid density, it was also used to determine whether the tunnel was in thermal equilibrium with the surroundings. By obtaining thermal equilibrium prior to performing measurements, it ensures that both current and future testing are performed at a constant temperature for a given velocity. Acquisition of the thermocouple measurements was performed using the same PCI-6251 data acquisition card used for the pressure transducers.

To facilitate the numerous pressure and temperature measurements, a program was created using LabVIEW. Within the interface, the sensitivity of pressure transducers are defined, along with atmospheric temperature and pressure. The atmospheric temperature is used to define the cold junction constant for the thermocouple measurements. A zeroing function was also created, enabling the transducer offsets to be evaluated for the stationary flow. The zero offset is determined by averaging samples over the duration of 1[s], as to prevent an erroneous data point from skewing the results. Using the defined and measured parameters, the velocity for each of the transducers is evaluated using Equation 6.1. Additional details of the LabVIEW program are presented in Appendix C.

Initially, the pressure transducers were sampled at a rate of 50[kHz], a rate carried forward from a previous experiment. Although this data rate was considered

excessive, it revealed a limitation of the selected data acquisition card. During initial tests, the three transducers returned different results for the same velocity. While this deviation was initially attributed to the sensitivity specifications, the transducers exhibited good agreement upon reducing the sampling rate to 10[kHz]. Thus, the error was attributed to the multiplexing performed by the data acquisition card, further increased by the fact that each channel exhibited a unique voltage range. Although this error can be readily explained, it presents concerns for future high sample rate experiments using this particular card. Proceeding with a data rate of 10[kHz], the three transducers were sampled for a duration of 25[s]. Although this data rate still exceeded the sampling requirements, it did not present any additional cost. After the sampling period was complete, the raw voltage measurements were exported to a data file, along with a header containing a summary of the mean and RMS quantities.

Prior to performing the velocity calibration, measurements were performed for the stationary flow. In addition to zeroing the pressure transducers, measurements were performed to quantify the sensor noise, as presented in Table 6.3. Although sensor noise does not affect mean velocity measurements, the random fluctuations do act to increase the RMS velocity. Given that the sensor noise exhibits a constant RMS voltage, it exhibits a greater effect on the measurements at lower velocities, as illustrated in Figure 6.11. By quantifying the contribution of sensor noise to the RMS velocity, corrections may be applied to the velocity measurements to obtain a more representative result.

To verify the calibration setup, an initial test was performed for a tunnel frequency of 20[Hz], enabling a simple comparison to the existing calibration. The mean velocity was measured to be 12.2[m s⁻¹], 9.6[%] lower than the predicted value. The RMS velocity was determined to be 0.13[m s⁻¹], with a turbulence intensity of 1.1[%], evaluated using Equation 6.2. Although this turbulence intensity is less than the specified 1.8[%], the measured value is higher than anticipated. This is simply because the turbulence with the wind tunnel is ideally comprised of small scale structures exhibiting high frequency fluctuations. It is these high frequency fluctuations which are effectively attenuated during Pitot-static tube measurements, due to the long sensing line lengths. As such, it was anticipated that the resulting turbulence intensity would be largely underpredicted. With the observed turbulence intensity approaching the specified value, it appears as if the free stream turbulence was primarily comprised of low frequency, large scale struc-

Pressure transducer	Specifications			
	Zero [V]	Range [V]	Sensitivity [V Pa ⁻¹]	RMS [mV]
Setra, 125[Pa] [85]	5.068	±5.0	0.040146	35.1
All Sensors, 249[Pa] [4]	2.206	±2.0	0.008029	15.6
Honeywell, 996[Pa] [33]	0.000186	±0.025	0.000025	0.028

Table 6.3: Pitot-static tube pressure transducers' RMS noise measurements.

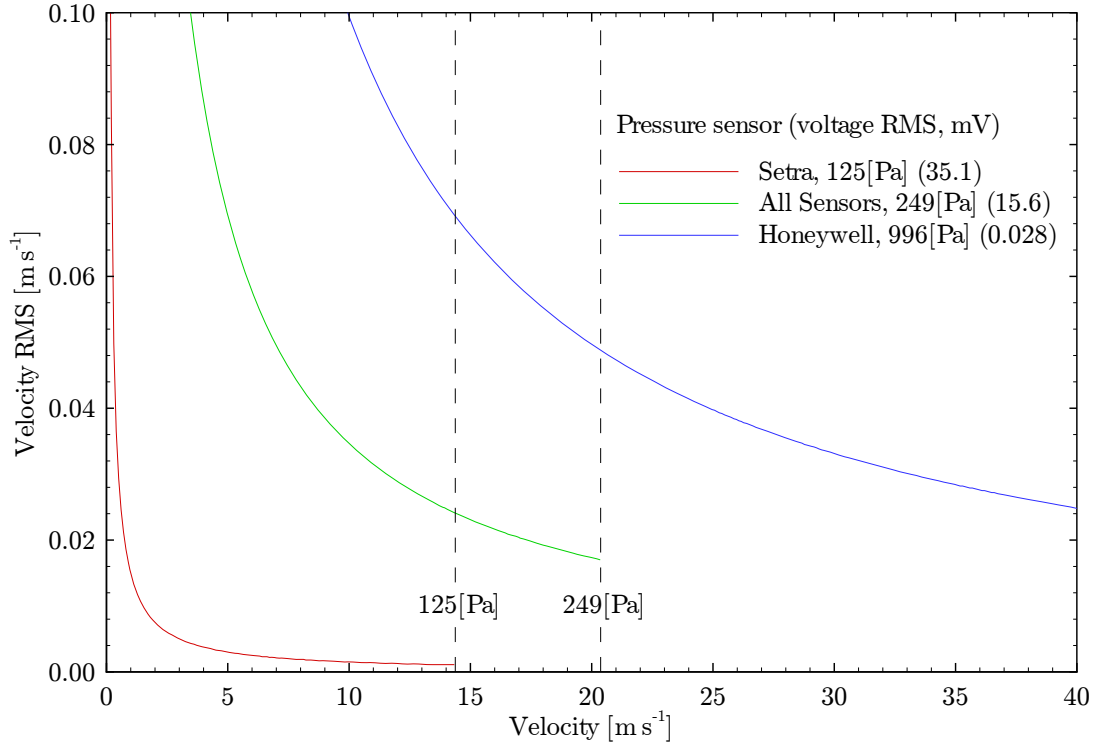


Figure 6.11: Noise induced velocity RMS versus velocity for defined Pitot-static tube pressure transducers.

tures. A quick assessment of other tunnel velocities revealed that the low frequency fluctuations extended across the entire operating range. Given that the presence of large scale turbulence can have a significant impact on the resulting unsteady flows structures, the problem needed to be resolved prior to performing the calibration.

$$I = \frac{u_{rms}}{u} \quad (6.2)$$

To improve the quality of the flow, efforts were made to locate the source of the low frequency fluctuations, which were initially perceived as surging. One potential source of surging was attributed to the axial fan. As a first attempt to rectify the problem, changes were made to the VFD drive. The slip compensation, which is intended to compensate for dynamic loading, was increased from 0.0 to 5.0[%], with no effect. The operation mode was also switched from constant-torque to constant-load, once again with no effect. Aside, in an attempt to reduce noise sources within the tunnel, the carrier or switching frequency was changed from 2.5 to 12.5[kHz]. This carrier frequency generates an audible noise at an identical frequency, with an increase in carrier frequency corresponding to a reduction in sound intensity.

Following the unsuccessful attempts to control the fluctuations using the VFD drive, the fan was removed from the tunnel for inspection, as shown in Figure 6.12. While removed, the fan and tunnel were cleaned and the retaining fasteners were verified to be sufficiently torqued. The inspection, however, did not reveal any

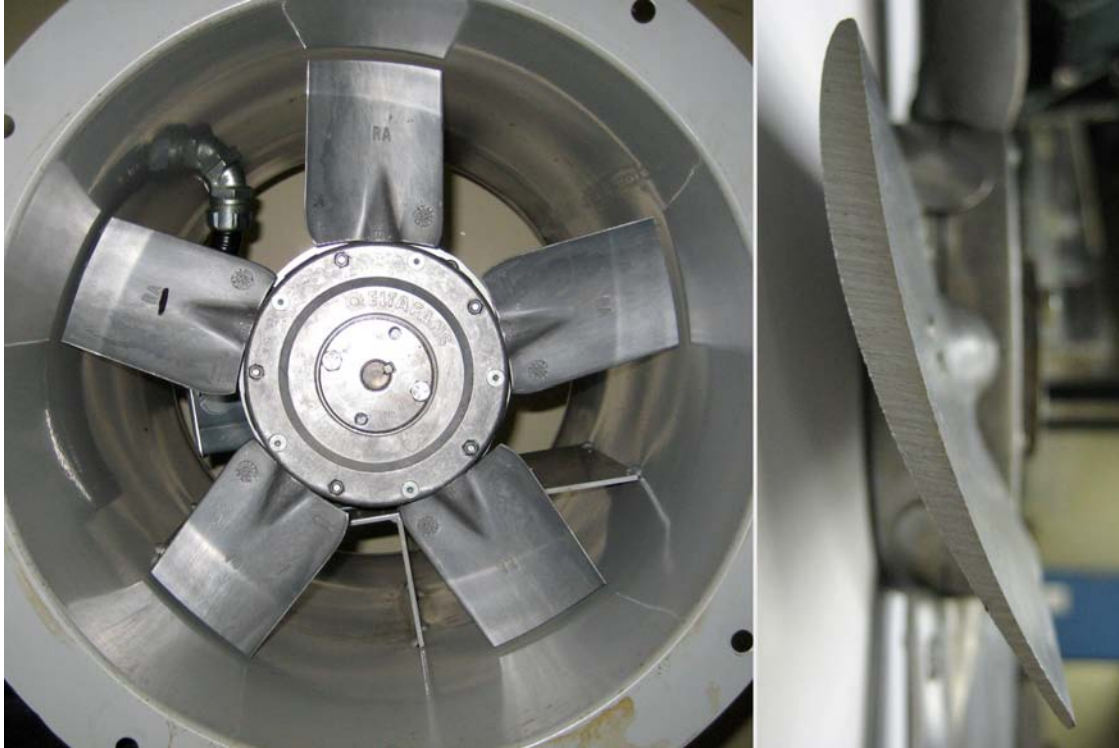


Figure 6.12: Wind tunnel axial fan.

obvious deficiencies. With a suspicion that the surging might be a result of a dynamic fan phenomenon, attention was turned to the fan geometry. The fan consists of five variable pitch blades, which were set to an angle of 30° , as shown in Figure 6.12. This aggressive angle of attack was selected to maximize the flow rate, however, it has the inadvertent effect of increasing the blades' susceptibility to dynamic stall. In an attempt to reduce the surging, the blade angles were reduced to 20° , at the cost of decreasing the maximum flow rate. Upon reinstalling the fan, the calibration was once again performed for a drive frequency of 20[Hz]. Although the mean velocity was reduced, there was no appreciable decrease in the turbulence intensity.

With alterations to the fan providing little improvement, attention was turned to the expansion section of the wind tunnel. With an expansion angle of 12.2° , the flow is highly susceptible to separation, resulting in the generation of large scale structures. It is possible that these structures were interacting with the fan, or were insufficiently homogenized prior to reaching the test section. As a first attempt to address potential flow separation, a screen was installed at the outlet of the test section, as shown in Figure 6.13. This approach, as discussed by Mehta [60], effectively reduces flow separation by decreasing the boundary layer thickness and turbulence intensity, as well as improving flow uniformity. The only perceived deficiency of installing the screen at the outlet is an increase in static pressure, the effects of which would be quantified during calibration. However, it is possible that the increase in static pressure may reduce the dynamic fan phenomenon by shifting



Figure 6.13: Screen installed at outlet of wind tunnel test section.

the operating point on the fan's performance curve.

Performing a simple calibration with the screen installed, it was observed that the low frequency fluctuations were effectively attenuated. The increase in pressure, however, came at a substantial cost to velocity, exhibiting a 30[%] reduction at 20[Hz]. To quantify the improvement in the turbulence intensity, the tunnel was set to 28.5[Hz] to obtain a velocity of 12.2[m s⁻¹]. The resulting turbulence intensity was determined to be 0.3[%], with the screen providing a 67[%] reduction.

With the low frequency turbulence problem resolved, the calibration could proceed. To perform the calibration, the VFD drive was varied from 5 to 50[Hz] in 1[Hz] increments. The lower limit was established by the drive and motor, whereas the upper limit was imposed due to excess noise and vibration. For each of the specified frequencies, measurements were not performed until the tunnel approached thermal equilibrium. Given that the temperature would never actually reach a maximum value, judgement was exercised to establish when equilibrium was obtained. By incrementing the frequencies sequentially, thermal equilibrium was obtained relatively quickly, requiring approximately 10 minutes between increments. If, however, the tunnel were at ambient temperature and set to the maximum velocity, it would take significantly longer to obtain an equilibrium state. Given that the testing was conducted over a period of several hours, the zero offset for the transducers was performed at the beginning and end of the calibration, to account for drift of sensor offsets. Although the drift was 0.76[%] of full scale at most, corrections were applied to results by linearly interpolating the offsets based on the time of the

measurements.

The results of the tunnel calibration, corresponding to an atmospheric pressure of 97.5[kPa], are shown in Figure 6.14. The results suggest a linear relationship between the mean velocity and drive frequency. Applying a linear fit, the relationship is defined by Equation 6.3, exhibiting a maximum deviation of 0.25[%] above 3[m s⁻¹]. The maximum uncertainty for the calibration was previously established to be 2[%], entirely attributed to the transducer measurements. The resulting RMS velocities are presented in Figure 6.15. To eliminate the contribution of sensor noise to the RMS velocities, the values presented in Figure 6.11 were subtracted from the results. The adjusted RMS velocities exhibit a more continuous variation across the numerous transducers. The resulting turbulence intensity exhibited a slight reduction over the range of velocities, with a value generally less than 0.45[%]. These turbulence results, however, are likely underpredicted, as previously established for Pitot-static tube measurements.

$$v = 0.4474f - 0.3872 \quad (6.3)$$

To assess the impact of adding the screen downstream of the test section, the static pressure was measured at the Pitot-static tube over the range of calibrated velocities. The measurements were performed using the 249[Pa] pressure transducer. Figure 6.16 summarizes the results, which shows that the tunnel pressure remains below atmospheric pressure. Furthermore, the static pressure exhibits little change over the range of velocities.

The tunnel calibration revealed a number of deficiencies with both the current and prior calibration methods. Previously, the calibration was performed using PIV. This technology is not well suited for precise calibrations, as measurement error can easily amount to 5-10[%] [56]. It is possible that the deviation in measured velocities is simply attributed to PIV measurement error, rather than being attributed to a potential decline in fan efficiency or the minor alterations of the test section. Another deficiency with PIV is the limited acquisition rate, which for the previous calibration was performed at a rate of approximately 3[Hz]. Due to the limited sampling rate, the presence of low frequency turbulence was not resolved, having been masked by the turbulence intensity. While the use of a Pitot-static tube addresses the issue of calibration uncertainty, deficiencies remain in the accurate determination of turbulence quantities.

To further characterize the flow within the tunnel, a series of experiments were performed by Orlando [77] using laser doppler velocimetry (LDV). Similar to PIV, this technique relies on the use of particle seeding. LDV, however, addresses the primary deficiencies with PIV, exhibiting lower measurement uncertainty and providing sampling rates upward of 50[kHz]. Performing a series of measurements at the centreline location, the velocity measurements were found to be within 0.8[%] of those predicted by Equation 6.3 and within the 2[%] uncertainty of the Pitot-static tube measurements. For the range of velocities tested, the turbulence intensities

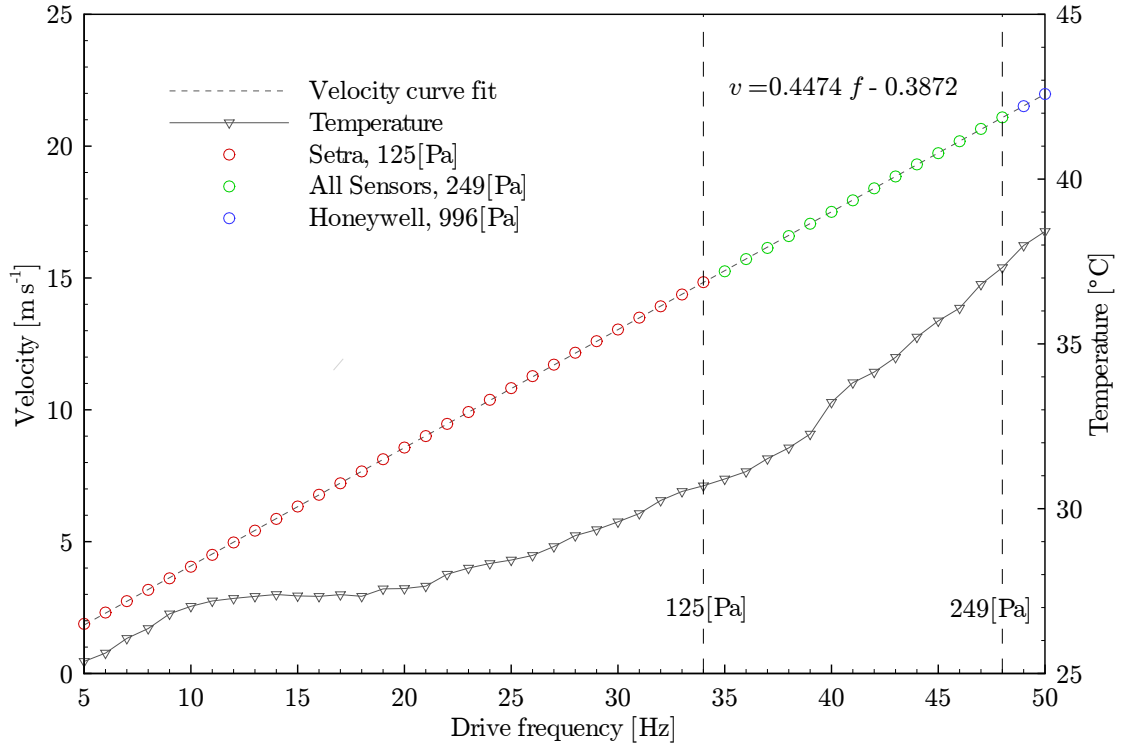


Figure 6.14: Wind tunnel mean velocity and temperature versus drive frequency at 100[mm] from inlet.

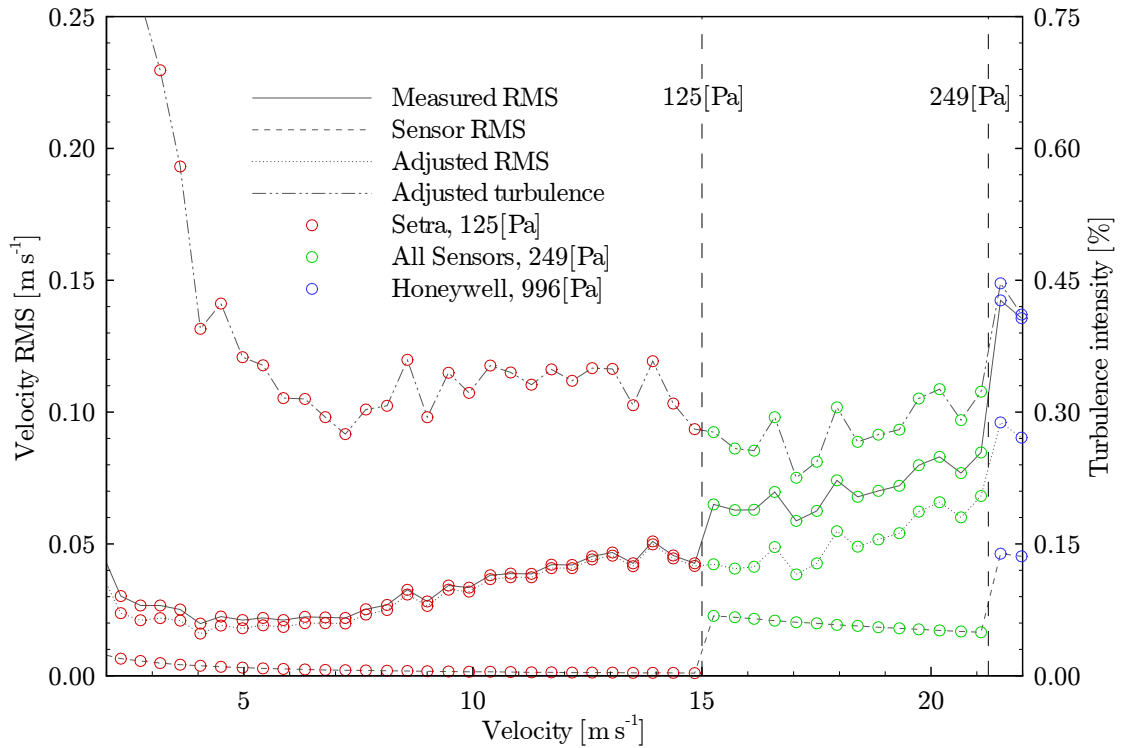


Figure 6.15: Wind tunnel RMS velocity and turbulence intensity versus centreline velocity at 100[mm] from inlet.

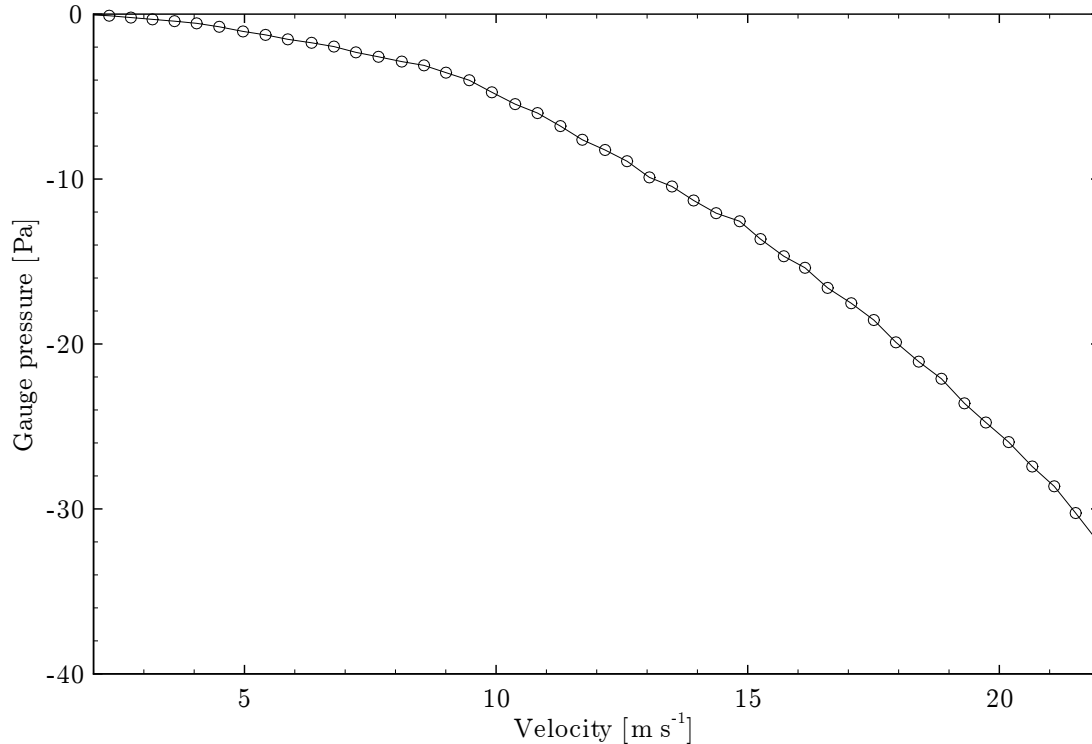


Figure 6.16: Wind tunnel static pressure versus centreline velocity at 100[mm] from inlet.

were also evaluated, as shown in Figure 6.17. The turbulence intensities were found to be approximately constant over the range of velocities, with values generally less than 0.8[%]. With the velocity measurements being performed at a sufficiently high sampling rate, these turbulence measurements were considered representative of the true values. This is a significant improvement over the turbulence of 1.8[%] specified by Sperandei [88], attributed to the measurement technique as well as the alterations made to improve the tunnel quality. Additional spatial measurements were performed at the defined streamwise location, with the resulting spatial uniformity over the range of velocities presented in Figure 6.17. The spatial uniformity was generally within 2.2[%] of the mean over the range of velocities tested. While these results are in good agreement with previous PIV measurements, the LDV technique provided greater insight into the nature of the spatial non-uniformity, as a depression was observed along the centreline of the flow. These measurements enabled the non-uniformity to be effectively attributed to the obstruction of the axial fan.

The use of LDV has shown to be an effective means of characterizing the flow, addressing many of the deficiencies of the PIV and Pitot-static tube techniques. Overall, the LDV results were in good agreement with the Pitot-static tube measurements, however, the LDV was able to more accurately resolve the turbulence intensities. With the wind tunnel calibrated, and the turbulence intensities and spatial uniformities resolved, attention was turned to the selection of an appropriate test specimen.

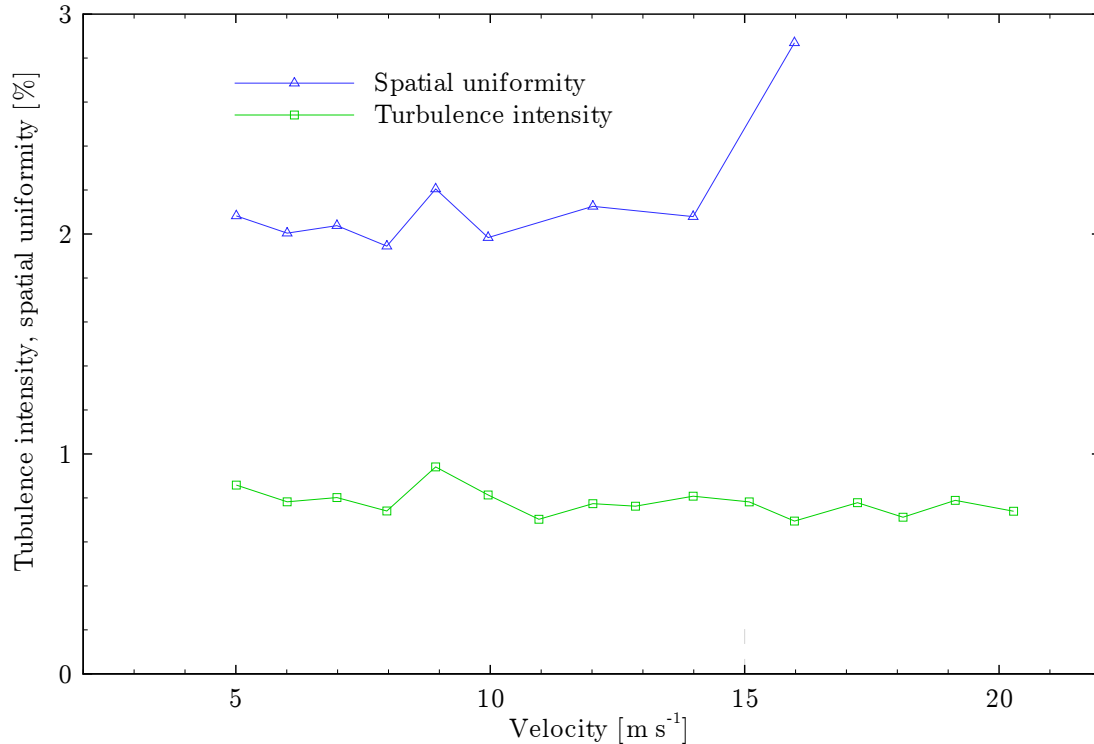


Figure 6.17: Wind tunnel turbulence intensity and spatial uniformity versus centreline velocity at 100[mm] from inlet. (Data from Orlando [77].)

6.1.2 Test Specimen

Geometric Considerations

Although the experimental technique was developed specifically for airfoils, performing experiments on such a complicated geometry presented numerous challenges. First, the far field emissions of an airfoil are comprised of numerous aeroacoustic sources, as discussed in the introduction. While it would be possible to resolve the individual sources, the resulting emissions would be difficult to distinguish from the tunnel noise. Second, to satisfy the constraints of the wind tunnel, the airfoil geometry would need to be custom manufactured at significant expense. As a result, the validation experiments were to be performed using a simple geometry, limiting the number of aeroacoustic sources and simplifying the manufacturing process.

The selection of a simple geometry was based on a number of considerations. First, the resulting flow field needed to exhibit strong periodic flow structures to maximize the intensity of the far field emissions. Second, sufficient literature needed to exist for the selected geometry. Third, the geometry needed to accommodate the near field pressure sensor, as the sensor needed to be placed within the test specimen. Finally, a geometry was desired which could be readily manufactured to exact dimensions.

Based on the aforementioned considerations, a cylinder was selected as the geometry for the validation experiments. Subject to a cross-flow, a cylinder exhibits a very predictable periodic wake structure [37]. The resulting aeroacoustic emissions are nearly tonal, commonly referred to as an *æolian tone* [37]. It is this periodic wake structure which is responsible for electrical wires “singing” in the wind. While rectangular and flat plate geometries exhibit a similar phenomenon, the cylindrical geometry has the added benefit of radial symmetry. This symmetry enables spatial measurements to be performed using a single near field pressure sensor, as the sensor can be simply rotated to any angular position. A cylinder can also be readily manufactured to any specified length and diameter. Perhaps the greatest benefit of the cylindrical geometry is the abundance of prior research. In addition to providing a wealth of experimental data for comparison, the underlying theory of the contributing mechanisms is well established.

Cylinder Theory

A cylinder subject to a cross-flow, for $Re < 47$, exhibits a wake region which is comprised of a pair of counter-rotating vortices. With increasing Reynolds number, a wake instability causes the vortices to shed periodically in an alternating pattern, referred to as Kármán vortex street, as shown in Figure 6.18. The resulting aeroacoustic emissions are associated with this vortex shedding process, attributed to the initial acceleration of the vortex to the free stream velocity [37]. This periodic vortex shedding occurs regularly for $47 < Re < 2 \cdot 10^5$ [22], which corresponds to the sub-critical flow regime. Within this regime, the boundary layer remains laminar and the Strouhal number is approximately constant at 0.21. Beyond the sub-critical flow regime, for $Re > 2 \cdot 10^5$, the boundary layer transitions from laminar to turbulent and the periodic shedding becomes less pronounced.

Although the Strouhal number is approximately constant within the sub-critical

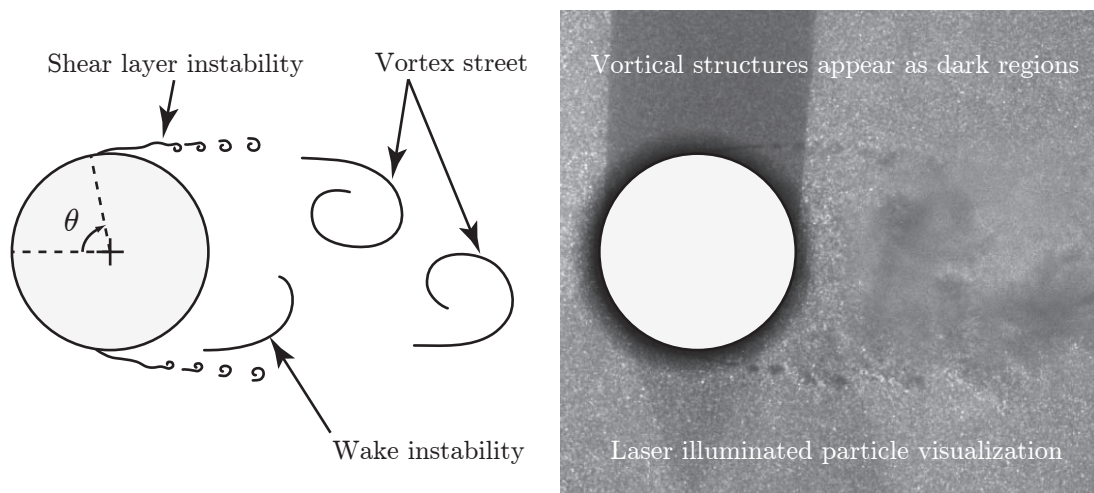


Figure 6.18: Unsteady flow structures for a cylinder subject to a cross-flow at $Re = 3.8 \cdot 10^4$.

flow regime, it does exhibit slight variation, as the shedding process is actually attributed to numerous instabilities. The individual instabilities may be attributed to distinct Reynolds number ranges within the sub-critical flow regime. Fey et al. [22] provide an excellent summary of the Reynolds number dependency as well as the contributing instabilities, as presented in Figure 6.19. It should be noted that, for a cylinder, both the Strouhal and Reynolds numbers are evaluated using the cylinder diameter as the characteristic length.

Aside from the wake vortices, periodic structures also exist in the shear layer between the wake and free stream regions, as shown in Figure 6.18. These secondary structures, a result of a shear layer instability, contribute little to the overall aeroacoustic emissions. The shedding frequency of the shear layer structures is commonly expressed relative to the wake vortices, which for the sub-critical flow regime, may be approximated using Equation 6.4, as suggested by Rajagopalan and Antonia [81].

$$\frac{f_{sl}}{f_v} = 0.029Re^{0.65} \quad (6.4)$$

In addition to the Reynolds number dependency of the Strouhal number, the effects of inflow turbulence, cylinder roughness, blockage ratio (d/h), and slenderness ratio (l/d) have all been studied extensively. Inflow turbulence and cylinder roughness exhibit similar effects, serving to reduce the Reynolds number at which the transition to critical flow occurs. While the Reynolds number range defining the sub-critical flow regime is marginally reduced as a result, the Strouhal numbers within this range remain unaffected [1]. For the slenderness ratio, previous studies have found that three dimensional effects can occur for $l/d < 3$, however these effects are primarily constrained to the critical flow regime [1]. Probably the most influential parameter on the resulting Strouhal number is the blockage ratio. The resulting increase in velocity experienced near the separation point causes the Strouhal number to be higher than anticipated. These blockage effects have been

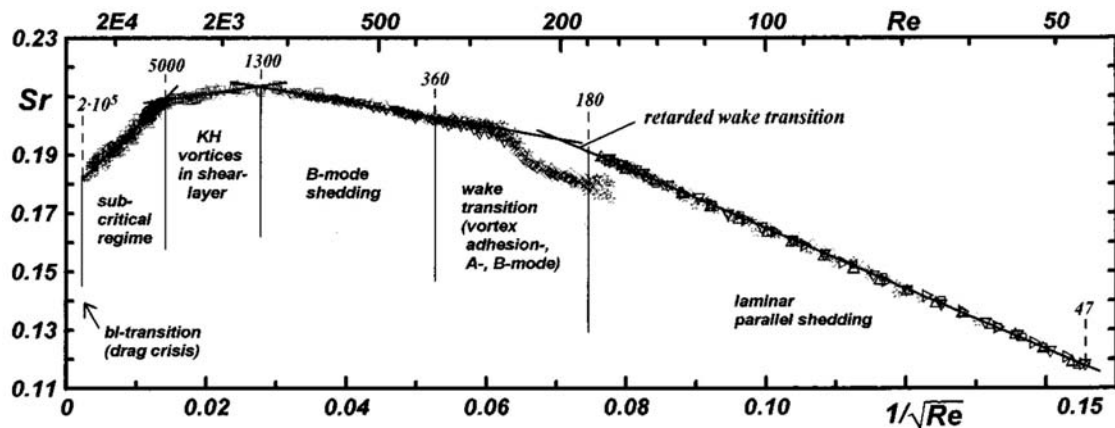


Figure 6.19: Strouhal number versus Reynolds number for a cylinder subject to a cross flow. (From Fey et al. [22].)

studied extensively in the past, and for $d/h < 0.10$, the corrected velocity may be approximated using Equation 6.5, as proposed by Allen and Vincenti [5]. The corrected velocity may then be used to more accurately evaluate the Strouhal number. Given that the blockage and slenderness ratios exhibit potential impacts on the resulting Strouhal number, these ratios served as primary considerations in the design of the test specimen.

$$\frac{u_c}{u} = 1 + \frac{1}{4}C_d \left(\frac{d}{h}\right) + 0.82 \left(\frac{d}{h}\right)^2 \quad (6.5)$$

Design and Manufacturing

The design of the test specimen was subject to numerous constraints. For the Strouhal number, constraints included the blockage and slenderness ratios, as well as the Reynolds number. In addition to requiring that the Reynolds numbers be within the sub-critical flow regime, the selected range was desired to correspond to a particular instability. Aside from the Strouhal number constraints, accommodating the depth of the near field pressure sensor imposed a minimum cylinder diameter of 0.012[m]. Furthermore, the predicted shedding frequencies needed to fall within the frequency response of the near and far field sensors. Finally, additional constraints were imposed by the tunnel specifications. A summary of the specimen constraints is presented in Table 6.4.

To satisfy the numerous constraints, the diameter and length of the cylinder were specified at 15.24[mm] and 152.4[mm], respectively. The length corresponds to the tunnel width, while the cylinder diameter was chosen to obtain a slenderness and blockage ratio of 10 and 0.10, respectively. The selected diameter was also considered adequate for accommodating the sensor geometry. Based on the range of tunnel velocities of 5 to 20[m s⁻¹], the resulting Reynolds numbers coincide with a single instability which is well within the sub-critical flow regime. Lastly, the lowest anticipated shedding frequency, corresponding to 5[m s⁻¹], was determined to be approximately 70[Hz]. Thus, through careful selection of the specimen geometry, all of the imposed constraints were satisfied.

Constraint			
		d/h	< 0.10
3	$<$	l/d	
47	$<$	Re	$< 2 \cdot 10^5$
50	$<$	f_v [Hz]	< 5000
0.012	$<$	d [m]	< 0.152
		l [m]	< 0.152
5	$<$	u [m s ⁻¹]	< 20

Table 6.4: Test specimen constraints.

Based on the specified geometry, the C_d value of the test specimen was determined to be approximately 0.82, corresponding to a smooth cylinder for the defined slenderness ratio and Reynolds number range [93]. This value was used with Equation 6.5 to evaluate the corrected velocity, which was determined to be 2.9[%] greater than the free stream velocity. For the instability corresponding to the defined Reynolds number range, the Strouhal number may be predicted using Equation 6.6, as suggested by Fey et al. [22]. Equation 6.6 is a correlation based expression which, for a Reynolds number range of 5000 to $2 \cdot 10^5$, provides Strouhal numbers accurate to within 0.003 of experimental results [22].

$$St = 0.1776 + \frac{2.2023}{\sqrt{Re}} \quad (6.6)$$

For manufacturing the test specimen, the material selection was based on a number of considerations. First, mounting of the test specimen was to be facilitated using a 12.70[mm] threaded shoulder, as previously presented in Figure 6.4. To ensure that the mount was sufficiently rigid, it was elected to make the shoulder integral to the test specimen. To accommodate both the mounting shoulder and cylindrical geometry, the test specimen needed to be manufactured from cylindrical rod stock. The use of solid rod stock, as opposed to thin walled tubing, provides the additional benefit of increased rigidity. For the material type, 4130 steel was selected due to its high strength and corrosion resistance. This material also enables the cylinder to act as an effective EMI shield for the embedded sensor.

Manufacturing of the test specimen began with a length of 15.88[mm] diameter 4130 rod stock. The test section portion was manufactured first, using a lathe to turn the diameter to a nominal 15.24[mm]. The cutting and feed rates were carefully selected to obtain the smoothest possible surface finish. Upon obtaining the specified diameter, the surface was polished using 400 grit emery paper. The resulting diameter measured 15.24[mm], with a maximum taper of 25[μ m]. During the same machining setup, a 12.70[mm] shoulder was turned and threaded to accommodate mounting. After cutting the material to the specified length, a 13.0[mm] hole was drilled to accommodate both the sensor and amplifier circuit. The amplifier circuit was to be placed within the test specimen, as to benefit from the additional EMI shielding. To accommodate the sensor cable, a 3.5[mm] hole was drilled from the opposite end, details of which are presented in Figure 6.20.

Integration of the near field pressure sensor presented numerous challenges, in part due to the small diameter of the test specimen. Due to the geometric constraints, it was not possible to install the sensor from below the surface. Instead, the sensor had to be passed through the surface. Rather than pressing the sensor directly into the test specimen, a nylon sleeve was used, as shown in Figure 6.21. This approach enabled the sensor to be easily contoured to the cylindrical surface, without permanently altering the sensor housing. Furthermore, the nylon sleeve permits the safe removal of the sensor, should it be required. With the sensor having an outer diameter of 5.6[mm], the nylon sleeve was manufactured with an outer diameter of 8.0[mm] and sensing port diameter of 0.3[mm].

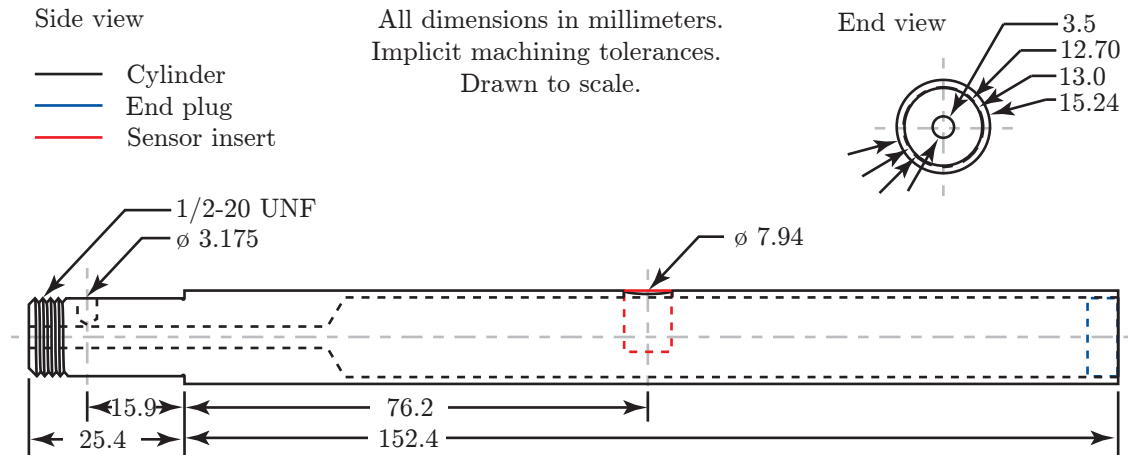


Figure 6.20: Test specimen specifications.



Figure 6.21: Test specimen showing nylon sleeve for near field pressure sensor.

To accommodate the nylon sleeve, the test specimen was set up on a mill and a 7.94[mm] hole was machined radially at the midspan. During the same machining setup, a 3.175[mm] dowel hole was machined into the shoulder, enabling the precise angular positioning of the pressure sensor during experiments. Upon installing the circuit into the test specimen, the sensor was pressed into the nylon sleeve, and the sleeve was pressed into the cylinder. The use of press fits was desirable, as it provides an excellent seal without the use of adhesives. Using a lathe, the assembly was turned and the nylon sleeve was machined close to the cylinder's surface. The

remaining contouring was performed using emery cloth, as to prevent a reduction in cylinder diameter. Nylon was selected as the sleeve material in part due to this consideration, as the material could be easily contoured without removing material from the cylinder. Upon verification of the sensor's operation, a nylon plug was pressed into the end of the cylinder, isolating the internal volume. The completed test specimen is shown in Figure 6.22.

With the test specimen completed, attention was turned to the method used to determine the cylinder angle, as defined by the pressure sensing port. To relate the dowel hole on the test specimen to an angular position, an 6.35[mm] aluminum plate was fabricated into a circular disk. A 12.70[mm] hole was drilled in the centre of the disk, allowing the disk to be located on the shoulder of the test specimen. A notch was machined into the inner diameter, enabling the disk to be aligned to the test specimen using a 3.175[mm] dowel. Relative to the notch, which served as a zero degree reference, an intricate hole pattern of five concentric hole circles was fabricated, with each hole being drilled and reamed to precisely 4.0[mm]. Each of the hole circles contained 36 holes spaced at five degree increments, with the hole circles each being offset by one degree. The result is a hole pattern containing 180 holes spaced at one degree increments. A corresponding hole pattern, consisting of just five holes, was fabricated into the test section wall. Using a 4.0[mm] dowel, the disk and test specimen could then be effectively constrained to a specified angle. Angular markings were machined into the edge of the disk in five degree increments, enabling the current angle to be read effectively. The resulting disk is



Figure 6.22: Test specimen completed.



Figure 6.23: Test specimen angular positioning disk.

shown in Figure 6.23.

The completed cylinder was inserted into the tunnel wall and the alignment dowel was installed. The measurement disk was then placed on the shoulder of the test specimen and the angular position was constrained using a 4.0[mm] dowel. A custom aluminum fastener was threaded onto the end of the cylinder, holding the assembly firmly in place, as shown in Figure 6.24. This clamping approach to mounting was preferred, as it allowed the cylinder to be quickly rotated to any angular position. With the test specimen installed in the wind tunnel, only a few details remained for the experimental setup.

6.1.3 Far Field Pressure Measurements

For the far field pressure measurements, the B&K microphone was accommodated using the 19.05[mm] mounting hole, located directly below the cylinder. To prevent the microphone mount from interacting with the flow, the mount needed to be flush with the tunnel wall. Flush mounting the microphone, however, exhibited a number of deficiencies. First, the fragile microphone diaphragm would be exposed and highly susceptible to damage. Second, the microphone would be subject to high intensity boundary layer turbulence, easily overpowering the low intensity far field measurements. The microphone's susceptibility to boundary layer noise can be mitigated by recessing the sensor into the surface. According to Mueller [67], even a small recess can provide a significant reduction in the observed boundary layer



Figure 6.24: Test specimen installed in wind tunnel.

noise. Recessing, however, has the inadvertent consequence of forming an open ended resonator. To address this deficiency, a commonly implemented approach is to cover the cavity with a porous fabric. The intent of the fabric is to keep the flow from entering the cavity while permitting the passage of sound waves.

To accommodate the porous fabric, the sensor mount was fabricated in two parts. The outer part was manufactured from aluminum and contained the necessary mounting provisions for the tunnel wall. The inner part was fabricated from Teflon and was used to retain the microphone. For the porous fabric, an $80[\mu\text{m}]$ thick sheet of Dacron, commonly referred to as aircraft fabric, was utilized. The porous fabric was pressed between the inner and outer portions of the sensor mount, resulting in a flush mount diaphragm. The microphone was then inserted into the mount and recessed $2[\text{mm}]$ from the surface. Although it was desired to maximize the depth of the recess, increasing the distance any further presented the risk of acoustic shadowing. Additional details of the far field mount are presented in Figure 6.25.

6.1.4 Data Acquisition

For the validation experiments, three voltage measurements needed to be acquired. For the near and far field pressure sensors, the National Instruments PCI-6143 data acquisition card was utilized, providing simultaneous sampling at a sufficient data

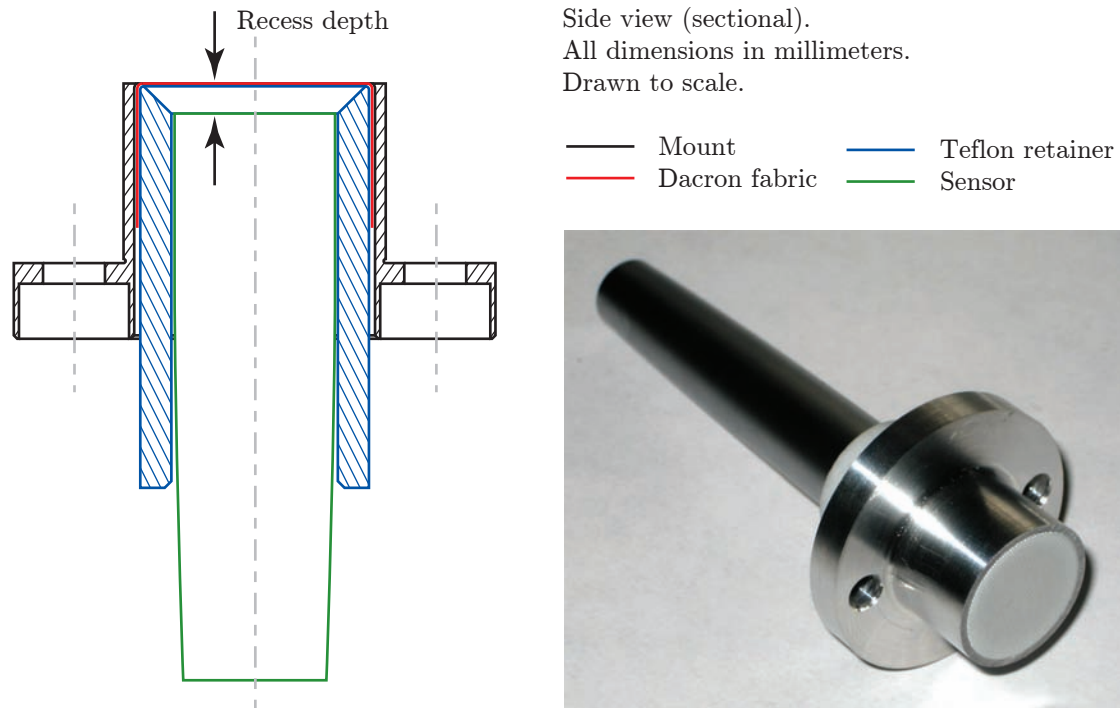


Figure 6.25: Wind tunnel far field sensor mount.

rate. The tunnel thermocouple was sampled using the National Instruments PCI-6251 data acquisition card, due to the availability of lower voltage ranges. In wiring the devices to the data acquisition cards, shielded cable was utilized and care was taken to properly ground the sensors. The test specimen and far field sensor were grounded to the tunnel wall, which was subsequently connected to a ground of the data acquisition cards.

To perform the experiments, an application was created using LabVIEW, part of which was used to facilitate the prior tunnel calibration. With the intent of post-processing the results, the primary function of the application was to acquire and export the voltage measurements. The remainder of the application was simply to provide immediate feedback regarding the acquired data.

For a given experiment, the application requires a number of parameters to be defined. Most notably, the application contains two operating modes: noise floor and cylinder measurements. The noise floor measurements are used to quantify the background noise, with a unique experiment corresponding to a specific tunnel velocity. For the cylinder measurements, however, a unique experiment corresponds to a specific tunnel velocity and cylinder angle. The two operating modes are functionally identical, with the only difference being the output of the data file. A unique identifier was introduced to prevent data files from being overwritten for a non-unique experiment. A standardized naming convention was used for the data files, based on the experimental parameters, to aid in the post-processing of the results.

A number of important parameters within the application pertain to sampling. Although the data acquisition system is capable of sampling at a rate of 250[kHz] for extensive durations, doing so for a large number of experiments would present challenges in terms of storing and processing the data. As such, the minimum sampling rate and duration required to obtain representative results needed to be evaluated.

For the sampling rate, a rate of at least twice the maximum observed frequency was required, for reasons presented earlier in Section 5.1.5. With anticipated cylinder shedding frequencies in the range of 70 to 280[Hz], the aeroacoustic emissions did not impose a significant constraint. A more pressing constraint was attributed to the observed tunnel noise. To assess the associated frequencies, the tunnel was operated at 10[m s⁻¹] and data was collected at a sampling rate of 192[kHz], the results of which are presented in Figure 6.26. The results clearly show an acoustic source at 12.0[kHz], corresponding to the carrier-frequency of the VFD drive and originating from the motor. Harmonics of this frequency extend across the entire spectrum and do not exhibit signs of diminishing. Given this observation, increasing the data rate further would not provide any additional benefits. Thus, sampling was to be performed at a rate sufficient to capture the primary frequency of 12.0[kHz]. To avoid the harmonics from overlapping at 0[Hz], a sampling rate of 24.5[kHz] was selected, as opposed to 24.0[kHz]. Doing so essentially distributes the aliased harmonics across the spectrum as opposed to forming defined peaks. With

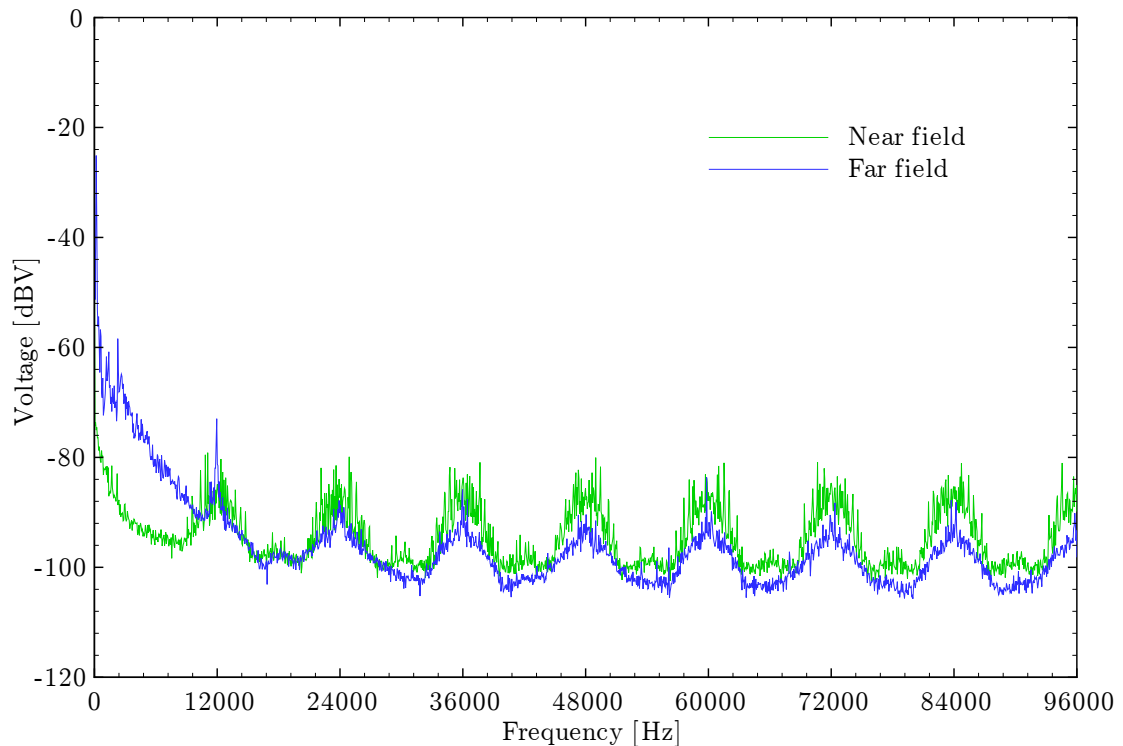


Figure 6.26: Sensor voltages versus frequency for wind tunnel noise measurements at a velocity of 10[m s⁻¹] and sampling rate of 192[kHz].

the remaining harmonics almost 20[dBV] lower than the observed tunnel noise, the resulting aliasing did not present a concern. Furthermore, the aliasing effects would be captured by the noise floor measurements. The presence of these noise sources illustrates the benefits of hardware filters, as they could be effectively used to attenuate both the primary frequency and subsequent harmonics.

The sampling duration was based on two defined parameters. The first parameter was the desired frequency resolution. Increasing the frequency resolution enables the peak frequency to be more precisely determined. The increase in resolution, however, comes at the cost of data storage. To permit the accurate determination of the shedding frequency, while minimizing the storage requirements, the frequency resolution was specified at 0.25[Hz]. The second parameter contributing to the sampling duration is the required number of FFT averages. Based on initial experiments, it was concluded that 25 FFT averages provided sufficient convergence. To satisfy the frequency resolution and FFT average requirements, a sampling duration of 100[s] was required, yielding $2.45 \cdot 10^6$ samples for each of the three channels. The resulting data file was found to be approximately 60[MB] for a single experiment.

Aside from the sampling parameters, the atmospheric temperature and pressure are also specified in the application, with the temperature serving as the cold junction constant for the thermocouple. Sensitivities of the pressure sensors are also specified, however, they are merely used to display the results. Values for all of the operating parameters are written to the header of the data file.

To display the results, FFT averaging is performed on both the near and far field measurements, using the specified sensitivities to convert the amplitudes from voltage to pressure. Peak detection is applied to the FFT results to determine the peak frequency and corresponding amplitude. The Strouhal number is then evaluated using the near field frequency and additional experimental specifications. As previously stated, the processed results are merely intended for instantaneous feedback and have no bearing on the resulting data files. Additional details of the LabVIEW application are presented in Appendix C.

6.2 Procedure

In performing the validation experiments, the efficacy of the technique in both locating and quantifying sources of aerodynamic sound was to be evaluated. Based on the constraints presented in the experimental setup, validation of the experimental technique was limited to flow over a cylinder for a range of velocities of 5 to 20[m s⁻¹].

Prior to performing the cylinder experiments, the noise within the tunnel needed to be quantified, enabling the background noise to be effectively subtracted from the acoustic measurements. To perform the noise measurements, the test specimen was placed external to the tunnel, sealing the mounting hole with a nylon plug. The tunnel was then varied from 5 to 20[m s⁻¹] in 1[m s⁻¹] increments, allowing

the tunnel to reach thermal equilibrium prior to performing the near and far field sensor measurements. It should be noted that the test specimen was unable to be placed inside the tunnel, as its presence would inevitably introduce noise. As a result, the near field sensor was only able to resolve the noise external to the test section. This was not considered a significant source of error, as it was anticipated that the near field pressures would be an order of magnitude larger than the tunnel noise.

To evaluate the efficacy of the technique in locating aeroacoustic sources, the first series of experiments pertained to the spatial dependency of the near field pressures. To obtain the spatial measurements, experiments were performed for cylinder angles of 0 to 180[°] in 5[°] increments, with 0[°] coinciding with the front of the cylinder as shown in Figure 6.18. It was only necessary to resolve the top portion of the cylinder, due to the symmetry of the flow field. The spatial resolution, which was partially attributed to data storage requirements, was considered adequate as a first approximation. To assess the Reynolds number dependency of the resulting pressure field, the spatial experiments were performed for velocities of 5 to 20[m s⁻¹]. Performing the spatial measurements in 1[m s⁻¹] increments would generate an overwhelming amount of data. As a result, the measurements were to be performed in 5[m s⁻¹] increments. This increment was considered adequate for assessing variations in the pressure fields.

A second series of experiments were performed as an extension of the spatial measurements. Given that the spatial measurements were only performed for the top portion of the cylinder, it was desired to validate the assumed symmetry of the pressure field. To do so, experiments were performed for cylinder angles of 0 to 355[°] in 5[°] increments. It was elected to perform the symmetry measurements for a single velocity of 15[m s⁻¹], as the variation in tunnel symmetry would likely be insignificant.

The final series of experiments pertained to the Reynolds number dependency of the contributing flow structures for a more detailed range of velocities. For the experiments, the cylinder was fixed at an angle corresponding to the peak near field intensity. Based on initial measurements, this corresponded to a cylinder angle of approximately 135[°]. Fixing the cylinder angle, experiments were performed for velocities of 5 to 20[m s⁻¹] in 1[m s⁻¹] increments. By evaluating the flow structures over the range of velocities, the results may be readily compared to existing literature.

Although three distinct series of experiments were defined, the series were to be executed simultaneously. This decision was due to thermal considerations, as the tunnel requires a significant amount of time to reach thermal equilibrium for a given velocity. To reduce the total required time, the tunnel was varied from 5 to 20[m s⁻¹] in 1[m s⁻¹] increments. Upon obtaining an approximately constant temperature within the test section, all of the experiments were performed for the given velocity. Following this procedure, only one velocity sweep was required to obtain all of the experimental results, as presented in Table 6.5.

Experiment(s)	Specifications	
	Velocity [m s^{-1}]	Angle(s) [$^{\circ}$]
1 to 37	5	0,5...180
38	6	135
39	7	135
40	8	135
41	9	135
42 to 78	10	0,5...180
79	11	135
80	12	135
81	13	135
82	14	135
83 to 155	15	0,5...355
156	16	135
157	17	135
158	18	135
159	19	135
160 to 196	20	0,5...180

Table 6.5: Validation experiments.

6.3 Results and Analysis

6.3.1 Data Processing

To permit the analysis of the experimental results, it was necessary to process the voltage measurements into a more usable form. However, with the experimental data amounting to 12.5[GB], an efficient means of processing the data was required. Given the large data sets, as well as the necessity to perform FFTs, windowing, and matrix manipulations, a MATLAB [89] program was created to facilitate the processing.

A standard MATLAB code was created to process the individual experiments. For a given cylinder experiment, the code began by loading the background noise measurements for the specified velocity. After applying a Hamming window to the time-resolved data, for reasons previously presented in Section 5.1.5, an average FFT was obtained for both the near and far field noise measurements. The RMS frequency spectrum was then converted from a voltage to pressure using the frequency response of the individual sensors. With the observed noise being primarily acoustic, as opposed to electrical, it was necessary to account for the free field response of the sensors. For the far field sensor, which was mounted to a planar surface, the free field response was double the pressure field response, due to superposition of incident and reflected sound waves [67]. For the near field sensor, the free field response was not corrected for, as it was not possible to differentiate between the hydrodynamic and acoustic pressure fields. However, given the relatively low magnitude of the background noise compared to the near field pressures, not

correcting for the free field response did not present a significant source of error.

With the background noise quantified, the measurements for the specified cylinder experiment were then processed. The pressure spectrum was obtained in an identical manner to the noise measurements. To isolate the aeroacoustic component of the observed pressures, the pressure spectrum of the noise measurements was subtracted from the results obtained for the cylinder experiment. For the near field measurements, the noise was substantially less than the cylinder measurements, as shown in Figure 6.27. The predicted aeroacoustic structures, determined using Equation 6.6, are easily resolved without the use of noise subtraction. For the far field measurements, however, the cylinder experiments were dominated by tunnel noise, as shown in Figure 6.28. Thus, for the far field measurements, noise subtraction was necessary to extract any useful aeroacoustic results.

Aside from the pressure spectra, additional processing was performed to extract information regarding the aeroacoustic structures. To account for the effects of tunnel blockage, the nominal velocities were corrected using Equation 6.5. The corrected velocity was then used with the measured temperature and pressure to evaluate the Reynolds number. Using the previously obtained pressure spectra, the peak frequency and amplitude were evaluated for both the near and far field measurements. The frequencies were then used, with the corrected velocity, to evaluate the corresponding Strouhal numbers.

Upon completion of the processing, the results were formatted for plotting and written to four separate data files. Three of the files are comprised of near and far field pressure spectra, corresponding to the cylinder and noise measurements, as well as the evaluated aeroacoustic component. The fourth file contains a summary of results, consisting of the temperature, atmospheric pressure, Reynolds number, as well as the peak amplitude, frequency, and Strouhal number for both the near and far field measurements.

Rather than executing the preceding code separately for the 196 experiments appearing in Table 6.5, an iterative routine was created to reduce the number of data files resulting from the processing. To perform the iterative process, the MATLAB program was created with three distinct operating modes, corresponding to the experimental series outlined in the procedure. For a given operating mode, defined for a range of angles or velocities, the program would iterate the aforementioned procedure for each of the defined experiments. The resulting data files were combined for the given operation, yielding either a spatial or velocity dependent pressure spectra. In addition to reducing the number of data files resulting from the processing, the iterative routine greatly reduced the required user interaction. Additional details of the MATLAB program are presented in Appendix D.

Through processing of the results, the data was effectively reduced to approximately 640[MB]. To further reduce the data, the results presented herein are limited to the resulting aeroacoustic component, unless otherwise specified. Furthermore, the pressure spectra are limited to 2000[Hz], as narrow band pressures were not observed above this frequency. Detailed experimental results, which do not appear

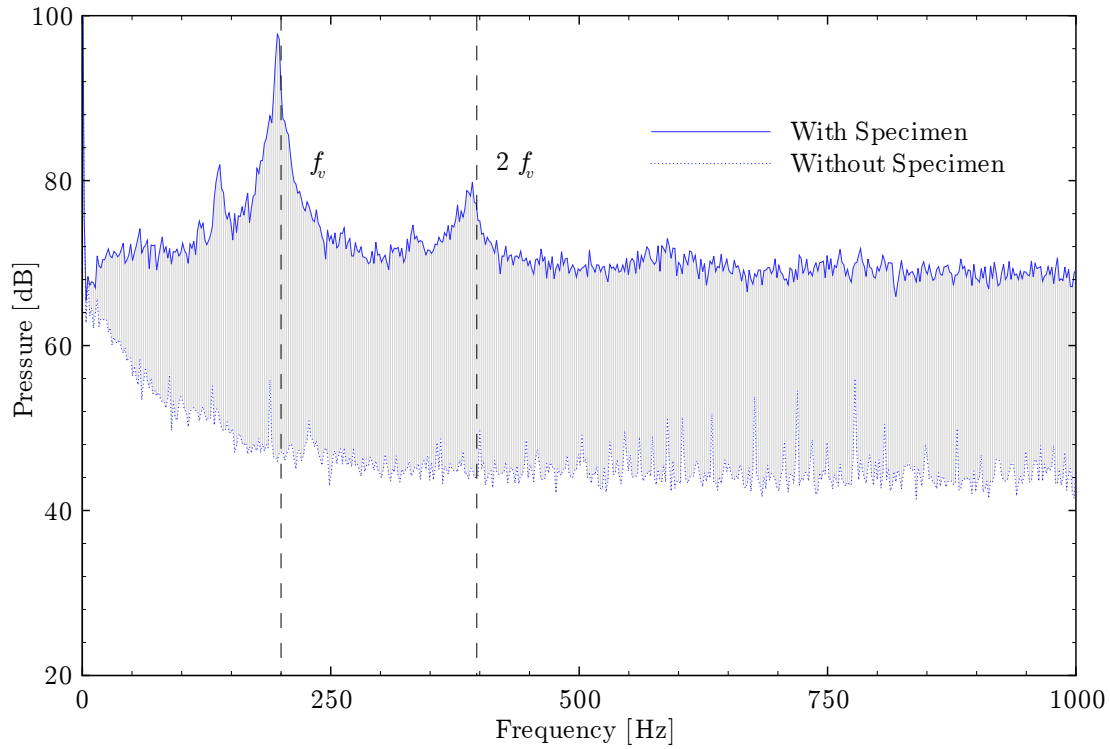


Figure 6.27: Near field pressure measurements for a nominal velocity of $15[\text{m s}^{-1}]$ and cylinder angle of $135[^\circ]$.

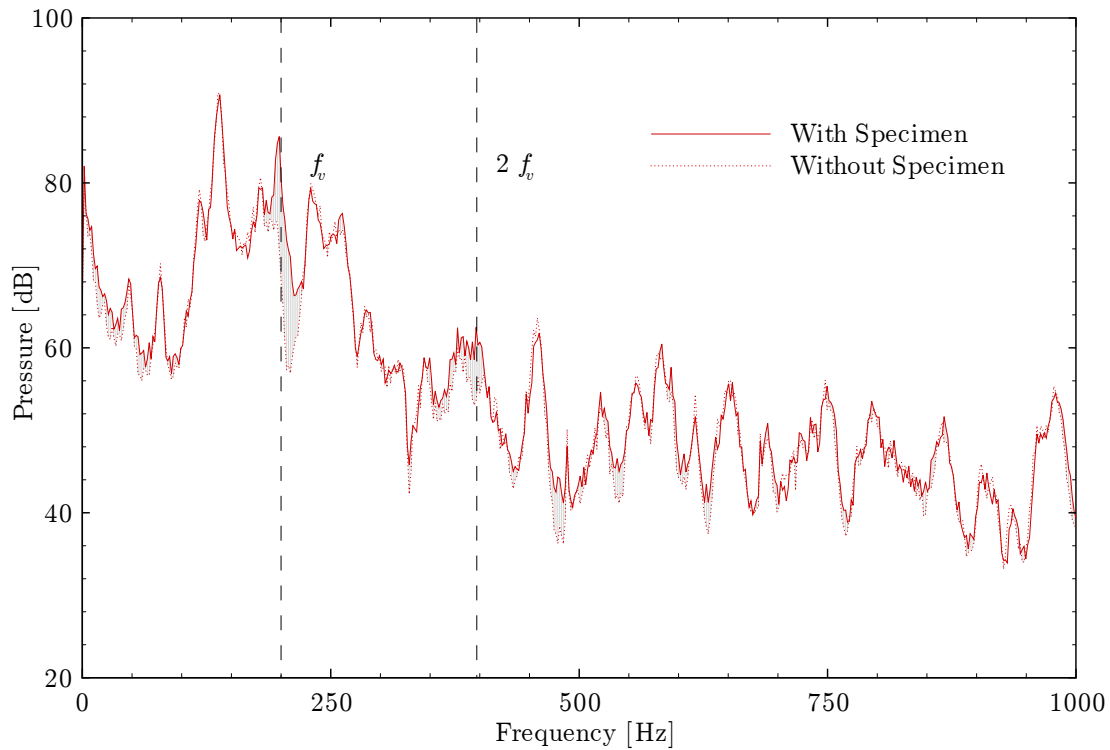


Figure 6.28: Far field pressure measurements for a nominal velocity of $15[\text{m s}^{-1}]$ and cylinder angle of $135[^\circ]$.

in text, are presented in Appendix E.

6.3.2 Quantifying Aeroacoustic Sources

Prior to performing an analysis of the results, it was necessary to validate that the tunnel velocities were accurately predicted by the calibration. To do so, the tunnel temperature and pressure of the cylinder experiments needed to be compared to the calibration. For the temperature, the values were plotted for the range of velocities, as shown in Figure 6.29. The two temperatures deviated by $1.5[^\circ\text{C}]$ at most, representing a maximum deviation of $0.5[\%]$. For the atmospheric pressure, the cylinder experiments were performed at a constant $98.1[\text{kPa}]$ which, compared to the calibration, represented a pressure increase of $0.6[\%]$. Although the effects of temperature and pressure on the resulting calibration were not quantified, the observed deviations were considered negligible. The corresponding Reynolds numbers are also presented in Figure 6.29, which due to the increase in tunnel temperature with velocity, exhibit a slight deviation from a linear trend.

To evaluate the presence of aeroacoustic structures, it was necessary to evaluate whether the pressure sources appearing in the near field actually propagated to the acoustic far field. To do so, the pressure spectra for both the near and far field measurements were plotted for a range of velocities, as shown in Figures 6.30 and 6.31, respectively. The near field pressures correspond to a cylinder angle of $135[^\circ]$. Comparing the near and far field pressure spectra, dominant peaks are observed

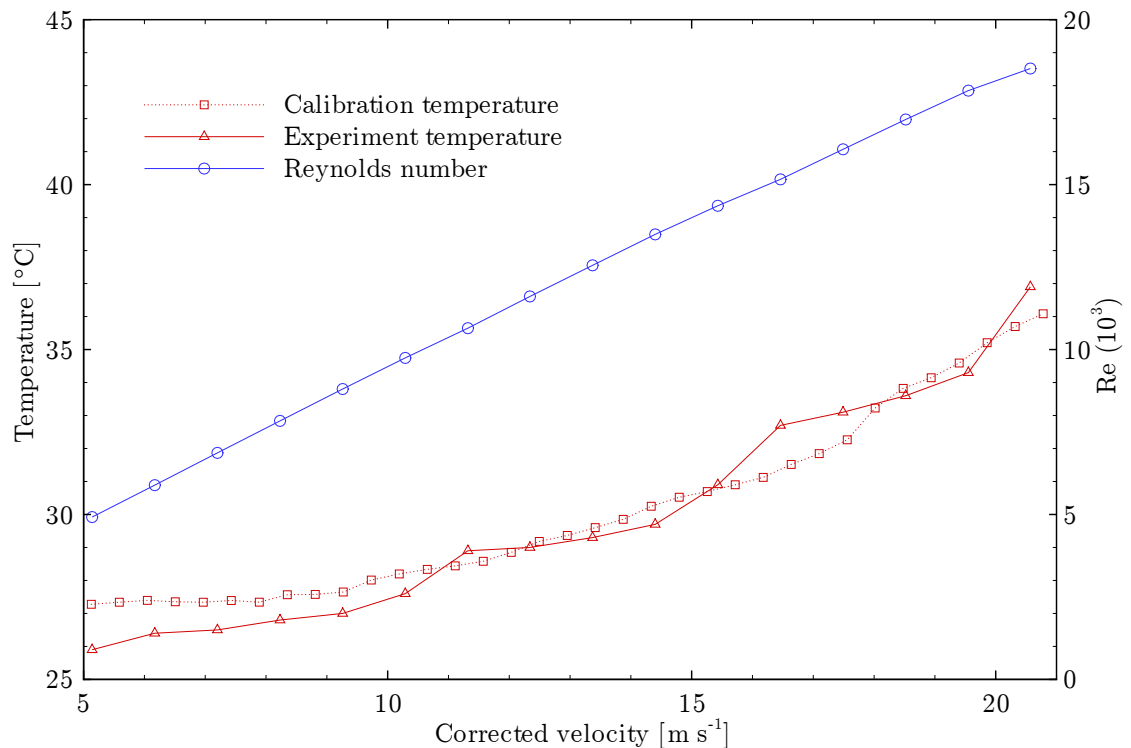


Figure 6.29: Temperature and Reynolds number versus corrected free stream velocity.

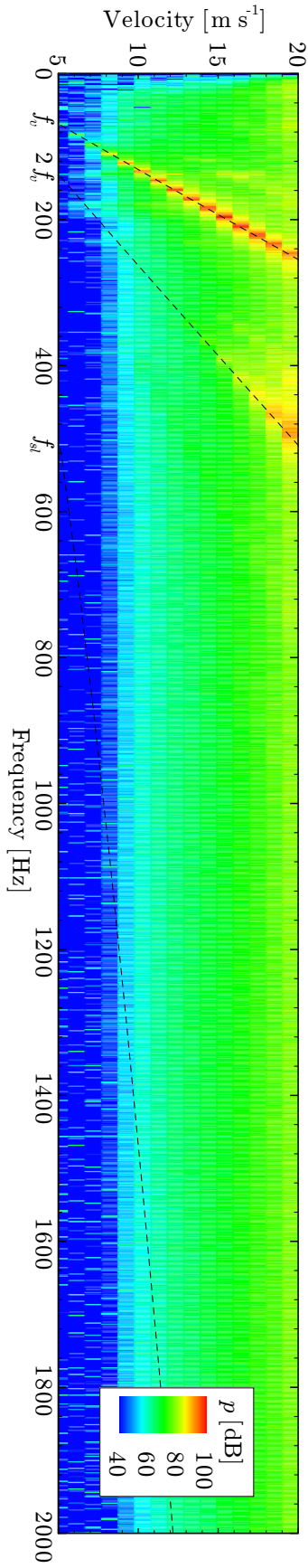


Figure 6.30: Near field pressure spectra for a range of corrected velocities and a cylinder angle of 135° .

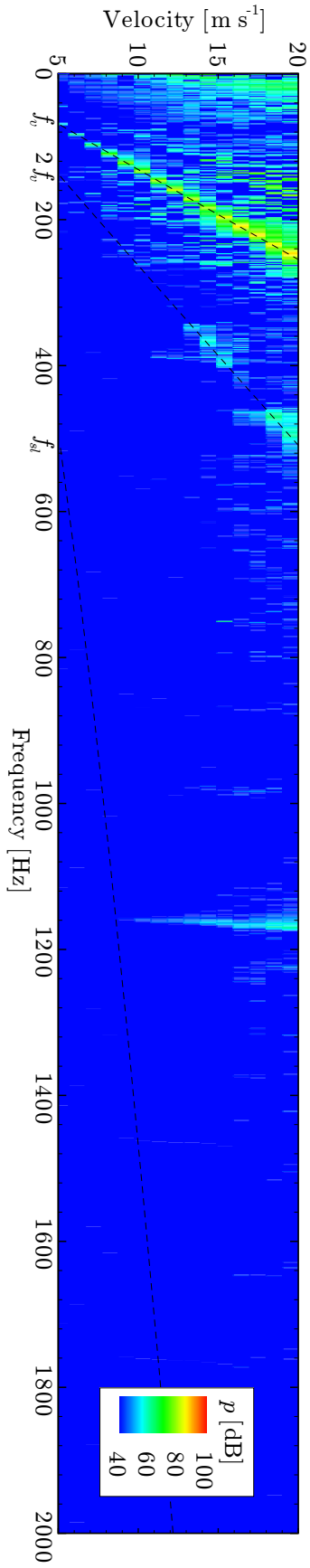


Figure 6.31: Far field pressure spectra for a range of corrected velocities and a cylinder angle of 135° .

at almost identical frequencies, with the peak frequencies exhibiting a linear relationship with velocity. Superimposing the predicted frequencies, as determined by Equation 6.6, it is evident that the aeroacoustic emissions are attributed to the periodic shedding of the wake vortices. In addition to the primary shedding frequency, a doubling of the frequency is evident at higher velocities in both the near and far field measurements. Aside from the wake vortices, the shear layer vortices were also of interest. Superimposing the anticipated frequencies, as determined by Equation 6.4, the structures were not apparent in either the near or far field measurements.

Aside from the anticipated frequencies in pressure spectra, a minor peak was observed in the far field spectra at approximately 1150[Hz]. However, with a similar peak observed in the noise measurements, and the lack of a corresponding peak in the near field, the peak was simply attributed to tunnel noise. It is possible that the presence of the cylinder resulted in an increase in tunnel noise for the observed frequency, due to a reflection off the cylinder's surface. Numerous non-dominant peaks were also observed throughout the far field spectra, considered artifacts of the noise subtraction. As a result of these peaks, it was difficult to detect the aeroacoustic emissions with certainty without the assistance of the predicted frequencies. By comparison, these peaks are not present in the near field spectra and the periodic structures are observed with certainty. This result emphasizes the benefits of near field measurements in the presence of excessive tunnel noise. An increase in broadband pressure with velocity was also observed in the near field measurements, attributed to the increasing turbulence of the near field flow.

To further assess the agreement of the measured and predicted peak frequencies, the near and far field Strouhal numbers were plotted against those predicted by Equation 6.6, as shown in Figure 6.32. The corresponding uncertainties of the measured values were evaluated by taking the root-sum-square of the individual contributing uncertainties, as outlined by Wheeler and Ganji [92]. The uncertainty of the frequency, diameter, and temperature measurements were all determined to be less than 0.25[%]. With the velocity exhibiting a dominant uncertainty of 2.0[%], the total uncertainty of both the Strouhal and Reynolds numbers was also determined to be approximately 2.0[%]. The uncertainty bars for the far field measurements are shown in Figure 6.32. The near field uncertainty bars, which have been omitted for clarity, are approximately equal in magnitude to the far field uncertainty bars. The upper and lower range of the prediction, based on the specified uncertainty of the correlation, are also presented in Figure 6.32. With the exception of three data points, the measured Strouhal numbers are within the uncertainty of the predicted and measured values. The three data points lying outside of the prediction, none of which are shown, lie at the extremes of the Reynolds number range, for which the peak pressures did not coincide with the wake vortices.

In addition to the peak frequencies, the corresponding pressures and signal-to-noise ratios (SNR) were plotted for the near and far field measurements, as shown in Figure 6.33. The amplitude uncertainty of the pressure measurements could not

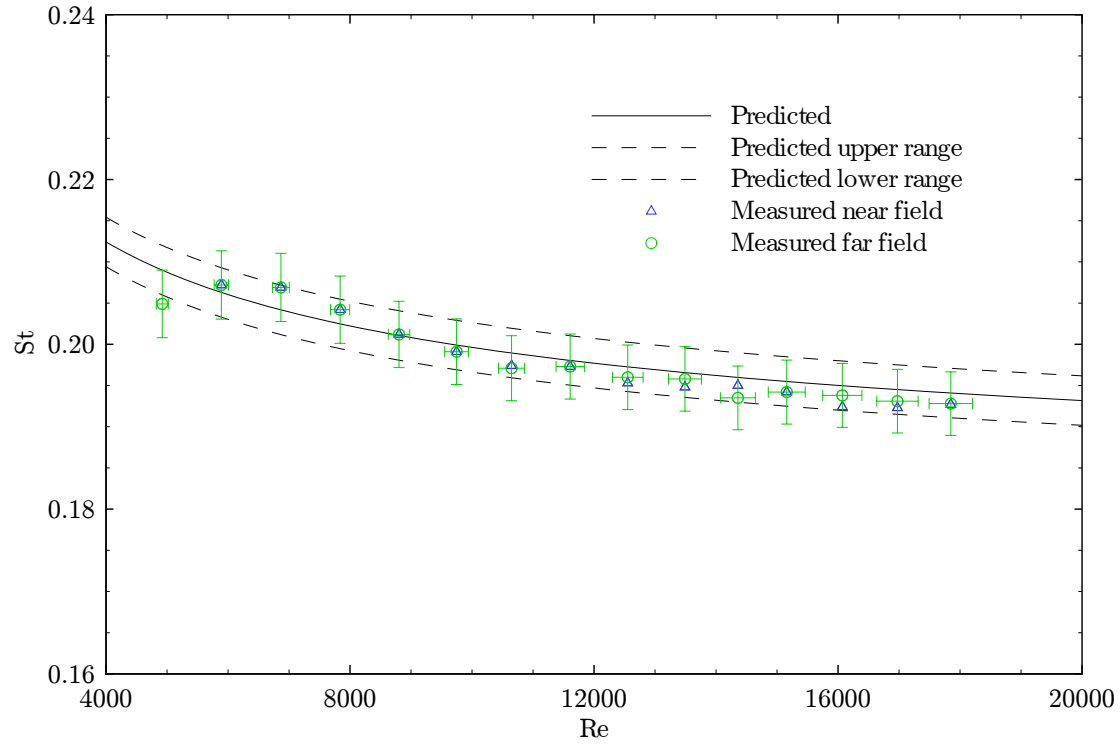


Figure 6.32: Measured and predicted peak Strouhal number versus Reynolds number.

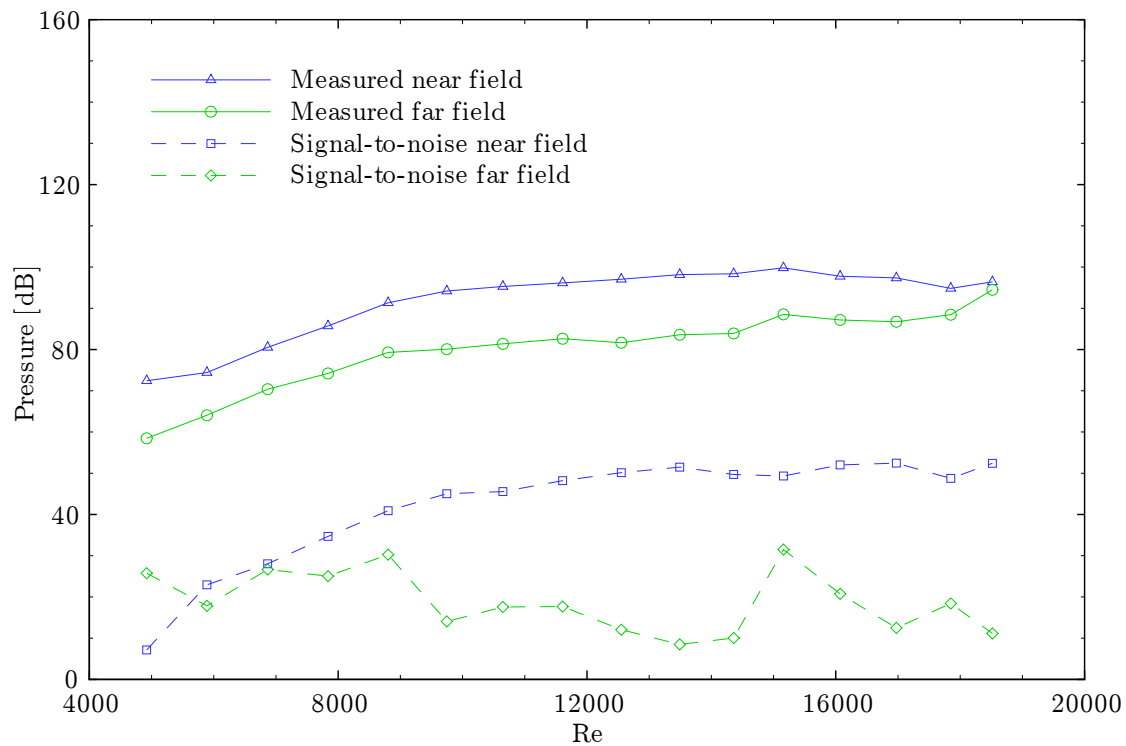


Figure 6.33: Peak pressures and signal-to-noise ratios versus Reynolds number.

be quantified, due to an insufficient characterization of the setup used to calibrate the custom piezoelectric sensor. Although the uncertainty was not quantified, it was still possible to make a number of observations. The peak pressures of near and far field measurements were found to exhibit similar trends, with the values generally increasing with Reynolds number. At higher Reynolds numbers, the peak pressures appear to plateau, likely a result of the increased turbulence causing the periodic structures to become less coherent. Observing the far field measurements, the aeroacoustic emissions increased from 58 to 94[dB]. The near field pressures were consistently 10 to 15[dB] higher than the far field, providing insight into the efficiency of the aeroacoustic source. The exact efficiency, however, was unable to be quantified, as the directivity of the source was not resolved. Although the peak pressures of the near field were significantly higher than the far field, the pressures were as low as 72[dB], or 0.08[Pa]. The ability to resolve this low intensity source was credited to the use of the custom piezoelectric sensor. Had a less sensitive sensor been used, the ability to detect the aeroacoustic structures at low Reynolds numbers would have been significantly impaired.

Observing the SNRs for the peak pressures, the near field values increase continuously from 7 to 52[dB]. For the far field measurements, the SNRs are less consistent, varying anywhere from 8 to 32[dB]. The deviations from the predicted Strouhal numbers, occurring at the extremes of the Reynolds number range, are likely attributed to the locally diminished SNRs. While the improved SNRs of the near field measurements are a direct consequence of the greater signal intensity, they are partially attributed to the undervaluation of the background noise.

6.3.3 Locating Aeroacoustic Sources

To assess the ability to locate aeroacoustic sources, the near field pressure spectra were plotted for angles of 0 to 180[°] at nominal velocities of 5, 10, and 20[m s⁻¹], as shown in Figures 6.34, 6.35, and 6.36, respectively. The predicted frequencies for the wake and shear layer vortices are also presented, as determined using Equations 6.6 and 6.4, respectively.

Observing the spatial plot for 5[m s⁻¹], a peak corresponding to the wake vortices was evident over a wide range of angles. A doubling of the wake frequency was not observed, neither was the presence of the shear layer vortices. Although the wake vortices were resolved, it was difficult to distinguish the peak without the far field emissions or prior knowledge of the contributing structures. This was partially attributed to the poor SNR, resulting in a dominant peak which does not coincide with the wake vortices. Rather, the dominant peak occurs at approximately 50[Hz], coinciding with a peak appearing in the background noise. This result further emphasizes the deficiency with the near field noise measurements. Harmonics of 216[Hz] were also observed in the near field pressure spectra, but were unable to be attributed to the background noise.

For the 10[m s⁻¹] measurements, the SNR was greatly improved, with the pe-

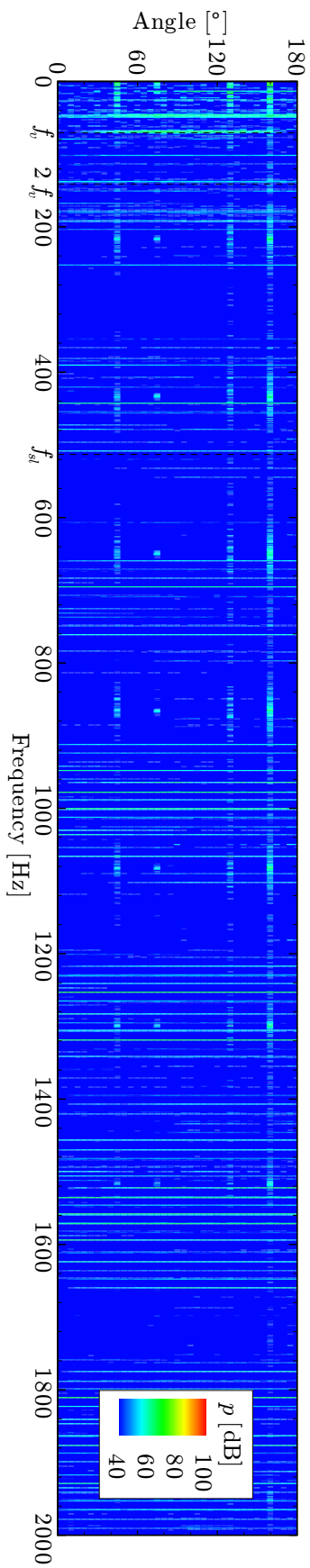


Figure 6.34: Near field pressure spectra spatial plot for a nominal velocity of 5[m s⁻¹].

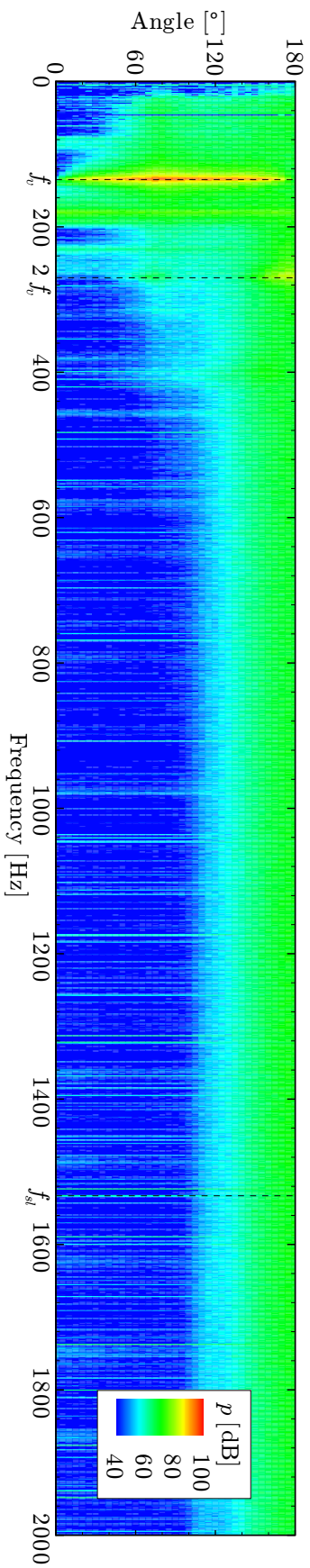


Figure 6.35: Near field pressure spectra spatial plot for a nominal velocity of 10[m s⁻¹].

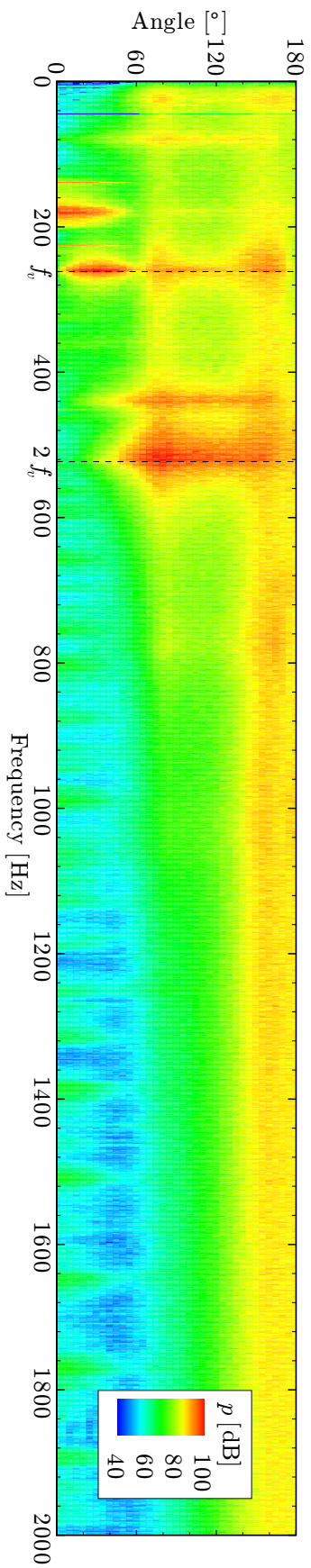


Figure 6.36: Near field pressure spectra spatial plot for a nominal velocity of 20[m s⁻¹].

riodic wake vortices appearing as a dominant peak. The observed peak is narrow in the frequency spectra, indicating the tonal nature of the aeroacoustic source. Similar to the results obtained at $5[\text{m s}^{-1}]$, the periodic pressures associated with the wake vortices occur over a broad range of angles. This spatial diversity was an unexpected result, as it was anticipated that the periodic pressures would be constrained to the wake region, the region corresponding to the origin of the aeroacoustic structures. This result, however, can be readily explained.

Due the intensity of the periodic wake structures, the flow field is affected well upstream of wake region. As a result of the vortex shedding, the near field flow is forced to rotate slightly about the cylinder, resulting in a displacement of the forward stagnation point. This rotation occurs as an oscillation, at an identical frequency to the vortex shedding. Due to the oscillation of the flow field, the resulting near field pressures exhibit an identical response, thus accounting for the shedding frequency appearing over a majority of the cylinder.

With the inability to localize the aeroacoustic structures, the current experiments establish a limitation of near field pressure measurements. It is important to recognize, however, that the limitation is entirely attributed to the periodic structures being communicated upstream of the origin. These upstream effects are particularly strong for the current experiments, for a number of reasons. First, the scale of the periodic structures are approximately one-half the cylinder diameter, having a dramatic effect on the surrounding flow field during the vortex shedding event. Second, the periodic structures are highly tonal, causing the excitation of the flow field. If the aeroacoustic sources in the wake region were broadband in nature, the upstream flow field would likely remain unaffected. Finally, the current experiments were performed for relatively low Reynolds numbers, with the inertial forces of the free stream flow being relatively low. It is anticipated that with increasing Reynolds number, the effects of the periodic structures on the upstream flow would be less pronounced. While these characteristics prevented the current experiments from locating aeroacoustic structures, it is anticipated that moderate Reynolds number airfoil flows would not exhibit similar deficiencies. This is simply because in addition to the increased Reynolds numbers, airfoil flow structures tend to be less tonal and exhibit a small scale relative to the airfoil chord.

Aside from the periodic wake vortices, a number of other features were observed in the $10[\text{m s}^{-1}]$ spatial plot. Unlike at $5[\text{m s}^{-1}]$, a doubling of the wake frequency is observed, with defined peaks at 75 and $180[^\circ]$. The doubling at $180[^\circ]$ was attributed to the interaction of the pair of periodic vortices occurring in the wake region. It was unclear as to the cause of the peak occurring at $75[^\circ]$. The shear layer instability was not observed in the spatial plot and the remaining peaks were attributed to tunnel noise. An important observation was the increase in broadband noise with cylinder angle. This was attributed to the turbulence of the flow, indicating low turbulence for the incoming flow and high turbulence for the wake region, as anticipated. These results may be used to infer the transition of the near field flow to turbulent, which appeared to occur at approximately $120[^\circ]$.

For the $20[\text{m s}^{-1}]$ plot, the primary frequency for the wake vortices was once again observed over a broad range of cylinder angles. However, compared to the $10[\text{m s}^{-1}]$ plot, a noticeable broadening of the associated pressures was observed in the frequency spectra. This is likely a result of the periodic structures becoming less coherent due to the increased turbulence. With the increase in velocity, the doubling of the primary frequency has become the dominant near field pressure for cylinder angles of 60 to $180[^\circ]$. The doubling exhibits an even broader frequency spectra, once again indicating the decreased coherence of the periodic structures. The broadband pressure, associated with the flow turbulence, was substantially increased from the $10[\text{m s}^{-1}]$ plot. Based on these results, it appears as if the flow transitions to turbulence fairly quickly, at approximately $80[^\circ]$. This is further reinforced by the presence of a broadband pressure occurring over limited cylinder angles about $80[^\circ]$. This band of turbulence is likely attributed to flow separation and the generation of a turbulent shear layer. Aside from the primary and doubling frequencies of the wake vortices, a peak also occurs at approximately $440[\text{Hz}]$. This frequency, which does not appear in the far field noise measurements, is possibly attributable to the observed breakdown of the periodic vortex shedding. The remaining near field peaks, most notably at 10 , 40 , and $180[\text{Hz}]$, were all observed in the far field noise measurements and attributed to tunnel noise. Additional tunnel noise was observed for low cylinder angles, where the flow turbulence was low and the sensor was directed upstream. This directivity emphasizes the difficulty in characterizing the tunnel noise for the near field measurements.

6.3.4 Near Field Symmetry

To validate the assumed symmetry of the near field, the pressure spectra were plotted for cylinder angles of 0 to $360[^\circ]$, for a nominal velocity of $15[\text{m s}^{-1}]$, as shown in Figure 6.37. The near field pressures exhibit excellent symmetry, with the periodic structures, broadband turbulence, and tunnel noise identically represented about the plane of symmetry. Thus, it was inferred that the measurements performed at 5 , 10 , and $20[\text{m s}^{-1}]$, accurately represent the near field spectra for the entire range of cylinder angles.

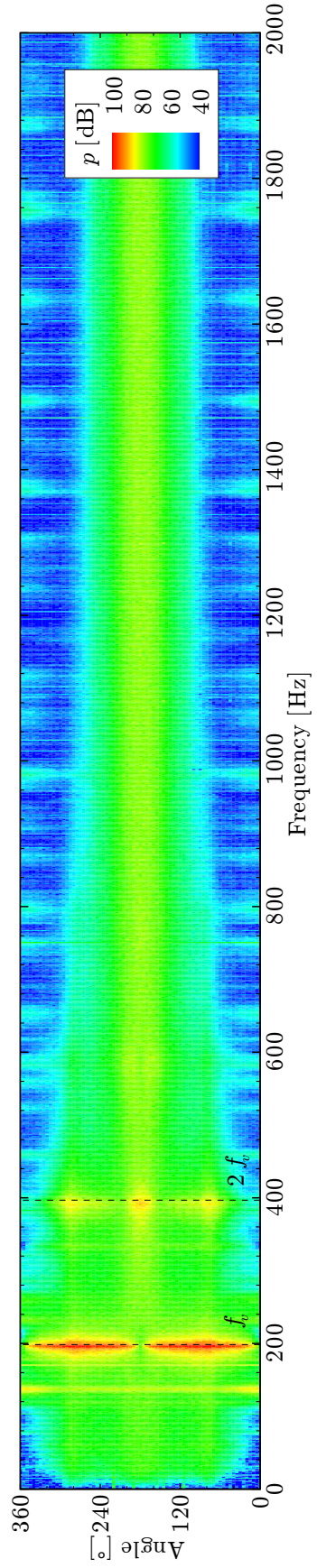


Figure 6.37: Near field pressure spectra spatial symmetry plot for a nominal velocity of 15[m s⁻¹].

Chapter 7

Conclusions

The aerodynamic sound generated by wind turbines was identified as a growing concern within the industry. The limited applicability of existing aeroacoustic research provided the motivation for current research. However, prior to investigating the origins of aerodynamic sound, a research technique suitable for studying low speed airfoils needed to be designed. This served as the primary objective of this research. A secondary objective was to validate the designed technique using results from literature.

The design of a suitable research technique began with a review of aeroacoustic theory. The efficiency of aeroacoustic sources was determined to be very low for the Mach numbers common to low speed airfoils. The low efficiency suggested that for low Mach number flows numerical methods are subject to significant error, favouring the use of experimental methods. Furthermore, the low efficiency and directivity of aeroacoustic sources indicated potential benefits of a technique based on near field as opposed to far field measurements.

A detailed evaluation of existing research techniques was performed using examples from literature. Analytical methods were determined to be an effective means of resolving an acoustic field without the introduction of numerical error, but limited to simple idealized flows. While numerical methods such as CFD address many of these limitations, attempts to control numerical errors place significant demands on computational resources. As a result, the use of CFD was found to be generally limited to higher Mach number flows where the efficiency of aeroacoustic sources is closer to unity. The use of semi-empirical methods was also reviewed, but was found to be constrained to the prediction of aerodynamic sound. The only techniques considered capable of definitively resolving the sources of aerodynamic sound were determined to be experimental. Evaluating the experimental methods appearing in literature, the far field pressure and near field flow measurement techniques were considered to be both cost prohibitive and exhibit relatively high uncertainty. As a result, the near field pressure measurement technique was selected, providing lower measurement uncertainty at a slight compromise to flexibility.

The design of the experimental technique focused primarily on the sensors re-

quired for the near field pressure measurements. Both piezoresistive and condenser type sensors were determined to be insufficient for the desired experiments, opting instead to develop a custom piezoelectric sensor. The constraints of high frequency and low amplitude pressure measurements placed significant demands on the sensor design, emphasizing the importance of electrical shielding as well as the implementation of the sensing line and sensing port. The sensor development led to successful fabrication of numerous prototypes, with the final sensor measuring 5.5[mm] in diameter and consisting of a 3.0[mm] diameter PVDF film diaphragm. Using a custom calibration facility, the sensitivity of the final sensor was determined to be 0.0039[V Pa⁻¹] at 1000[Hz], with a pressure and frequency range of approximately 67 to 140[dB], and 100 to 10 000[Hz], respectively. Aside from the near field pressure sensors, a far field sensor and suitable data acquisition system were selected to facilitate future airfoil experiments.

To satisfy the secondary research objective, a series of validation experiments were performed using a non-anechoic wind tunnel. A number of alterations were made to the wind tunnel to improve the quality of the flow, with the resulting turbulence intensity and spatial uniformity measuring 0.8 and 2.2[%], respectively. A calibration was performed to establish the relationship between the tunnel drive frequency and velocity, exhibiting a maximum uncertainty of 2.0[%]. For the validation experiments, a simple cylindrical geometry was utilized as the test specimen, with a slenderness and blockage ratio of 10.0 and 0.10, respectively. The piezoelectric sensor was mounted flush to the surface of the cylinder while the far field sensor was placed directly below the test specimen.

Observing the near and far field pressure spectra for velocities of 5 to 20[m s⁻¹], the technique was shown to be effective in resolving the aeroacoustic sources, with the dominant peaks coinciding with the predicted shedding frequencies of the wake vortices. The corresponding Strouhal numbers were within 1.5[%] of predicted values, with the exception of three data points, and were within the specified accuracy of the correlation based prediction. With increasing velocity, a broadening of the dominant peak was observed in the frequency spectra, attributed to the decreasing coherence of the periodic structures. This decrease in coherence was further evidenced by the amplitude of the peak pressures, which appeared to plateau with increasing Reynolds number. The far field aeroacoustic emissions ranged from 58 to 94[dB], with the near field pressures consistently 10 to 15[dB] higher, quantifying the gain associated with measuring the near field. Although the near field measurements benefited from the larger signal intensity, the ability to resolve aeroacoustic structures at low Reynolds number was largely attributed to the successful development of the piezoelectric sensor. The signal-to-noise ratio of the near field measurements was also found to be consistently higher than the far field, emphasizing the benefit of near field pressure measurements in a non-anechoic environment.

To assess the ability to locate aeroacoustic sources, the near field pressure spectra were evaluated for cylinder angles of 0 to 180[°]. The dominant peaks corresponding to the wake vortices were observed over a broad range of cylinder angles, attributed to the periodic flow structures being communicated upstream of their

origin. This inability to localize aeroacoustic structures presented a limitation of the near field pressure measurement technique, although it was anticipated that airfoil flows would not exhibit a similar deficiency. The near field pressure measurement technique was shown to be effective in determining the transition of the near field flow to turbulence, such result inferred from the increase in broadband pressure with cylinder angle. The near field pressure spectra were also evaluated for cylinder angles of 0 to 360[°], for which the pressure field was shown to exhibit excellent symmetry.

Through design and validation of the near field pressure measurement technique, the objectives of this research have been satisfied. The validation has shown that near field measurements, when performed using a highly sensitive piezoelectric sensor, serve as an effective means of characterizing low speed flow structures contributing to aerodynamic sound.

Chapter 8

Recommendations

With the developed research technique validated for a simple geometry, the technique may now be used to investigate the aerodynamic sound generated by low speed airfoils common to wind turbines. The preferred method of implementation involves the fabrication of numerous 2D airfoils, embedding the developed piezoelectric sensors in the surface of the airfoils in a chordwise arrangement. The technique would enable the aeroacoustic sources to be resolved, leading to the development of more accurate wind turbine noise prediction models or methods of attenuating sources of aerodynamic sound. Prior to performing airfoil experiments, however, a number of improvements could be made to further develop the experimental technique.

The first potential improvement to the experimental technique involves the further development of the piezoelectric sensor, whether to improve the frequency response, dynamic range, or packaging. All of these parameters are largely dependent on the manufacturing processes, details of which should be refined prior to manufacturing the sensors in large quantities. By making improvements to the sensor design, the ability to resolve low pressure or low frequency sources could be greatly improved.

Another potential improvement could be obtained through the use of PIV, as opposed to near field pressure measurements. This technology, which enables the entire flow field to be visualized instantaneously, was established in Section 4 as exhibiting great potential. In addition to enhancing the flexibility of the experimental setup, PIV would serve to address the minor issues of source localization and tunnel noise associated with the near field pressure measurement technique. The primary reason for not pursuing the PIV technique in this research was the high initial costs, however, the costs are low if the required technology is available. The secondary deficiency, involving measurement uncertainty, can be effectively managed through particle considerations and advance data processing methods. Using high speed PIV, with sampling rates exceeding 10[kHz], it would be possible to visualize the origin and evolution of the contributing flow structures. Given that PIV is relatively new to the field of aeroacoustics, this technology could provide a

unique perspective on the sources of aerodynamic sound.

Regardless of whether the near field pressure or near field flow measurement technique is selected for the airfoil experiments, the simple far field measurement could also be improved. While the far field measurements were shown to be effective in resolving the aeroacoustic emissions, the measurements suffered from a poor signal-to-noise ratio. One method of reducing the noise is to increase the number of far field sensors, as discussed in Section 3.3.1. This could be accomplished by using a pair of sensors, performing a cross-correlation to isolate the common acoustic components. The noise could be further reduced, and the source directivity resolved, by implementing a 1D phased microphone array. By resolving the source directivity, the near and far field pressure measurements could then be used to assess the efficiency of the aeroacoustic sources. The use of a 2D phased microphone array would not provide a significant reduction in background noise and would merely serve as a redundant method of locating aeroacoustic sources.

An alternative method of improving the far field measurements involves the development of an anechoic wind tunnel. This would significantly reduce the uncertainty of the far field measurements, but would come at a significant cost.

Although the developed experimental technique was shown to effective, a number of improvements have been suggested to further enhance the technique. These improvements serve to address the limitations of near and far field measurements, enabling airfoil experiments to be performed with greater flexibility and less measurement uncertainty.

References

- [1] E. Achenbach and E. Heinecke. On vortex shedding from smooth and rough cylinders in the range of Reynolds numbers 6×10^3 to 5×10^6 . *Journal of Fluid Mechanics*, 109:239–251, 1981.
- [2] Acoustical Solutions, Inc. *Technical Data Sheet AlphaMax Anechoic Foam Data Sheet*, November 2008. http://www.acousticalsolutions.com/datasheets/data_alphamax.asp.
- [3] Agilent Technologies, Inc. *E363xA Series Programmable DC Power Supplies Data Sheet*, October 2007. <http://www.national.com/ds/LM/LM1875.pdf>.
- [4] All Sensors Corporation. *Miniature Amplified Low Pressure Sensors*, January 2006. http://www.allensors.com/datasheets/commercial_temp/DS-0101_RevA.pdf.
- [5] H Julian Allen and Walter G. Vincenti. Wall interference in a two-dimensional-flow wind tunnel, with consideration of the effect of compressibility. Technical report, National Advisory Committee for Aeronautics, 1944. Report No. 782.
- [6] Chris Andreou, Will Graham, and Ho-Chul Shin. Aeroacoustic study of airfoil leading edge high-lift devices. AIAA Paper 2006-2515, 12th AIAA/CEAS Aeroacoustics Conference, Cambridge, MA, May 8-10, 2006.
- [7] B&C Speakers. *6MDN44 Midrange*, June 2008. <http://www.bcspeakers.com/download/prodotti/PDF/6MDN44.pdf>.
- [8] B&C Speakers. *DE10 HF Drivers*, February 2008. <http://www.bcspeakers.com/download/prodotti/PDF/DE10.pdf>.
- [9] Thomas F. Brooks and T. H. Hodgson. Trailing edge noise prediction from measured surface pressures. *Journal of Sound and Vibration*, 78:69–117, September 1981.
- [10] Thomas F. Brooks and William M. Humphreys, Jr. A deconvolution approach for the mapping of acoustic sources (DAMAS) determined from phased microphone arrays. AIAA Paper 2004-2954, 10th AIAA/CEAS Aeroacoustics Conference, Manchester, UK, May 10-12, 2004.

- [11] Thomas F. Brooks and Michael A. Marcolini. Scaling of airfoil self-noise using measured flow parameters. *AIAA Journal*, 23(2):207–213, February 1985.
- [12] Thomas F. Brooks and Michael A. Marcolini. Airfoil tip vortex formation noise. *AIAA Journal*, 24(2):246–252, February 1986.
- [13] Thomas F. Brooks and Michael A. Marcolini. Airfoil trailing-edge flow measurements. *AIAA Journal*, 24(8):1245–1251, August 1986.
- [14] Thomas F. Brooks, D. Stuart Pope, and Michael A. Marcolini. Airfoil self-noise and prediction. Technical report, National Aeronautics and Space Administration (NASA), July 1989. NASA-RP-1218.
- [15] Brüel & Kjær. *Product Data Falcon Range 1/2" Microphone Preamplifier — Type 2669*, September 1996. <http://www.bksv.com/doc/bp1422.pdf>.
- [16] Brüel & Kjær. *The NEXUS Range of Conditioning Amplifiers — Types 2690, 2691, 2692 and 2693*, February 2002. <http://www.bksv.com/doc/bp1702.pdf>.
- [17] Brüel & Kjær. Brüel & Kjær, November 2008. <http://www.bksv.com/>.
- [18] Brüel & Kjær. *Product Data 1/2" Pressure-field Microphone — Type 4192*, June 2008. <http://www.bksv.com/doc/bp2213.pdf>.
- [19] John A. Ekaterinaris. Upwind scheme for acoustic disturbances generated by low-speed flows. *AIAA Journal*, 35(9):1448–1455, September 1997.
- [20] Endevco Corporation. *Endevco Model 8507C-1,-2,-5,-15 Piezoresistive pressure transducer*, June 2008. <http://www.endevco.com/product/prodpdf/8507C.pdf>.
- [21] F. Farassat. Linear acoustic formulas for calculation of rotating blade noise. *AIAA Journal*, 19(9):1122–1130, September 1981. AIAA 80-0996R.
- [22] Uwe Fey, Michael König, and Helmut Eckelmann. A new Strouhal-Reynolds-number relationship for the circular cylinder in the range $47 < Re < 2 \times 10^5$. *Physics of Fluids*, 10(7):1547–1549, July 1998.
- [23] Jonathan Gershfeld, William K. Blake, and Charles W. Knisely. Trailing edge flows and aerodynamic sound. AIAA Paper 1988-3826, AIAA Thermophysics, Plasmadynamics and Lasers Conference, San Antonio, TX, June 27-29, 1988.
- [24] Ferdinand W. Grosveld. Prediction of broadband noise from horizontal axis wind turbines. *Journal of Propulsion*, 1(4):292–299, August 1985.
- [25] Y. P. Guo, M. C. Joshi, P. H. Bent, and K. J. Yamamoto. Surface pressure fluctuations on aircraft flaps and their correlation with far-field noise. *Journal of Fluid Mechanics*, 415:175–202, 2000.

- [26] Donald B. Hanson. Near-field frequency-domain theory for propeller noise. *AIAA Journal*, 23(4):499–504, April 1985.
- [27] J. C. Hardin and D. S. Pope. An acoustic/viscous splitting technique for computational aeroacoustics. *Theoretical and Computational Fluid Dynamics*, 6(5-6):323–340, October 1994.
- [28] Henkel Corporation. *TDS LOCTITE 3888*, July 2003. <http://tds.loctite.com/tds5/docs/3888-EN.PDF>.
- [29] Henkel Corporation. *TDS LOCTITE Hysol E-120HP*, May 2006. [https://tds.us.henkel.com//NA/UT/HNAUTTDS.nsf/web/8FD3ABAA09A649FE882571870000DB2F/\\$File/HysAE-120hp-EN.pdf](https://tds.us.henkel.com//NA/UT/HNAUTTDS.nsf/web/8FD3ABAA09A649FE882571870000DB2F/$File/HysAE-120hp-EN.pdf).
- [30] Michaela Herr and Werner Dobrzynski. Experimental investigations in low-noise trailing-edge design. *AIAA Journal*, 43(6):1167–1175, June 2005.
- [31] A. Herrig, W. Würz, T. Lutz, and E. Krämer. Trailing-edge noise measurements using a hot-wire based coherent particle velocity method. AIAA Paper 2006-3876, 24th AIAA Applied Aerodynamics Conference, San Francisco, CA, June 5-8, 2006.
- [32] R. C. Hibbeler. *Mechanics of Materials, Fourth Edition*. Prentice Hall, Upper Saddle River, New Jersey, 2000.
- [33] Honeywell International, Inc. *Pressure Sensor XPCL Series Chart*, April 2001. <http://sccatalog.honeywell.com/pdbdownload/images/xpcl.series.chart.1.pdf>.
- [34] W. Clifton Horne, Kevin D. James, Thomas K. Arledge, Paul T. Soderman, Nathan Burnside, and Stephen M. Jaeger. Measurements of 26%-scale 777 airframe noise in the NASA Ames 40- by 80 Foot Wind Tunnel. AIAA Paper 2005-2810, 11th AIAA/CEAS Aeroacoustics Conference, Monterey, CA, May 23-25, 2005.
- [35] Stephen Horowitz, Toshikazu Nishida, Louis Cattafesta, and Mark Sheplak. A micromachined piezoelectric microphone for aeroacoustics applications. In *Solid-State Sensors, Actuators and Microsystems Workshop*. Hilton Head, SC, June 4-8, 2006.
- [36] J. Hougen, O. Martin, and R. Walsh. Dynamics of pneumatic transmission lines. *Journal of Control Engineering*, 10(3):114–117, September 1963.
- [37] M. S. Howe. *Acoustics of fluid-structure interactions*. Cambridge University Press, Cambridge, UK, 1998.
- [38] Chunchieh Huang, Ahmed Naguib, Elias Soupos, and Khalil Najafi. A silicon micromachined microphone for fluid mechanics research. *Journal of Micromechanics and Microengineering*, 12(6):767–774, November 2002.

- [39] William M. Humphreys, Jr., Thomas F. Brooks, William W. Hunter, Jr., and Kristine R. Meadows. Design and use of microphone directional arrays for aeroacoustic measurements. AIAA Paper 98-0471, 36th AIAA Aerospace Sciences Meeting and Exhibit, Reno, NV, January 12-15, 1998.
- [40] William M. Humphreys, Jr., Qamar A. Shams, Sharon S. Graves, Bradley S. Sealey, Scott M. Bartram, and Toby Comeaux. Application of MEMS microphone array technology to airframe noise measurements. AIAA Paper 2005-3004, 11th AIAA/CEAS Aeroacoustics Conference, Monterey, CA, May 23-25, 2005.
- [41] Arlinda Huskey, Harold F Link, and Charles P Butterfield. Wind turbine generator system acoustic noise test report for the AOC 15/50 wind turbine. Technical report, National Renewable Energy Laboratory, July 1999. NREL/EL-500-34021.
- [42] International Organization for Standardization. ISO 266:1997 - acoustics — preferred frequencies, May 2008. http://www.iso.org/iso/iso_catalogue/catalogue_tc/catalogue_detail.htm?csnumber=1350.
- [43] P. Kankainen, E. Brundrett, and J. A. Kaiser. A small wind tunnel significantly improved by a multi-purpose, two-flexible-wall test section. *Journal of Fluids Engineering*, 116:419–423, September 1994.
- [44] Knowles Acoustics. *Knowles Acoustics MB3015ASC-2H Product Specification*, January 2008. http://www.knowles.com/search/prods_pdf/MB3015ASC-2H.pdf.
- [45] Daniel König, Wolfgang Schröder, and Matthias Meinke. Numerical analysis of sound generating mechanisms of a high-lift device. *New Results in Numerical and Experimental Fluid Mechanics VI*, 96:421–429, 2007.
- [46] L. Koop, K. Ehrenfried, and A. Dillmann. Reduction of flap side-edge noise: Passive and active flow control. AIAA Paper 2004-2803, 10th AIAA/CEAS Aeroacoustics Conference, Manchester, UK, May 10-12, 2004.
- [47] Kulite Semiconductor Products, Inc. *Kulite High Intensity Microphones*, June 2004. http://www.kulitesensors.com.cn/pdf_Data_Sheets/Mic.pdf.
- [48] Kulite Semiconductor Products, Inc. *Kulite Cryogenic Ultraminiature IS Pressure Transducer*, January 2008. http://www.kulitesensors.com.cn/pdf_Data_Sheets/CCQ-062.pdf.
- [49] Kulite Semiconductor Products, Inc. *Kulite Ultraminiature Thin Line IS Pressure Transducers*, January 2008. http://www.kulitesensors.com.cn/pdf_Data_Sheets/LQ.LE-062.pdf.
- [50] I. Lee and H. J. Sung. Development of an array of pressure sensors with PVDF film. *Experiments in Fluids*, 26(1-2):27–35, January 1999.

- [51] LEMO. *Compact Multipole Connectors F Series*. http://www.lemo.com/pdfs/catalog/ROW/UK_English/f_series.pdf.
- [52] Wen H. Lin and Roy H. Loh. Numerical solutions to aerodynamic sound generations by viscous flows. AIAA Paper 2005-3062, 11th AIAA/CEAS Aeroacoustics Conference, Monterey, CA, May 23-25, 2005.
- [53] Martin V. Lowson. Applications of aero-acoustics to wind turbine noise prediction and control. AIAA Paper 93-0135, 31st Aerospace Sciences Meeting and Exhibit, Reno, NV, January 11-14, 1993.
- [54] Martin V. Lowson. Theory and experiment for wind turbine noise. AIAA Paper 1994-119, 32nd AIAA Aerospace Sciences Meeting and Exhibit, Reno, NV, January 10-13, 1994.
- [55] Denis A. Lynch, III, William K. Blake, and Thomas J. Mueller. Turbulence correlation length-scale relationships for the prediction of aeroacoustic response. *AIAA Journal*, 43(6):1187–1197, June 2005.
- [56] Adam D. McPhee. Experimental evaluation of particle induced PIV measurement errors associated with large fluid accelerations. Technical report, University of Waterloo, Mechanical Engineering, May 2007.
- [57] Kristine R. Meadows, Thomas F. Brooks, William M. Humphreys, William W. Hunter, and Carl H. Gerhold. Aeroacoustic measurements of a wing-flap configuration. AIAA Paper 1997-1595, 3rd AIAA/CEAS Aeroacoustics Conference, Atlanta, GA, May 12-14, 1997.
- [58] Measurement Specialties. Measurement Specialties—sensors & sensor-based systems, November 2008. <http://www.meas-spec.com/>.
- [59] Measurement Specialties, Inc. *Piezo Film Sensors Technical Manual*, March 2006. http://www.meas-spec.com/downloads/Piezo_Technical_Manual.pdf.
- [60] R. Mehta. The aerodynamic design of blower tunnels with wide-angle diffusers. *Progress in Aerospace Sciences*, 18:59–120, 1984.
- [61] Jeff M. Mendoza, Thomas F. Brooks, and William M. Humphreys. Aeroacoustic measurements of a wing/slat model. AIAA Paper 2002-2604, 8th AIAA/CEAS Aeroacoustics Conference, Breckenridge, CO, June 17-19, 2002.
- [62] P. Migliore, J. van Dam, and A. Huskey. Acoustic tests of small wind turbines. Technical report, National Renewable Energy Laboratory, October 2003. NREL/CP-500-34662.
- [63] Paul Migliore and Stefan Oerlemans. Wind tunnel aeroacoustic tests of six airfoils for use on small wind turbines. Technical report, National Renewable Energy Laboratory, December 2003. NREL/CP-500-35090.

- [64] Patrick J. Moriarty, Gianfranco Guidati, and Paul G. Migliore. Recent improvement of a semi-empirical aeroacoustic prediction code for wind turbines. AIAA Paper 2004-3041, 10th AIAA/CEAS Aeroacoustics Conference, Manchester, UK, May 10-12, 2004.
- [65] Patrick J. Moriarty and Paul G. Migliore. Semi-empirical aeroacoustic noise prediction code for wind turbines. Technical report, National Renewable Energy Laboratory (NREL), December 2003. NREL/TP-500-34478.
- [66] Philip J. Morris, Lyle N. Long, and Kenneth S. Brentner. An aeroacoustic analysis of wind turbines. AIAA Paper 2004-1184, 42nd AIAA Aerospace Sciences Meeting and Exhibit, Reno, NV, January 5-8, 2004.
- [67] Thomas J. Mueller. *Aeroacoustic Measurements*. Springer, Berlin, Germany, 2002.
- [68] National Instruments Corporation. *NI 6143 Specifications*, February 2004. <http://www.ni.com/pdf/manuals/370835a.pdf>.
- [69] National Instruments Corporation. *NI 625x Specifications*, June 2007. <http://www.ni.com/pdf/manuals/371291h.pdf>.
- [70] National Instruments Corporation. NI LabVIEW - the software that powers virtual instrumentation - products and services - National Instruments, November 2008. <http://www.ni.com/labview/>.
- [71] National Semiconductor Corporation. *LM1875 20W Audio Power Amplifier*, July 2002. <http://www.national.com/ds/LM/LM1875.pdf>.
- [72] National Semiconductor Corporation. *LMC6001 Ultra Ultra-Low Input Current Amplifier*, December 2003. <http://www.national.com/ds/LM/LMC6001.pdf>.
- [73] National Semiconductor Corporation. *LMP7701/LMP7702/LMP7704 Precision, CMOS Input, RRIO, Wide Supply Range Amplifiers*, June 2008. <http://www.national.com/ds/LM/LMP7701.pdf>.
- [74] National Semiconductor Corporation. *LMP7715/LMP7716/LMP7716Q Single and Dual Precision, 17 MHz, Low Noise, CMOS Input Amplifiers*, October 2008. <http://www.national.com/ds/LM/LMP7715.pdf>.
- [75] S. Oerlemans and B. Méndez López. Acoustic array measurements on a full scale wind turbine. Technical report, National Aerospace Laboratory NLR, June 2005. NLR-TP-2005-336.
- [76] OMEGA ENGINEERING, Inc. *Thermocouple Wire Duplex Insulated*, April 2007. http://www.omega.com/Temperature/pdf/XC_K_TC_WIRE.pdf.

- [77] Stephen Orlando. LDV flow characterization of the University of Waterloo 0.15 by 0.15[m] closed return wind tunnel. Technical report, University of Waterloo, Mechanical Engineering, September 2008.
- [78] Robert W. Paterson and Roy K. Amiet. Noise and surface pressure response of an airfoil to incident turbulence. *Journal of Aircraft*, 14(8):729–736, August 1977.
- [79] Clayton R. Paul. *Introduction to Electromagnetic Compatibility*. John Wiley & Sons, Inc., New York, NY, 1992.
- [80] Pro-Power. *7-1-C Series Screened Multicore Cable*, May 2005. <http://www.farnell.com/datasheets/64943.pdf>.
- [81] S. Rajagopalan and R. A. Antonia. Flow around a circular cylinder—structure of the near wake shear layer. *Experiments in Fluids*, 38(4):393–402, April 2005.
- [82] Alan Rich. Shielding and guarding. *Analog Dialogue*, 17(1):8–13, 1983.
- [83] Erik M. Salomons. *Computational Atmospheric Acoustics*. Springer, New York, NY, 2002.
- [84] A. Schröder, M. Herr, T. Lauke, and U. Dierksheide. A study on trailing edge noise sources using high-speed particle image velocimetry. *New Results in Numerical and Experimental Fluid Mechanics V*, 92:373–380, 2006.
- [85] Setra Systems, Inc. *Model 267/267MR Pressure Transducer*, September 2003. http://www.setra.com/tra/pro/pdf/267_267m.pdf.
- [86] Wen Zhong Shen and Jens Norkaer Sorensen. Aeroacoustic modeling of turbulent airfoil flows. *AIAA Journal*, 39(6):1057–1064, June 2001.
- [87] P. T. Soderman and S. C. Noble. A four-element end-fire microphone array for acoustic measurements in wind tunnels. Technical report, National Aeronautics and Space Administration (NASA), January 1974. NASA-TM-X-62331.
- [88] Bryan Sperandei. The application of particle image velocimetry in a small scale wind tunnel. Master’s thesis, University of Waterloo, Mechanical Engineering, Waterloo, Ontario, Canada, November 2002.
- [89] The MathWorks, Inc. The MathWorks - MATLAB and Simulink for technical computing, November 2008. <http://www.mathworks.com/>.
- [90] United Sensor Corporation. *Pitot Static Pressure Sensing Probes from United Sensor Corporation*, November 2008. <http://www.unitedsensorcorp.com/pitot.html>.
- [91] Meng Wang. Aerodynamic sound of flow past an airfoil. Technical report, NASA Ames Research Center, December 1995.

- [92] Anthony J. Wheeler and Ahmad R. Ganji. *Introduction to Engineering Experimentation, Second Edition*. Pearson Prentice Hall, Upper Saddle River, New Jersey, 2004.
- [93] Frank M. White. *Fluid Mechanics, Fifth Edition*. McGraw-Hill, New York, NY, 2003.
- [94] John P. Wojno, Thomas J. Mueller, and William K. Blake. Turbulence ingestion noise, part 1: Experimental characterization of grid-generated turbulence. *AIAA Journal*, 40(1):16–25, January 2002.
- [95] John P. Wojno, Thomas J. Mueller, and William K. Blake. Turbulence ingestion noise, part 2: Rotor aeroacoustic response to grid-generated turbulence. *AIAA Journal*, 40(1):26–32, January 2002.
- [96] Nobuhiro Yamazaki, Kiyoshi Nagakura, Mitsuru Ikeda, and Akio Sagawa. Methods to measure acoustic sources in a closed wind tunnel test section. AIAA Paper 2005-3003, 11th AIAA/CEAS Aeroacoustics Conference, Monterey, CA, May 23-25, 2005.
- [97] Zeus Industrial Products, Inc. PTFE,FEP,PFA,ETFE extruded tubing - AWG sizes, November 2008. http://www.zeusinc.com/awg_sizes.asp.

Appendix A

Sensor Calibration: LabVIEW Software

Calibration | Extended | Source Signal | Calibrated Signal | Uncalibrated Signal

Manual Test

Enables manual operation of settings. Start

Frequency (Hz)
 Amplitude (V)
 Reference Calibrated Signal

Sensor Information

Unique Identifier
 Calibration Notes
 Default Calibration

Frequency Response Test

Frequency test should be performed at 94dB (1Pa) or 114dB (10Pa). Frequency steps are as recommended by ISO 266; Ref 1000Hz. Start

Frequency Start (Hz)
 Frequency End (Hz)
 Steps per Octave

A log-log plot showing Response (1000Hz, dB SPL) on the y-axis (ranging from -20 to 20) and Frequency (Hz) on the x-axis (ranging from 10 to 10000). The plot area is currently empty.

Convergence

Convergence Level (%)
 Required Samples

Sensitivity Test

Amplitude test should be performed at 250, 251.2 or 1000Hz. Start

Amplitude Start (dB)
 Amplitude End (dB)
 Steps per dB

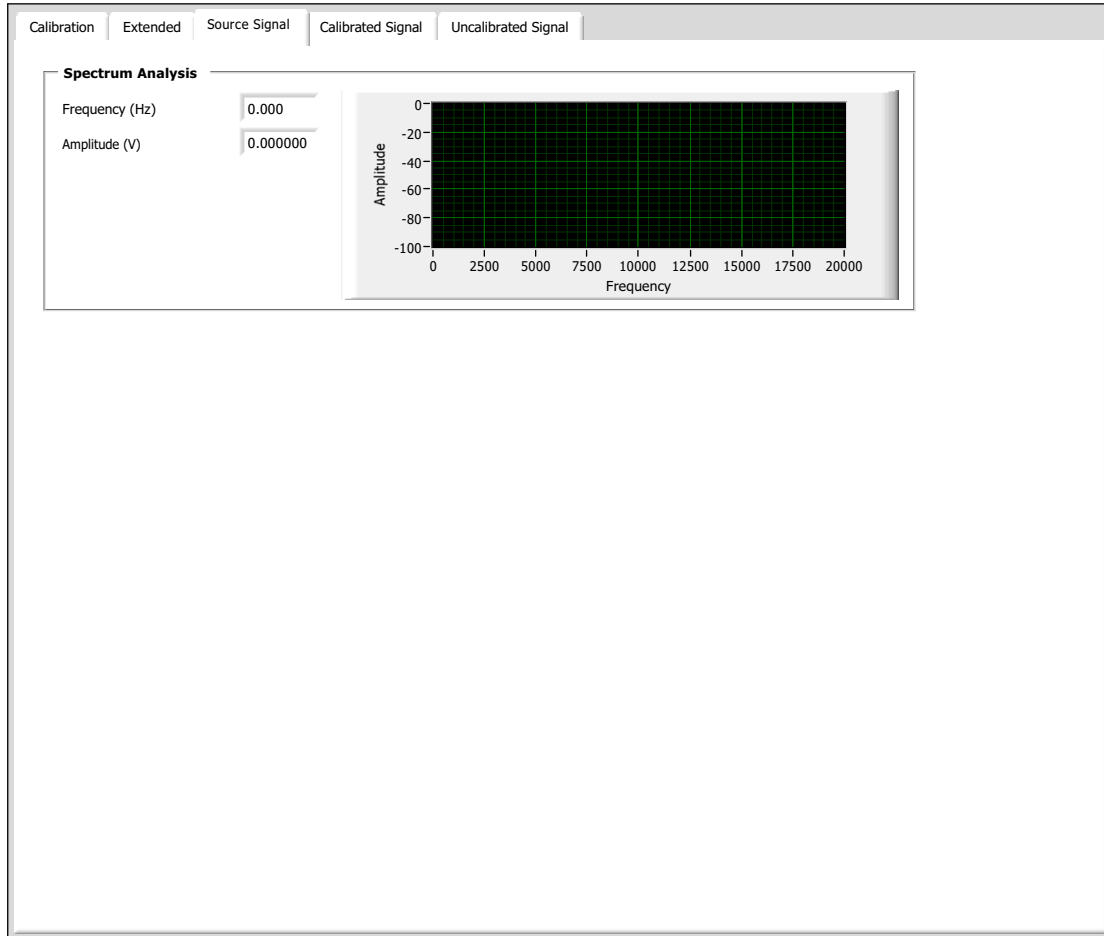
A linear plot showing Sensitivity (94 dB SPL, dB) on the y-axis (ranging from -10 to 4) and Sound Pressure (dB SPL) on the x-axis (ranging from 40 to 160). The plot area is currently empty.

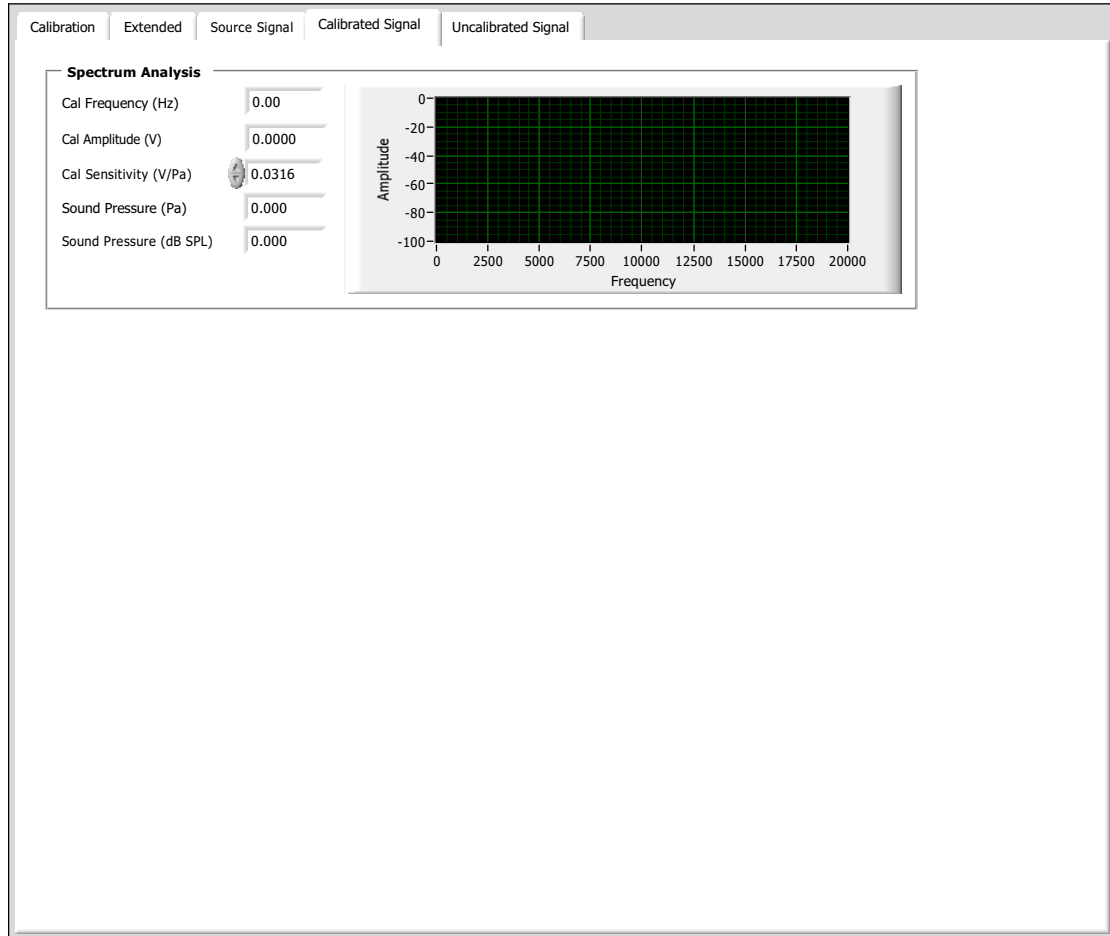
Status

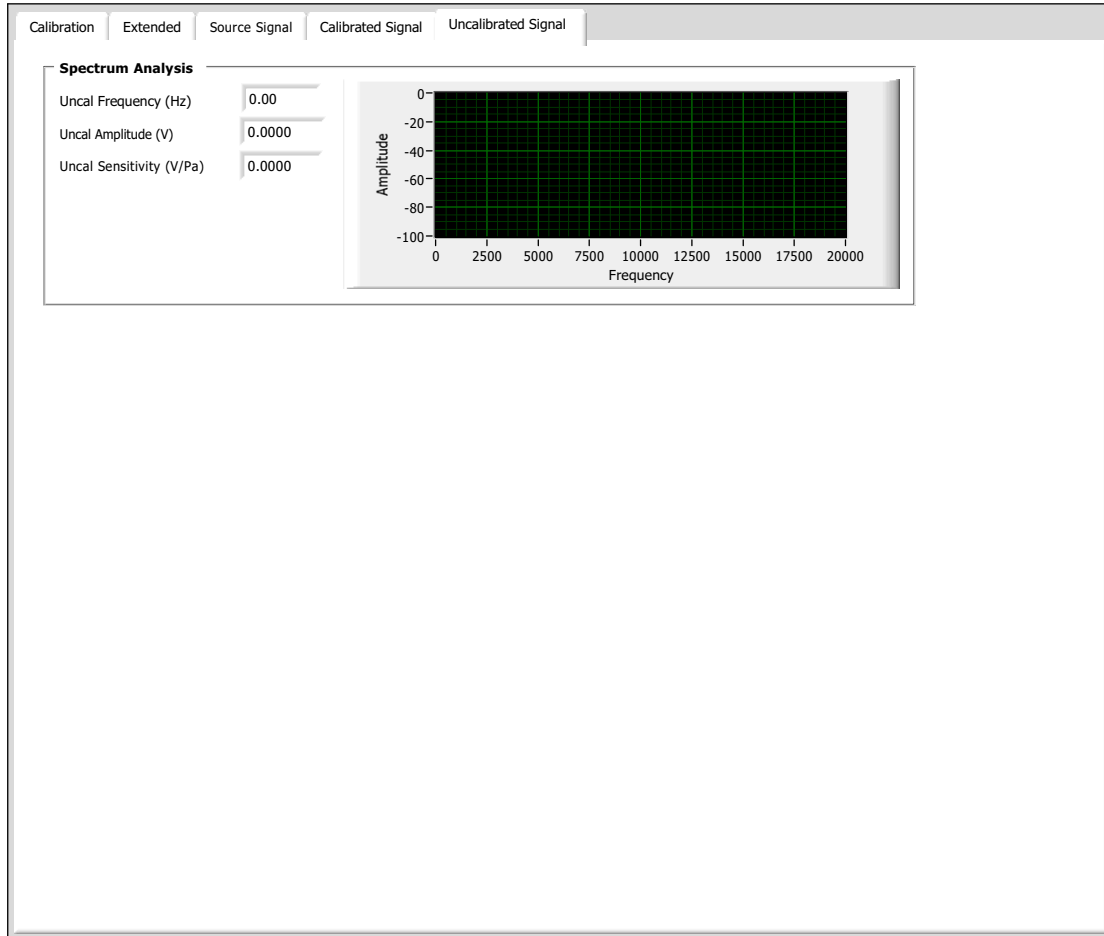
Frequency (Calibrated, Hz)
 Amplitude (Calibrated, V)
 Sensitivity (Uncalibrated Mean, V/Pa)

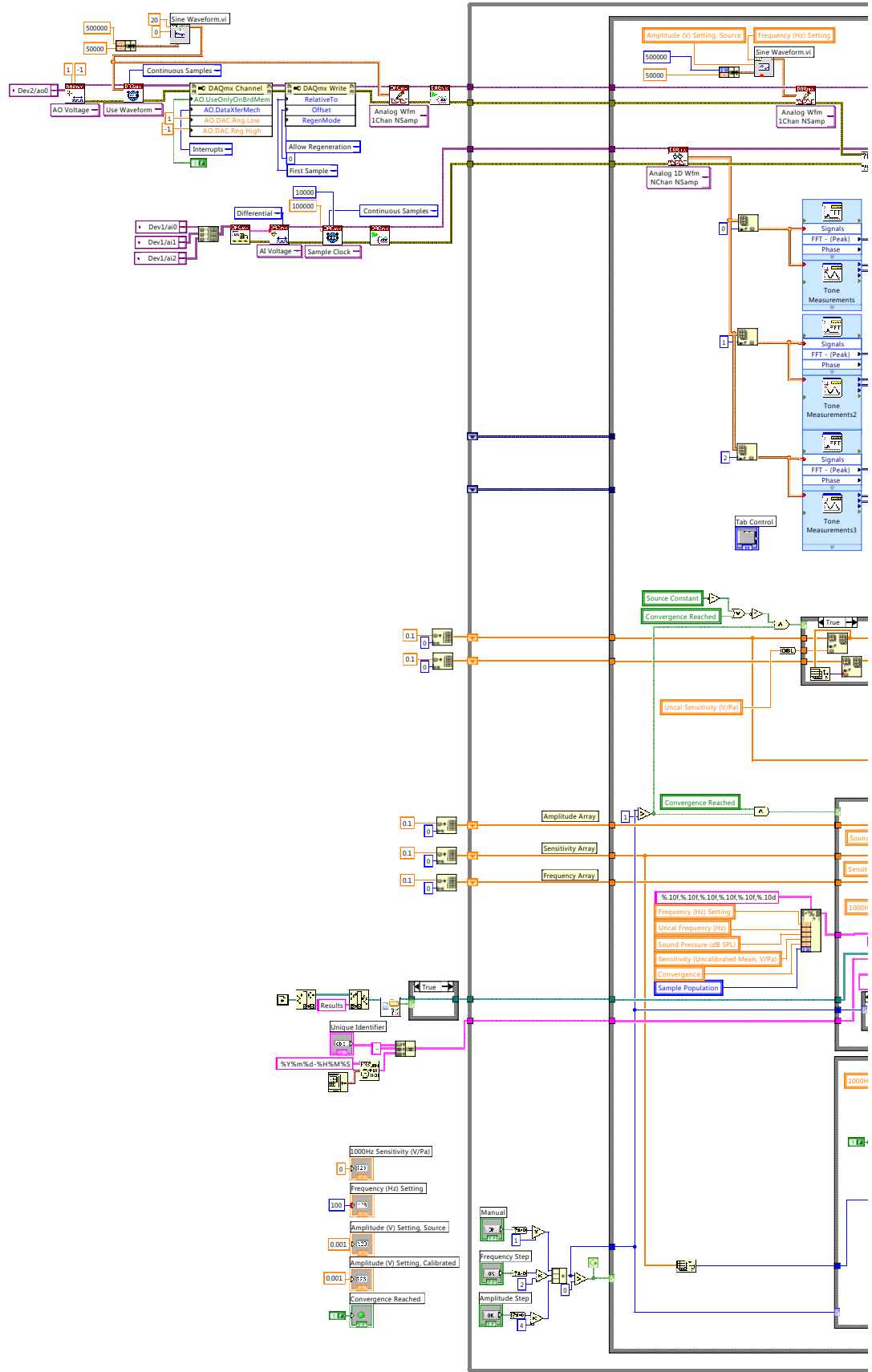
A linear plot showing Sensitivity (V/Pa) on the y-axis (ranging from 0.0000 to 0.1000) and Sample (N) on the x-axis (ranging from 0 to 20). The plot area is currently empty.

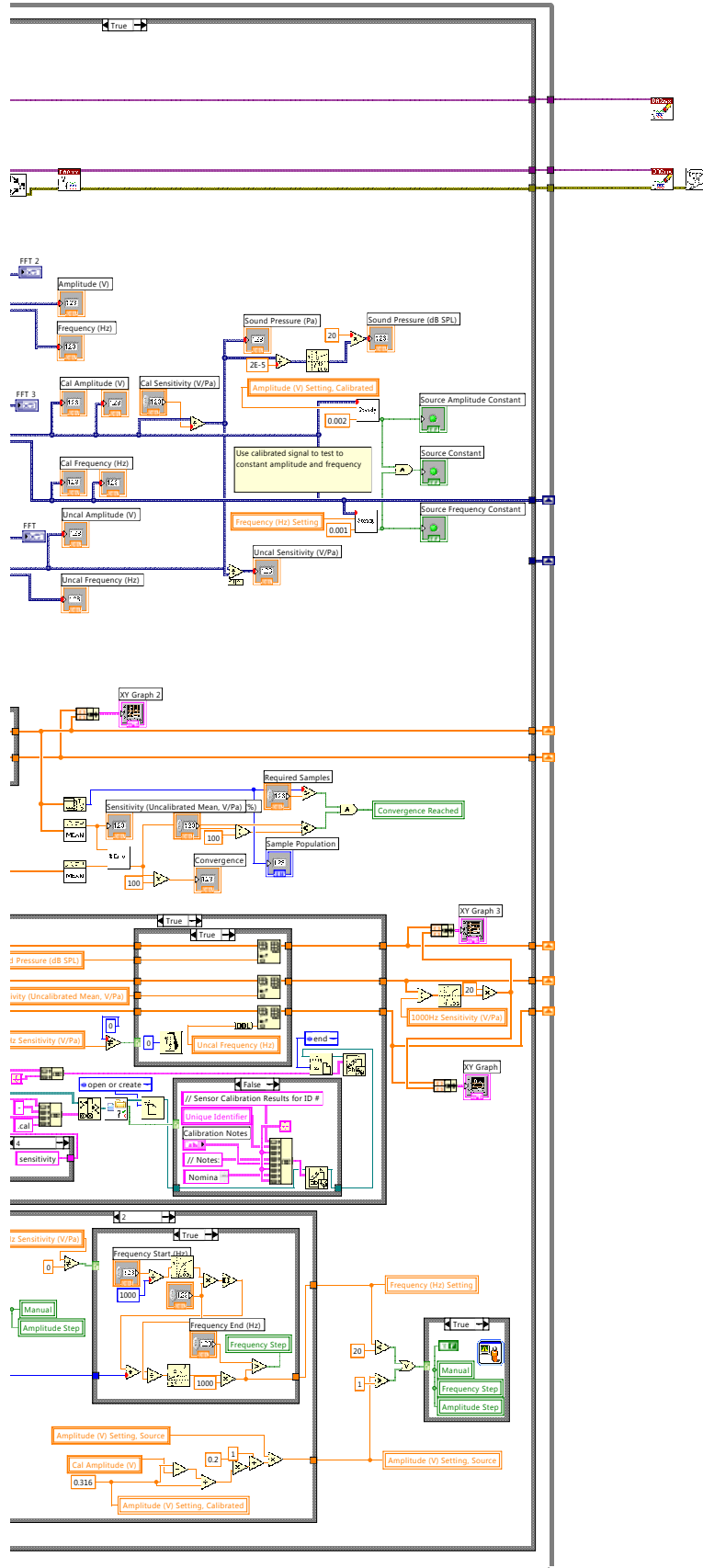
Calibration	Extended	Source Signal	Calibrated Signal	Uncalibrated Signal
Current Settings				
Frequency (Hz) Setting		100		
Amplitude (V) Setting, Source		0.001		
Amplitude (V) Setting, Calibrated		0.001		
Source Constant		<input type="checkbox"/>		
1000Hz Sensitivity (V/Pa)		0		
Convergence		0		
Sample Population		0		

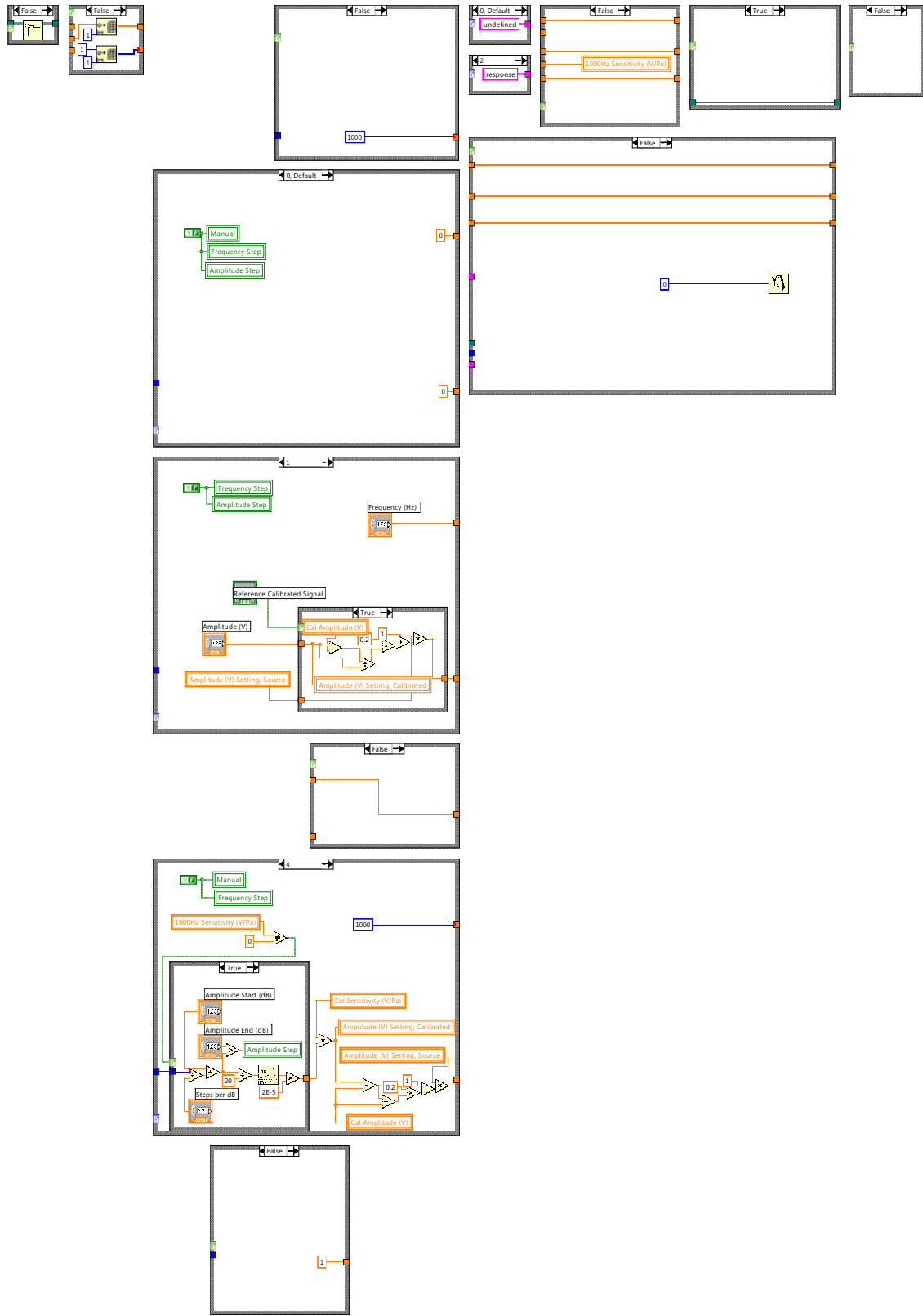


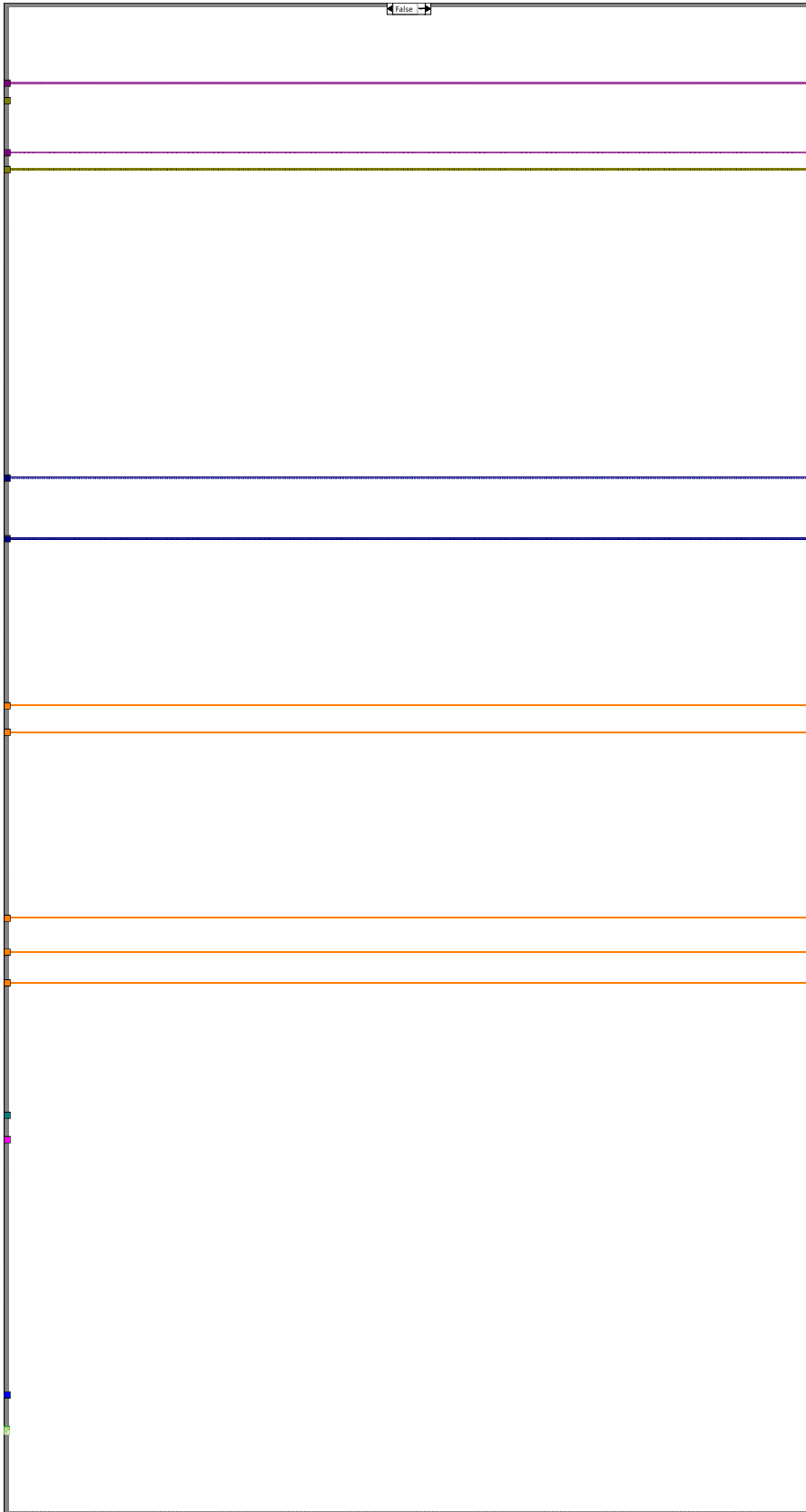






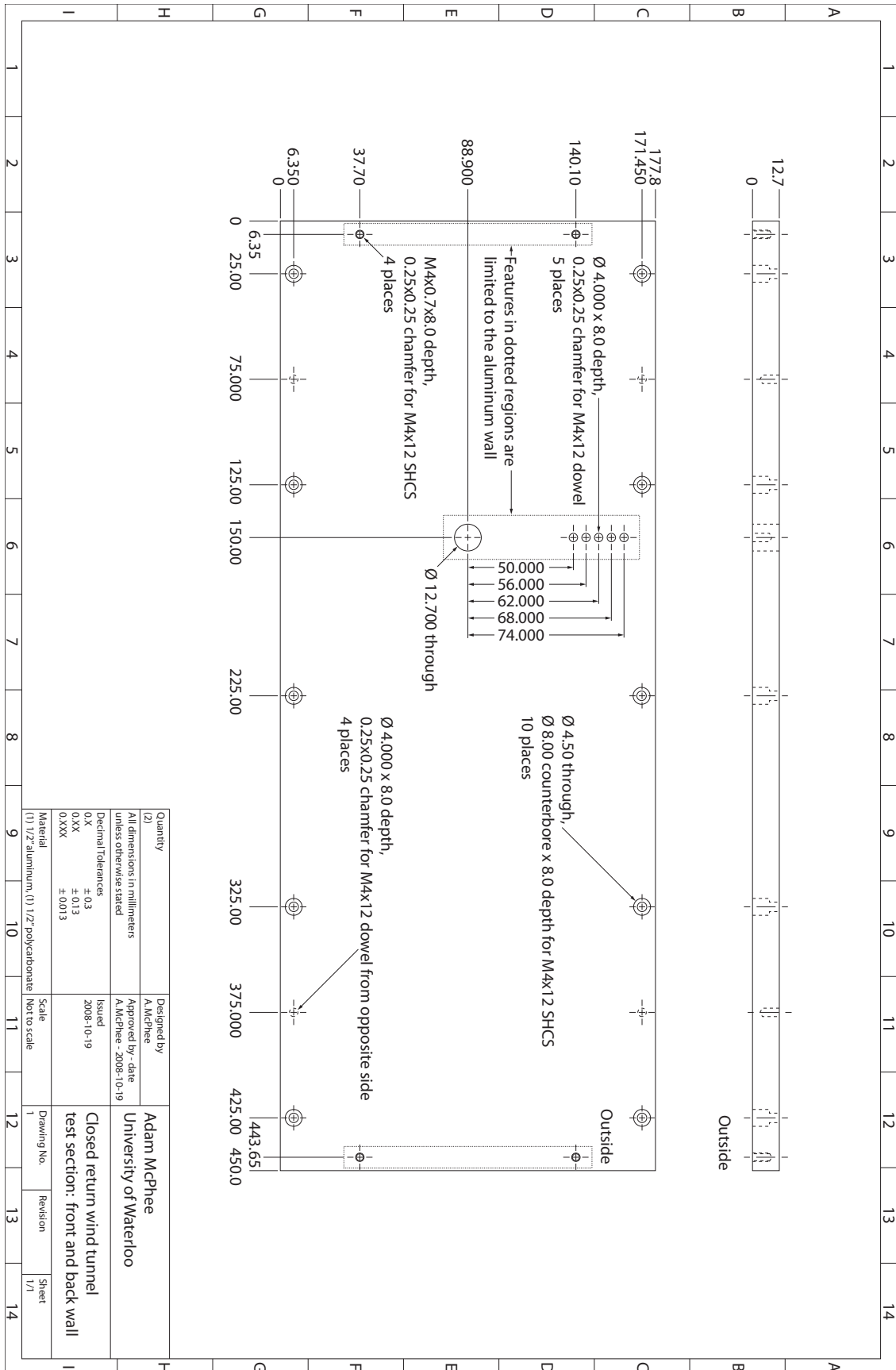


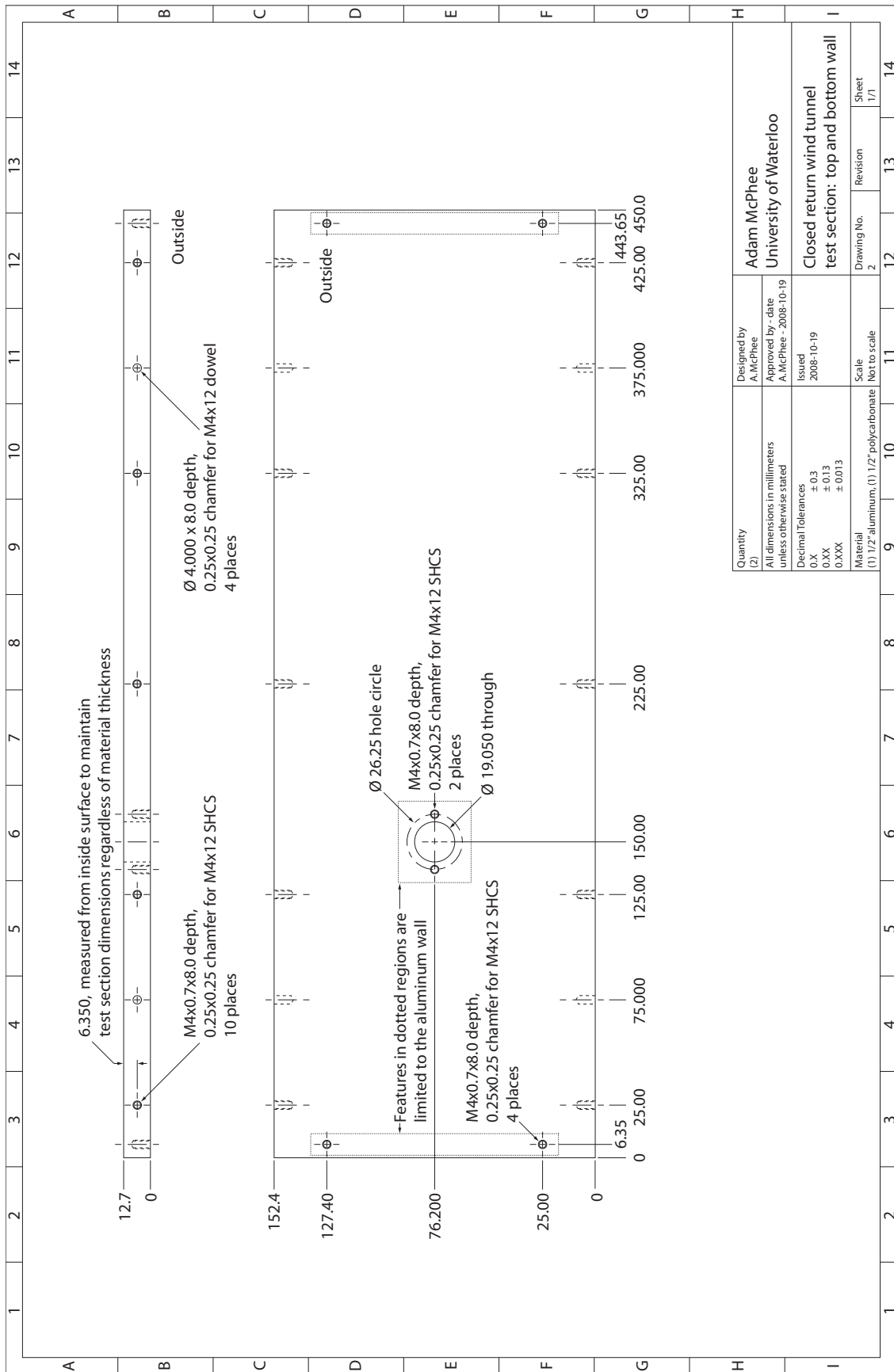




Appendix B

Wind Tunnel Test Section: Manufacturing Drawings





Quantity (2)	Designed by A. McPhee	Adam McPhee University of Waterloo
All dimensions in millimeters unless otherwise stated	Approved by - date A. McPhee - 2008-10-19	
Decimal Tolerances: 0.X 0.XX 0.XXX	Issued 2008-10-19	Closed return wind tunnel test section: top and bottom wall
Material (1) 1/2" aluminum, (1) 1/2" polycarbonate	Scale Not to scale	Revision 2
		Sheet 1/1

Appendix C

Validation Experiments: LabVIEW Software

Experiment

These parameters define the current experiment being performed. The unique identifier should remain constant for a given specimen. These parameters form the file name (id_speed_angle.out) and are also commented within the individual data files.

Unique Identifier: 0001 Tunnel Speed (Hz): 0

Velocity (m/s): 20 Specimen Angle (Deg): 0

Comments: _____

Start Time: 10:27:44 PM

Operation Mode:

Velocity Calibration

Noise Floor Measurement

Cylinder Measurement

Sampling

These parameters define the sampling rate and with the required FFT averages and resolution, determine the duration of the experiment.

Sampling Rate (Hz): 24500

Frequency Resolution (Hz): 0.25

Sampling Blocks (Averages): 25

Number of Averages: 0

Number of Samples per FFT: 0

Number of Samples: 0

Atmospheric Temperature (C): 21

Atmospheric Pressure (Pa): 101325

Sensor Specifications

Sensitivities are merely used for presentation purposes, as the results are exported as voltages and requiring post-processing.

B&K Sensitivity (V/Pa): 0.0316

Piezo Sensitivity (V/Pa): 0.003

Pitot, 125(Pa) Sens (V/Pa): 0.0316

Pitot, 250(Pa) Sens (V/Pa): 0.0316

Pitot, 1000(Pa) Sens (V/Pa): 0.0316

Trans. Offset (125Pa): 0.000

Trans. Offset (250Pa): 0.000

Trans. Offset (1000Pa): 0.000

Status

The status of the measurements for the current experiment.

Temperature: 0.00

Velocity (125Pa): 0.000

Velocity (250Pa): 0.000

Velocity (1000Pa): 0.000

Velocity RMS (125Pa): 0.000

Velocity RMS (250Pa): 0.000

Velocity RMS (1000Pa): 0.000

Measurements

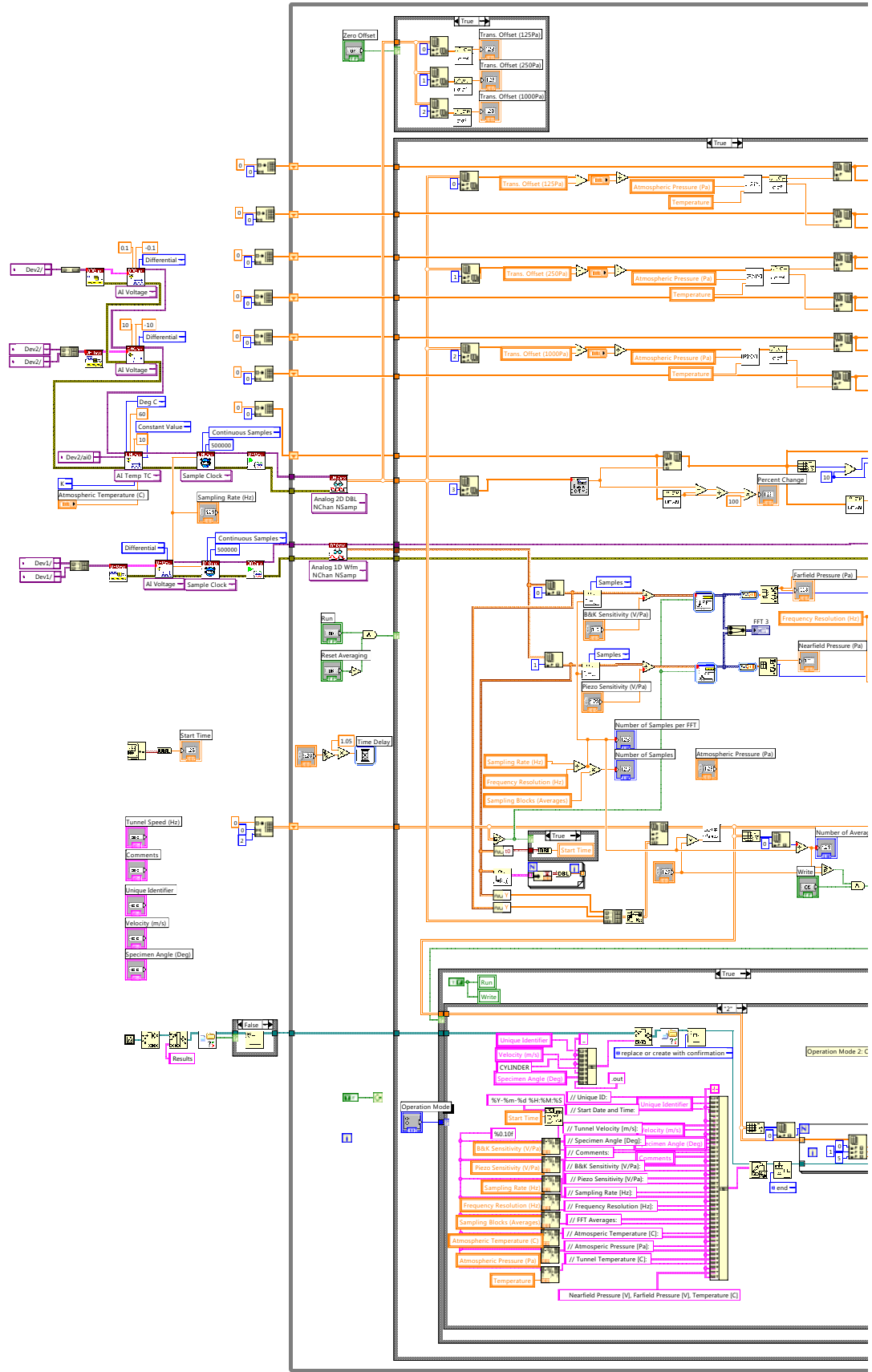
Nearfield Frequency (Hz): 0.00

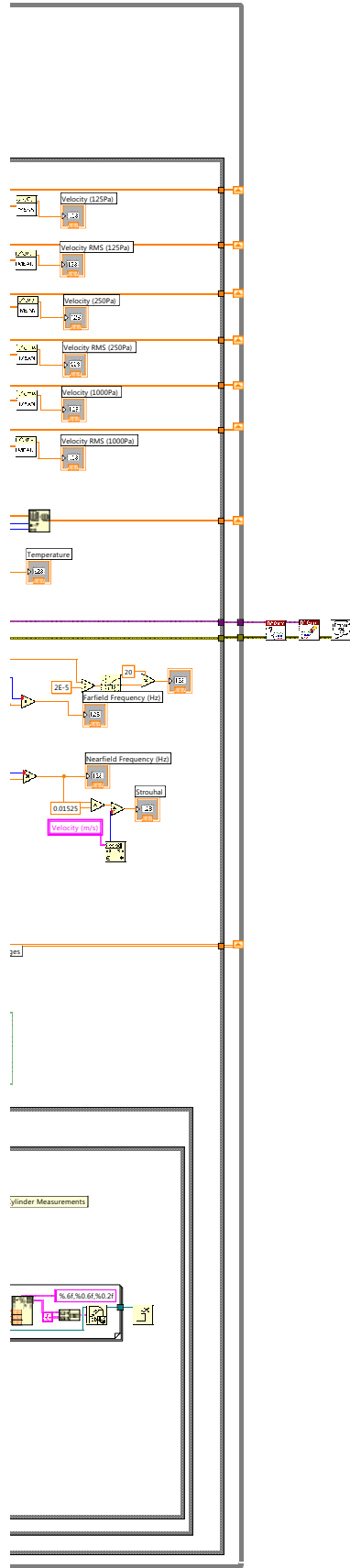
Nearfield Pressure (Pa): 0.0000

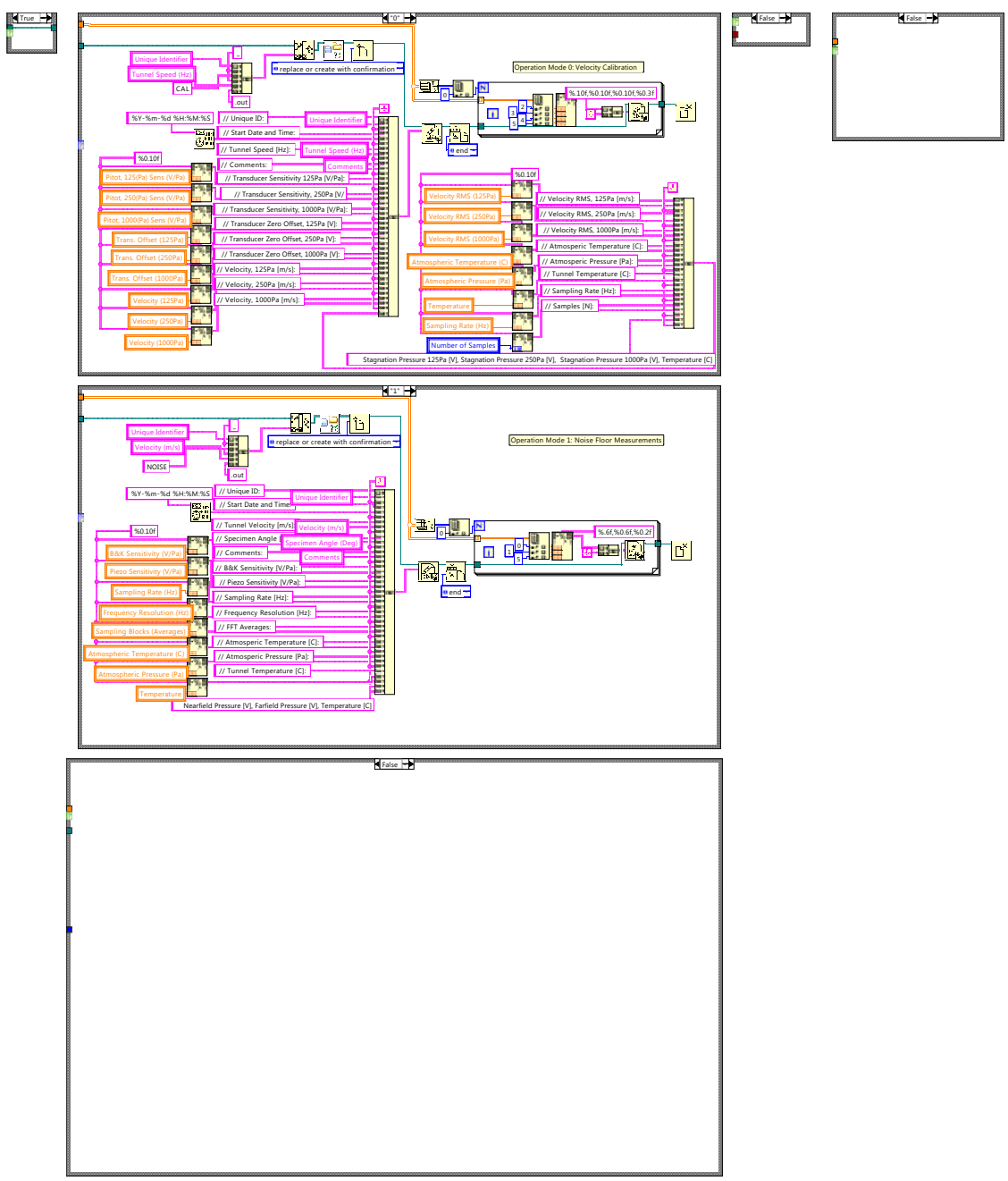
Strouhal: 0

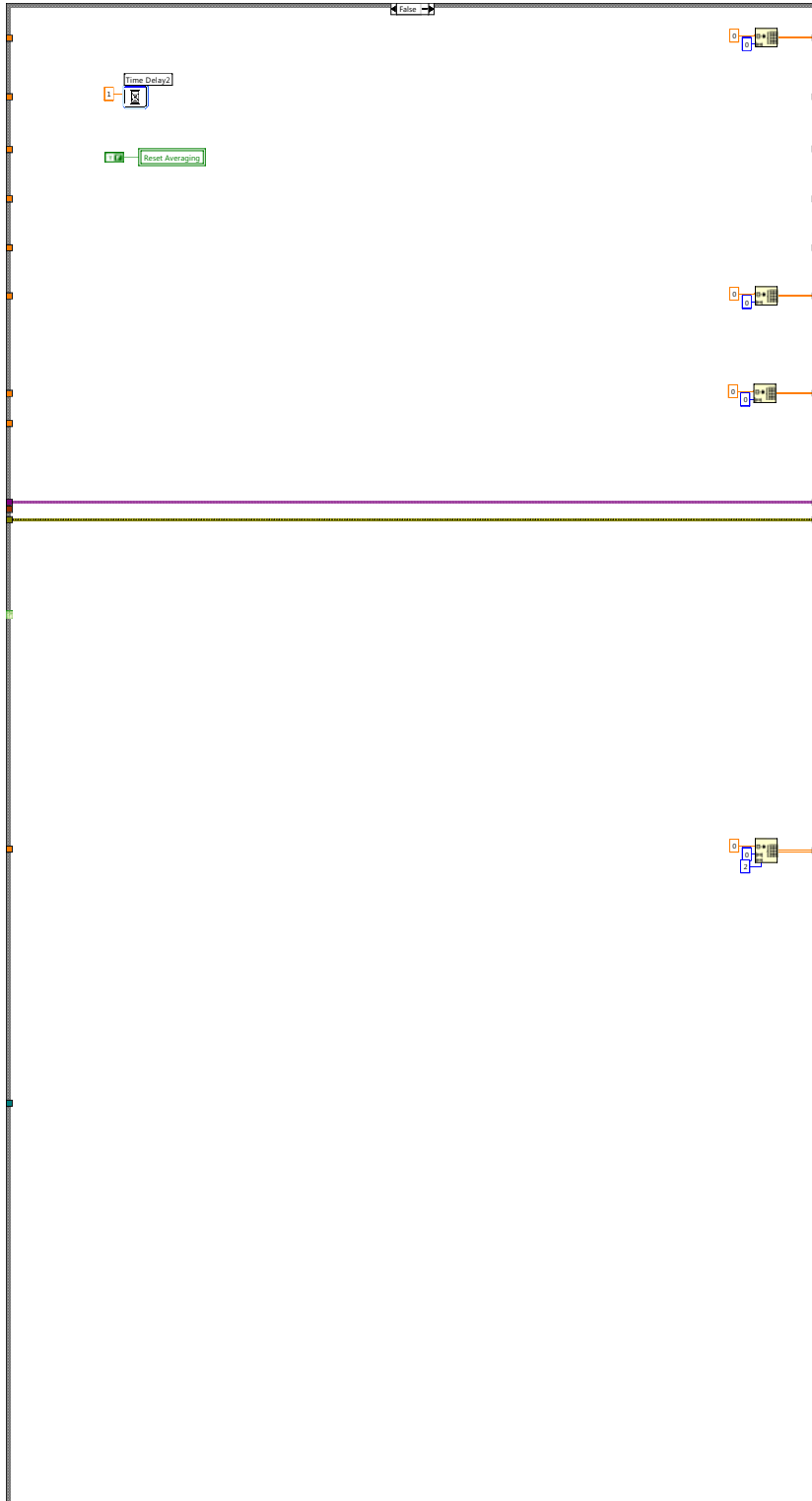
Farfield Frequency (Hz): 0.00

Farfield Pressure (Pa): 0.0000









Appendix D

Validation Experiments: MATLAB Software

17/10/08 7:36 PM Z:\My Research\Mechanical Engineering - Graduate\Research\Cylinder...\Main.m 1 of 5

```

%%
%% Author: Adam McPhee, University of Waterloo
%% File: Main.m
%% Last Updated: October 17, 2008
%%
%% Description: Main application for processing time resolved near and far
%% field pressure measurements over a range of angles and velocities.
%% The processed results are output as frequency spectra.
%%
%%

clear all
clc

addpath('..\Results');
addpath('..\Data');

flag = 1;
setappdata(gcf, 'run', flag);
set(gcf, 'name', 'Data Analysis');
set(gcf, 'Position', [100 100 800 600]);
h = uicontrol('style', 'pushbutton', 'String', 'Cancel', 'callback', 'setappdata(gcf, 'run', 0)');
tinit = cputime;

textField = uicontrol('Style','edit','Min',0,'Max',2,'Position',[20 400 760 180],'String', '
{''}, 'BackgroundColor',[1,1,1], 'HorizontalAlignment', 'Left', 'FontSize', 8);
UpdateStatus(textField, 'Initiating analysis.', 0);

% Modes of operation
% 1) Fixed velocities, range of cylinder angles at spec. increment (Angle
% vs freq vs amplitude)
% 2) Range of velocities of a specific angle (St vs Re)
% 3) Symmetry test, Mean velocity, range of cylinder angles at spec
% increment (for symmetry)

piezoSens = Sensitivity('0001-20080425-142406-response-rev.cal', textField);
piezoSens = Sensitivity('0001-20080415-205829-response.cal', textField);
refSens = Sensitivity('0001-reference-mic-corr.cal', textField);

mode = 2;%2,3;
uniqueID = '0001';

% Define velocity start, end, increment
% Define angular start, end, increment

switch mode
case 1
    vel_start = 20;
    vel_end = vel_start;
    vel_inc = 1;
    ang_start = 0;
    ang_end = 180;
    ang_inc = 5;
    exp_desc = ['Angular (spatial) analysis for ', num2str(vel_start), '[m/s] over ', num2str(
(ang_start), '-', num2str(ang_end), ' degrees in ', num2str(ang_inc), ' degree increments.'];
    file_out = ['./Results/', uniqueID, '_SPATIAL_', num2str(vel_start)];
case 2
    vel_start = 5;
    vel_end = 20;

```

17/10/08 7:36 PM Z:\My Research\Mechanical Engineering - Graduate\Research\Cylinder...\Main.m 2 of 5

```

        vel_inc = 1;
        ang_start = 135;
        ang_end = ang_start;
        ang_inc = 5;
        exp_desc = ['Strouhal analysis for ',num2str(ang_start), ' degrees over ',num2str(
(vel_start), '- ',num2str(vel_end), '[m/s] in ',num2str(vel_inc), '[m/s] increments.'];
        file_out = ['./Results/',uniqueID,'_VELOCITY_',num2str(ang_start)];
    case 3
        vel_start = 15;
        vel_end = vel_start;
        vel_inc = 1;
        ang_start = 0;
        ang_end = 360;
        ang_inc = 5;
        exp_desc = ['Angular (spatial) symmetry analysis for ',num2str(vel_start), '[m/s] over ',
num2str(ang_start), '- ',num2str(ang_end), ' degrees in ',num2str(ang_inc), ' degree increments.'];
        file_out = ['./Results/',uniqueID,'_SPATIAL_',num2str(vel_start)];
    end

    vel_range = linspace(vel_start,vel_end,(vel_end-vel_start)/vel_inc+1);
    ang_range = linspace(ang_start,ang_end,(ang_end-ang_start)/ang_inc+1);
    iterations = size(vel_range,2)*size(ang_range,2);

    UpdateStatus(textField,['Performing type ',num2str(mode), ': ',exp_desc],1);
    UpdateStatus(textField,['Number of file iterations: ',num2str(iterations)],1);

    fileNames={' '};
    fidAvg = fopen([file_out,'_1_AVGFFT.dat'],'w');
    fidNoise = fopen([file_out,'_2_NOISE.dat'],'w');
    fidPressure = fopen([file_out,'_3_PRESSURE.dat'],'w');
    fidSummary = fopen([file_out,'_4_SUMMARY.dat'],'w');
    fidLog = fopen([file_out,'.log'],'w');

    % Reduction used to reduce the freq resolution / number of data points
    reduction = 1;

    for vel_count=1:size(vel_range,2)

        UpdateStatus(textField, '-----',1);
        UpdateStatus(textField,['Loading noise floor data for ',num2str(vel_range(vel_count)), '[m/s]'],1);
        UpdateStatus(textField,['Validating file existence ',uniqueID,'_NOISE_',num2str(vel_range(
(vel_count)), '.out'],1);
        if exist([uniqueID,'_NOISE_',num2str(vel_range(vel_count)), '.out'],'file')
            UpdateStatus(textField, [uniqueID,'_NOISE_',num2str(vel_range(vel_count)), '.out found.'],1);
            [f_noise,Y1_noise,Y2_noise,T,P,Re] = AverageFFT([uniqueID,'_NOISE_',num2str(vel_range(
(vel_count)), '.out'],textField,reduction);
            if size(Y1_noise,1)==0
                flag=0;
                break;
            end
            Y1_noise = Y1_noise./interp1(piezoSens(:,1),piezoSens(:,2),f_noise,'linear');
            Y2_noise = Y2_noise./interp1(refSens(:,1),refSens(:,2),f_noise,'linear');

            % Adjust for pressure doubling for the acoustic measurements by dividing far field result by
two
            Y2_noise = Y2_noise./2;

        else

```

17/10/08 7:36 PM Z:\My Research\Mechanical Engineering - Graduate\Research\Cylinder...\Main.m 3 of 5

```

UpdateStatus(textField, [uniqueID, '_NOISE_', num2str(vel_range(vel_count)), '.out not found.'], 1);
1);
    flag = 0;
    break;
end

for ang_count=1:size(ang_range,2)
    fileCount = (vel_count-1)*size(ang_range,2)+ang_count;
    fileNames((vel_count-1)*size(ang_range,2)+ang_count) = {[uniqueID, '_CYLINDER_', num2str(
(vel_range(vel_count)), '_', num2str(ang_range(ang_count)), '.out' ]};
    UpdateStatus(textField, '-----', 1);
    UpdateStatus(textField, ['Validating file existence ', fileNames{fileCount}], 1);
    if exist(fileNames{(vel_count-1)*size(ang_range,2)+ang_count}, 'file')
        UpdateStatus(textField, [fileNames{(vel_count-1)*size(ang_range,2)+ang_count}, ' found.'], 1);
1);

    [f, Y1, Y2, T, P, Re] = AverageFFT(fileNames{fileCount}, textField, reduction);
    if size(Y1,1)==0
        flag=0;
        break;
    end

    if (vel_count-1)*size(ang_range,2)+ang_count==1
        % Init file output
        fprintf(fidAvg, '%s\n', 'VARIABLES = "Frequency [Hz]", "Free-Stream Velocity Corr
[m/s]", "Angle [°]", "Nearfield [Pa]", "Nearfield [dB]", "Farfield [Pa]", "Farfield [dB]");
        fprintf(fidAvg, '%s\n', ['ZONE I=', num2str(size(Y1,1)), ', J=', num2str(iterations), ',
F=POINT' ]]);
        fprintf(fidNoise, '%s\n', 'VARIABLES = "Frequency [Hz]", "Free-Stream Velocity Corr
[m/s]", "Angle [°]", "Nearfield [Pa]", "Nearfield [dB]", "Farfield [Pa]", "Farfield [dB]");
        fprintf(fidNoise, '%s\n', ['ZONE I=', num2str(size(Y1,1)), ', J=', num2str(iterations), ',
F=POINT' ]]);
        fprintf(fidPressure, '%s\n', 'VARIABLES = "Frequency [Hz]", "Free-Stream Velocity Corr
[m/s]", "Angle [°]", "Nearfield [Pa]", "Nearfield [dB]", "Farfield [Pa]", "Farfield [dB]");
        fprintf(fidPressure, '%s\n', ['ZONE I=', num2str(size(Y1,1)), ', J=', num2str(iterations), ',
F=POINT' ]]);
        fprintf(fidSummary, '%s\n', 'VARIABLES = "Free-Stream Velocity Corr [m/s]", "Angle [°]",
"Temperature [°C]", "Atmospheric Pressure [Pa]", "Re [1]", "Peak Pressure (Nearfield) [Pa]", "Peak
Pressure (Nearfield) [dB]", "Signal-to-Noise (Nearfield) [dB]", "Peak Frequency (Nearfield) [Hz]",
"Peak Strouhal (Nearfield) [1]", "Peak Pressure (Farfield) [Pa]", "Peak Pressure (Farfield) [dB]",
"Signal-to-Noise (Farfield) [dB]", "Peak Frequency (Farfield) [Hz]", "Peak Strouhal (Farfield) [1]");
        fprintf(fidSummary, '%s\n', ['ZONE I=', num2str(iterations), ', F=POINT' ]]);
    end

    ang(size(Y1,1)) = ang_range(ang_count);
    ang(1,:) = ang_range(ang_count);

    vel(size(Y1,1)) = vel_range(vel_count);
    vel(1,:) = vel_range(vel_count);

    % Apply velocity correction to account for tunnel blockage

    Cd = 0.82;
    d = 0.01524;
    h = 0.1524;

    vel = (1+0.25*Cd*(d/h)+0.82*(d/h)^2)*vel;
    Re = (1+0.25*Cd*(d/h)+0.82*(d/h)^2)*Re;

```

17/10/08 7:36 PM Z:\My Research\Mechanical Engineering - Graduate\Research\Cylinder...\Main.m 4 of 5

```

% Use sensor sensitivity to determined pressures

Y1 = Y1./interp1(piezoSens(:,1),piezoSens(:,2),f,'linear');
Y2 = Y2./interp1(refSens(:,1),refSens(:,2),f,'linear');

% Adjust for pressure doubling by dividing far field result by
% two

Y2 = Y2./2;

% Y1 = nearfield, Y2 = farfield

fprintf(fidAvg, '%-6.2f %-3.2f %-3.1f %-4.3f %-4.3f %-3.2f %-3.2f\n', [f.'; vel; ang; Y1.';
Decibel(Y1.'); Y2.'; Decibel(Y2.')]);
fprintf(fidNoise, '%-6.2f %-3.2f %-3.1f %-4.8f %-4.8f %-3.2f %-3.2f\n', [f.'; vel; ang;
Y1_noise.'; Decibel(Y1_noise.'); Y2_noise.'; Decibel(Y2_noise.')]);

UpdateStatus(textField, ['Noise subtraction... 0%'],1);
Y1 = Y1 - Y1_noise;
Y2 = Y2 - Y2_noise;
UpdateStatus(textField, ['Noise subtraction... 100%'],0);

%Y1db = 20*log10(Y1./(20*10^-6));
%Y2db = 20*log10(Y2./(20*10^-6));

fprintf(fidPressure, '%-6.2f %-3.2f %-3.1f %-4.3f %-4.3f %-3.2f %-3.2f\n', [f.'; vel; ang;
Y1.'; Decibel(Y1.'); Y2.'; Decibel(Y2.')]);

% Eliminate the DC component of the spectrum prior to
% performing peak detection

Y1(1:10)=0;
Y2(1:10)=0;

[VAL1, IND1] = max(Y1);
S1 = Strouhal(f(IND1),d,vel(1));
N1 = Y1_noise(IND1);
UpdateStatus(textField, ['Peak pressure (nearfield): ', num2str(VAL1)],1);
UpdateStatus(textField, ['Peak frequency (nearfield): ', num2str(f(IND1))],1);
UpdateStatus(textField, ['Peak strouhal number (nearfield): ', num2str(S1)],1);

[VAL2, IND2] = max(Y2);
S2 = Strouhal(f(IND2),d,vel(1));
N2 = Y2_noise(IND2);
UpdateStatus(textField, ['Peak pressure (farfield): ', num2str(VAL2)],1);
UpdateStatus(textField, ['Peak frequency (farfield): ', num2str(f(IND2))],1);
UpdateStatus(textField, ['Peak strouhal number (farfield): ', num2str(S2)],1);

fprintf(fidSummary, '%-3.2f %-3.1f %-3.1f %-6.0f %-6.0f %-4.3f %-3.2f %-3.2f %-6.2f %-3.4f
%-4.3f %-3.2f %-3.2f %-6.2f %-3.4f\n', [vel(1); ang_range(ang_count); T; P; Re; VAL1; Decibel(VAL1);
Decibel(VAL1)-Decibel(N1); f(IND1); S1; VAL2; Decibel(VAL2); Decibel(VAL2)-Decibel(N2); f(IND2); S2]);

UpdateStatus(textField, ['Completed processing ', fileNames{fileCount}],1);
else
UpdateStatus(textField, [fileNames{(vel_count-1)*size(ang_range,2)+ang_count}, ' not
found.'],1);
flag = 0;

```

17/10/08 7:36 PM Z:\My Research\Mechanical Engineering - Graduate\Research\Cylinder...\Main.m 5 of 5

```
        break;
    end
    pause(0.1);
end
end

fclose(fidAvg);
fclose(fidNoise);
fclose(fidPressure);
fclose(fidSummary);

%progress = waitbar(0,'Initiating analysis for specimen at 10[m/s] and 0
[deg].','CreateCancelBtn','analyze_close');
%%% hamming windowing details
%%% http://www.dsprelated.com/showmessage/52448/1.php
%UpdateStatus(textField,'Loading calibration file for 10m/s',1);
pause(1);

if flag
    UpdateStatus(textField, ['-----'],1);
    UpdateStatus(textField, ['Analysis completed. Required CPU time: ',num2str(cputime-tinit), 's'],
1);
else
    UpdateStatus(textField, ['Analysis terminated.'],1);
end

statusOutput = get(textField,'string');
for stringIndex=1:size(statusOutput,1)
    fprintf(fidLog,'%s\n',statusOutput{stringIndex});
end
fclose(fidLog);
```

17/10/08 7:36 PM Z:\My Research\Mechanical Engineering - Graduate\Research\Cy...\AverageFFT.m 1 of 3

```

%%
%% Author: Adam McPhee, University of Waterloo
%% File: AverageFFT.m (function)
%% Last Updated: October 17, 2008
%%
%% Description: Function loads time resolved data contained within the
%% specified data file and performs an FFT average. A reduction may be
%% specified to reduce the frequency resolution of the resulting spectra.
%%

function [XFFT,Y1FFT,Y2FFT,T,P,Re] = AverageFFT3(fileName,textField,reduction)

updateStatus(textField,['Loading data file ',fileName],1);
fid = fopen(fileName);

updateStatus(textField,'> Parsing header... 0%',1);
headerDetail = textscan(fid, '// %[:]:%[\n]');
columnNames = textscan(fid, '%[\n]', 1);
fclose(fid);

numberOfComments = size(headerDetail{1},1);
f_sampling = str2double(headerDetail{2}{strmatch('Sampling Rate [Hz]',headerDetail{1})});
f_resolution = str2double(headerDetail{2}{strmatch('Frequency Resolution [Hz]',headerDetail{1})});
fft_averages = str2double(headerDetail{2}{strmatch('FFT Averages',headerDetail{1})});
pressure = str2double(headerDetail{2}{strmatch('Atmospheric Pressure [Pa]',headerDetail{1})});
velocity = str2double(headerDetail{2}{strmatch('Tunnel Velocity [m/s]',headerDetail{1})});

% If a reduction is defined, override the settings in the file header

if reduction>1
    f_resolution = f_resolution*reduction;
    fft_averages = fft_averages*reduction;
end

fft_num_samples = f_sampling / f_resolution;

value = UpdateStatus(textField,'> Parsing header... 100%',0);

UpdateStatus(textField,'> Parsing data... 0%',1);
data = csvread(fileName, numberOfComments+1, 0);
UpdateStatus(textField,'> Parsing data... 100%',0);
UpdateStatus(textField,['Processing data (',num2str(f_sampling),' Hz, ',num2str(
fft_num_samples*fft_averages),' samples)'],1);
UpdateStatus(textField,'Processing FFT...',1);

if fft_num_samples*fft_averages==size(data,1)

    fft_results = [];
    fft_results_average = [];

    T = mean(data(1:fft_num_samples*fft_averages,3),1);

    for fft_averaging = 1:fft_averages

        UpdateStatus(textField,['Processing FFT... ',num2str(fft_averaging),' of ',num2str(
fft_averages)],0);

        y1 = data(1+(fft_averaging-1)*fft_num_samples:fft_averaging*fft_num_samples,1);

```

17/10/08 7:36 PM Z:\My Research\Mechanical Engineering - Graduate\Research\Cy...\AverageFFT.m 2 of 3

```

y2 = data(1+(fft_averaging-1)*fft_num_samples:fft_averaging*fft_num_samples,2);

window = hamming(length(y1), 'periodic');
windowConstant = sum(window)/length(y1);
y1 = y1.*window;
y2 = y2.*window;

NFFT = 2^nextpow2(fft_num_samples); % Next power of 2 from length of y
Y1 = fft(y1,NFFT)/fft_num_samples;
Y2 = fft(y2,NFFT)/fft_num_samples;

Y1_results(:,fft_averaging)=abs(Y1(1:(NFFT/2+1)))/windowConstant;
Y2_results(:,fft_averaging)=abs(Y2(1:(NFFT/2+1)))/windowConstant;

% To get the true amplitude, the fft amplitude are scaled by a factor of 2.
% The DC and Nyquist values are unique and are omitted from the scaling.

Y1_results(2:NFFT/2,fft_averaging)=Y1_results(2:NFFT/2,fft_averaging).*2;
Y2_results(2:NFFT/2,fft_averaging)=Y2_results(2:NFFT/2,fft_averaging).*2;

Y1_average = mean(Y1_results,2);
Y2_average = mean(Y2_results,2);

f = f_sampling/2*linspace(0,1,NFFT/2+1);
subplot(2,1,2);

p1 = plot(f,Y1_average);
set(p1,'lineStyle','-','lineWidth',0.1,'color','k',
[0.3,0.3,0.3],'Marker','none','MarkerEdgeColor',[0.2,0.2,0.2],'MarkerSize',1);
hold on;
p2 = plot(f,Y2_average);
set(p2,'lineStyle','-','lineWidth',0.1,'color',[0.4,0.4,1],'Marker','none','MarkerEdgeColor',
[0.1,0.1,0.5],'MarkerSize',1);
hold off;

title('FFT Result','FontSize',8);
xlabel('Frequency (Hz)','FontSize',8);
ylabel('|Y(f)|','FontSize',8);
% set(gca,'FontSize', 8,'YScale','log','YTick',
[0.000001,0.00001,0.0001,0.001,0.01,0.1,1,10,100],'YLim',[0.000001 100],'YLimMode','Manual');
set(gca,'FontSize', 8,'YScale','log','XLim',[0,1000],'XLimMode','Manual','YLim',[0.000001
100],'YLimMode','Manual');

flag = getappdata(gcf, 'run');
if flag==0
    UpdateStatus(textField,'Analysis Terminated! Results were not compiled.',1);
    break;
end
end
end

y1=[];
y2=[];
Y1=[];
Y2=[];

if flag==1
    UpdateStatus(textField,'Processing FFT...100%',0);

```


17/10/08 7:36 PM Z:\My Research\Mechanical Engineering - Graduate\Research\Cy...\AverageFFT.m 3 of 3

```
Y1FFT = Y1_average;
Y2FFT = Y2_average;
XFFT = f.';
T=T;
P=pressure;
Rho=pressure/(287*(273.15+T));
Nu=(1.71*10^-5)*((T+273.15)/273.15)^0.7;
Re=Rho*velocity*0.01525/Nu;

else
Y1FFT = [];
Y2FFT = [];
XFFT = [];
T=0;
P=0;
Re=0;
end

%pause(2);
%while flag
%   flag = getappdata(gcf, 'run');
%end

else

Y1FFT = [];
Y2FFT = [];
XFFT = [];
T=0;
P=0;
Re=0;
UpdateStatus(textField, 'Erraneous data set',1);
pause(2);
%delete(gcf);

end
```

17/10/08 7:44 PM Z:\My Research\Mechanical Engineering - Graduate\Research\C...\Sensitivity.m 1 of 1

```
%%
%% Author: Adam McPhee, University of Waterloo
%% File: Sensitivity.m (function)
%% Last Updated: October 17, 2008
%%
%% Description: Function loads frequency (f) dependant
%% sensitivity (v) data for a specified pressure sensor.
%%

function [S] = Sensitivity(fileName,textField)

UpdateStatus(textField,['Loading sensor data file ',fileName],1);
fid = fopen(fileName);

UpdateStatus(textField,'> Parsing header... 0%',1);
headerDetail = textscan(fid, '// %[^:]:%[\n]');
columnNames = textscan(fid, '%[\n]', 1);
fclose(fid);

numberOfComments = size(headerDetail{1},1);
%f_sampling = str2double(headerDetail{2}{strmatch('Sampling Rate [Hz]',headerDetail{1})});
value = UpdateStatus(textField,'> Parsing header... 100%',0);

UpdateStatus(textField,'> Parsing data... 0%',1);
data = csvread(fileName, numberOfComments+1, 0);
UpdateStatus(textField,'> Parsing data... 100%',0);

f = data(1:size(data,1),1);
v = data(1:size(data,1),4);

S = [f,v];
```

17/10/08 7:44 PM Z:\My Research\Mechanical Engineering - Graduate\Research\Cylin...\Decibel.m 1 of 1

```
%%
%% Author: Adam McPhee, University of Waterloo
%% File: Decibel.m (function)
%% Last Updated: October 17, 2008
%%
%% Description: Function converts an array of pressures from Pascals to Decibels.
%%

function [dBArray] = Decibel(linearArray)

% Replace non-zero values with a value of equivalent to -100dB
zero = find(linearArray <= 0);
linearArray(zero) = 0.0000000002;
dBArray = 20*log10(linearArray./(20*10^-6));
```

17/10/08 7:45 PM Z:\My Research\Mechanical Engineering - Graduate\Research\Cyli...\Strouhal.m 1 of 1

```
%%  
%% Author: Adam McPhee, University of Waterloo  
%% File: Strouhal.m (function)  
%% Last Updated: October 17, 2008  
%%  
%% Description: Function evaluates the Strouhal number (St) for a  
%% specified frequency, diameter, and velocity.  
%%
```

```
function [St] = Strouhal(f,d,U)
```

```
St = f*d/U;
```

17/10/08 7:47 PM Z:\My Research\Mechanical Engineering - Graduate\Research\...\UpdateStatus.m 1 of 1

```
%%  
%% Author: Adam McPhee, University of Waterloo  
%% File: UpdateStatus.m (function)  
%% Last Updated: October 17, 2008  
%%  
%% Description: Function updates display window with status string.  
%%  
  
function statusString = UpdateStatus(stringField,stringValue,new)  
  
stringArray = get(stringField, 'string');  
if new  
    stringArray(size(stringArray,1)+1)={stringValue};  
else  
    stringArray(size(stringArray,1)+0)={stringValue};  
end  
set(stringField, 'string', stringArray);  
drawnow;  
  
statusString=1;
```


Appendix E

Validation Experiments: Results

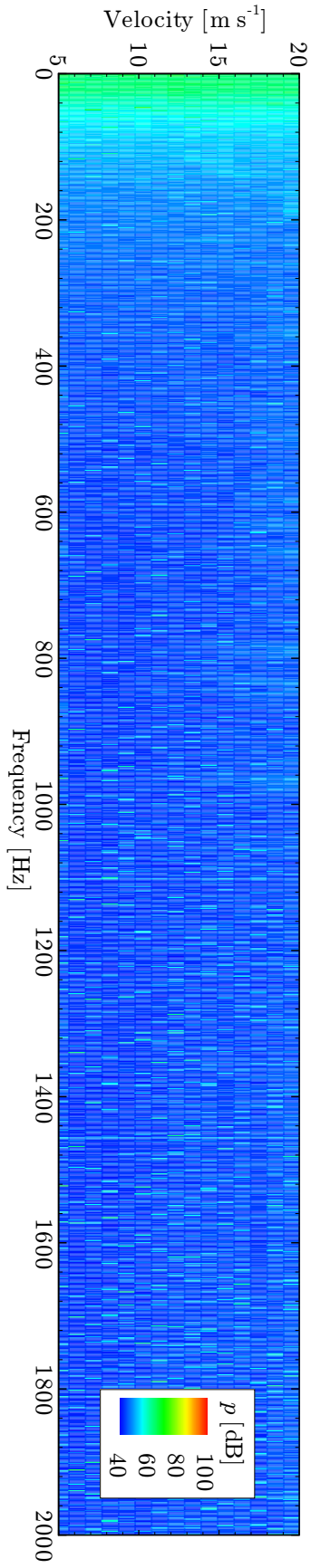


Figure E.1: Near field noise pressure spectra for a range of corrected velocities.

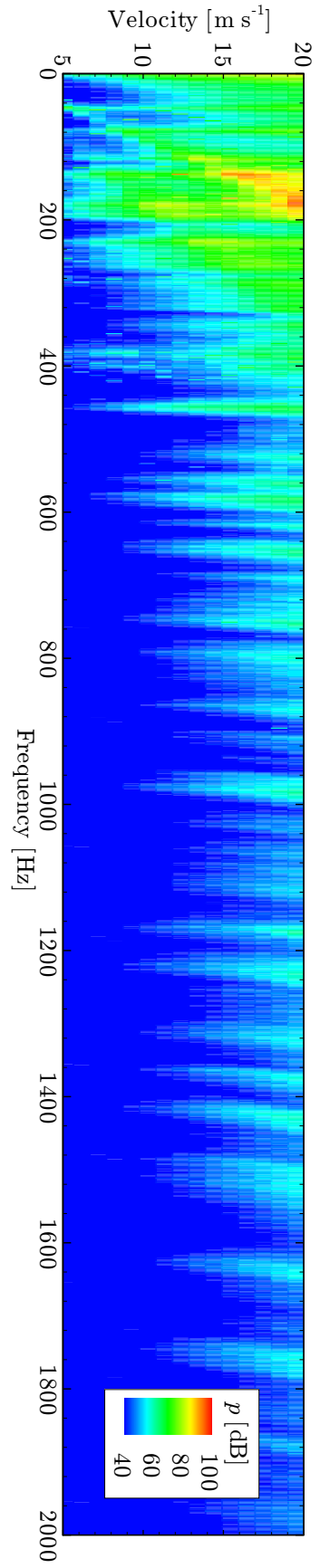


Figure E.2: Far field noise pressure spectra for a range of corrected velocities.